Dielectric Layers of Hybrid Gold@Polystyrene Nanoparticle Inks

Dissertation

zur Erlangung des Grades
des Doktors der Ingenieurwissenschaften
der Naturwissenschaftlich-Technischen Fakultät
der Universität des Saarlandes

von

M.Sc. Roman Buchheit

Saarbrücken

2022

Tag des Kolloquiums: 19.07.2022

Dekan: Prof. Dr. Jörn Walter

1. Berichterstatter: Prof. Dr. Tobias Kraus
2. Berichterstatter: Priv.-Doz. Dr.-Ing. habil. Guido Falk
Vorsitzender: Prof. Dr. Karen Lienkamp
Akad. Mitarbeiter: Dr. Andreas Tschöpe

"Es gibt eine Wirklichkeit hinter der Welt, wie sie uns erscheint, möglicherweise eine vielschichtige Wirklichkeit, von der die Erscheinungen die äußersten Schichten sind. Der große Wissenschaftler stellt nun kühne Vermutungen, riskante Schätzungen darüber an, wie diese inneren Realitäten beschaffen sind."

Karl R. Popper (Lesebuch. Tübingen 1995, S. 107)

Zusammenfassung

Dielectric Layers of Hybrid Gold@Polystyrene Nanoparticle Inks

von M.Sc. Roman Buchheit

Ein neuartiges hybrides Dielektrikum aus Nanopartikeln mit Goldkernen eines Durchmessers von 2, 9-8,2 nm und kovalent gebundenen Thiol-terminierten Polystyrolhüllen (M_n = 5000 und 11 000 Da) wird gezeigt. Aus den Partikeldispersionen wurden durch Rotationsbeschichten dielektrische Filme für Dünnschichtkondensatoren mit Metallgehalten von 5-31 vol% präpariert. Die Partikel ordneten sich je nach Polymerhülle in zufälligen oder kubisch-flächenzentrierten Strukturen an. Filme mit 9 vol% Metall und 2,9 nm großen Kernen hatten Dielektrizitätskonstanten von 98@1 Hz. Kleinwinkel-Röntgenstreuung, Transmissionselektronenmikroskopie und Impedanzspektroskopie deuten an, dass klassische zufallsbedingte Kondensator-Widerstand-Netzwerkmodelle die Materialien teilweise beschreiben. Die Polymerhüllen ermöglichten hohe Metallgehalte ohne das Risiko leitender Pfade. Die dielektrischen Eigenschaften hingen vom Metallgehalt und der Kerngröße ab, nicht aber von der Netzwerkstruktur. Die dielektrische Polarisation findet primär an den Grenzflächen statt und wird in den klassischen Modellen nicht berücksichtigt. Kleinere Kerne erhöhten die internen Grenzflächen bei ähnlichen Metallanteilen um 46 %, was zu 40 % größeren Dielektrizitätskonstanten gemäß dem Maxwell-Wagner-Sillars-Modell führte. Kondensatoren mit einer Kapazität von $2,0 \pm 0,1$ nF@10 kHz über eine Fläche von 0,79 mm^2 wurden mit Tintenstrahldruck auf starren Substraten hergestellt; sie blieben auf flexiblen Substraten über 3500 Biegezyklen intakt.

Abstract

Dielectric Layers of Hybrid Gold@Polystyrene Nanoparticle Inks

by M.Sc. Roman Buchheit

A new type of hybrid dielectric based on nanoparticles with gold cores with diameters of 2.9-8.2 nm and covalently bound thiol-terminated polystyrene shells ($M_n = 5000$ Da and $M_n = 11\,000$ Da) is introduced. Particle dispersions were spin coated as dielectric films of thin film capacitors. The metal contents were 5-31 vol%, and the particles packed randomly or in face-centred-cubic superstructures, mainly depending on the polymer shell. Films with 9 vol% metal and 2.9 nm cores had dielectric constants of 98@1 Hz. Small-angle X-ray scattering, transmission electron microscopy, and impedance spectroscopy indicate that classical random capacitor-resistor network models partially describe the hybrid materials. The covalently attached polymer shells enabled higher metal contents than in conventional nanocomposites without the risk of conductive breakdown. Dielectric properties depended on the metal content and the core size, but not on the network structure. The frequency-dependent dielectric polarization mainly takes place at the interfacial areas, but is not considered in the classical models. Smaller core sizes increased internal interfacial areas at comparable metal fractions by 46 %, resulting in 40 % larger dielectric constants in agreement with the Maxwell-Wagner-Sillars model. Inkjet-printed capacitors were prepared with a capacitance of 2.0 ± 0.1 nF@10 kHz over an area of 0.79 mm^2 on rigid substrates; they retained their functionality over 3500 bending cycles on flexible substrates.

Statement of Contributions and Publication Report

This dissertation project was performed at the INM - Leibniz Institute for New Materials in the program division Structure Formation and is based on contributions of many people from the institute. I want to acknowledge the contributions of these people to the contents of this thesis.

Chapter 4 The TEM images were taken by Dr. Marcus Koch. The FIB cuts were prepared by Birgit Nothdurft. The Raman measurements were performed by Indra Backes. The TGA experiments were performed by Robert Drumm. The AFM measurements were performed by Wiebke Buhrow from the group of Prof. Dr. Roland Bennewitz.

Chapter 5 The contents of Chapter 5 were published in a peer reviewed journal in reference [1].

Buchheit, R., Kuttich, B., González-García, L., Kraus, T., Hybrid Dielectric Films of Inkjet-Printable Core–Shell Nanoparticles. *Advanced Materials* 2021, 2103087.

Author contributions:

The AuNP synthesis, preparation, and analysis of the dielectric layers was performed by Roman Buchheit. Björn Kuttich performed and analyzed the SAXS experiments. Roman Buchheit wrote the manuscript with contribution of Tobias Kraus, Lola González-García, and Björn Kuttich. The research project was directed by Tobias Kraus and Lola González-García. The authors thank Dr. Marcus Koch and Birgit Nothdurft for performing the FIB cuts and TEM images of this work, Robert Drumm for performing the TGA measurements, Prof. Roland Bennewitz and co-workers for the AFM measurements, and Robert Strahl for his support in inkjet printing.

Chapter 6 The TEM images were taken by Dr. Marcus Koch. The FIB cuts were performed by Birgit Nothdurft. The TGA experiments were performed by Robert Drumm. The AFM measurements were performed by Wiebke Buhrow from the group of Prof. Dr. Roland Bennewitz. The SAXS experiments were performed by Dr. Björn Kuttich and Dr. Bart-Jan Niebuur. The inkjet printing and bending experiments were performed with the help of Robert Strahl.

List of Abbreviations and Symbols

AC	alternating current
AFM	atomic force microscopy
AlNP	aluminium nanoparticle
AuNP(s)	gold nanoparticle(s)
CPB	concentrated polymer brush
DC	direct current
DLS	dynamic light scattering
DLVO	Derjaguin, Landau, Verwey, Overbeek
fcc	face-centred cubic
FET(s)	field-effect transistor(s)
FIB	focused ion beam
h-BN	hexagonal boron nitride
HPMC	hydroxypropyl methylcellulose
MSA	mercaptosuccinic acid
MWS	Maxwell-Wagner-Sillars
OAm	oleylamine
OFET(s)	organic field effect transistor(s)
PDI	polydispersity index
PEG	polyethylen glycol
PET	polyethylene terephthalate
PMMA	poly(methyl methacrylate)
povidone	polyvinylpyrrolidone
PP	polypropylene
PS	polystyrene
PS-SH	thiol-terminated polystyrene
PS_{5000}	PS with $M_n = 5000\,\mathrm{Da}$
PS_{11000}	PS with $M_n = 11\,000\,\mathrm{Da}$
PVDF	poly(vinyliden fluoride)
PVDF-TrFE	polyvinylidene fluoride–trifluoroethylene
PVP	poly(4-vinylphenol)
PZT	$Pb(Zr, Ti)O_3$
SAXS	small angle X-ray scattering
SDPB	semidiluted polymer brush
SEM	scanning electron microscopy
TBAB	tetrabutylammonium bromide
TEM	transmission electron microscopy
TFT(s)	thin film transistor(s)
TGA	thermogravimetric analysis
vdW	Van-der-Waals
WLI	white light interferometry
1-D	1-dimensional
2-D	2-dimensional
3-D	3-dimensional
A	area
M_n	number average molecular weight
M_{PS}	molar mass polystyrene
m_{AuNP}	mass of gold core
$m_{organic}$	mass of organic shell per nanoparticle
N	number
N_{AuNP}	number of AuNP
$N_{measured}$	number of measured capacitors
$N_{working}$	number of working capacitors
n	refractive index
n_{mono}	number of monomers
n_{PS}	number of polystyrene ligands per nanoparticle
P	dielectric polarization
Q	electric charge
Q_0	charge of capacitor in vacuum
Q_P	polarization charge
q	wavenumber or critical exponent
$q*$	wavenumber of peak in SAXS
q_{hkl}	wavenumber of reflections of crystallographic planes
R_a	arithmetic average roughness
R_p	resistor/resistivity in parallel
r	radius
r_h	hydrodynamic radius
s	critical exponent
T	temperature
T_{stir}	stirring temperature
t	thickness or time
t_i	thickness of i-th measurement
t_{stir}	stirring time
t_{TBAB}	timing of adding reducing agent
$\tan\delta$	dielectric loss
U	voltage
$\underline{U}$	voltage vector
U_m	maximum voltage
V_{Au}	volume of gold fraction
V_{AuNP}	volume of gold core
V_{bd}	breakdown voltage
V_C	volume of thin film capacitor
w_1, w_2	width of Gaussian peaks
W_{max}	maximal storable energy
$x_{0,1}, x_{0,2}$	position of Gaussian peaks
X_{C_p}	reactance of capacitor in parallel
$x_{w,Au}$	gold weight fraction
Y_{C_p}	modulus of admittance of capacitor in parallel
$\underline{Y}_p$	complex admittance of parallel circuit

A_0	pre-factor
A_{AuNP}	surface of gold core
$A_{\mathrm{interface}}$	interfacial area
a	lattice constant
$a_{\mathrm{s,interface}}$	specific interfacial area
C	capacitance
C_0	capacitance of capacitor in vacuum
C_{p}	capacitor/capacitance in parallel
C'_{p}	real part of capacitance in parallel
c_{Au}	gold concentration
D	dielectric displacement
$\langle D \rangle$	average distance between anchoring points
D_{trans}	translational diffusion coefficient
d_{cc}	centre-to-centre distance
$d_{\mathrm{cc}}^{(\mathrm{rp})}$	centre-to-centre distance random particle packing
d_{core}	core diameter
d_{h}	hydrodynamic diameter
d_{ss}	surface-to-surface distance
d_{TEM}	diameter from TEM size histogramm
E	electric field
E_{bd}	breakdown field strength
F	Flory radius
f_{c}	percolation threshold
f_{v}	volume fraction of filler material
$f_{\mathrm{v,Au}}$	gold volume fraction
$g_1(q,t)^2$	correlation function
I'	real part of complex current
I''	imaginary part of complex current
$\underline{I}$	current vector
$\underline{I}_C$	current through capacitor
I_C	modulus of current through capacitor
I_{m}	maximum current
$I(q,t)$	scattering intensity
$\underline{I}_R$	current through resistor
I_R	modulus of current through resistor
i	imaginary unit
$K(q,r,\Delta\eta)$	form factor
k_{B}	Boltzmann constant

Y'_{p}	real part of admittance of parallel circuit
Y''_{p}	imaginary part of admittance of parallel circuit
$Y_{R_{\mathrm{p}}}$	modulus of admittance of resistor in parallel
$\underline{Z}_{\mathrm{p}}$	complex impedance of parallel circuit
Z'_{p}	real part of impedance of parallel circuit
α	length of a monomer
γ_{l}	surface energy of liquid
γ_{s}	surface energy of solid surface
γ_{sl}	interfacial energy between solid and liquid
$\Delta t_{\mathrm{individual}}$	thickness uncertainty due to local height variation
Δt_{stdv}	standard deviation of thickness
$\Delta\eta$	scatterling length density difference
δ	loss angle
ε_0	vacuum permittivity
ε_{r}	dielectric constant
$\underline{\varepsilon}_{\mathrm{r}}$	complex dielectric constant
$\varepsilon'_{\mathrm{r}}$	real part of complex dielectric constant
$\varepsilon''_{\mathrm{r}}$	imaginary part of complex dielectric constant
$\varepsilon_{\mathrm{r},0}$	dielectric constant connected to insulating component
$\varepsilon_{\mathrm{r},1/2}$	dielectric constant of material 1/2
$\varepsilon_{\mathrm{r,eff}}$	effective dielectric constant
$\varepsilon_{\mathrm{r,s}}$	dielectric constant in static case
$\varepsilon_{\mathrm{r},\infty}$	dielectric constant at infinite high frequency
η	viscosity
θ	scattering angle
θ_{Y}	wetting angle
λ	wavelength
ν	frequency
$\rho_{\mathrm{A,ligand}}$	ligand density
ρ_{Au}	bulk density of gold
ρ_{PS}	bulk density of polystyrene
σ	width of distribution
σ_{M}	conductivity of the matrix
τ	correlation time or relaxation time
φ	phase angle or phase shift
ω	angular frequency or angular velocity
$\dot{\omega}$	angular acceleration

Content

Chapter 1

Motivation

Printed and flexible electronics has become an interesting area for both academia and industry in recent years, showing large potential in addition to the current state-of-the-art silicon-based electronics [2]. Printed electronics enable the cost-effective and flexible design of "smart devices". Such devices play an increasingly important role considering the interconnectivity in technology with more spread usage of automated and interconnected devices. Printed electronics are a promising solution for the widespread, cost-effective, large-scale, and yet flexible production of such devices [2]. Improved inks for printed electronics open up new possibilities in the application of this new technology and are object of research.

Printing and liquid processing is used for different basic electronic elements such as conductive circuits [3] or dielectric layers for capacitors [4–10]. Furthermore, full devices or elements of devices have been developed by liquid processing such as transparent electrodes [11, 12], radio frequency components [13], energy storage devices, e.g. electrochemical capacitors [14], sensors, e.g. for strain [15], or thin film transistors [16–20]. Additionally, printed electronics found applicability in complex devices such as light emitting diodes [21], photovoltaic cells with solution processed components [22], fully printed circuits on textiles or skin [23], or in the medical sector such as printed and customized receiver coils for better magnetic resonance imaging [24].

Dielectric layers are a key component of electronic circuits. Their applications reach from insulation layers [25], dielectric layers in capacitors [26, 27] to gate dielectrics in thin film transistors [28]. For capacitors or gate dielectrics, a high dielectric constant of the dielectric material is desired: the high dielectric constant increases the capacity of a capacitor while maintaining small sizes [29]. In gate dielectrics of thin film transistors, the high dielectric constant allows a reduction of the operational voltage and enhances energy efficient operation of the transistor [30]. For higher effective capacities and small size of the electronic devices, the dielectric layers should be thin while still reliably

insulating to prevent failure of the devices. To allow the usage in flexible electronics, the layers should be mechanically flexible, too. Classical dielectric materials with high dielectric constants such as ceramics cannot be used because they are brittle. For easy processing, the inks should be compatible with common printing and liquid processing methods. Methods such as spin coating, slot-die coating, screen printing, or inkjet printing have been used. Inkjet printing has recently attracted increasing attention in research, as it allows the flexible and digital fabrication process that is compatible both with rapid prototyping and large and cost-effective production while making efficient use of the used materials [31, 32]. Hence, a liquid processable dielectric layer should ideally have a high dielectric constant, allow the fabrication of thin layers, and be compatible with the inkjet printing process.

Flexible solution processed dielectrics can be made from polymers and have been used as printed dielectric layer in capacitors [5, 33]. These polymer dielectrics are easily processed by solution techniques and allow the fabrication of flexible layers, but their dielectric constant is limited due to rather low polarizability of polymers. Hence, dielectric nanocomposites have been investigated in the past decades to combine the flexibility of polymer layers with a high dielectric constant. First, oxide particles with high dielectric constants were combined with polymer solutions [34]. These approaches are limited in filling ratios mainly due to inhomogeneous electric fields: the large contrast of the dielectric constant of the oxide particles and the polymer matrix causes field intensifications that can lead to dielectric breakdown at much lower electric fields than the intrinsic breakdown strength of the polymer [29, 35]. Recently, functional inks with oxide particles that were functionalized with covalently attached polymers have been used successfully to print dielectric layers in fully inkjet printed capacitors [10].

Another promising approach is the incorporation of conductive particles into an insulating polymer matrix. As predicted by the percolation theory, which was initially used to analyze the appearance of conductivity in globally connected systems, the dielectric constant increases dramatically near a critical value of the volume ratio of the conductive phase in heterogeneous materials with a conductive and insulating component. This critical value is called percolation threshold and describes the point where a global connection of the conductive phase in the composite is expected. The dielectric constant increases in a non-linear manner when the volume fraction of the conductive particles approaches the percolation threshold [36]. The increase of the dielectric constant is physically explained by the formation of a microcapacitor network, which is formed by the conductive filler particles that are separated by the insulating matrix [37, 38]. The high dielectric constant relates to an increased polarization of the composite material in the electric field of the capacitor. An important polarization mechanism of these conductor-insulator composites is the interfacial polarization at the interfaces between

the conductive and the insulating phase, but also at the interfaces to the electrodes [36]. Therefore, nanocomposites with conductive nanoparticles in an insulating matrix are a promising candidate for this kind of materials as large interfacial areas are formed between the conductive and insulating component. For instance, gold nanoparticle dispersions mixed with polymer solutions have been used to create dielectric layers via spin coating [39, 40]. The gold volume fraction was limited due to the formation of agglomerates and observed failure of the dielectric layer when a conductive path is formed. Another approach was the creation of aluminium/polypropylene nanocomposites, where the polypropylene layers were covalently attached on the Al cores and led to effective insulation of the Al particles to prevent percolation [41]. The catalytic growth of the polypropylene chains on the Al nanoparticle surface needed the inert environment of a glove box and the resulting nanocomposite was processed via pressing to dielectric layers. Thus, this approach was not compatible with liquid processing methods. To the author's best knowledge, dielectric layers of conductive particles embedded in insulating matrix and fabricated by inkjet printing have first been reported in the literature with the publication of results that form part of this thesis [1].

This thesis extends the concept of hybrid inks of functionalized gold nanoparticle that has successfully been used before to formulate inks for the printing of conductive layers without a post-printing sintering step [3, 42, 43]. The thesis is structured as follows: in Chapter 2, the theoretical background and the current state of the art in liquid processed dielectric layers and Au nanoparticles are discussed. In Chapter 3, the experimental methods for the ink synthesis, the layer preparation, and for investigating the ink and layer properties are described in detail. Succeeding, Chapters 4, 5, and 6 demonstrate and discuss the results obtained in this thesis: dielectric layers based on gold-polystyrene core-shell nanoparticles (Au@PS NPs) are fabricated by Au@PS hybrid inks and investigated in a bottom-up approach [44]. In the first results chapter, basic studies for the usage of Au@PS hybrid inks, such as influences on the ligand exchange process or suitable substrates, are presented. The second results chapter shows a study of the dielectric layer properties with constant Au core size but varying organic content and particle packing due to different ligand density and ligand length. Furthermore, thin film capacitors with dielectric layers printed on rigid substrates are demonstrated in this chapter. The last results chapter presents the influence of varying Au core size on the properties of the Au@PS inks and on the properties of Au@PS dielectric layers. Additionally, the printing of Au@PS layers on flexible PET substrates is demonstrated. Finally, Chapter 7 summarizes the main results obtained in this thesis and gives an outlook for possible future studies.

Chapter 2

Theory and State of the Art

In this chapter, the state of the art about the topics important for this thesis is provided. In the first section, basics about dielectric materials and the common application of dielectrics in capacitors are presented. Thereafter, examples for liquid processed dielectrics are given. First, standard dielectrics based on polymers, spin-on, or sol-gel inorganic materials are presented. Then, the state of the art in dielectric nanocomposites that combine the advantages of different material classes as well as the new concept of the hybrid dielectric material, which is investigated in this thesis, are presented. Finally, the basics of non-polar gold nanoparticles with a polymer-shell that were used in this work for the hybrid dielectrics are summarized. To this end, their behaviour depending on the ligand molecules and the solvent is presented.

2.1 Basics dielectrics

Dielectric materials are insulating materials that influence electric fields, e.g. between the electrodes of a capacitor, by electrical dipoles. Those dipoles can be permanent, oriented, or induced by electric fields [27]. The important material constants to describe a dielectric material are the volume conductivity, which is classically below the range of $\mathrm{nS\,cm^{-1}}$ [27], the relative dielectric permittivity ε_r, which is often called dielectric constant (in electrical engineering also called k-factor), the dielectric loss tangent $\tan\delta$, and the breakdown field strength E_bd.

Two main classes of dielectrics are distinguished by comparison with the dielectric constant of SiO_2, a very common dielectric material ($\varepsilon_{\mathrm{r,SiO2}} = 3.9$ [30]). "Low-k dielectrics" or "passive dielectrics" have a dielectric constant below that of SiO_2 [27, 30, 34] and are commonly used for the insulation of signal carrying conductors. The low dielectric constant reduces unwanted parasitic capacitances [34] and can be achieved for instance by fabrication of porous dielectrics with void volume [45].

"High-k dielectrics" have dielectric constants above that of SiO_2 [30, 34]. These "active dielectrics" possess a high polarizability of the materials and are used as dielectrics in capacitors [26], as dielectric gate dielectrics in field-effect transistors (FETs) [28, 46–48], as ferroelectric materials with permanent polarization [49], and as piezoelectric materials with conversion between mechanical and electrical signals [50]. Here, high dielectric constants are important to increase the amount of charges stored in a capacitor at small geometrical sizes or to obtain a good switching behaviour of field-effect transistors at low operational voltage (Figure 2.1). Additionally, the leakage currents should be minimal as they either lead to charge losses in capacitors or increased power consumption in FETs. This thesis focuses on high-k dielectrics and their usage in capacitors.

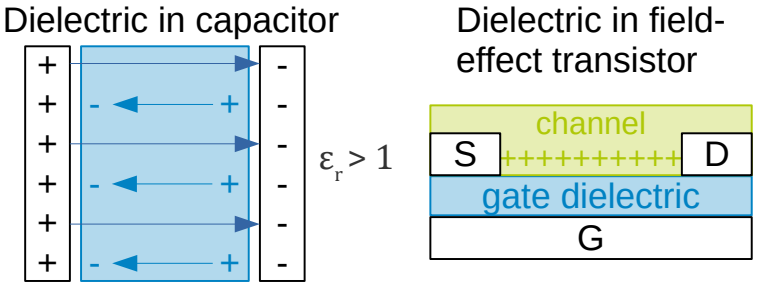

FIGURE 2.1: Schematic examples for common applications of active dielectrics. Left: In capacitors, the field that forms due to polarization of the dielectric opposes the external electric field and more charges are bound on the capacitor plates. Right: In field-effect transistors, the gate dielectric enhances the field that is created when a switching voltage is applied at the gate (G). Charges are accumulated in the semiconducting channel and can flow from source (S) to drain (D).

2.1.1 Capacitors

A capacitor is a passive electrical device that can store electric charge and the related energies in an electric field. The stored electric charge Q depends on the applied voltage U; the amount of stored charge is then given by the capacitance C [51]:

$$C = \frac{Q}{U} \tag{2.1}$$

The capacitance of a parallel plate capacitor is given by [51]:

$$C = \varepsilon_0 \varepsilon_\mathrm{r} \frac{A}{t} \tag{2.2}$$

where $\varepsilon_0 = 8.854\,19 \times 10^{-12}\,\frac{\mathrm{F}}{\mathrm{m}}$ is the vacuum permittivity [52], ε_r the dielectric constant or (the real part of) the relative permittivity of the dielectric between the capacitor plates, A the area of the capacitor plates, and t the distance between the two capacitor plates.

If the space between the capacitor plates is filled with vacuum or air, the capacitance is only determined by the geometry of the parallel plates. A dielectric material increases the capacitance due to polarization effects that are discussed in Section 2.1.2.

The maximum energy that can be stored in a capacitor depends on the capacitance and on the electric breakdown strength, E_{br}, the maximum electric field that the dielectric material of the capacitor can sustain. Exceeding of the electric breakdown strength leads to a dielectric breakdown, where an electric current will flow through the dielectric, and failure of the capacitor occurs [27, 53]. The maximum storable energy $W_{\max}$ is given by [26, 51]:

$$W_{\max} = \frac{1}{2}\varepsilon_0\varepsilon_{\mathrm{r}} A t E_{\mathrm{br}}^2 = \frac{1}{2} C \left(t E_{\mathrm{br}}\right)^2 \tag{2.3}$$

If an alternating current (AC) voltage is applied at an ideal capacitor, the current will always lead the voltage by the phase shift $\varphi = 90°$ in the current-voltage vector diagram [27]. The ideal capacitor can release again all the energy of stored charge without any dissipation effects.

A real capacitor always shows "losses" due to remaining conductance of the dielectric layer and energy dissipation during the polarization processes. A "lossy" capacitor is often represented by an equivalent circuit of an ideal capacitor and an ideal resistor connected in parallel or in series [53]. In this thesis, an equivalent circuit of an ideal capacitor C_{p} and an ideal resistor R_{p} in parallel will be used (Figure 2.2).

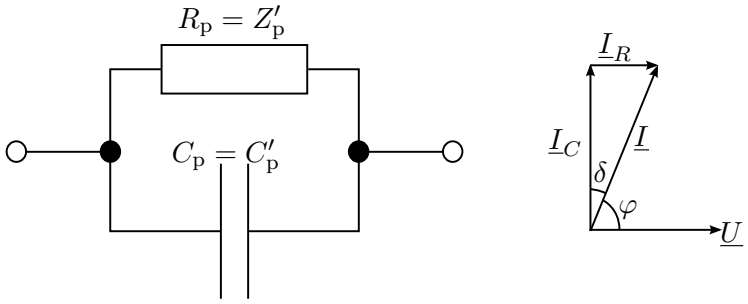

FIGURE 2.2: Parallel equivalent circuit with an ideal resistor R_{p} and an ideal capacitor C_{p} for description of a real capacitor with losses and the corresponding current-voltage vector diagram (adapted from [54]). If a voltage $\underline{U}$ is applied, the current through the ideal resistor $\underline{I}_R$ is in phase with the voltage and the current through the ideal capacitor $\underline{I}_C$ lags behind the voltage by a phase shift of 90°. The vector sum of the two currents results in $\underline{I}$ and represents the behaviour of the real capacitor. The phase shift between voltage and current $\varphi < 90°$ is reduced by the loss angle δ.

The current-voltage vector diagram in Figure 2.2 shows that the phase shift in a real capacitor will be reduced by the loss angle δ. At every charge/discharge cycle of the capacitor, some of the energy will be dissipated to heat and cannot be restored. This

energy loss is often specified by the loss tangent $\tan\delta$ [26, 27]

$$\tan\delta = \frac{\varepsilon_\mathrm{r}''}{\varepsilon_\mathrm{r}'} = \frac{I_R}{I_C} \tag{2.4}$$

where ε_r'' and ε_r' are the imaginary and real part of the complex dielectric constant and I_R and I_C the modulus of the current through the resistor and the current through the capacitor in an RC parallel equivalent circuit of a "lossy" capacitor.

Equation (2.4) implies that $\underline{\varepsilon}_\mathrm{r}$ is a complex number [55]:

$$\underline{\varepsilon}_\mathrm{r}(\omega) = \varepsilon_\mathrm{r}'(\omega) - \mathrm{i}\varepsilon_\mathrm{r}''(\omega) \tag{2.5}$$

with the imaginary unit i. The complex dielectric constant $\underline{\varepsilon}_\mathrm{r}$ is generally dependent on the angular frequency ω of the applied AC voltage, as the underlying polarization mechanisms are frequency dependent. In this thesis, the real part of the complex dielectric constant will generally be noted simply as ε_r.

In short, an effective capacitor should contain a dielectric material, which provides both a high dielectric constant ε_r and a low dielectric loss $\tan\delta$.

2.1.2 Polarization mechanisms in dielectrics

The modulus of the homogeneous electric field E in a capacitor with vacuum between the electrodes ($\varepsilon_\mathrm{r} = 1$) is caused by the amount of charges Q_0 stored on the capacitor plates (see Equation (2.1) and Equation (2.2)):

$$E = \frac{U}{t} = \frac{Q}{Ct} \overset{(\varepsilon_\mathrm{r}=1)}{=} \frac{Q_0}{C_0 t} = \frac{Q_0}{\varepsilon_0 A} \tag{2.6}$$

In a dielectric material with conductivity $\sigma_d = 0$ located between the capacitor plates, the mobile permanent or induced dipoles interact with the external field and will partly align like it is schematically shown in Figure 2.1 on the left. Additional polarization charges Q_P can be stored at the capacitor plates. The dielectric displacement D is defined as the charge density with the sum of both charges Q_0 and Q_P [56]:

$$D \equiv \frac{Q}{A} = \frac{Q_0 + Q_\mathrm{P}}{A} \tag{2.7}$$

The dielectric polarization is defined as the charge density of these additional charges [56]:

$$P \equiv \frac{Q_\mathrm{P}}{A} \tag{2.8}$$

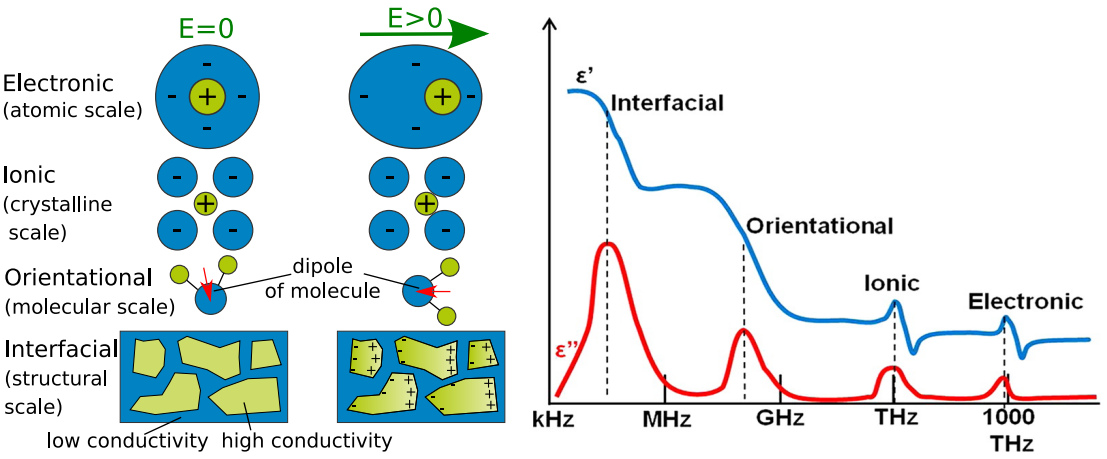

FIGURE 2.3: Left: Fundamental polarization mechanisms. Right: Frequency dependency of polarization mechanisms (adapted and reprinted with permission from [57]. Copyright 2012 American Chemical Society.).

The dielectric displacement can be expressed by the sum of the electric field strength and the polarization [27, 56]

$$D = \varepsilon_0 \varepsilon_\mathrm{r} E = \varepsilon_0 E + P \tag{2.9}$$

with ε_r being the relative permittivity of the dielectric constant.

Because the orientation of the induced or permanent dipoles shows different time characteristics, the four polarization mechanisms show different dependencies on the frequency (see Figure 2.3).

The first mechanism is electronic polarization caused by a shift of the negatively charged electron shell around the positively charged atomic core [27, 53, 55]. The second mechanism is based on ions that undergo an elastic displacement in the electric field [27, 53]. Both mechanisms show characteristic resonance frequencies where the real part of the relative permittivity ε'_r changes its sign and the imaginary part ε''_r has a maximum at high frequencies of around 1×10^{15} Hz for electrons and of around 1×10^{13} Hz for ions [53].

The third mechanism is the orientational polarization in materials with permanent dipoles. The dipoles orient themselves in the electric field, but molecules or segments of molecules move relatively slowly and the mechanism depends strongly on the temperature [53]. Entropic reasons however favour a random alignment of the dipoles; therefore, the orientational polarization is temperature dependent. Furthermore, the orientational polarization is characterized by a relaxation process [27]. This relaxation is described

by the Debye equations: the real part of the dielectric constant is given by [53]

$$\varepsilon'_{\mathrm{r}} = \frac{\varepsilon'_{\mathrm{r,s}} - \varepsilon'_{\mathrm{r},\infty}}{1 + \omega^2\tau^2} + \varepsilon'_{\mathrm{r},\infty} \tag{2.10}$$

and the imaginary part of the dielectric constant is given by [53]

$$\varepsilon''_{\mathrm{r}} = (\varepsilon'_{\mathrm{r,s}} - \varepsilon'_{\mathrm{r},\infty})\frac{\omega\tau}{1 + \omega^2\tau^2} \tag{2.11}$$

with the real part of the dielectric constant in the static (or low frequency) case $\varepsilon'_{\mathrm{r,s}}$, the real part of the dielectric constant at infinite high frequencies $\varepsilon'_{\mathrm{r},\infty}$, the angular frequency ω, and the relaxation time τ. The visualization of Equation (2.10) and Equation (2.11) is characterized by a drop in the real part of the relative permittivity $\varepsilon'_{\mathrm{r}}$ and a peak of the imaginary part $\varepsilon''_{\mathrm{r}}$. The orientational polarization is observed at rather low frequencies until up to 1×10^{10} Hz [53].

In materials with conductive and non-conductive phases, for example nanocomposites, interfacial polarization can take place [34, 58]. It is also known as space charge polarization [27] or Maxwell-Wagner-Sillars (MWS) polarization [39, 59–61]. MWS polarization often is more precisely used for the polarization at interfaces within the dielectric material, in contrast to the polarization at the interface of the electrodes and the dielectric material [57]. The interfacial polarization is observed at low frequencies in the MHz range or even below [57]. The charge carriers in the conductive areas are accumulated at the interfaces to the non-conductive areas. This polarization effect depends strongly on the morphology of the dielectric material. For instance, the conductive phase could be grains of an polycrystalline materials with insulating grain boundaries [27]. Also, metallic nanoparticles in an insulating polymer matrix can cause large space charge polarization at the large interface between the conductive and non-conductive areas (see Figure 2.4). As the accumulation of charges is a process that involves the displacement of charge carriers, it is characterized by a relaxation time that depends on the morphology and microstructure of the dielectric material [27]. The polarization of composites can be described by the MWS theory [57, 59]: First Wagner theoretically described the polarization of conductive spheres in an insulating matrix [62] and later Sillars extended this theory by the inclusion of conductive particles with planar, cylindrical, and ellipsoidal shape in an insulating matrix [63].

2.2 Liquid processing of particle-based inks

Dielectric layers can be created by easy and cost-effective liquid processing [64], e.g. layers of polymers, nanocomposites, or ceramics. A liquid precursor of the later solid

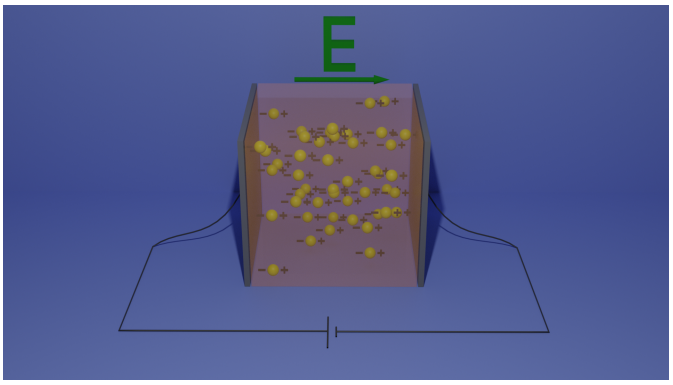

FIGURE 2.4: Schematic mechanism of the increase of dielectric constant by conductive fillers. An external field moves the free charges in the conductive filler materials to the interface of the non-conductive matrix and Maxwell-Wagner-Sillars polarization occurs.

dielectric layer or particles dispersed in a solvent are required. In this thesis, spin coating and inkjet printing of an ink were used for preparation of dielectric layers. Particle-based inks should be stable against aggregation of solid substances in the ink for a long shelf life [32]. Sometimes opposing objectives must be considered: a very stable and easily recoverable ink uses a solvent that possesses low evaporation rates. However, after the application, the solvent must evaporate to form the dry film [65]. These dry films should show a sufficient adhesion to the substrate [32]. In the following, the general ink-substrate interaction and the spin coating and inkjet printing methods will be discussed.

2.2.1 Ink-substrate interaction

The liquid precursors — solutions or dispersions — are generally called "ink". For a high wettability, the surface energy (or surface tension) of the ink and the surface energy of the substrate are important parameters [65]. As a rule of thumb, the wettability improves with decreasing surface energy of the liquid ink and with increasing surface energy of the substrate [65]. The thermodynamic equilibrium of a droplet's wetting is described by the Young's equation [66]

$$\cos\theta_{\mathrm{Y}} = \frac{\gamma_{\mathrm{s}} - \gamma_{\mathrm{sl}}}{\gamma_{\mathrm{l}}} \tag{2.12}$$

where θ_{Y} is the wetting angle, γ_{s} is the surface energy of the solid substrate surface, γ_{sl} is the interfacial energy between solid and liquid, and γ_{l} is the surface energy of the liquid ink. For good wetting, on the one hand, the surface energy of the substrate can be increased by wet chemical treatment, e.g. thoroughly cleaning or etching, or by plasma activation [67]. On the other hand, the surface tension of the inks depends strongly on the solvent. For instance, water has generally larger surface tension than isopropyl alcohol that can form the base of an organic ink [65]. Also, for slower evaporation, solvent mixtures or slow evaporating solvents can be used [68].

2.2.2 Spin coating

Spin coating is a procedure to coat substrates homogeneously with thin layers by spreading a liquid ink on the substrate via centrifugal forces. The layer thickness depends on the ink (e.g. on the concentration of the ink) and on the process parameters, mainly the rotation velocity of the substrate during the coating process. After dispensation of the ink, the rotation of the substrate causes spreading of the ink. In the first phase of rotation, a smooth liquid film is formed. Then, the solvent will start to evaporate, which is mainly influenced by the solvent vapour pressure [69]. When the solvent evaporates, the liquid film is drying and finally a dry film is formed [70]. As a rule of thumb, the final film thickness will increase with the concentration of the solid content of the ink and with the ink viscosity and will decrease with the square root of the rotational velocity [71].

For the dispensation, the ink is put on a substrate by either a static dispense (on a not rotating substrate) or by a dynamic dispense (on a rotating substrate). The spin coating process can be applied with small amounts of ink and smooth surfaces with homogeneous thickness can be achieved. However, droplets of excess ink fall from the substrate during rotation and cannot always be retained. In this case, the process wastes some of the used material.

2.2.3 Inkjet printing

Inkjet printing technology deposits liquid droplets on the substrate [31]. The promising advantages of inkjet printing are the possibility of automatized layer fabrications, the easy variance of printing patterns, e.g. for rapid prototyping, and the very economical usage of the ink that can save costs.

The droplets are either ejected via a “continuous inkjet”, where unprinted drops are deflected by an electric field and returned for reuse, or in a “drop-on-demand inkjet”, where droplets are only formed when required [32]. For high precision and reproducibility of the inkjet printing process, the droplets should be ejected in a controlled direction and with the right velocity, while the requirements of precision increase with increasing distance between print head and substrate [32]. In the initial ejection process, the ink is flowing from a tank to the print head, where the ink is ejected by a piezo crystal (or by heating in thermal inkjet printing) and an ink ligament leaves the print head at the nozzle. When the ink ligament breaks down, the droplets are formed. Often, the ligament not only breaks into large main droplets, but also in several other small “satellite” droplets [65]. These satellite droplets are usually not desired, as they possess

rather uncontrollable direction and velocity and reduce the printing quality. The main material parameter that influences the droplet formation is the surface tension of the ink: as a rule of thumb, the droplet volume will decrease with lower surface tension of the ink [72]. Next to the surface tension, other important material parameters are the ink viscosity, the ink density, and the particle size in particle-based inks. These material parameters of the ink together with process parameters such as the nozzle diameter or the droplet velocity of the print head are often combined to dimensionless numbers of fluid mechanics to predict the "window of operation" of an ink with a certain print head [73]; the Reynold number, the Weber number, or the Ohnesorge number are often used in literature [65].

Clogging of the nozzle has to be avoided. As a rule of thumb, particles and particle agglomerates in the ink should not exceed 1 % of the nozzle diameter because large agglomerates will increase the viscosity of the ink and hinder the flow of ink to the print head, which can ultimately lead to clogging of the nozzle [65]. Furthermore, the solvent should not evaporate before jetting. After the droplets hit the substrate, the drying of the droplets is also important for the layer quality. The so-called "coffee-ring effect" arises from pinning of the edge of the droplet on the substrate and accumulation of solid material at the droplet edge during solvent evaporation [74]. As a result, the solid material in the final dried droplet is more concentrated on the edges than in the centre of the droplet, causing an inhomogeneous printing result.

2.3 State of the art in liquid processing of dielectric films

Well-established dielectric materials have been prepared by liquid processing methods. On the one hand, polymer materials have been used that are easily soluble at low temperatures but have rather low dielectric constants [34]. On the other hand, ceramic materials were fabricated that have high dielectric constants but require high process temperatures [34]. Nanocomposites have been developed to combine the advantages of both material classes. Table 2.1 shows examples of the different material classes that were processed by inkjet printing (for conductor-insulator composites also by spin coating or hot pressing), the typical post-treatment temperatures, which influence the compatibility with substrates, and the resulting layer properties. Details of the different material classes and their processing are discussed in the following.

TABLE 2.1: Dielectric layers reported in literature with the respective dielectric constant ε_r and respective thickness t. The focussed fabrication method was inkjet printing, conductor-insulator composites were also prepared by spin coating and hot pressing.[1]

Material	Solvent	Processing	Post-treatment	Dielectr. const. ε_r	Thickness t	Reference
PVP	N/A	inkjet	curing 130 °C	3.9	70 to 200 nm	[75]
polymethylsilsesquioxane spin-on-glass	alcohol mixture	inkjet	anneal 135 °C	3	210 nm	[76]
tantalum-oxide sol-gel	2-methoxyethanol, glycerol, 1,3-propanediol	inkjet	anneal 450 °C	20	60 nm	[6]
Al_2O_3 sol-gel	ethanol, 2-methoxyethanol	inkjet	anneal 400 °C	6.2	120 nm	[13]
$Ba_{0.6}Sr_{0.4}TiO_3$ sol-gel	butanol	inkjet	anneal 1100 °C	1000	420 nm	[77]
$BaTiO_3$ in epoxy resin	N,N-dimethylformamide	inkjet	cure resin 280 °C	70	20 µm	[78]
$BaTiO_3$ in PVP	ethanol	inkjet	N/A	7.4	1.06 µm	[79]
$Ba_{0.6}Sr_{0.4}TiO_3$ in PMMA	particle dispersion: diglycol, solvent of PMMA: butanone	inkjet	anneal 150 °C	28	7.2 µm	[80]
$Ba_{0.6}Sr_{0.4}TiO_3$ in PMMA	particle dispersion: butyldiglycol, solvent PMMA: butanone	inkjet	anneal 120 °C	20-55 @1kHz	≈ 4 µm	[8]
$Ba_{0.6}Sr_{0.4}TiO_3$ in PEG diacrylate	particle dispersion: butyl diglycol, crosslinker dispersion: isopropanol	inkjet	not needed	40	700 nm	[10]
h-BN	propylene glycol, H_2O, xanthan gum	inkjet	anneal 150 °C	6.1	3 µm	[9, 81]
h-BN in HPMC	H_2O with propylene glycol	aerosol inkjet	drying 80 °C	3.01	2.54 µm	[82]
Ag@MSA in epoxy	acetone	spin coating	curing 160 °C	300	10 µm	[83]
Ag@C in epoxy	ethylene glycol monomethyl ether	spin coating	drying 40 °C	400	85 µm	[84]
Au@C12-SH in SU-8	chloroform	spin coating	baking 95 °C	13.6 @1kHz	2 µm	[39]
Au@povidone in PVDF	N,N-dimethylformamide	spin coating	dry 100 °C	22 @1kHz	N/A	[40]
Al@Al_2O_3 in PP	-	hot pressing	pressing 130 °C	15.4	10 µm	[41, 57]

[1] Abbreviations: poly(4-vinylphenol) (PVP), poly(methyl methacrylate) (PMMA), hexagonal boron nitride (h-BN), hydroxypropyl methylcellulose (HPMC), poly(ethylene glycol) (PEG), polyvinylpyrrolidone (povidone), mercaptosuccinic acid (MSA), poly(vinyliden fluoride) (PVDF), polypropylene (PP).

2.3.1 Polymer dielectrics

The first insulating dielectric inks were polymer solutions. Various polymer-based inks were processed by inkjet printing. This allowed the fabrication of fully printed and flexible capacitors. For example, SU-8 and poly(4-vinylphenol) (PVP) based dielectrics for radio frequency capacitors were inkjet printed on polyimide [85]. SU-8 has a dielectric constant of 3.4 to 4.0 [7], which reduces the achievable capacities in comparison to capacitors with oxide dielectric layers of the same geometry. To increase the capacity with polymer dielectrics, very thin dielectric layers can be used. Exploiting the coffee-ring effect, the thin and homogeneous valley area in the centre of the dried droplets was used to inkjet print dielectric layers for capacitors and gate dielectrics of thin film transistors (TFTs) with a PVP based commercial ink [75]. A UV-curable dielectric ink based on PVP was printed on textile for flexible capacitors in wearable electronics [86]. Another PVP based dielectric ink was used for inkjet printed radio frequency inductors and capacitors [13] or for inkjet printed capacitors on flexible polyimide substrates [33]. Polymer-based inks are commercially available. Commercial inks containing UV-curable high resistivity polymers were used in printing of microfluidic devices [87] or in inkjet printing of capacitive circuits for biosensors [88].

Polymer dielectrics were also used as gate dielectrics in printed and flexible electronics. A challenge for flexible polymer foil substrates can be high curing temperatures over 200 °C after printing for polyimides [76]. In TFT gate dielectric applications, polymer dielectrics can cause problems due to trap states, especially for n-type semiconductors [89, 90]. For instance, PVP as dielectric possesses many trap states, which could be reduced by cross linking of the polymer and improve the performance of an organic field-effect transistor (OFET) with n-type semiconductor [76].

Higher dielectric constants can be achieved by polymers with permanent dipoles in the polymer chain, for instance poly(vinyliden fluoride) (PVDF) and derived fluoropolymers [91]. These ferroelectric polymers additionally show a high breakdown strength and reach high energy densities up to $27\,\mathrm{J\,cm^{-3}}$ as calculated by Equation (2.3) [29]. PVDF based inks were developed for inkjet printing, but the layers had to be sintered after printing at 140 °C to form the crystalline β-phase [92], which is the phase with a spontaneous polarization in a unit cell due to a uniform *all-trans* conformation of the molecules [93].

2.3.2 Spin-on dielectrics and sol-gel inorganic dielectric layers

Solution processed inorganic dielectric layers include spin-on glass materials based on polysiloxane solutions and sol-gel layers that are printed from precursor inks. The necessary curing step at temperatures ranging from 135 °C (spin-on-glass, [76]) to 1100 °C (sol-gel, [77]) after printing can limit the compatibility of the ink with flexible polymer substrates.

2.3.2.1 Spin-on dielectric layers

Spin-on glass layers can be fabricated with comparatively low curing temperatures and can be compatible with flexible polymer substrates. For instance, cross linked spin-on glass layers with few trap states for electrons on a n-type semiconductor channel material and a low annealing temperature of 135 °C allowed OFETs on flexible polyethylene terephthalate (PET) foil substrates by inkjet printing [76]. The thickness was 210 nm and could be tuned by dilution of the ink with solvents.

Cross linked spin-on glass layers were also used as dielectric in fully inkjet printed resistively switching memory cells in a Ag/spin-on-glass/poly(3,4-ethylenedioxythiophene) polystyrene sulfonate stacking; a curing temperature as low as 200 °C permitted printing on flexible polyethylene naphthalate foil [94]. Resistively switched memory cells in a Ag/spin-on-glass/Ag stacking were also inkjet printed with an integrated microbattery [95].

2.3.2.2 Sol-gel dielectric layers

Reports of sol-gel dielectric layers used considerably higher annealing temperatures after printing of a precursor ink, limiting the compatibility with flexible substrates. Early work used $Ba_{0.6}Sr_{0.4}TiO_3$ dielectrics for tunable circuits (the capacitance could be reduced by application of a direct current (DC) bias) from sol-gel precursors, where the layers were annealed at 1100 °C for 3 h in O_2 on MgO substrates [77]. Other oxides as a ZrO_2 dielectric for TFT [96], Sr-doped Al_2O_3 layers on inkjet printed channels of TFTs [18], or ZrO_x and $Sc_1Zr_1O_x$ dielectrics for thin film transistors on glass [19, 97] were also created by inkjet printing or spin coating of precursor inks. However, dielectric inks were prepared by a top-down approach, too, where ZnO powder was milled until a stable dielectric ink in ethylene glycol could be achieved that was suitable for inkjet printing [98]. Arrabito *et al.* provided a detailed review how to process ZnO nanocrystalline inks to different electronical devices [99].

Various groups reported inkjet printed sol-gel layers as dielectric in capacitors. Dielectric layers for radio frequency capacitor application were inkjet printed with an ink based on $Al(NO_3)$ and a solvent mixture of 2-methoxyethanol and ethanol resulting in Al_2O_3 films with dielectric constants of 6.2 and a low loss tangent of 0.005 [13]. A mixture of solvents reduced the coffee ring effect of sol-gel precursor inks to print capacitors with Ta_2O_5 dielectric layers [100]. Also, fully transparent thin film capacitors were inkjet printed with indium-zinc-oxide electrodes and tantalum oxide as the dielectric layer [6].

Printed sol-gel dielectrics have also been used as gate dielectric. An Al_2O_3 dielectric was inkjet printed as gate dielectric in TFTs [20]. Finally, also alternative printing techniques were used for sol-gel based dielectric layers, e.g. slot die coating, to print organic-inorganic nanohybrid dielectric films as organic TFT gate dielectric on silicon [101].

2.4 Structure, theoretical description, and studies on dielectric nanocomposite materials

Composite materials are fabricated from at least two ingredient materials. Furthermore, dielectric composite materials combine the properties of polymer and inorganic materials. Dielectric composite materials with particles embedded in a matrix material do not show interparticle air void volumes, which would lower the dielectric constant and reduce the breakdown strength [29]. The composite materials are often classified following Newnham *et al.* as shown in Figure 2.5. Particles (0-dimensional objects) that are surrounded by a 3-dimensional (3-D) matrix are referred as 0-3 composites, wires (1-dimensional (1-D) objects) that are surrounded by a 3-D matrix would be 1-3 composites, and a layered material (2-dimensional (2-D) objects separated by a 2-D matrix) would be a 2-2 composite.

In the following, nanocomposite materials with dielectric particles of a high dielectric constant (e.g. ceramics) in a dielectric medium (e.g. polymer) are called “Type I” composites. Nanocomposites with conductive particles (e.g. metals) randomly dispersed in an insulating dielectric medium are called “Type II” composites. A new type with conductive nanoparticles that are individually insulated by covalently attached shells is named “Type III” hybrid. The different nanocomposites are shown in Figure 2.6.

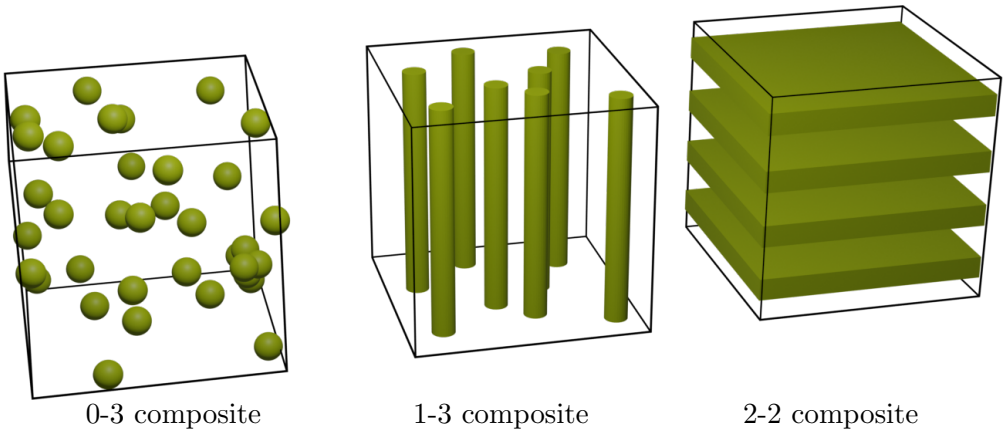

FIGURE 2.5: Types of nanocomposite materials following the classification of Newnham [102].

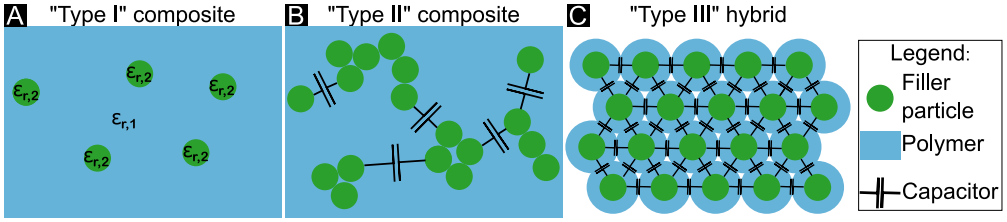

FIGURE 2.6: Types of particle-based dielectrics and their electrical modelling. a) Type I composites have dielectric particles in a dielectric medium. b) Type II composites have conductive particles randomly dispersed in a dielectric medium. c) Type III hybrids that will be studied in this thesis have metal nanoparticles that are individually insulated by covalently attached polymer shells. Reprinted with permission of Wiley-VCH GmbH, from [1].

2.4.1 Type I nanocomposites: particles of high dielectric constant in a low dielectric constant matrix

In Type I nanocomposites, filler materials with a high dielectric constant (e.g. ceramics) are introduced in an insulating matrix (e.g. a polymer) to combine a high effective dielectric constant and the easy processing properties of polymers (see Figure 2.6a). For instance, the nanocomposites can be applied by an ink and much lower annealing temperatures are needed for drying in comparison to sintering temperatures of a ceramic material allowing the usage of polymer foil substrates. Additionally, the nanocomposites can show flexibility for bending or stretching even when ceramic particles are used, which usually have brittle mechanical properties.

2.4.1.1 Mixing rules and effective medium theories

A linear mixing rule is the simplest approximation to estimate the effective dielectric constant $\varepsilon_{r,eff}$ of a Type I composite from the dielectric constant of the matrix $\varepsilon_{r,1}$,

the dielectric constant of the filler material $\varepsilon_{r,2}$, and the volume fraction f_v of the filler material [103]:

$$\varepsilon_{r,eff} = (1 - f_v)\varepsilon_{r,1} + f_v\varepsilon_{r,2} \tag{2.13}$$

Because experimental results often deviate from the predictions of the linear mixing rule, more elaborated mixing rules were developed. The dielectric constant is mainly increased by a gradient of the electric field at the matrix-particle interfaces [35], which can be described with the effective medium theory and its extensions [103, 104].

The Maxwell equation assumes a single spherical filler particle surrounded by an infinite matrix and is therefore often only valid at low filler concentrations [103, 105]:

$$\varepsilon_{r,eff} = \varepsilon_{r,1}\frac{\varepsilon_{r,2} + 2\varepsilon_{r,1} - 2f_v(\varepsilon_{r,1} - \varepsilon_{r,2})}{\varepsilon_{r,2} + 2\varepsilon_{r,1} + f_v(\varepsilon_{r,1} - \varepsilon_{r,2})} \tag{2.14}$$

The Bruggeman model considers the composite materials as repeated unit cells of the matrix material with a spherical filler particle in the centre [103, 105]. The effective dielectric constant of such a binary mixture is given by the solution of the equation [103]:

$$(1 - f_v)\left(\frac{\varepsilon_{r,1} - \varepsilon_{r,eff}}{\varepsilon_{r,1} + 2\varepsilon_{r,eff}}\right) + f_v\left(\frac{\varepsilon_{r,2} - \varepsilon_{r,eff}}{\varepsilon_{r,2} + 2\varepsilon_{r,eff}}\right) = 0 \tag{2.15}$$

2.4.1.2 Printed Type I nanocomposites and their applications

Printed Type I nanocomposites are widely reported in the literature for various applications. Early works of liquid processed Type I nanocomposites used liquid precursors with $BaTiO_3$ particles and epoxy, which were processed by comma roll coating [106], or with $BaTiO_3$ particles and polycarbonate or poly(vinylidenefluoride-co-hexafluoropropylene), which were processed by spin coating [107]. Furthermore, gravure printed $BaTiO_3$ particles with a sol-gel network as matrix and curing temperatures of up to 160 °C proved that Type I dielectrics can be compatible with flexible PET substrates [108].

Screen printing as a large scalable printing technique was used for oxide particle-based dielectrics; e.g. printing of $Pb(Zr, Ti)O_3$ (PZT) particles was combined with subsequent spin coating of the sol-gel precursor solution to densify the dielectric [109] or printed PZT particles were printed together with a polyvinylidene fluoride–trifluoroethylene (PVDF-TrFE) matrix [110]. The variance in application of screen printed Type I dielectrics was shown by layers of $BaTiO_3$ particles together with silica in PMMA and PVDF-TrFE polymer acting as the gate dielectric of fully printed OFETs [111] or by layers printed with a $BaTiO_3$ ink (*Conductive Compounds BT-101*) and a UV-curable resin dielectric

ink (*Creative Materials 116-20*) that were used as receiver coils for magnetic resonance imaging [24].

Researchers aimed for inkjet printable Type I dielectrics to increase the flexibility in the fabrication process. A polymer matrix was used in the work of Lim *et al.* where voids between inkjet printed $BaTiO_3$ particles were filled in a second inkjet printing step with an ink of dissolved epoxy [78]. Kang *et al.* added $BaTiO_3$ and Ni−Zn particles to a PVP-based insulating ink to inkjet print capacitors and inductors [79]. In another work, it was shown that Al_2O_3 nanoparticles can be inkjet printed in microchannels on steel when co-solvents and an additional polymer polyethylene glycol are used next to the aqueous dispersion media to prevent nozzle clogging and coffee ring effect [112]. Mikolajek *et al.* developed an ink based on $Ba_{0.6}Sr_{0.4}TiO_3$ particles in a PMMA matrix that allowed inkjet printing of capacitors on flexible substrates [8, 80, 113]. However, the printed films of these systems were quite thick with various microns, which will reduce the absolute capacitances. An ink recently reported by Reinheimer *et al.* with silane-functionalized $Ba_{0.6}Sr_{0.4}TiO_3$ particles that covalently bound to a poly(ethylene glycol) diacrylate crosslinker after printing reached a sub-micrometer thickness of 700 nm [10]. Oxide particle-based inks are already commercially available, e.g. an ink from *Torrecid S.L.* containing HfO_2 particles was used to inkjet print resistive random access memory [114].

As mentioned before, the dielectric constant of Type I composites will increase with the filling ratio of the oxide particles. The high volume ratio of rigid oxide particles complicate the processability of the inks, e.g. resulting in thick layer thicknesses [34, 115]. Furthermore, strong local field gradients at high filler levels will cause hot spots in the electric field that reduce the breakdown strength of the dielectric [35]. Finite element analysis showed that the usage of non-spherical particles in comparison to spherical particles can reach high dielectric constants at lower volume ratios [34]. Consequently, atomically flat and insulating 2-D materials such as hexagonal boron nitride (h-BN) also became interesting candidates for filler materials in Type I dielectrics. Joseph *et al.* reported the fabrication of screen printed capacitors with a h-BN ink with polycarbonate binder [116]. Recently, also inks for inkjet printing could be prepared by exfoliation [81] and 2-D material graphene/h-BN/graphene capacitors were inkjet printed on paper [9]. A similar h-BN ink was used to create gate dielectrics on flexible Kapton substrate with printed semiconducting carbon nanotube channels without heating the sample over 80 °C [82].

2.4.2 Type II nanocomposites: conductive particles in an insulating matrix

Type II nanocomposites use conductive fillers such as metal particles in an insulating dielectric matrix material (see Figure 2.6b). If the filling ratio of the conductive materials stays below the percolation threshold, the resulting material is dielectric. Charges accumulate at the interface of the conductive filler material and insulating matrix and lead to interfacial polarization [34, 36]. Due to the pronounced effect of the conductive particles, a strong increase of the dielectric constant can already be achieved with comparable low filler volumes.

2.4.2.1 Percolation theory and interfacial polarization

Percolation theory originally describes compounds with an insulating and conductive component and the transition from insulating to conductive behaviour when the volume fraction of the conductive component f_v is increased above the percolation threshold f_c. A good overview about the percolation theory is provided by Kirkpatrick [117]. The theory was extended to dielectric compounds by Dubrov *et al.* [37] and by Efros and Shklovskii [38] who introduced a network of resistor-capacitor (RC) elements [37]. The composite only maintains its dielectric behaviour below the percolation threshold; if the volume ratio of the conductive component reaches the percolation threshold, a percolating path forms through the compound and leads to dielectric failure. Close to the percolation threshold, the effective dielectric constant at DC (angular frequency $\omega = 0$) diverges and is described by [37, 38]

$$\varepsilon_{\mathrm{r,eff}}(0, f_\mathrm{v}) = \frac{\varepsilon_{\mathrm{r},0}}{|f_\mathrm{v} - f_\mathrm{c}|^q} \tag{2.16}$$

where $\varepsilon_{\mathrm{r},0}$ is a prefactor connected to the dielectric constant of the insulating component and q is a critical exponent that depends on the dimensionality of the network and equals 1.3 for 2-D systems and 1 for 3-D systems [38]. The dielectric constant diverges at the percolation threshold only for ideal insulating matrices without any DC conductivity; in real dielectric compounds with a small but final DC conductivity of the matrix $\sigma_\mathrm{M} > 0$, the maximum of the permittivity at the percolation threshold at the angular frequency ω is [38]

$$\varepsilon_{\mathrm{r,eff}}(\omega, f_\mathrm{c}) = \varepsilon_{\mathrm{r},0} \left(\frac{4\pi\sigma_\mathrm{M}}{\varepsilon_{\mathrm{r},0}\omega} \right)^{1-s} \tag{2.17}$$

with s being another critical exponent.

While percolation theory extended for dielectric compounds originated from considerations at DC, it makes reasonable predictions on the dielectric behaviour of Type II

nanocomposites at low AC frequencies. Moreover, percolation theory predicts that at large volume fractions with decreasing interparticle distances, conductive clusters get interconnected and aggregates of particles can behave like a bigger single particle [57].

Percolation theory does not make prediction of relaxations in polarization that must be considered at high frequencies. The dominant polarization making possible the large dielectric constants in conductor-insulator composites is the MWS polarization [34]. MWS modelling originates from the Debye formulas (Equations (2.10) and (2.11)) and from Wagner's considerations [62] to predict the frequency of the loss factor maximum [118]. Fredin *et al.* employed MWS modelling and showed that the formation of particle aggregates in Type II nanocomposites can, on the one hand, increase the dielectric constant because of an enhanced MWS polarization response at the larger interface area of the joint particle surface, and, on the other hand, reduce the relaxation frequency of MWS polarization leading to a drop of the dielectric constant at lower frequencies [57].

Dang *et al.* stated that nanoparticle fillers are suitable to increase the polarization and resulting dielectric constant of nanocomposites while maintaining the facile processability and flexibility of the polymer matrix as nanoparticle-based composites possess large internal surface areas at comparatively low filler ratios [29]. Another advantage of small nanoparticle fillers is the reduction of hopping currents in the resulting dielectric layer by exploiting the Coulomb blockade effect, which describes a quantum effect for conductive nanoparticles creating an additional barrier for a tunnelling electron due to the charging energy, and thus the decrease of dielectric losses as it was stated by Lu *et al.* [119, 120].

Inhomogeneous distribution of the filler particles makes prediction of the properties of Type II nanocomposites difficult. For random distributions, the filler concentration can vary locally and due to clusters, a percolation path between the electrodes can be formed at lower filler level than for a composite with homogeneously dispersed fillers [118]. This causes that the percolation thresholds of Type II dielectrics observed in experiments varies strongly with the preparation method and shape of the filler particles ranging from as low as 1 % to as high as 17 % [34].

2.4.2.2 Development in preparation of Type II nanocomposites

Pecharromán and Moya reported first experimental proof of large dielectric constants in Type II insulator-conductor composites with a mullite/Mo functionally graded material [121]; Pecharromán *et al.* reported a dielectric compound made up of Ni microparticles inside of a $BaTiO_3$ ceramic matrix reaching dielectric constants up to $\varepsilon_r = 81000@10\,\mathrm{kHz}$ [122]. Dang *et al.* obtained composite layers of Li-doped NiO in PVDF by sol-gel reactions [123]. Shen *et al.* created a dielectric compound of Bi_2S_3 nanorods that were

synthesized by a solvothermal method and that were dispersed in PVDF [124]. Several groups reported the mixing of Ag [83, 84, 125] or Al [126, 127] metallic particles into epoxy matrices; Yang *et al.* studied carbon black and carbon nanotubes in epoxy [128]. Lu *et al.* formed composites with metallic Ag nanofillers that were formed *in-situ* from $AgNO_3$ precursors in an epoxy polymer [119, 129].

Aggregation and agglomeration of fillers causing a heterogeneous distribution of the filler material is a common problem in Type II composites. Toor *et al.* prepared "dielectric inks" from metallic nanoparticles and polymers by solution mixing: colloidal gold nanoparticles (AuNPs) were mixed with a SU-8 polymer solution [39, 61, 130] and PVDF polymer solution [40, 61, 131] in the same solvent. Particle agglomerates and voids at higher filling ratios were observed and the achievable dielectric constant was limited. If a conductive path is formed by agglomeration in Type II composites close to the percolation threshold — where the dielectric constant is greatest — short-circuits lead to failure of the device. This problem is especially prominent for very thin dielectric layers were agglomerates at the scale of the layer thickness can easily form. Therefore, Fredin *et al.* embedded aluminium nanoparticles in polypropylene shells by in-situ polymerization on the native oxide layer of the aluminium nanoparticles in order to reduce the risk of short-circuits at the cost of a reduced filling fraction and elaborated preparation process [41, 57].

In other studies, Type II dielectric composites were also prepared by liquid processing methods such as spin coating [39, 40, 61, 83, 84] or processes less troubled by agglomerates such as bar coating [127], doctor-blade coating [119, 129], or hot pressing [41, 57], but not via inkjet printing.

In a summary, conductive filler materials allow the fabrication of dielectric layers with large dielectric constants. Random mixing of these particles in the matrix can lead to locally varying filler volume fractions and therefore varying material properties. Individually insulating shells solve the problem of conductive pathways that can form especially at high filler ratios or in the presence of agglomerates and were investigated in this thesis.

2.5 Type III nanocomposite: hybrid dielectric of Au@PS core-shell particles

"Type III" dielectric hybrid materials contain hybrid nanoparticles with a conductive core and an individual insulating polymer shell (see Figure 2.6c). Inks based on these hybrid particles are suitable for inkjet printing of very thin dielectric layers. In this thesis, an ink of dispersed hybrid AuNPs with covalently bound polystyrene (PS) will

be presented and the resulting hybrid dielectric layers will be investigated. The low-viscosity inks will not contain free polymer, all polymer chains are covalently bound to the Au cores. The individual polymer shells insulate the particles from each other and prevent the creation of conductive pathways through the dielectric layer.

In order to understand the properties of such an ink, the basics of AuNPs with insulating organic shells, their colloidal stability, their optical properties, and the energetically driven ligand exchange process will be discussed. Concluding, the structure and self-assembly of polymer-shell AuNPs will be reviewed looking at the conformation of the polymer ligands and the interaction of polymer molecules with the solvents of the dispersion.

2.5.1 Metal nanoparticles with insulating organic shells

In this thesis, metal nanoparticles were selected as conductive phase for the hybrid dielectric materials for enhanced MWS polarization at internal interfaces and to enable large dielectric constants. As many synthesis protocols are known for AuNPs and these particles are stable after synthesis, AuNPs were selected as model for metallic particles. A functional hybrid ink should contain AuNPs with complete polymer shells to ensure the individual insulation, possess a long shelf life, and the AuNPs should be stable in the liquid dispersion without the formation of agglomerates. In the following, the synthesis of AuNPs and the stabilization mechanisms of AuNP dispersions are presented.

2.5.1.1 Synthesis of gold nanoparticles

Protocols for synthesis of monodisperse Au particles with varying diameter in water by reduction of gold acid with sodium citrate have been known for a long time. In Frens' synthesis, sodium citrate reduces gold acid to metallic gold, forming AuNPs, and additionally forms a charged surface layer on the AuNP surface [132]. Generally, nanoparticles in a dispersion tend to aggregate due to Van-der-Waals (vdW) forces attracting the particles to each other. In aqueous polar solvents, the particles get stabilized by electrostatic forces caused by the present surface charges as described by the DLVO (Derjaguin, Landau, Verwey, Overbeek) theory [133].

In this work, the synthesis of the gold particles was performed in an organic, non-polar solvent, due to a larger yield of particles in a synthesis batch, which allows the preparation of comparably highly concentrated inks, and the solubility of the used PS polymer ligands in organic solvent. Hence, AuNPs with oleylamine (OAm) ligand shells were synthesized following a modified synthesis protocol of Wu *et al.* [134]. During the

synthesis, gold acid is reduced by a borane complex as a reducing agent in the presence of oleylamine, which acts as stabilizing ligand shell of the individual particles and the core sizes are defined by the interaction of the solvent molecules and the oleylamine ligands [134]. In this thesis, the core size was adjusted with diameters in the range of 2.9 nm to 8.2 nm by using different solvents during synthesis.

2.5.1.2 Colloidal stability of gold nanoparticles in non-polar solvent

In contrast to the DLVO theory for charged particles in polar solvent, no general theory for the colloidal stability for particles without surface charges in non-polar solvent exists [135]. Overall, the elastic deformation of the ligand and the mixing enthalpy between the solvent and ligand is considered to describe a "sterical stabilization" of the nanoparticles in the solvent [136]. As the mixing enthalpy strongly depends on the solvent, a strong dependence of colloidal stability on the solvent was observed. For instance, the agglomeration of AuNPs that are capped with alkanethiol ligands and dispersed in a non-polar solvent can be induced by addition of polar solvent [137, 138]. The role of the ligand length and of the solvent quality for the stability of nanoparticle dispersions against agglomeration was studied for alkanethiol capped inorganic particles in various non-polar organic solvents in the literature. It was found by Kister *et al.* by small angle X-ray scattering and molecular dynamics simulations for inorganic nanoparticles in non-polar solvent that the agglomeration is ligand shell-dominated for small cores (diameter 4 nm to 8 nm) whereas it is core-dominated due to vdW forces between the cores for larger core sizes (diameter above 9 nm) [139]. Additionally, Monego *et al.* found with the same methods a decrease of colloidal stability with increasing length of the alkanethiol ligands [140]; this was explained by ordered structures that the short ligand molecules formed at low temperatures. These ordered ligand molecules influenced the shell-dominated agglomeration behaviour important for small core sizes and finally caused an increase of the colloidal stability [140]. This ordered structure of the alkanethiol ligands was observed to be enhanced when shorter solvent molecules are used like hexane in comparison to hexadecane, which had the same length as the ligands of hexadecanethiol capped AuNPs that were used in the study [141]. Molecular dynamics simulations showed additionally that cyclohexane suppresses very effectively the ordering transition in the ligand shell hindering agglomeration even better than the short linear hexane solvent molecules [141]. In agreement with this simulation result, Doblas *et al.* experimentally determined different solvent qualities by SAXS measurements of hanging droplets of alkanethiol stabilized AuNP dispersions and by determining the stability against agglomeration with increasing concentration of nanoparticles [142]; they found that the best solvent is cyclohexane, before linear alkanes and toluene being the poorest solvent for such particles.

The insights in the agglomeration behaviour of nanoparticles upon solvent evaporation was used to improve a nanoimprinting process: shorter ligands like butanethiol lead to fast agglomeration upon solvent evaporation while longer ligands like dodecanethiol assured longer stability of the dispersion upon solvent evaporation and better printing quality of conductive lines [12].

All these insights on the stability of AuNPs capped with short molecules in non-polar solvent indicate that the stability of AuNPs with a covalently attached polymer shell also bases on the steric stabilization of the nanoparticles, which is likely to depend on the polymer shell conformation and the used solvent. These points are discussed later in this section.

2.5.1.3 Optical properties of gold nanoparticle dispersions

The colloidal gold concentration of the hybrid inks prepared in this thesis were determined by the optical absorption of the AuNP dispersions. Mie theory can be used to describe the scattering of light at small particles in the size range of the wavelength of visible light [143]. Due to collective oscillations of free electrons in noble metals such as gold, silver, and copper, plasmon resonances with a typical absorption at a certain wavelength are observed and cause the appearance of characteristic colours for dispersions of these metal nanoparticles [144]. The position of the plasmon resonance peak in the absorption spectrum depends on the complex permittivity of the metal the nanoparticles are made of, the dielectric constant of the solvent, and the size of the particle. For AuNPs, the position of the plasmon peak in the absorption spectrum is at about 520 nm [145]. As the plasmon peak gets generally shifted to larger wavelengths with increasing particle size [144], colloidal AuNPs can be easily distinguished by the colour of the dispersions. Particles with diameter in the range of 10 nm appear red, however in the presence of agglomerates of single nanoparticles the dispersion appears blue, e.g. when agglomeration is provoked by temperature change [146]. The determination of the gold concentration can be performed by observing the absorption of the AuNP dispersion at 400 nm where both the plasmon peak and the absorption of the solvent have no influence [147].

2.5.1.4 Energetically driven ligand exchange

In this thesis polystyrene polymer ligands were used to insulate the AuNPs in the hybrid layers. Polymer ligands can either be applied as complete synthesized macromolecules ("grafting to" approach) or via polymerization from dissolved monomers on the nanoparticle surface ("grafting from" approach) [148, 149]. To adjust the nanoparticle properties

for the application in dielectric layers, the original oleylamine ligand after synthesis was replaced by thiol-functionalized polystyrene ligands in a "grafting to" approach. The bonding energy of the oleylamine ligand (amine to gold: 0.2 eV[150]) is about one order of magnitude lower than the bonding energy of the thiol-functionalized polystyrene (thiol to gold: 1.7 eV [151, 152]), therefore this ligand exchange is energetically preferred. In the following, the properties of such polymer-shell AuNPs are presented.

2.5.2 Shell structure, polymer conformation, and self-assembly of polymer-shell gold nanoparticles

In this thesis, polymer ligands were used to obtain a sufficiently insulating shell around the conductive cores of the metal nanoparticles. As stated above, the ligand shell plays an important role on the agglomeration behaviour of sterically stabilized AuNPs and the resulting structures during solvent evaporation. In a dry hybrid dielectric layer with all polymer covalently attached on the metallic nanoparticle cores, the ligand density directly influences the volume fractions of the conductive metallic phase and of the insulating organic phase. Therefore, this section provides an overview on the structure, stability, and self-assembly of polymer-shell gold nanoparticles.

2.5.2.1 Structure of polymer-shells of gold nanoparticles

Covalently bound polymer molecules on a solid surface, such as the surface of a nanoparticle, form a polymer-shell, which can adopt different structures. The shell structure is mainly determined by the ligand density of the polymer ligands, which contributes together with the ligand length to the thickness of the polymer shell, and by the conformation of the polymer ligand molecules in the solvent, which in turn depends on the ligand density.

A systematic study of thiol-functionalized polyethylene glycol ligands used in aqueous AuNP dispersions was performed by Rahme *et al.* [153]. The hydrodynamic radius was found to correlate with the length of the polymer ligand whereas the ligand density was measured by thermogravimetric analysis (TGA). It was found that the ligand density depends on the geometrical conditions on the nanoparticle surface: higher curvatures on the particle and smaller polymer ligands allowed higher ligand densities on the nanoparticle surface. The ligand density decreased with polymer length and increasing core diameter (see Figure 2.7). Corbierre *et al.* found that the grafting density of thiol-functionalized polystyrene ligands was higher on AuNPs than on flat Au surfaces and that the ligand density decreased with increasing polymer length [154]. A similar trend

was measured for AuNPs capped with thiolated-polystyrene dispersed in dimethylformamide, where Sindram *et al.* recently found a decreasing ligand density with increasing molecular weight [155].

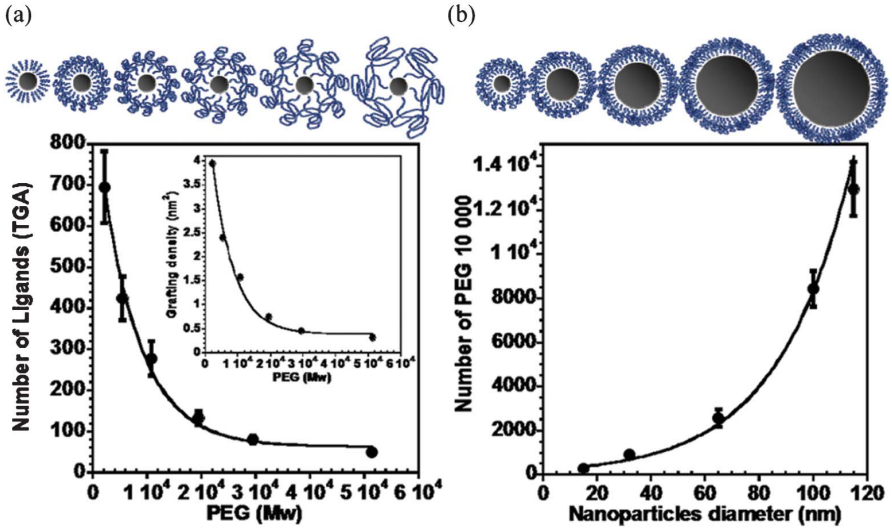

FIGURE 2.7: Ligand density of polyethylene glycol (PEG) polymer ligands on AuNPs as they were measured by Rahme *et al.* [153]. a) Number of ligands and grafting density as it was measured by TGA depending on the molecular weight of the ligands. b) Number of PEG ligands with molecular weight 10 000 Da depending on the diameter of the AuNP core. Reprinted with permission of The Royal Society of Chemistry, from [153]. Copyright 2013 The Royal Society of Chemistry; permission conveyed through Copyright Clearance Center, Inc.

Dukes *et al.* measured the hydrodynamic radii of polymer capped nanoparticles and applied the mean field theory of Wijmans and Zhulina [156, 157]. They found a mushroom ligand conformation for low ligand density and low radius of gyration of the polymer ligand (Figure 2.8a), a semidilute polymer brush for intermediate ligand density (Figure 2.8b), and a transition to concentrated polymer brush conformation for high ligand densities (Figure 2.8c) [157]. In mushrooms, the polymer chains are coiled on the nanoparticle surface and occupy a large surface area. In brushes, the polymer chains are unfolded and a single chain occupies much less space on the nanoparticle surface. Sindram *et al.* reported a concentrated brush conformation for AuNPs capped with thiol-functionalized polystyrene (Au core size ≈12 nm, PS molecular weight from 6500 Da to 33 000 Da) and with ligand densities in the range of $1\,\mathrm{nm}^{-2}$ to $10\,\mathrm{nm}^{-2}$ [155].

2.5.2.2 Conformation of dissolved polymers

The geometrical arrangement of the polymer ligand depends on its surface (or grafting) density and determines the final conformation. The solvent also strongly influences the conformation of polymer ligands in dispersed polymer-shell nanoparticles. The solvent effect on the polymer molecules can be studied by polymer solutions as model system.

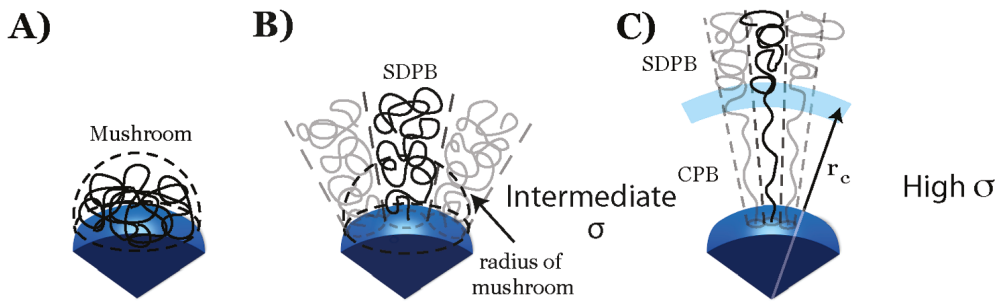

FIGURE 2.8: Models of polymer ligand conformation in dependence of the ligand density on the nanoparticle surface following Dukes *et al.* [157]. a) Mushroom conformation at low ligand densities. b) Semidiluted polymer brush (SDPB) at medium ligand densities. c) Concentrated polymer brush (CPB) at high ligand densities. Reprinted (adapted) with permission from [157]. Copyright 2010 American Chemical Society.

Macromolecule solutions deviate considerably from ideal solutions as the large polymer molecules displace a lot of solvent molecules [158]. The free energy of mixing of a binary mixture between a polymer and a solvent can be described by the Flory-Huggins equation with terms of entropic origin that always promote mixing and a term of energetic origin [159]. The sign of the energetic term depends on the sign of the Flory interaction parameter χ which is often described by the empirical equation [159]

$$\chi(T) = A + \frac{B}{T} \tag{2.18}$$

where A is a parameter that represents the "entropic part" of χ, B represents the "enthalpic part" of χ, and T is the temperature.

In the case of $\chi < 0$, the solvent and polymer have a net attraction and the solution is always stable. In the case of $\chi = 0$, there is an ideal solution and in the case of $\chi > 0$, the solvent and polymer have a net repulsion, which is observed for many polymer/solvent systems. There exists an upper or lower critical solution temperature depending on the sign of the parameter B: for $B > 0$, an upper, for $B < 0$, a lower critical solution temperature can exist. Both exist if B changes the sign with temperature [159, 160], e.g. for polystyrene in cyclopentane [159]. The theta temperature is a special temperature, where the steric repulsion between the solvent molecules, causing unfolding of the polymer chains, is cancelled by the solvent-mediated attraction of monomer units, causing coiling of the chain. As a result, the polymer chain obtains its ideal conformation at the theta temperature [159].

A good solvent influences the conformation of the polymer chains towards unfolding of the chain, whereas a bad solvent drives collapse of the polymer chain to coils [161]. Forster *et al.* found a less pronounced swelling of polystyrene/polyvinylpyridine diblock copolymer brushes in cyclohexane in comparison to toluene, which they saw as better solvent [162]. The coiling of polystyrene in cyclohexane has been observed with dynamic

light scattering by Yu *et al.* from its unfolded state at 35 °C — the theta temperature for polystyrene in cyclohexane — to the collapsed state at 29 °C with a reduced hydrodynamic radius [163].

Therefore, the used solvent and the solvent temperature are expected to influence the ligand exchange performed in this thesis from AuNPs capped with oleylamine to thiol-functionalized polystyrene. For good stability of the final dispersion of polystyrene capped AuNPs, a good solvent is expected to be beneficial and the unfolded conformation of the polymer molecules during ligand exchange is expected to result in higher grafting densities of the polystyrene ligands.

2.5.2.3 Self-assembly of polymer-shell nanoparticles

Simulations showed that the self-assembly of nanoparticles is determined by the balance of the attractive vdW forces between the particle cores and the energy of mixing and elastic compression of the particle ligands [136]. Akcora *et al.* experimentally observed the different self-assembly of SiO_2 nanoparticles with grafted polystyrene ligands in its matrix [164]. The authors explained the different self-assembly with varying grafted chain length and varying grafting density by the shifting balance between the energy gain of the attracting nanoparticle cores and the loss of entropy caused by reduced freedom for overlapping polymer chains in the shells [164]. Therefore, the interparticle distance during self-assembly is influenced by the polymer shell. So called "patchy" particles possess an anisotropic decoration of the particle surface [165], which causes anisotropic interaction of the nanoparticles and can result in chain or ring like self-assembly [166]. When the polymer-shell conformation is changed, the self-assembly of the nanoparticles also changes. For instance, Huebner *et al.* showed for AuNPs grafted with a photoresponsive polymer made up of a methacrylate type monomer with an azobenzene sidechain that a transition of a well dispersed self-assembly to a densely aggregated self-assembly takes place when the molecules in the light responsive polymer shell are switched from an elongated *trans*-state to the collapsed *cis*-state via UV light [167]. These studies indicate that the self-assembly of the investigated Au@PS hybrid nanoparticles in this thesis possibly depends on the polymer shell.

Chapter 3

Methods

This chapter describes all experimental methods used in this thesis. The synthesis of the Au@PS NPs, the analysis of the Au@PS NP dispersions and layers, and the preparation of thin film capacitors are described.

3.1 Au nanoparticle synthesis

The synthesis of the Au@PS hybrid core-shell nanoparticles was performed in two steps. First, oleylamine (OAm) capped AuNPs were synthesized in organic solvent using an adapted method from Wu et al. [134]. The size of the Au cores was tuned by the selection of the solvent and by the timing of addition of the reduction specious. In a second step, the ligand OAm was exchanged by thiol-terminated polystyrene (PS-SH) using a grafting-to approach following Corbierre *et al.* [154]. Unless noted otherwise, all chemicals were used without further purification as received from the suppliers.

3.1.1 Synthesis of Au@OAm nanoparticles of different core sizes

The core sizes of AuNPs were tuned by different organic solvents and different stirring times (t_{TBAB}) until the reducing agent tetrabutylammonium bromide (TBAB) was added. The different core sizes, solvents, and stirring times are listed in Table 3.1.

For the synthesis of gold nanoparticles with oleylamine (OAm) shells (Au@OAm), a mixture of 20 mL filtered OAm (*ACROS Organics*, USA, C18 content 80 % to 90 %) and 20 mL of the solvent (see Table 3.1) was prepared. 200 mg $HAuCl_4 \cdot 3\,H_2O$ (*ACROS Organics*, USA) were dissolved in 32 mL of the OAm-solvent mixture. The solution turned immediately red and was stirred at room temperature for the time t_{TBAB} (see Table 3.1). Then, a solution of 100 mg tetrabutylammonium bromide (*Sigma-Aldrich*,

TABLE 3.1: Parameters for the synthesis of Au@OAm nanoparticles in this thesis. The core size d_{core} depends on the used solvent and the time t_{TBAB} when the reducing agent is added.

Name	d_{core} [nm]	Solvent	t_{TBAB}
Small AuNP@OAm	$\approx$ 2.9	*n*-pentane (*Sigma-Aldrich*, USA, 99 % purity)	90 min
Medium AuNP@OAm	$\approx$ 4.7	*n*-hexane (*abcr GmbH*, Germany, 99 % purity)	20 min
Large AuNP@OAm	$\approx$ 7.0	benzene (*Sigma-Aldrich*, USA, 99 % purity)	45 s

USA) in the remaining 8 mL of the OAm-solvent mixture was added. The solution turned dark blue and was stirred further for about 1 h at room temperature.

All glass vessels were flooded with argon and capped with a lid during the reaction. The gold acid was pestled to ensured fast dissolution in the OAm-solvent mixture.

The product was purified by adding 50 mL ethanol and 10 mL methanol to 40 mL of the as-prepared AuNP@OAm dispersion. The mixture changed its colour to blueish due to particle agglomeration after addition of the polar alcohols. It was distributed in two centrifuge tubes of 50 mL and centrifuged (Rotanta 460 RS, *Hettich*, Germany, 1550 rcf, $t = 5$ min). Then, the clear supernatant was decanted and the NPs redispersed in 40 mL of cyclohexane (*Roth*, Germany, 99.9 % purity). The resulting particle dispersion was mixed with 40 mL ethanol and 20 mL methanol, and the cycle was repeated. Finally, the Au@OAm NPs were redispersed in 40 mL of the final solvent toluene (*Roth*, Germany, 99.8 % purity).

One overgrow step was performed to increase the core size and to obtain batches of larger nanoparticles. To this end, 40 mL of washed AuNP@OAm with core diameter ≈ 7.0 nm dispersed in toluene were stirred on a hot plate at 63 °C. A mixture of 2 mL filtered OAm (*ACROS Organics*, USA, C18 content 80 % to 90 %) and 2 mL toluene (*Roth*, Germany, 99.8 % purity) was prepared. 100 mg $HAuCl_4 \cdot 3\,H_2O$ (*ACROS Organics*, USA) were rapidly dissolved in the OAm-toluene mixture by vigorous shaking and immediately added to the AuNP@OAm dispersion. The stirring was continued for about 24 h at 63 °C. Purification was followed as above. However, for the second centrifugation cycle, the centrifuge was set to 5230 rcf for $t = 20$ min to obtain a clear supernatant. The overgrown Au@OAm particles with core diameter of ≈ 8.2 nm were redispersed in 40 mL of the final solvent toluene (*Roth*, Germany, 99.8 % purity).

To store the inks in inert atmosphere, the ink vessels were flushed with argon after each ink usage.

3.1.2 Ligand exchange to polystyrene

Thiol-functionalized polystyrene (PS-SH) was grafted onto the gold nanoparticles following Corbierre *et al.* [154]. The amount of provided polystyrene was estimated considering the length of the polystyrene chains (larger ligand densities were reported for shorter polystyrene ligands [154]), the surface area of the Au@OAm particles, and their concentration as estimated from the used gold acid in synthesis.

Thiol-functionalized polystyrene with molecular weights $M_\mathrm{n} = 5000\,\mathrm{Da}$ (polydispersity index (PDI) $\leq$ 1.1, PS_{5000}-SH) and $M_\mathrm{n} = 11\,000\,\mathrm{Da}$ (PDI $\leq$ 1.1, PS_{11000}-SH) were obtained from *Sigma-Aldrich*, USA. PS-SH (see Table 3.2 for masses) was dissolved in 6 mL toluene with the aid of 3 min of ultrasonication. The PS-SH solution was added to the Au@OAm nanoparticle dispersions as synthesized above.

TABLE 3.2: Amount of PS-SH used in the ligand exchange reaction of a batch of Au@OAm particles synthesized from 200 mg gold acid.

Name	$m_{PS_{5000}}$ [mg]	$m_{PS_{11000}}$ [mg]
Small AuNP@OAm with PS_{5000}	480	-
Small AuNP@OAm with PS_{11000}	-	500
Medium AuNP@OAm with PS_{5000}	350	-
Medium AuNP@OAm with PS_{11000}	-	390
Large AuNP@OAm with PS_{5000}	236	-
Large AuNP@OAm with PS_{11000}	-	237

Standard ligand exchange was performed by stirring of the mixture on a hot plate at 60 °C for one week. Particles with low and high grafting densities were synthesized by varying the stirring conditions: Hybrid particles with high grafting density of PS_{11000} were obtained by stirring at 20 °C for one week, particles with low grafting density of PS_{11000} were obtained by stirring at 60 °C for four weeks (additionally for eight weeks in Chapter 4).

After ligand exchange, the dispersions were centrifuged for purification in an ultracentrifuge (Optima XE-90, *Beckman Coulter*, USA). Medium-sized and large particles were centrifuged at 174 900 rcf and 25 °C for $t = 165$ min using a SW 32 Ti rotor and 38.5 mL centrifuge tubes. Small particles were centrifuged at 485 000 rcf and 25 °C for $t = 210$ min using a SW 60 Ti rotor and 4.2 mL centrifuge tubes. The clear supernatant was carefully removed with a pipette and the NPs were dispersed in toluene (or in cyclohexane for experiments in Section 4.2 of Chapter 4) at the desired concentration with the aid of an ultrasonic bath.

3.2 Reference thiol-terminated polystyrene ink

Reference capacitors were prepared with dielectric layers that only contained thiol-functionalized polystyrene. Inks containing 5 wt% PS_{5000}-SH or PS_{11000}-SH were prepared by dissolving the polymer with the aid of an ultrasonic bath in toluene. These polystyrene solutions were used in spin coating.

3.3 Layer formation by wet processing

3.3.1 Substrate preparation

Rigid samples were prepared on silicon substrates. Silicon <100> wafers (*Siegert Wafer*, Germany) with intrinsic SiO_2 layers were coated with aluminium layers through magnetron sputtering using argon plasma (PVD 3 - Lesker PVD 75 Deposition System, *Kurt J. Lesker Company*, USA). The sputter time was adjusted (typically $\approx$ 90 min with 50 W sputter energy) to reach a layer thickness of (60 ± 14) nm. The substrate was cleaved into square pieces of 18 mm x 18 mm. The substrates were cleaned in acetone, isopropanol, and water for 10 min each in an ultrasonic bath.

Flexible samples were prepared on polyethylene terephthalate (PET) foil. PET foil (Melinex ST504, *Pütz Folien*, Germany) with thickness 125 µm was coated with aluminium layers through magnetron sputtering (sputter time 90 min, sputter energy 50 W) using argon plasma on the non-pre-treated side of the foil. Square pieces in the size of 18 mm x 18 mm were cut and cleaned as above.

For silicon substrates with gold bottom contact (used in Chapter 4) and the top contacts, gold was evaporated on the samples with a UNIVEX 300 evaporation machine (*oerlikon leybold vacuum*, Germany). For evaporation of gold on silicon, a titanium interlayer was evaporated on the silicon for better adhesion (evaporation rate $\leq 0.01\,\mathrm{nm\,s^{-1}}$, thickness 5 nm). Gold top contacts were directly evaporated on the hybrid Au@PS dielectric layers without an adhesion layer. For gold layers, the evaporation rate was set below $0.02\,\mathrm{nm\,s^{-1}}$ till a layer thickness of 3 nm and the evaporation rate was then kept at $\leq 0.2\,\mathrm{nm\,s^{-1}}$ until the final thickness of $\approx$ 150 nm.

The surface profiles of the substrates were measured by atomic force microscopy (AFM) using a NanoWizard 3 device (*JPK*, Germany). Measurements were performed in tapping mode with a PPP-NCL-50 cantilever (*Nanosensors*, Switzerland) under ambient conditions with a resolution of 512 pixels and a line rate of 0.3 Hz. The measured area was 100 µm x 100 µm for silicon, aluminium coated silicon, and aluminium coated PET

and 90 µm x 90 µm for silicon substrates with evaporated gold. The Data Processing Software from JPK was used to calculate the average surface roughness R_a from the surface profiles as the arithmetic average deviation from the best fit plane.

3.3.2 Spin coating

Smooth dielectric layers on rigid substrates were prepared via spin coating in a laminar flow box with a RC 5/8 spin coater (*Karl Suss Technique S.A.*, France). The cleaned substrate pieces were fully covered with the liquid ink, accelerated at $\dot{\omega} = 1000\,\mathrm{rpm\,s^{-1}}$, and rotated at $\omega = 1000\,\mathrm{rpm}$ for 60 s. A metallic bottom contact was formed by removing the dielectric coating with a toluene-soaked cotton bud at one edge of the sample. The spin coated samples were dried overnight in a vacuum oven at 25 °C to evaporate residual solvent. Using a shadow mask, Au circular top contacts of diameter 1 mm and thickness $(157 \pm 4)\,\mathrm{nm}$ were evaporated on the sample. One sample thus contained 9 to 16 thin film capacitors that were contacted for dielectric measurement as shown in Figure 3.1.

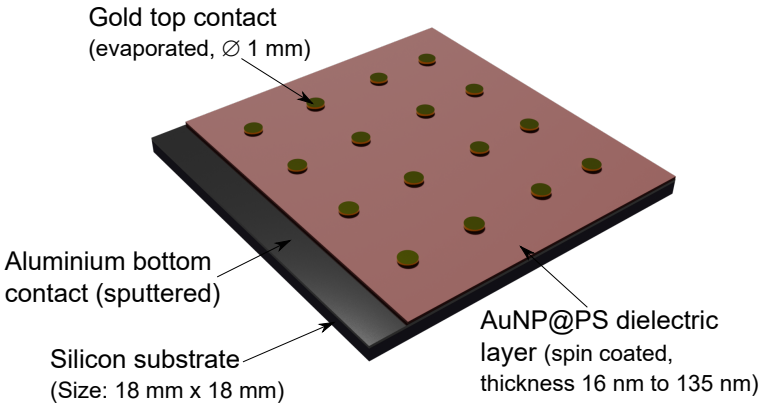

FIGURE 3.1: Scheme of a spin coated dielectric sample with 9 to 16 thin film capacitors that can be contacted via the aluminium bottom and the gold top contact.

3.3.3 Inkjet printing

Thin film capacitors with inkjet printed dielectric layers were prepared on aluminium coated rigid and flexible substrates. Dispersions of medium-sized Au@PS_{11000} particles in toluene with medium ligand density, which were also used for spin-coating, were used for printing (see above for synthesis).

The dispersion was filled in the cartridge of a PIXDRO LP50 inkjet printer (*SÜSS MicroTec SE*, Germany) mounted on a piezo print head (DMC-11610, *FUJIFILM Dimatix*, USA) with nozzle diameter of 21.5 µm. A single nozzle was used for printing, where the piezo actuator was driven with a pulse shape waveform (holding voltage 8 V,

pulse voltage 29 V). The pulse length was set to 9 µs and the ejection frequency was set to 1000 Hz. To stabilize droplet formation, a negative pressure of −1 mbar was applied to the ink vessel. The printing was performed in a temperature and humidity-controlled laboratory (22 °C with 50 % relative humidity). The droplet formation before printing was observed with a camera and a stroboscope.

For the rigid samples, squares of 10 mm x 10 mm dielectric film were printed with two passes at a droplet density of 400 DPI on aluminium coated silicon wafers, where the printing direction in the first pass was orthogonal to the printing direction in the second pass. To ensure the full evaporation of the solvent, the sample was dried in a vacuum oven at 25 °C and ≈50 mbar after printing. Thermal evaporation was used to deposit gold top contacts with circular shapes and diameters of 1 mm as described for the spin coated samples.

For the flexible samples, squares of 10 mm x 10 mm were printed with two passes at a droplet density of 500 DPI on aluminium coated PET foil, where the printing direction in the first pass was orthogonal to the printing direction in the second pass. Once again, the samples were dried in a vacuum oven after printing. Gold top contacts with circular shape and diameter of 1 mm were evaporated on top, as described above for the rigid samples.

Optical micrographs of the inkjet printed samples were obtained in bright field using a ZEISS Axio microscope (*Zeiss*, Germany).

3.4 Ink and layer characterization

3.4.1 UV-Vis spectroscopy

UV-Vis spectrograms of the hybrid particle dispersions were recorded with a Cary 300 UV-Vis spectrometer (*Agilent Technologies*, USA) with dual-beam setup in a wavelength range from 800 nm to 300 nm in steps of 1 nm and 0.1 s per step. The absorption spectrum of the pure solvent was subtracted as background. The gold concentrations of the dispersions were determined by the absorbance at the wavelength of 400 nm after calibration [147]. Calibration measurements were performed with two different standard dispersions of *"NanoXact"* AuNPs capped with citrate (both with gold concentration 0.05 mg mL^{-1}, 5 nm and 10 nm core diameter) that were obtained from *nanoComposix* (USA). The transmissions of standard solutions were measured in undiluted concentration and diluted with H_2O (volume dilution ratios: 1:1, 1:3, 1:5, 1:9, and 1:11). From these measurements, a calibration curve of the UV-Vis absorption at 400 nm versus the

known gold concentration in the (diluted) standard dispersions was obtained. For concentration determination of synthesized inks, the calibration curve of the 5 nm AuNP standard dispersion was used for small and medium-sized AuNPs. For large AuNPs, the calibration curve of the 10 nm AuNP standard dispersion was used.

3.4.2 Thermogravimetric analysis

Metal and polymer contents of the dry Au@PS NPs were quantified using thermogravimetric analysis (TGA). To this end, approximately 250 µL of the respective dispersion were dried in a TGA crucible first on a hot plate at 60 °C and then in a vacuum oven at 30 °C overnight. The solid samples (6 mg to 9 mg dry mass) were heated to 1000 °C in a Netzsch STA 449 F3 TGA (*Netzsch*, Germany) under Ar gas with a heating rate of $10\,\mathrm{K\,min^{-1}}$. At 1000 °C, the gas flow was switched to O_2 and the temperature was held for 10 min for complete oxidation of the organic part. Two TGA measurements were performed for each prepared ink. As most of the mass loss occurred below ≈ 520 °C, it was assumed that that all residual mass at 520 °C was elemental gold; the mean value of the two measurements for each layer type was used as the measured gold weight fraction $x_{\mathrm{w,Au}}$ for further calculations.

The fraction of Au in the dry Au@PS samples was calculated from the residual Au mass under the assumption of compact films. The density of bulk Au ($\rho_{\mathrm{Au}} = 19.32\,\mathrm{g\,cm^{-3}}$ [52]) and the mean density of amorphous polystyrene ($\rho_{\mathrm{PS}} = 1.05\,\mathrm{g\,cm^{-3}}$ [168]) were used to calculate the volume fraction of Au $f_{\mathrm{v,Au}}$:

$$f_{\mathrm{v,Au}} = \frac{x_{\mathrm{w,Au}}}{x_{\mathrm{w,Au}} + \frac{\rho_{\mathrm{Au}}}{\rho_{\mathrm{PS}}}(1 - x_{\mathrm{w,Au}})} \tag{3.1}$$

The ligand density was calculated assuming that all organic molecules in the layer were bound as ligand molecules and that the organic fraction was only made up by PS ligands. The mass of the organic shell per nanoparticle m_{organic} was calculated by

$$m_{\mathrm{organic}} = m_{\mathrm{AuNP}} \left(\frac{1}{x_{\mathrm{w,Au}}} - 1 \right) = \rho_{\mathrm{Au}} \frac{4}{3} \pi \left(\frac{d_{\mathrm{core}}}{2} \right)^3 \left(\frac{1}{x_{\mathrm{w,Au}}} - 1 \right) \tag{3.2}$$

where m_{AuNP} is the mass of a single gold core, d_{core} the core diameter, ρ_{Au} the gold bulk density, and $x_{\mathrm{w,Au}}$ the gold weight fraction. The number of PS ligands per nanoparticle n_{PS} can be calculated using the molecular mass M_{PS} of the used PS ligand:

$$n_{\mathrm{PS}} = m_{\mathrm{organic}} / M_{\mathrm{PS}} \tag{3.3}$$

Finally, the ligand density $\rho_{\mathrm{A,ligand}}$ was obtained by dividing the number of PS ligands per particle by the surface of the gold core A_{AuNP}:

$$\rho_{\mathrm{A,ligand}} = \frac{n_{\mathrm{PS}}}{A_{\mathrm{AuNP}}} = \frac{n_{\mathrm{PS}}}{4\pi\left(\frac{d_{\mathrm{core}}}{2}\right)^2} \tag{3.4}$$

3.4.3 Transmission electron microscopy

Transmission electron microscopy (TEM) was used for imaging of individual Au@PS nanoparticles using a JEM-2011 and a JEM-2100 LaB_6 TEM (*JEOL*, Germany), both with high-resolution pole pieces at 200 kV acceleration voltage. Bright field electron micrographs were acquired with a Orius SC1000 CCD camera (*Gatan*, USA). Samples were prepared by diluting the Au@OAm NP or Au@PS NP inks with toluene and dropping on a carbon TEM grid. A fast Fourier transform of the binary TEM images (using auto threshold filter) was performed with the Fiji software in order to identify order in the AuNPs arrangement. The size distribution of particles was determined by TEM images using the Fiji software: the "analyze particle" function was employed after removing background noise, auto adjusting the brightness and contrast, and using the auto threshold filter.

Cross sections of thin film capacitors were prepared by covering the samples with a conducting carbon layer (to prevent charging of the samples) and two protecting platinum layers via electron and ion beam deposition. Thin lamellae were then cut using a focused ion beam (FIB) of a combined FIB/SEM - dual beam scanning microscope (Versa 3D Low Vac, *FEI Company*, USA). The ion current was 7 nA for fast cutting and 0.3 nA with beam spot diameter of 0.8 nm for fine cutting. The FIB lamellae were connected to an Omniprobe nanomanipulator, mounted on a TEM sample holder, and analyzed using TEM (see above for the instrument).

3.4.4 Dynamic light scattering

Dynamic light scattering (DLS) was performed on ALV/CGS-3 Goniometer System (*ALV GmbH*, Germany) using a laser wavelength λ of 632.8 nm at room temperature (if not stated differently), with acquisition times of 180 s (600 s for particles with small Au cores), and at scattering angles θ from 30° to 150° in steps of 10°. At each scattering angle θ, the wavenumber q follows from the wavelength of the laser λ and the refractive index n of the solvent [169]:

$$q = \frac{4\pi n}{\lambda}\sin\frac{\theta}{2} \tag{3.5}$$

The autocorrelation of the measured intensity $I(q,t)$ during the experiment yields the autocorrelation function $g_1(q,t)^2$ that was fit to a squared exponential function describing the decay of $g_1(q,t)^2$ in many applications [169, 170]

$$I(q,t) \overset{\text{autocorrelation}}{\rightarrow} g_1(q,t)^2 = A_0 \left(\exp\left[\frac{-t}{\tau} \right] \right)^2 \tag{3.6}$$

yielding the correlation time τ at this scattering angle (A_0 is a pre-factor). The correlation time can be used to determine the diffusion coefficient of the particles that undergo Brownian motion in the solvent [170]. The plot of τ^{-1} versus q^2 yields the translational diffusion coefficient D_{trans} as the slope of a linear fit [170]:

$$\frac{1}{\tau} = q^2 D_{\text{trans}} \tag{3.7}$$

Finally, the hydrodynamic diameter d_{h} and hydrodynamic radius r_{h} were calculated from D_{trans} using the Stokes-Einstein relation [52, 170]:

$$d_{\text{h}} = 2r_{\text{h}} = 2\frac{k_{\text{B}}T}{6\pi\eta D_{\text{trans}}} \tag{3.8}$$

where $k_{\text{B}} = 1.381 \times 10^{-23}\,\text{J}\,\text{K}^{-1}$ is the Boltzmann constant [52], T the temperature, and η the viscosity of the solvent.

In temperature dependent measurements, the sample temperature was set with a thermostat in the range 20 °C to 60 °C. The system was relaxed for at least 15 min at a specific temperature, before the DLS measurement was started. Temperature dependent values for the refractive index and viscosity of toluene were taken from the literature [171, 172].

3.4.5 Raman spectroscopy

Raman spectroscopy was used to identify ligand molecules on Au nanoparticles by its vibrational modes. Samples were prepared by depositing the Au@OAm NP and Au@PS NP dispersions on steel substrates. The solvent was evaporated at room temperature and a confocal Raman microscope inVia (*renishaw*, United Kingdom) was used for the analysis. The excitation laser had a wavelength of 633 nm for Au@OAm NP and Au@PS NP samples. The spectra were recorded in a range of $100\,\text{cm}^{-1}$ to $700\,\text{cm}^{-1}$.

For analysis of the Raman spectra, a baseline was subtracted from the raw data. The Raman intensity was normalized by the highest signal in the recorded spectra. The peaks in the Raman spectra were related to ligand molecules using the literature.

3.4.6 Small angle X-ray scattering

Small angle X-ray scattering (SAXS) from Au@PS NP dispersions and dry drop-casted films was recorded in a Xeuss 2.0 laboratory set-up (*Xenocs SAS*, France). X-rays at the copper K_α-line with a wavelength of $\lambda = 0.154\,\mathrm{nm}$ were provided by a GeniX 3D source (*Xenocs SAS*, France). Scattered intensities were detected by a Pilatus 3R 1M detector (*DECTRIS*, USA) of scattering vectors $q = 4\pi\lambda^{-1}\sin\theta$ between $0.1\,\mathrm{nm}^{-1}$ and $10\,\mathrm{nm}^{-1}$. Since the scattering from all samples was isotropic, intensities were radially averaged.

The Au@PS NP dispersions were measured in transmission SAXS experiments using borosilicate capillaries sealed by epoxy. The spectra were radially integrated with the Foxtrot software (*Xenocs SAS*, France). Pure solvent scattering was used as background and subtracted from the data. The spectra were fitted with the sasfit software to a spherical form factor model $K(q, r, \Delta\eta)$ given as [173]

$$K(q, r, \Delta\eta) = \frac{4}{3}\pi r^3 \Delta\eta 3 \frac{\sin(qr) - qr\cos(qr)}{(qr)^3} \tag{3.9}$$

where q is the wavenumber, $r = \frac{d_{\mathrm{core}}}{2}$ is the particle radius, and $\Delta\eta$ is the scattering length density difference between particle and matrix [174]. A Schulz-Zimm distribution of the particle size distribution was assumed in the fits to consider polydispersity and to obtain the average particle diameter d_{core} and the width of the particle size distribution σ.

Films for SAXS experiments on dried samples were prepared by drop casting Au@PS NP dispersions on Kapton foil and evaporation of the solvent at room temperature. The recorded SAXS transmission spectra were radially integrated with the Foxtrot software. The SAXS transmission spectrum of the pure Kapton foil was used as background and subtracted from the data. The structure factor of the drop-casted samples was calculated by dividing the recorded transmission spectrum by the form factor of the particular nanoparticle in liquid dispersions. A python script was used where a shifting factor and interpolation were used to adjust the fit of the form factor in intensity and in q-positions to the measured transmission spectrum of the drop-casted films.

The centre-to-centre distance d_{cc} of the AuNPs in the drop casted samples follows from the position q^* of the first order structure factor peak. In case of random packing [175]:

$$d_{\mathrm{cc}}^{(\mathrm{rp})} = \frac{2\pi}{q^*}, \tag{3.10}$$

For ordered particle superlattices, reflections of various crystallographic planes with the Miller indices h, k, l are recorded. In a cubic crystal sytem with lattice constant a, the reflections of these crystallographic planes are seen at the positions q_{hkl} [176]:

$$q_{hkl} = \frac{2\pi\sqrt{h^2 + k^2 + l^2}}{a} \tag{3.11}$$

All these reflections can be observed for a simple cubic structure. Extinction rules apply for fcc ordered particles and only reflections with h, k, l all odd or all even can be measured [176]. The nearest neighbour distance in an fcc structure d_{cc} is related to the lattice constant a by the equation:

$$d_{\mathrm{cc}}^{(\mathrm{fcc})} = \frac{a}{\sqrt{2}} \tag{3.12}$$

The first order structure factor peak q^* for fcc belongs to the crystallographic planes $(hkl) = (111)$. The centre-to-centre distance is then calculated using Equation (3.11) and Equation (3.12):

$$d_{\mathrm{cc}}^{(\mathrm{fcc})} = \frac{2\pi\sqrt{1^2 + 1^2 + 1^2}}{\sqrt{2}q^*} = \frac{\sqrt{6}\pi}{q^*} \tag{3.13}$$

The particles' surface-to-surface distance d_{ss} follows for both the random and the ordered structure from the centre-to-centre distance by subtraction of the core diameter d_{core}:

$$d_{\mathrm{ss}} = d_{\mathrm{cc}} - d_{\mathrm{core}} \tag{3.14}$$

3.4.7 Thickness measurement

The thickness of dielectric layers was measured with white light interferometry and on TEM cross sections.

3.4.7.1 White light interferometry

Reference samples using the Au@PS NP inks and the PS–SH inks were prepared on borosilicate glass microscope cover slips (*Menzel-Gläser*, Germany) of the size 22 mm x 22 mm for thickness measurement via spin coating as described above. The height was measured with a white light interferometer (Zygo New View 5000 and Zygo New View 7300, *Zygo Corporation*, USA) on a cross-like scratch in the layer. Each sample was measured $N = 4$ times in 5 mm distance from the centre of the sample (see Figure 3.2, left part). The MetroPro software (*Zygo Corporation*, USA) was used to extract

the height histogram of each individual measurement. These height histograms were fit with two Gaussian peaks; the peak at lower height level corresponds to the substrate, the peak at higher height level corresponds to the layer. The layer thickness t_i and its uncertainty resulting from the i-th measurement was calculated using the positions, $x_{0,1}$ and $x_{0,2}$, and the width, w_1 and w_2, of the Gaussian peaks (see Figure 3.2 on the right): [177]:

$$t_i \pm \Delta t_i = |x_{0,1} - x_{0,2}| \pm 0.5\sqrt{w_1^2 + w_2^2} \tag{3.15}$$

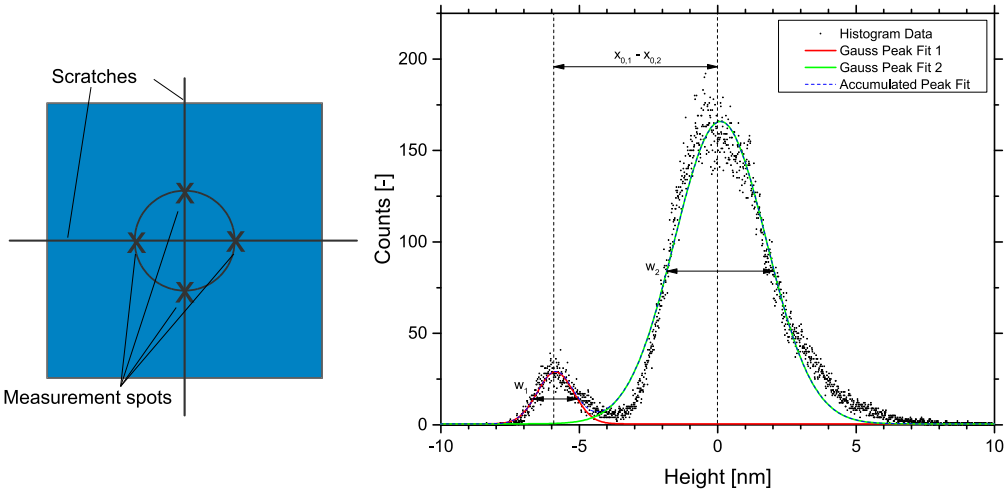

FIGURE 3.2: Left: Cross-like scratches were created on the spin coated layers on glass cover slips. The measurements were performed on 4 points (marked with X), which were located 5 mm from the sample centre. Right: The resulting thickness of one measurement was determined by the distance of the peaks in the height histogram.

To calculate the final thickness of the layer, the arithmetic mean value of the four measured spots was taken. The uncertainty of the thickness measurements is composed of the standard deviation of the four thickness values of the measured spots, Δt_{stdv}; it reflects the layer thickness variation all over the sample. The second contribution, $\Delta t_{\mathrm{individual}}$, propagates from the error of each of the four individual measurement Δt_i when calculating the arithmetic mean value from the four measured spots; it reflects the local height variation, e.g. from the roughness of the sample:

$$\Delta t_{\mathrm{individual}} = \frac{1}{4}\sqrt{\sum_i \Delta {t_i}^2} \tag{3.16}$$

The overall thickness uncertainty Δt is then:

$$\Delta t = \sqrt{\Delta t_{\mathrm{stdv}}^2 + \Delta t_{\mathrm{individual}}^2} \tag{3.17}$$

3.4.7.2 Transmission electron microscopy

The thickness of selected dielectric layers was measured in TEM images of FIB cross sections of prepared thin film capacitors (see Section 3.4.3). The comparison of the thickness values from WLI and TEM cross section images in Figure A.1 in the appendix shows good conformity. The thickness measurement by WLI, covering larger sample areas and better statistics, was selected as the standard method to determine layer thicknesses in this thesis.

3.4.8 Dielectric characterization

The dielectric properties of the prepared layers were measured by impedance spectroscopy of thin film capacitors, where the dielectric layers were coated on metal-covered substrates, which formed the bottom contact, and evaporated Au contacts on top (see Figure 3.3).

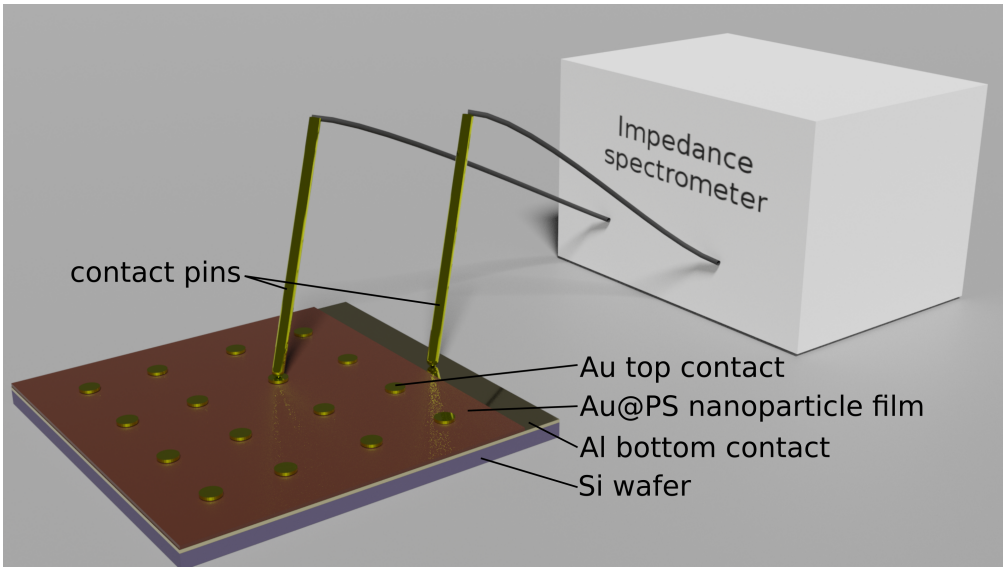

FIGURE 3.3: Impedance characterization/spectroscopy of the prepared thin film capacitors in this thesis in order to determine the dielectric properties of the dielectric thin films.

3.4.8.1 Impedance spectroscopy

For impedance spectroscopy, an Alpha Analyzer spectrometer (*Novocontrol Technologies*, Germany) was employed. A sinusoidal voltage of the form $U(\omega, t) = U_{\mathrm{m}} \sin(\omega t)$ was applied with the maximum voltage $U_m = 50\,\mathrm{mV}$ and covering the frequency range $\nu = \frac{\omega}{2\pi} \in [1\,\mathrm{Hz}; 1\,\mathrm{MHz}]$ while measuring the resulting current response $I = I_{\mathrm{m}} \sin(\omega t + \varphi)$, where t is the time and φ the phase shift between current and voltage [53, 178]. Micro

manipulators (DPP105-M-AI-S, *FormFactor Beaverton Inc.*, USA) with feather contact pins were used to contact the bottom and top contact of the measured samples with the ZG4 test interface of the Alpha Analyzer.

From the measured raw data, the complex impedance $\underline{Z}_\mathrm{p}$ for a parallel circuit of a resistor R_p and a capacitor C_p (see Figure 2.2) can then be derived with the equation [179]:

$$\underline{Z}_\mathrm{p} = U/I' + \mathrm{i}U/I'' = R_\mathrm{p} + \mathrm{i}X_{C_\mathrm{p}} \tag{3.18}$$

where I' and I'' are the real and the imaginary part of the complex current, and $X_{C_\mathrm{p}} = \frac{1}{\omega C_\mathrm{p}}$ is the reactance of the capacitor [51].

In the parallel circuit, the complex admittance $\underline{Y}_\mathrm{p}$ is given by the moduli of the admittance of the resistor Y_{R_p} and of the admittance of the capacitor Y_{C_p} [51, 54]:

$$\underline{Y_\mathrm{p}} = Y_\mathrm{p}' + \mathrm{i}Y_\mathrm{p}'' = Y_{R_\mathrm{p}} + \mathrm{i}Y_{C_\mathrm{p}} = \frac{1}{R_\mathrm{p}} + \mathrm{i}\frac{1}{X_{C_\mathrm{p}}} = \frac{1}{Z_\mathrm{p}'} + \mathrm{i}\omega C_\mathrm{p} \tag{3.19}$$

Finally, the capacitance in parallel is calculated for each frequency by comparison of the imaginary parts in Equation (3.18) and in Equation (3.19)

$$C_\mathrm{p} = \frac{Y_\mathrm{p}''}{\omega} \tag{3.20}$$

and the loss tangent following Equation (2.4) by

$$\tan\delta = \frac{Y_\mathrm{p}''}{Y_\mathrm{p}'} \tag{3.21}$$

The determination of the capacitance in parallel and the loss tangent, as shown in Equation (3.20) and in Equation (3.21), were performed with the *WinDETA* software (*Novocontrol Technologies*, Germany).

When the data analysis did not reveal a dielectric behaviour, e.g. because the resistance in parallel R_p was in the Ω range or because the dielectric loss $\tan\delta$ was way above 1, defects such as pin holes were assumed; in this case the data were disregarded. Before a sample was measured, both contact pins were connected to the metal coated substrate that formed the bottom contact and the resistivity was measured to assure good contact formation between the contact pins and the substrate ($R_\mathrm{p} < 100\,\Omega$ for a short circuit with good contact formation). The yield of all measured, valid and disregarded thin film capacitors with the layers investigated in this thesis is shown in Table A.1 in the appendix.

3.4.8.2 Analysis of dielectric properties

The dielectric constant ε_r of the dielectric layer was extracted from the capacitance in parallel C_p using Equation (2.2):

$$\varepsilon_\mathrm{r} = C_\mathrm{p} \frac{1}{\varepsilon_0} \frac{t}{A} \tag{3.22}$$

where A is the area of the top contact and t the dielectric layer thickness.

The arithmetic mean and the standard deviation for ε_r and the loss tangent $\tan\delta$ of the measured thin film capacitors were used to determine the dielectric properties of each sample type.

For layers with larger variation in layer thickness, e.g. the layers with small and large core sizes in Section 6, a more detailed estimation of the uncertainty of the dielectric constant was performed involving the thickness variation Δt (see Equation (3.17)). Given that a data set of a certain sample type was made up of i samples and in total N capacitors were measured, the sample has a thickness variation $\Delta t^{(i)}$. The uncertainty of the dielectric constant, $\Delta\varepsilon^{(j)}_\mathrm{r,thickness}$, of the j-th ($j = 1, 2, ..., N$) capacitor that is part of the i-th sample of one data set is calculated with:

$$\Delta\varepsilon^{(j)}_\mathrm{r,thickness} = \frac{\partial\varepsilon^{(j)}_\mathrm{r}}{\partial t^{(i)}} \Delta t^{(i)} = C^{(j)}_\mathrm{p} \frac{1}{\varepsilon_0 A} \Delta t^{(i)} \tag{3.23}$$

This uncertainty propagates to an uncertainty $\Delta\varepsilon_\mathrm{r,thickness}$ due to calculation of the arithmetic mean value from the individual measured capacitors:

$$\Delta\varepsilon_\mathrm{r,thickness} = \frac{1}{N} \sqrt{\sum_{j=1}^{N} {\Delta\varepsilon^{(j)}_\mathrm{r,thickness}}^2} \tag{3.24}$$

The overall uncertainty in dielectric constant is then determined as the sum of independent uncertainties from the standard deviation and the arithmetic mean, which contains the uncertainty of the thickness variation:

$$\Delta\varepsilon_\mathrm{r} = \sqrt{\Delta\varepsilon^2_\mathrm{r,stdev} + \Delta\varepsilon^2_\mathrm{r,thickness}} \tag{3.25}$$

3.4.8.3 Dielectric breakdown estimation

The breakdown voltages V_bd of two capacitors of each sample type were measured under DC voltage. Using a Model 2450 SourceMeter (*Keithley Instruments*, USA), a voltage ramp starting from 0.01 V with 0.01 V steps in 0.1 s per step was applied and the resulting

current recorded until the current strongly rose at the breakdown voltage from less of 10 mA to 100 mA, which was set as the upper current limit; the measurement was stopped at the upper voltage in the range 5 V to 16.5 V several volts above the determined breakdown voltage.

The breakdown field strength E_{bd} was estimated by dividing the breakdown voltage by the thickness t of the dielectric layer:

$$E_{\mathrm{bd}} = \frac{V_{\mathrm{bd}}}{t} \tag{3.26}$$

Chapter 4

Synthesis and Deposition of Au@PS Nanoparticle Hybrid Dielectric Ink

The formation and modification of the polymer shell of hybrid Au@PS nanoparticles via the ligand exchange from oleylamine (OAm) to PS are investigated in the first section of this chapter. The layer formation characteristics of the synthesized Au@PS hybrid inks, to be suitable as dielectric in thin film capacitors, in dependence on the substrate and solvent is investigated in the second section.

4.1 Influences on polymer shell by the ligand exchange from oleylamine to thiol-functionalized polystyrene

The polymer shell plays an important role for the dielectric properties of Au@PS NP layers. It should be dense enough to provide an effective insulation of the conductive cores from each other and to prevent leakage currents. The grafting density of the cores directly influences the Au volume fraction in the final layers under the assumption that all polymer left after washing is bound to the surface of the Au cores. This section will show the ligand exchange of Au@OAm to Au@PS nanoparticles and how to modify the polymer shell via the conditions during ligand exchange.

4.1.1 Tracking of ligand exchange with UV-Vis and Raman spectroscopy

To form the polymer layer, a ligand exchange to thiol-terminated polystyrene (PS-SH) was performed and was tracked with UV-Vis and Raman spectroscopy.

4.1.1.1 UV-Vis spectroscopy

After the synthesis, the AuNP are capped with OAm ligand. Typical medium-sized particles ($d_{\text{core}} = 4.7\,\text{nm}$) are shown in Figure 4.1. The TEM image indicates that the particle size distribution after synthesis was monodisperse. The ligand molecules are bound on the facets of the polycrystalline AuNPs whose individual atomic layers can be seen at the high zoom level. As the OAm molecules are too short and loosely bound to the Au cores, they are not suitable to form an effective insulation layer between the Au cores. The Au@OAm particles were stirred together with thiol-functionalized PS (PS-SH) to graft an insulating polymer shell on the Au cores, as stated in the Chapter 3. The Au cores should not be modified in the ligand exchange process to maintain the controlled AuNP core size from the synthesis.

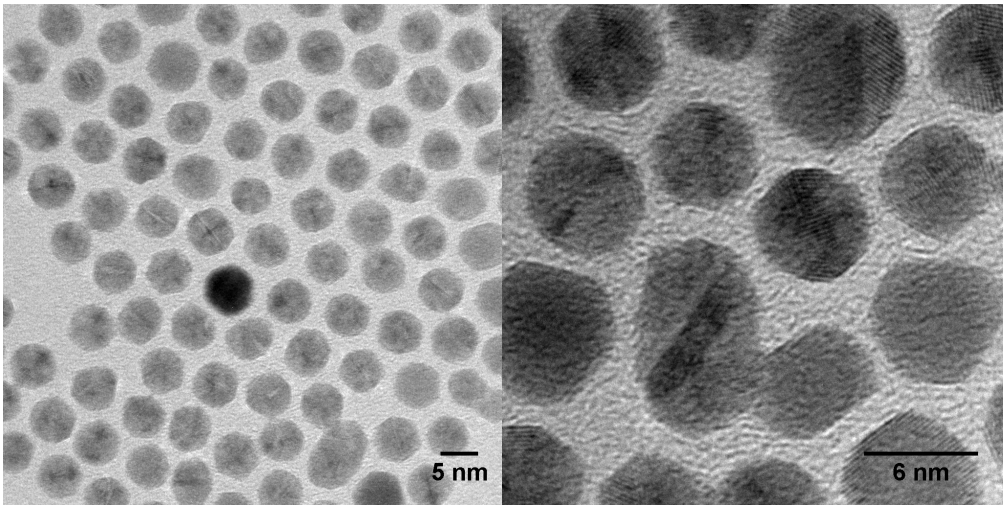

(A) (B)

FIGURE 4.1: Transmission electron micrographs of Au@OAm nanoparticles after synthesis.

Figure 4.2 shows the UV-Vis spectra of a Au@OAm NP dispersion (medium core size, black curve) and a Au@PS_{11000} NP dispersion (medium core size, high ligand-density, ligand exchange with stirring at 20 °C for 1 week, blue curve). The samples were diluted for measurement. Both spectra were then normalized in y-direction so that the absorption intensity at the plasmon peak was the same. The shape of the plasmon peak does not change, but its position shifted from 517 nm to 508 nm. It is known that ligand exchange causes a shift of the plasmon peak position if the dielectric environment around the Au NP core changes [180]. The shift of the peak position from Au@OAm NPs to Au@PS NPs indicate the modified dielectric environment due to ligand exchange. Au@PS NPs with the same medium core size but lower ligand densities (orange and green curve, see Section 3.1 in Chapter 3 for ligand exchange conditions) or shorter PS

chains (PS_{5000} ligand) used in the ligand exchange (red curve) did not change the shape of the spectra. This indicates that the plasmonic properties of the Au particles changed due to the exchanged PS ligand shell but not with varying ligand length or grafting density on the Au@PS particles.

The absorption at 400 nm was used to determine the Au concentration in the prepared inks. At this wavelength neither the plasmon peak nor the solvent has a large influence on the absorption. After calibration measurements, the UV-Vis absorption was used to directly derive the Au concentration [147] (see Chapter 3 for details).

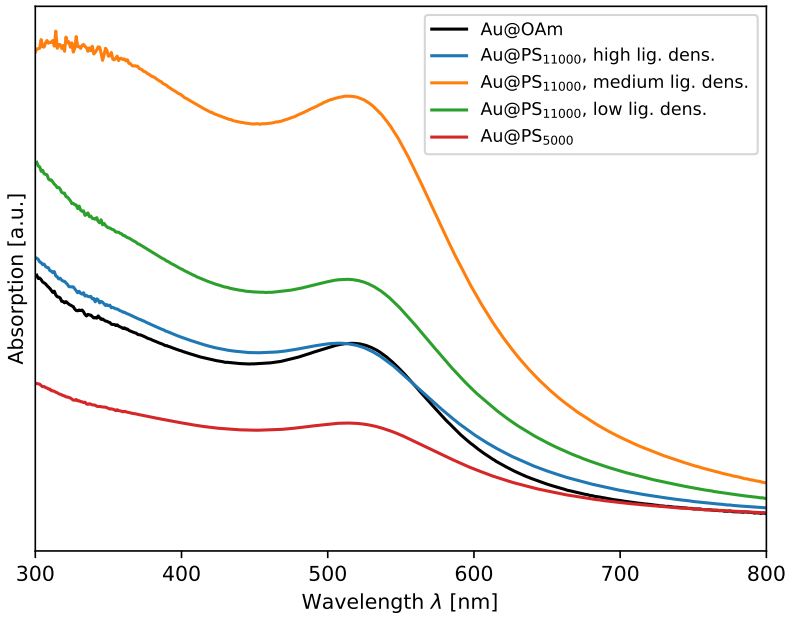

FIGURE 4.2: UV-Vis absorption spectra of $Au@PS_{11000}$ nanoparticles dispersed in toluene with high (blue curve), medium (orange curve), and low (green curve) ligand density and of $Au@PS_{5000}$ nanoparticles (red). The absorption spectrum of Au@OAm nanoparticles that were used to synthesize the $Au@PS_{11000}$ NPs with high ligand density is shown as the black curve; it was shifted in y-direction so that the absorption intensity at the plasmon peak was the same as for the blue curve.

4.1.1.2 Raman spectroscopy

A Raman spectrogram of Au@OAm NPs before the ligand exchange and of Au@PS NPs after ligand exchange (ligand exchange via stirring for 1 week at 60 °C) is shown in Figure 4.3. The peak at 246 cm^{-1} for Au@OAm was connected to gold-nitrogen bonds [181]. The origin of the peak at 553 cm^{-1} has not been reported in literature but is likely connected to a gold-nitrogen bonding. The Raman spectrum of the NPs after ligand exchange to Au@PS exhibited none of the peaks observed for Au@OAm. Instead, a peak at 300 cm^{-1} emerged; peaks in this region were assigned to the stretching

of Au-S bonds [182] representing the newly formed gold-sulphur bond. The new peaks at 259 cm^{-1} and 620 cm^{-1} are connected to the in-plane bending [183, 184] and to the in-plane vibration [183–188] of the phenyl ring in PS. It has long been known that the localized surface plasmon resonances of metal nanoparticles enhance the Raman activity of surface bound organic molecules, permitting the detection of small quantities of these organic molecules [189]. Because no traces of the Au@OAm peaks were seen in the spectrum of Au@PS, the Raman measurements indicate that the ligand exchange protocol effectively replaced the OAm ligand with PS-SH ligand and no considerable amount of residual OAm is present after ligand exchange.

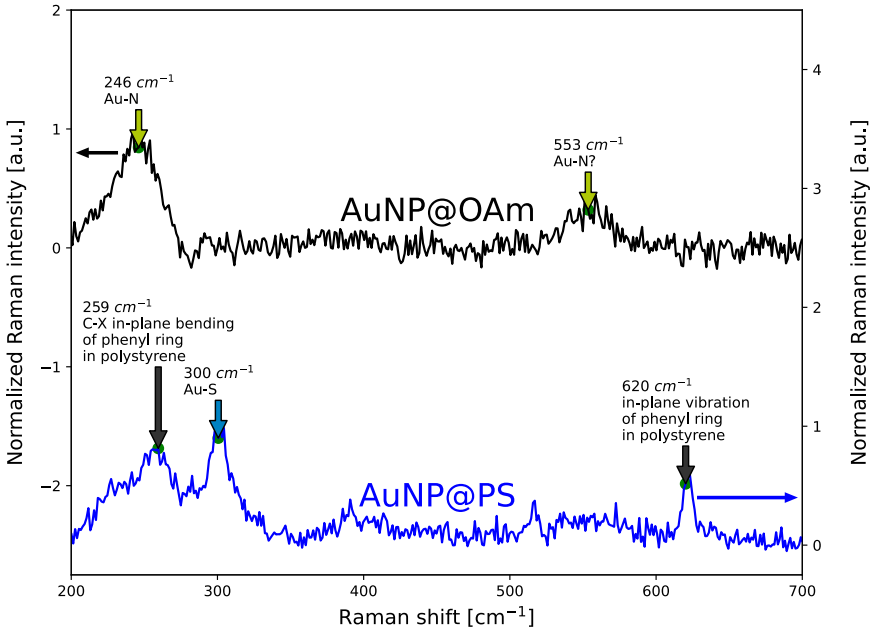

FIGURE 4.3: Raman spectra of Au@OAm nanoparticles (black, top) and Au@PS_{11000} nanoparticles (blue, bottom).

4.1.2 Structure of the polymer shell in dependence of ligand exchange conditions and ligand length

The polymer shell of the final Au@PS hybrid particles depended on the ligand exchange conditions, which influenced the grafting density of the selected polymer on the particle surface. In this section, the dependence of the polymer shell structure on the stirring time and solvent temperature during ligand exchange and on the ligand length is investigated employing DLS measurements to determine the hydrodynamic diameters and TGA measurements to determine the grafting densities.

The hydrodynamic diameters gave an indication for the polymer ligand conformation. The DLS measurements were performed in the temperature range between 20 °C and 60 °C for dispersions of Au@PS hybrid particles with ≈ 4.6 nm core diameter and for solutions of PS-SH in toluene, which were measured as a model system. The change of the polymer conformation depending on the solvent temperature was tracked by observed changes in the hydrodynamic diameters of Au@PS NPs and dissolved PS-SH. Representative for all DLS measurements, the data of Au@PS_{11000} NPs are shown in Figure 4.4: the left part shows the correlation functions, which were fit to obtain the correlation times τ, the right part shows the linear regression of the inverse correlation time τ^{-1} versus the squared wavenumbers q^2 (see Chapter 3 for details).

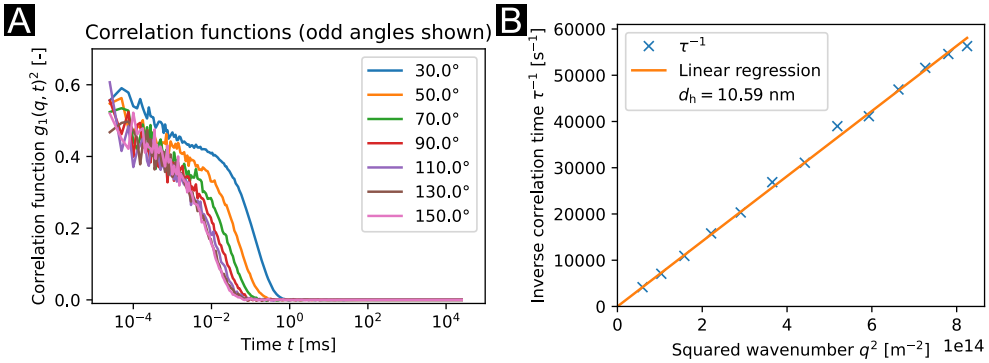

FIGURE 4.4: Dynamic light scattering and data analysis procedure for Au@PS_{11000} nanoparticles with medium ligand density measured at 20 °C. a) DLS measurements provided the correlation functions for measurement angles in the range 30° to 150°. b) Linear regression of the inverse correlation time τ^{-1} versus q^2 provided the hydrodynamic diameter d_h.

Figure 4.5 shows the temperature-dependent hydrodynamic diameters of various Au@PS NP dispersions and of PS-SH solutions. The ligand length of the Au@PS hybrid particles, the stirring time, and temperature during ligand exchange were varied as indicated in the legend in Figure 4.5a (see Chapter 3 for details). The changes in the hydrodynamic diameters are expected to correlate with changes in the polymer shell: Unfolded polymer chains cause larger hydrodynamic diameters in comparison to collapsed polymer chains. High grafting densities of the PS ligand with steric interaction between the ligands cause polymer brushes with unfolded chains, therefore a larger grafting density should correlate with larger hydrodynamic diameters.

4.1.2.1 Influence of stirring time

Figure 4.5a shows that the hydrodynamic diameters of Au@PS_{11000} NPs with stirring for 1 week at 60 °C (orange dots, $d_h \approx 16$ nm@20 °C) are above the hydrodynamic diameters of Au@PS_{11000} NPs with stirring for 4 weeks at 60 °C (green dots, $d_h \approx 12$ nm@20 °C).

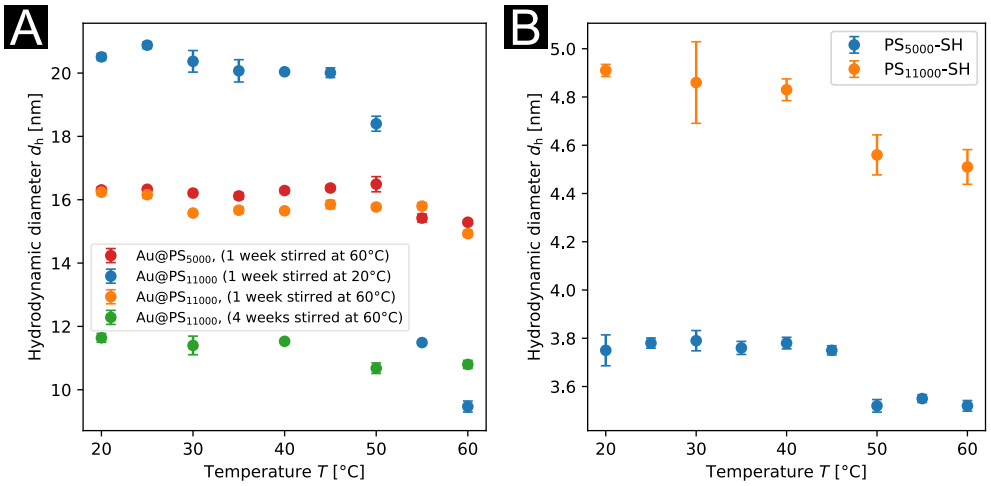

FIGURE 4.5: Temperature-dependent hydrodynamic diameters d_h of a) Au@PS hybrid nanoparticles ($d_{core} \approx 4.6\,nm$) and b) thiol-functionalized polystyrene in toluene. The ligand exchange for the Au@PS hybrid nanoparticles was performed in toluene with varying stirring times and solvent temperatures as indicated in the legend. Error bars indicate the uncertainty of the determined hydrodynamic diameters after linear regression of the inverse correlation times τ^{-1} versus the square of the wavenumber q^2.

The smaller hydrodynamic diameters of the latter sample at the same core diameter and ligand length indicated a mushroom conformation of collapsed polymer ligands in the polymer shell, which is a sign for a lower ligand density [157].

The Au mass fractions determined by TGA measurements of dried Au@PS$_{11000}$ particles whose ligand exchange was performed with stirring at 60 °C for 1 to 8 weeks allowed a more direct determination of the ligand density in dependence of the stirring time. Figure 4.6a shows the mass loss of two samples for each AuNP type during the TGA measurements. The main mass loss occurred at about 400 °C. The temperature of the thermal decomposition of PS is known to be between the temperature 350 °C to 400 °C [190–192], so this mass loss can be connected with the decomposition of PS. As the relative mass then hardly changed until 1000 °C or when the atmosphere was changed to oxygen at 1000 °C, the relative mass at about 520 °C was taken as the Au weight fraction of the dry samples.

Figure 4.6b shows the values of the Au weight fraction of the first and second measurements (crosses) and the mean value of these two measurements (blue circles) in dependence of the stirring time during ligand exchange. The data show that the Au mass fraction – and hence the ligand density – changed considerably from 1 week (66.5 wt% Au) to 4 weeks stirring time (83.1 wt% Au). Using Equations (3.2) to (3.4), the calculated ligand densities were $0.4\,nm^{-2}$ after 1 week stirring time and $0.2\,nm^{-2}$ after 4 weeks stirring time. Therefore, the longer stirring time led to a reduced ligand density and a thinner polymer shell. The reason for this could be that with increased stirring time,

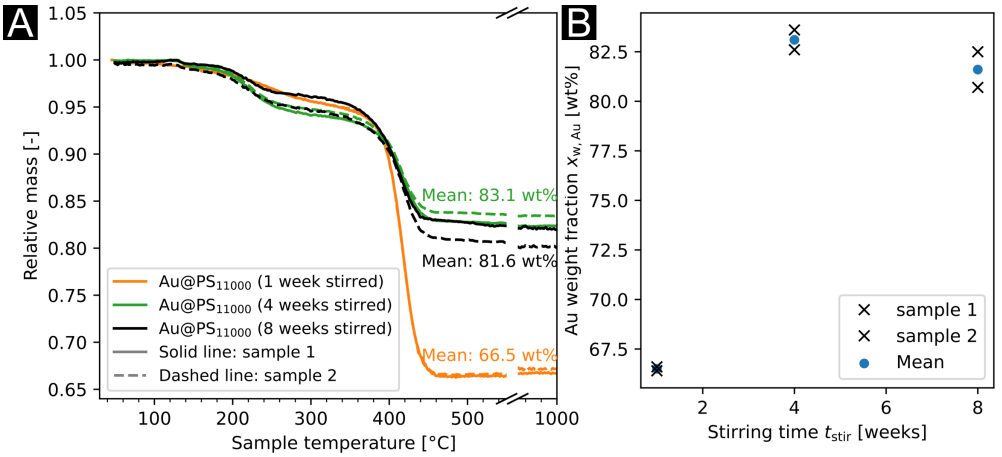

FIGURE 4.6: a) TGA results for hybrid Au@PS_{11000} particles with ligand exchange at 60 °C and different stirring times and b) the resulting Au weight fraction $x_{w,Au}$ in dependence of the stirring time t_{stir} by the mean of the TGA measurements.

part of the PS detaches from the Au core again and will be removed in the washing step after ligand exchange. Such a dynamic behaviour of the sulphur-Au bond is known for alkanethiol capped Au surfaces, i.e. the desorption of the covalently bound molecules was observed with the respective activation energies provided [193–195].

The measured Au weight fraction of 81.6 wt% for Au@PS_{11000} particles with stirring for 8 weeks at 60 °C during ligand exchange did not deviate considerably from Au@PS_{11000} NPs with stirring for 4 weeks. Therefore, the ligand density maintained the same value with increase of the stirring time during ligand exchange from 4 weeks to 8 weeks. It is assumed that a dynamic equilibrium between desorbed and adsorbed PS-SH ligands was already reached after 4 weeks.

4.1.2.2 Influence of solvent temperature

Another important parameter to influence the polymer shell during the ligand exchange is the solvent temperature. To understand this influence of the solvent temperature, the development of the hydrodynamic diameters of Au@PS hybrid NPs with the solvent temperature is analyzed. It is seen in Figure 4.5a for all measurements of the Au@PS hybrid particles that the hydrodynamic diameter dropped above 45 °C. To understand this observation, the development of the hydrodynamic diameter of PS-SH dissolved in toluene will be discussed as a model system.

Figure 4.5b shows the hydrodynamic diameters of pure PS_{5000}-SH with M_n = 5000 Da and PS_{11000}-SH with M_n = 11 000 Da. Their hydrodynamic diameters decreased at the temperature of about 45 °C from 3.8 nm to 3.6 nm for PS_{5000}-SH and from 4.9 nm to 4.6 nm for PS_{11000}-SH. Toluene is a known good solvent for PS with a theta temperature

of about 40 °C [162]. The polymer chains should be unfolded in a good solvent; at the theta temperature, the polymer chains should behave like in an ideal solvent. The drop in the measured hydrodynamic diameters indicated unfolded molecules at low temperatures that collapsed above 45 °C to coils. The reason for the worse solubility of the thiol-functionalized PS at high temperatures might be the polar nature of the thiol end group that reduced the compatibility with the non-polar toluene solvent.

As the drop of the hydrodynamic diameters was also observed for the Au@PS nanoparticles, it is assumed that the PS chains also collapse on the AuNP surface at temperatures above 45 °C while they are unfolded at lower temperatures. Higher ligand densities are expected for AuNPs where the ligand exchange was performed with unfolded instead of collapsed PS chains. The decrease in hydrodynamic diameter of the hybrid Au@PS NPs upon heating should be more evident for particles with high ligand density than for particles with low ligand density. Furthermore, the difference of the hydrodynamic diameters of Au@PS NPs and the core diameters should increase with ligand density as more PS is bound around the Au core. Such influences of the solvent temperature during ligand exchange can be seen by comparing the values of $Au@PS_{11000}$ NPs where the ligand exchange was performed at 20 °C (blue dots) or at 60 °C (orange dots) (both with 1 week stirring time). The hydrodynamic diameter at room temperature is higher for the $Au@PS_{11000}$ particles that were stirred at 20 °C. Additionally, the reduction of the hydrodynamic diameter upon solvent heating from $\approx$ 20 nm to $\approx$ 10 nm is much more pronounced for these particles implying a higher ligand density.

TGA measurements were used as described above to determine the ligand densities from the Au weight fractions of dried Au@PS samples. The Au weight fraction of Au@PS nanoparticles with ligand exchange at 20 °C was 48.6 wt% while it was 66.5 wt% for Au@PS nanoparticles with ligand exchange at 60 °C, indicating ligand densities of 0.7 nm^{-2} and 0.4 nm^{-2} (see Figure 5.3 and Table 5.3 in Chapter 5). This suggests that the unfolded state of the polymer chains during ligand exchange at a solvent temperature of 20 °C led to a high ligand density, while ligand exchange at higher solvent temperatures of 60 °C caused collapsing of the polymer chains, resulting in a polymer shell with a mushroom conformation and a lower ligand density.

4.1.2.3 Influence of ligand length

It is expected that the length of the polymer ligands also influences the polymer shell of Au@PS hybrid nanoparticles. The comparison of the hydrodynamic diameters of $Au@PS_{5000}$ and $Au@PS_{11000}$ NPs with the same ligand exchange conditions (both stirred

at 60 °C for 1 week) gives a first insight into this influence. Both samples have similar hydrodynamic diameters (see red and blue circles in Figure 4.5a), although PS_{5000} ligands are shorter. Therefore, it is assumed that the polymer shell with PS_{5000} is denser than with PS_{11000} due to a higher ligand density. On TEM images of these particles dried on a carbon grid, a grey layer around particles close to the edge indicated the polymer shell. Figure 4.7a shows that the dark Au core of $Au@PS_{5000}$ particles is covered by a homogeneous organic PS shell. Figure 4.7b shows $Au@PS_{11000}$ particles with a much thinner organic PS shell. This indeed indicates that the ligand density at the $Au@PS_{11000}$ particles is lower and the polymer shell is less regular than for the $Au@PS_{5000}$ particles.

As stated before, TGA measurements of dried Au@PS samples were used to determine the ligand densities. The Au weight fraction of Au@PS nanoparticles with PS_{5000} shell was 58.6 wt% while it was 66.5 wt% for Au@PS nanoparticles with PS_{11000} shell, resulting in ligand densities of $1.3\,nm^{-2}$ and $0.4\,nm^{-2}$ (see Figure 5.3 and Table 5.3 in Chapter 5). Therefore, the TGA results confirm that shorter PS ligands led to a higher ligand density, thus favouring a more regular polymer shell.

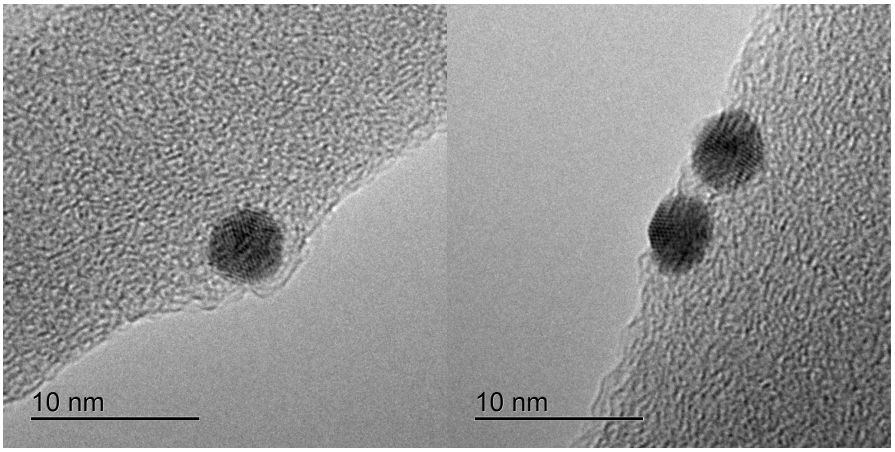

(A) $Au@PS_{5000}$ (B) $Au@PS_{11000}$

FIGURE 4.7: TEM images of Au@PS nanoparticles. a) A $Au@PS_{5000}$ nanoparticle with higher ligand density appears completely covered with the grey organic shell. b) In a TEM image of $Au@PS_{11000}$ nanoparticles with lower ligand density, the grey organic shells are much thinner and less regular.

4.2 Formation of hybrid dielectric on substrates suitable for thin film capacitors

Layer formation is influenced by the wetting of an ink and depends both on the substrate and on the solvent (see Equation (2.12)). In this section, the dependence of the formation

of the hybrid dielectric on the solvent used for the ink and the prerequisites of substrates used for thin film capacitors are discussed.

4.2.1 Solvent effects on layer formation

The final solvent of the nanoparticle ink is introduced in the redispersion step after ligand exchange of the oleylamine (see Chapter 3). Cyclohexane is known as good solvent for alkane-thiol capped nanoparticles [142], while toluene is a good solvent for PS [162]. These two solvents were selected for inks with Au@PS nanoparticles to test the dependence of the layer formation behaviour on the solvents. Due to simplicity, the pure solvents were used first and the surface profiles of layers fabricated from the inks were measured by white light interferometry (WLI).

First, a Au@PS dielectric layer was prepared on a silicon/gold substrate via spin coating of Au@PS_{5000} NPs dispersed in cyclohexane. The sample had a matte appearance after spin coating. A surface profile of the sample as measured by WLI in Figure 4.8a suggests that islands of the solid nanoparticles formed during cyclohexane evaporation and impeded the formation of homogeneous layers. The reason for this is probably the high vapour pressure of cyclohexane, causing aggregation of the Au@PS hybrid particles in islands during the rapid solvent evaporation and leading to a surface roughness of $R_a = 108\,\text{nm}$ as determined from the WLI measurements.

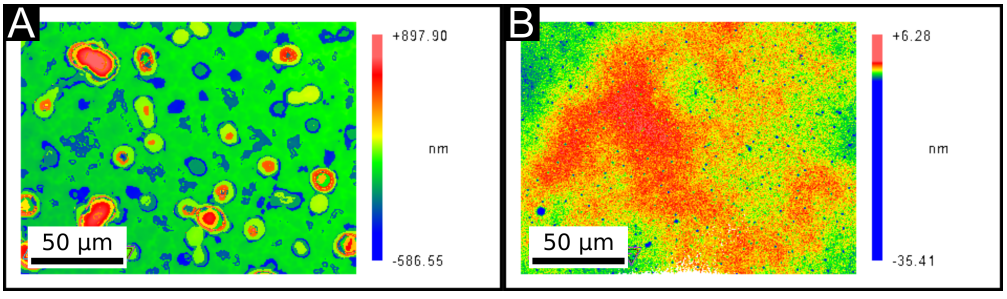

FIGURE 4.8: Surface profile as measured by white light interferometry of a spin coated layer of Au@PS_{5000} dispersed in a) cyclohexane and b) cyclohexane and toluene in a volume ratio of 10:1 on silicon/gold substrate.

It is known from studies on the coffee-ring effect that drying of functional inks can be governed by solvent mixtures of a volatile and less volatile solvent: a strong Marangoni flow is induced that causes a flow of the solvent from the edge to the centre of the droplet due to thermal gradients, which opposes the coffee-ring effect [196]. In a second experiment, such a solvent mixture of 200 µL of the cyclohexane-based dispersion and 20 µL of toluene was used to spin coat Au@PS hybrids on a silicon/gold substrate. The sample prepared with this solvent mixture had a glossy surface after spin coating.

The surface roughness as determined with WLI was only $R_a = 1\,nm$, two orders of magnitude below that from pure cyclohexane solvent. These results show that the usage of toluene solvent permitted a regular layer formation of the Au@PS hybrid particles in spin coating. Due to simplicity, pure toluene solvent was used instead of solvent mixtures in the studies shown in Chapter 5 and Chapter 6.

4.2.2 Substrates for thin film capacitors

For the dielectric characterization of the Au@PS hybrids, thin film capacitors were prepared in this thesis. As the nanoparticles and the thicknesses of the dry dielectric layers are in the nm range, the substrate should have a smooth surface to fulfil the assumptions of a parallel plate capacitor with a homogeneous electric field. For good functionality in the thin film capacitor, the substrate as bottom electrode should have a high conductivity. Different substrates were investigated for their suitability as a bottom electrode for thin film capacitors by roughness measurements with AFM, conductivity measurements, and by the estimation of the layer quality with WLI surface profiles.

Figure 4.9 shows the surface profile from AFM of pristine silicon <110> as received by the supplier, silicon substrates with aluminium layers sputtered at energies of 50 W or 100 W, and silicon substrates coated with evaporated gold layers. The average surface roughness values R_a were determined as the arithmetic average deviation from the best fit plane (see Table 4.1). They indicate that the evaporated gold layer had the smoothest surface, smoother even than for pristine silicon wafers. The aluminium sputtered at 100 W had small "spikes" in the AFM surface profile, possibly due to inhomogeneous layer growth during sputtering, and a surface roughness that was more than double than for 50 W. Due to this result, the sputter energy of 50 W was used for the preparation of the aluminium bottom electrodes of the thin film capacitors in this thesis.

TABLE 4.1: Average surface roughness R_a of a) silicon, b) silicon with sputtered aluminium (sputter energy 50 W), c) silicon with sputtered aluminium (sputter energy 100 W), and d) silicon with evaporated gold as measured with AFM.

Name	Preparation method	R_a [nm]
Si	pristine	3.7
Si+Al (50 W)	sputtered	3.0
Si+Al (100 W)	sputtered	6.5
Si+Au	evaporated	0.6

The pristine silicon wafer is not suitable as bottom electrode in thin film capacitors. The metal of the contact pin and the semiconductor substrate would form Schottky contacts that complicate the measurements [197]. The metal coated silicon wafers are

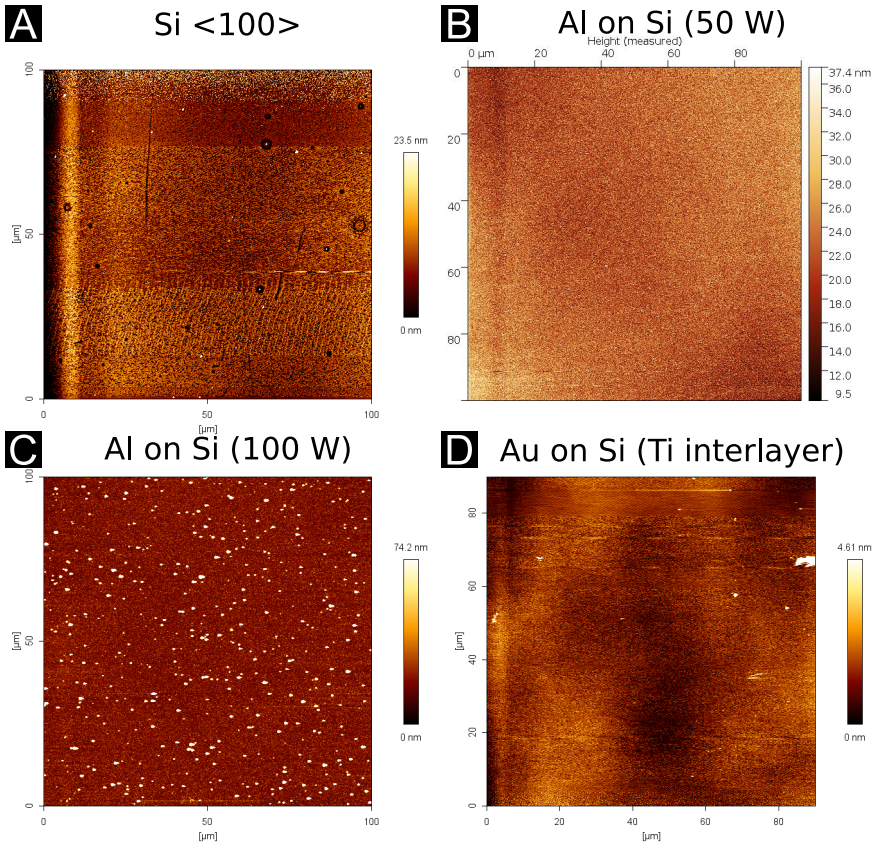

FIGURE 4.9: Surface profiles of substrates from AFM. a) Pristine silicon <110> surface of silicon wafer as received from supplier. b) Silicon with sputtered aluminium (sputter energy 50 W). c) Silicon with sputtered aluminium (sputter energy 100 W). d) Silicon with evaporated gold layer (titanium layer as adhesion interlayer).

suitable bottom electrodes when they show metallic conductivity during dielectric characterization. The conductivity of these substrates was measured by connecting both contact pins to the substrate (short circuit) in the impedance measurement. This resulted in very low values for the resistance parallel to a capacitor in an equivalent circuit ($R_\mathrm{p} \leq 1\,\Omega$) for the silicon/gold substrates. The aluminium/silicon substrates showed in similar measurements a resistance in parallel of $R_\mathrm{p} = 5\,\Omega$ to $R_\mathrm{p} = 100\,\Omega$ when the measurement pins formed good contacts to the substrates. Values of $R_\mathrm{p} > 1\,\mathrm{M}\Omega$ were observed for bad contacts between pins and substrates. As large contact resistances between the measurement pin and the substrate falsify the impedance measurements, the contact pins were placed until good contacts were formed. In short, evaporated gold coated silicon showed higher smoothness, higher conductivity, and less problems with contact resistances, probably due to the missing oxide layer that forms on aluminium coated substrates.

A second requirement for the characterization of the Au@PS hybrids is a complete dielectric layer without pinholes in the thin film capacitors. Pinholes form due to localized dewetting, e.g. by the presence of dust particles during layer formation, but possibly

also by the influence of the surface energy of the substrates, and lead to a short circuit and dielectric failure. Thin film capacitors were prepared from Au@PS_{5000} NP dispersion (AuNP core diameter 4.7 nm) via spin-coating on the metal coated substrates. A cross section of a thin film capacitor on silicon/Au substrate is shown in Figure 4.10a: the thickness of the dielectric layer was 58 nm, the top contacts were evaporated gold. However, dielectric spectroscopy of the thin film capacitors on silicon/Au substrates showed no functional capacitors and all measurements exposed a short circuit. The WLI measurements of the sample surface revealed pinholes (see surface profile along the marked line in Figure 4.10b). The origin of the pinholes remained unclear; it could be due to localized dewetting of the ink caused by the surface energy of gold. Hence, the silicon/gold substrates were not suitable as substrates for the thin film capacitors in this thesis.

For Au@PS layers spin coated on silicon/aluminium substrates, these pinholes were not observed (see results in Chapter 5 and Chapter 6). Therefore, for further experiments silicon/aluminium substrates were used.

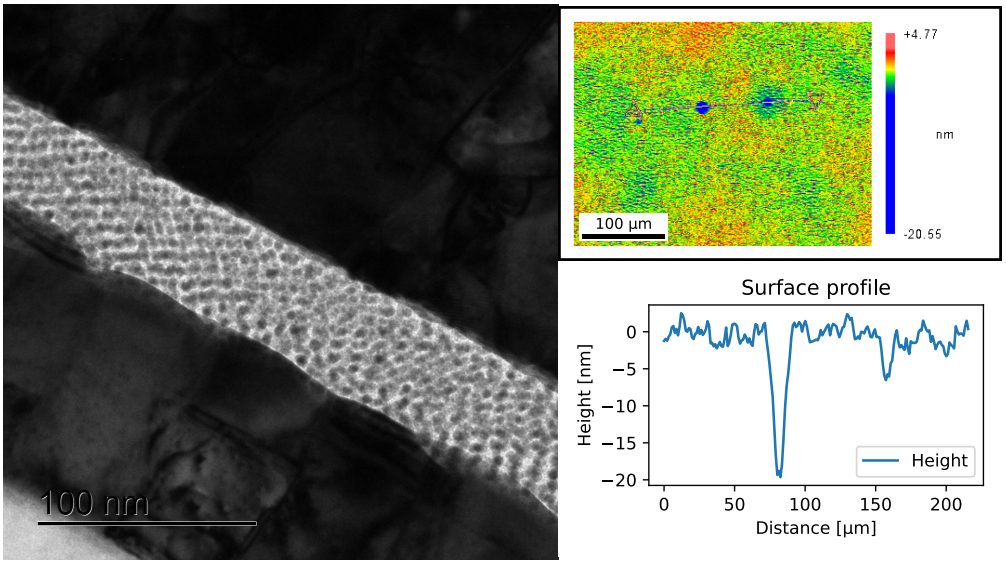

(A) (B)

FIGURE 4.10: a) Transmission electron micrograph of focused ion beam cross-sections of a thin film capacitor with a spin-coated Au@PS_{5000} hybrid dielectric layer on a Au/silicon substrate. The top contact is evaporated gold. b) Surface profile as measured by white light interferometer. The bottom shows the surface profile along the marked line.

4.3 Conclusions

This section introduced the preparation and processing of the hybrid Au@PS dielectric ink. Successful ligand exchange from OAm to thiol-functionalized PS was shown via

UV-Vis and Raman measurements. It was found by DLS measurements that the ligand density in Au@PS particles is influenced by the conditions during ligand exchange. The polymer coils at temperatures of above 45 °C and the ligand densities were lower when the ligand exchange was performed at 60 °C than at 20 °C. Longer stirring time decreased ligand density. These insights were used in the Chapter 5 to prepare dielectric layers with varying gold volume fractions (see Table 5.3). The modification of the polymer shell directly influences the expected properties of the Au@PS hybrid. A reduced ligand density leads to thinner polymer shells and an increased Au volume fraction, so higher dielectric constants of the hybrid are expected.

Layers of Au@PS hybrids on silicon/aluminium substrates were prepared. The layer thickness was in the range of 50 nm while the formed layers on these substrates were dense enough to prevent short circuits and to be a suitable dielectric for thin film capacitors. To ensure good dielectric measurements of these thin film capacitors with the homogeneous electric fields of parallel plate capacitors, lower sputter energy of 50 W was used to improve substrate smoothness. During impedance spectroscopy, good contact formation between the contact pins and the silicon/aluminium substrate should be checked via the measured resistance in parallel when a short circuit on the substrate is applied.

Chapter 5

Variation of Polymer Shell and Printing on Rigid Substrates[1]

This chapter introduces a new "Type III" class of dielectric hybrid materials that is suitable for inkjet printing of very thin dielectric layers and based on hybrid nanoparticles with individual, molecular insulating shells. As it was presented in Chapter 2, Type I (Figure 2.6a) and Type II (Figure 2.6b) dielectric nanocomposites were already reported in the literature. In this chapter, the preparation of Type III hybrids from Au@PS functional inks and their application as dielectric in thin film capacitors is demonstrated. "The low-viscosity inks of Type III dielectrics contain no free polymer; all polymer is covalently bound to the inorganic cores to maximize the metal content and, therefore, increase the dielectric constant."[1] The concept of using polystyrene of two different molecular weights that is covalently grafted onto nanoscale gold crystals is demonstrated. Core-shell particles (Au@PS NPs) are obtained, which are stable enough for inkjet printing. "The polymer shells cause filming that aids the formation of closed films, similar to classical dispersion paints [198, 199], while electrically insulating the metal cores, thus suppressing percolation even in dense packings. Previous studies on inorganic nanoparticles with polymer shells aimed at electrical conductors, not dielectrics. Schlicke *et al.* prepared free-standing films of gold nanoparticles that were connected by alkanedithiols [200]. Recently, Liu *et al.* used thin layers of AuNPs that were separated by entangling covalently bound PS for sensing applications [201]."[1] Dielectric measurements were not reported.

[1]**Publication note:** Following the guidelines for a dissertation at Saarland University, the publication of partial results of the doctoral thesis in peer-reviewed journals is explicitly desired prior to submission of the dissertation. Hence, the results presented in this chapter were published in:

Buchheit, R., Kuttich, B., González-García, L., Kraus, T., Hybrid Dielectric Films of Inkjet-Printable Core–Shell Nanoparticles. *Advanced Materials* 2021, 33, 2103087. `https://doi.org/10.1002/adma.202103087`

With permission of all authors, the figures and tables were reprinted and the text was adjusted to the form of the monograph and reprinted. Verbatim reproduced text is shown in quotation marks.

The chapter is structured as follows: "we first describe the synthesis of gold cores and their covalent grafting with two different thiolated PS types, PS_{11000} with 11 000 Da average molecular weight and PS_{5000} with 5000 Da molecular weight (see Figure 5.1). The grafting density of the PS_{11000} ligand was varied during synthesis in order to further adjust the composition and structure of the final films.

Dispersions of the particles in toluene were then deposited as dielectric layers by spin coating. We analyzed their structure using transmission electron microscopy (TEM) cross-sections and small angle X-ray scattering (SAXS) and found that the polymer shell affects the order of the films: PS_{11000} led to disordered particle packings in the film independent of grafting density, while PS_{5000} yielded superlattice films with regular particle packing. The organic content of all dry films was analyzed by thermogravimetric analysis (TGA) in order to obtain the exact metal content."[1]

From all films, thin film capacitors were prepared. The thin film capacitors were characterized using dielectric spectroscopy. "Dielectric losses and polarization were quantified in a frequency range from 1 Hz to 1×10^6 Hz and correlated with the metal fractions. Type III dielectric hybrids with disordered particle packing behaved similar to Type II dielectric composites, with a non-linear increase of the dielectric constant with the increasing Au volume fraction. Type III hybrids with regular particle packing exhibited similar dielectric constants but a lower minimum of the loss tangent."[1]

Finally, a functional capacitor with an inkjet printed Au@PS hybrid dielectric layer of ≈ 17 nm thickness was built. This demonstrated the printability and reliability of the material. It is the first demonstration of an inkjet printed capacitor based on core-shell particles with a conductive core to the author's knowledge.

5.1 Fabrication process for thin film capacitors

"Thin film capacitors were prepared by spin coating AuNP@PS hybrid particles of various types on silicon substrates with a sputtered Al layer as bottom contact and an evaporated Au top contact (Figure 5.1). Additional samples were prepared by inkjet printing on the same substrate."[1]

The film structure was tuned by using particles with different ligand densities and ligand lengths. "Gold cores with increasing PS_{11000} grafting densities yielded disordered films with decreasing Au volume fractions (Figure 5.1 on the left), while gold cores with PS_{5000} shells yielded films with regular particle packing (Figure 5.1 on the right). The structures were reproducible and formed upon drying both for the spin coated and inkjet

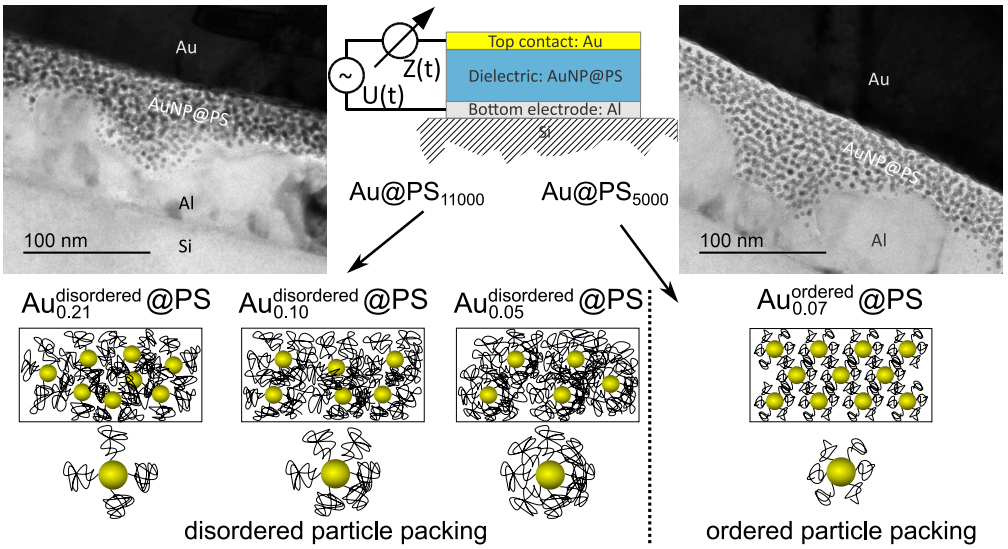

FIGURE 5.1: Thin film capacitors with hybrid dielectric films of gold nanoparticles having covalently attached polystyrene shells. We varied the polymer grafting density to adjust the metal fraction of the films. Films with regular particle packing were prepared using thin polystyrene shells in order to study the effect of particle packing on dielectric properties. Reprinted with permission of Wiley-VCH GmbH from [1].

printed samples. In the following, we refer to the different films as $\mathrm{Au}_{0.xx}^{\mathrm{disordered}}$@PS and $\mathrm{Au}_{0.xx}^{\mathrm{ordered}}$@PS, where $0.xx$ represents the Au volume fraction in the dielectric layer.

The thickness of the spin coated hybrid dielectric layers was measured by white light interferometry (WLI). It was homogeneous across the entire sample area and was found to be in the range of (27.4 ± 2.2) nm to (79.9 ± 3.1) nm. The thin dielectric layers have to be handled with care; they are soft and susceptible to scratches. White light interferometry was used instead of atomic force microscopy to avoid scratching and falsification of the thickness values. The dielectric layers in the full capacitor were protected by the metal electrodes.

Measured dielectric properties of all fabricated thin film capacitors are listed in Table 5.1."[1] The dielectric spectroscopy measurements were evaluated by representing the thin film capacitors with an equivalent circuit of an ideal capacitor with capacitance C_{p} and an ideal resistor R_{p} representing leakage currents in parallel. "The permittivity was calculated from the measured capacities assuming a parallel plate capacitor model (see Equation (3.22))."[1] The roughnesses of the sputtered aluminium electrodes and of the dielectric films were measured.

The surface profiles of aluminium electrodes were obtained using AFM in tapping mode. The surface profiles of the spin coated dielectric layers were measured with WLI. Areas of 100 µm x 100 µm were numerically analyzed using MetroPro software to obtain the roughness values listed in Table 5.2. Figure 5.2a and Figure 5.2b show the profiles of the electrode and of the dielectric layer surface profile of the spin coated sample

TABLE 5.1: Dielectric properties of thin film capacitors with hybrid dielectric films of thickness t at 10 kHz. C_p is the real part of the capacitance in parallel. Dielectric constants ε_r and loss $\tan\delta$ were obtained by dielectric spectroscopy on at least 14 measured thin film capacitors for the spin coated hybrid dielectric samples and 2 measured capacitors for the inkjet printed hybrid dielectric sample. Reprinted with permission of Wiley-VCH GmbH from [1].

Sample label	preparation method	t [nm]	C_p [pF]	ε_r [−]	$\tan\delta$ [−]
$Au_{0.05}^{disordered}$@PS	spin coated	79.9 ± 3.1	271 ± 7	3.1 ± 0.1	0.0247 ± 0.0045
$Au_{0.10}^{disordered}$@PS	spin coated	51.1 ± 1.4	654 ± 16	4.8 ± 0.1	0.0682 ± 0.0042
$Au_{0.21}^{disordered}$@PS	spin coated	27.4 ± 2.2	8724 ± 170	34.3 ± 0.7	0.0510 ± 0.0048
$Au_{0.07}^{ordered}$@PS	spin coated	48.1 ± 3.0	490 ± 33	3.4 ± 0.2	0.0289 ± 0.0550
$Au_{0.10}^{disordered}$@PS	inkjet printed	16.7 ± 9.8	2021 ± 98	4.8 ± 2.8	0.0569 ± 0.0060
PS_{5000}-SH	spin coated	248.0 ± 6.4	79 ± 4	2.8 ± 0.1	0.0080 ± 0.0037
PS_{11000}-SH	spin coated	265.7 ± 7.1	68 ± 2	2.6 ± 0.1	0.0094 ± 0.0002

$Au_{0.10}^{disordered}$@PS, which was representative of all spin coated samples. Figure 5.2c shows the surface profile of the inkjet printed sample. As the roughnesses of the sputtered aluminium electrodes ($R_a = 2.96$ nm) and of the dielectric films ($R_a = 0.26$ nm) are both considerably smaller than the dielectric film thicknesses, the simplification of the parallel plate capacitor model is justified.

TABLE 5.2: Average surface roughnesses R_a of the aluminium electrode (from AFM) and hybrid dielectric layers (from WLI). Reprinted with permission of Wiley-VCH GmbH from the Supporting Information of [1].

Sample label	coating method	R_a [nm]
$Au_{0.05}^{disordered}$@PS	spin coated	1.08
$Au_{0.10}^{disordered}$@PS	spin coated	0.26
$Au_{0.21}^{disordered}$@PS	spin coated	0.36
$Au_{0.07}^{ordered}$@PS	spin coated	0.40
$Au_{0.10}^{disordered}$@PS	inkjet printed	19.58
Al coated silicon	sputtered	2.96

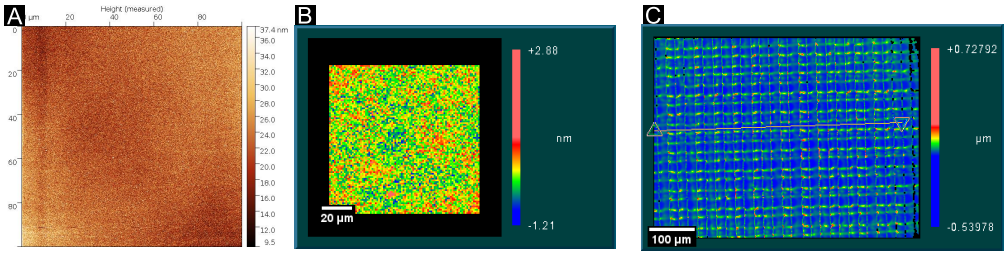

FIGURE 5.2: Surface profile measurements. a) Surface profile of Al coated silicon from AFM. b) Surface profile of the spin coated sample $Au_{0.10}^{disordered}$@PS from WLI. c) Surface profile of an inkjet printed sample $Au_{0.10}^{disordered}$@PS from WLI. Reprinted with permission of Wiley-VCH GmbH from the Supporting Information of [1].

The results from impedance spectroscopy were analyzed using the measured thickness and the contact area of the top contact that was defined in the evaporation process (see Chapter 3, page 35 and page 41 for details).

5.2 Variation of Au volume fraction by different ligand densities

The first part of the results presented in this chapter illustrates the effects of varying the Au volume fraction in the AuNP@PS dielectric layers by changing the grafting density of PS_{11000} during hybrid particle synthesis (Table 5.3). As it was discussed in Chapter 4, the polymer shell of the Au@PS nanoparticles can be adjusted by different conditions during the ligand exchange process. It was found that different stirring times and stirring temperatures and the selected ligand length had a strong impact on the polymer shell, mainly due to different grafting densities. Here, we used different ligand exchange conditions to prepare Au@PS hybrids with the same Au core size but varying polymer shell structures. Au@PS hybrid particles with medium ligand density (stirring at 60 °C for 1 week) were synthesized with PS_{11000} and PS_{5000} ligands, Au@PS hybrid particles with high grafting density (stirring at 20 °C for 1 week) and low grafting density (stirring at 60 °C for 4 weeks) were synthesized with PS_{11000} ligand (see Table 5.3). The details of the synthesis and ligand exchange process are described in Chapter 3, page 31 ff. "The Au volume fractions for all films that we report in Table 5.4 were obtained from TGA data assuming bulk densities for the Au core and the PS ligand shell and compact film structures."[1] Two TGA measurements for each prepared ink (Figure 5.3) indicated main mass losses occurred below the temperature ≈ 520 °C and all remaining mass at 520 °C was gold. The grafting densities were calculated assuming that all organic mass originated from covalently bound PS ligand molecules (see Chapter 3, page 37 for additional details).

TABLE 5.3: Measured properties of the prepared Au@PS hybrid nanoparticle inks in this chapter (in toluene) with the stirring time t_{stir} and stirring temperature T_{stir} during the exchange of oleylamine with polystyrene, the ligand density $\rho_{A,ligand}$, the diameter of the Au cores d_{core}, and the gold concentration in the inks c_{Au}. Reprinted with permission of Wiley-VCH GmbH from [1].

Ink label	Ligand	t_{stir}, T_{stir}	$\rho_{A,ligand}$ [nm^{-2}]	d_{core} [nm]	c_{Au} [$mg\,mL^{-1}$]
$Au_{0.05}^{disordered}$@PS	PS_{11000}	1 week, 20 °C	0.7	4.2	17.7
$Au_{0.10}^{disordered}$@PS	PS_{11000}	1 week, 60 °C	0.4	4.6	34.0
$Au_{0.21}^{disordered}$@PS	PS_{11000}	4 weeks, 60 °C	0.2	4.4	20.1
$Au_{0.07}^{ordered}$@PS	PS_{5000}	1 week, 60 °C	1.3	4.7	12.8

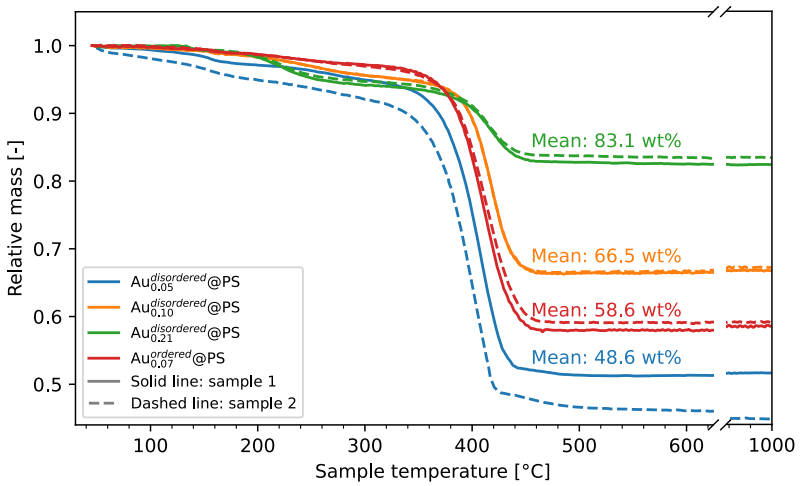

FIGURE 5.3: TGA results for all dielectric layers prepared for this chapter. The mean value of two measured samples is reported. Reprinted with permission of Wiley-VCH GmbH from the Supporting Information of [1].

TABLE 5.4: Experimental results from TGA and SAXS for Au content and surface-to-surface distance between Au cores for $Au_{0.xx}^{disordered}$@PS with the weight and volume content $x_{w,Au}$ and $f_{v,Au}$ of gold in the dielectric layers and the characteristic surface-to-surface distances d_{ss}^1 and d_{ss}^2 of the AuNPs in the dielectric layers. Reprinted with permission of Wiley-VCH GmbH [1].

Sample name	$x_{w,Au}$ [wt%]	$f_{v,Au}$ [vol%]	d_{ss}^1 [nm]	d_{ss}^2 [nm]
$Au_{0.05}^{disordered}$@PS	48.6	4.9	8.6	1.0
$Au_{0.10}^{disordered}$@PS	66.5	9.7	6.2	0.7
$Au_{0.21}^{disordered}$@PS	83.1	21.1	22.9	0.8

"The grafting densities affected the distance between the Au cores, which is likely to change the capacitance between the metal cores and the leakage currents due to tunnelling (see Figure 2.6c). We used SAXS in transmission in order to quantify the particle-particle spacing."[1]

We measured SAXS spectra of Au@PS particles drop casted on Kapton foil as described in Chapter 3 and calculated the effective structure factors from these measurements. The transmission SAXS of the drop casted films with PS_{11000} shells is shown in Figure 5.4. Broad peaks are found for all layers, indicating disorder. This is consistent with the disordered particle packing in TEM cross sections of these dielectric Au@PS layers in Figures 5.5 and 5.6. The brightness in the TEM cross sections correlates with the electron transparency depending on the thickness of the sample and the electron absorbance, which is much higher for Au than for the organic fraction. Since the thicknesses of the TEM lamella were not uniform due to the preparation process, the Au volume fractions were derived from TGA measurements rather than from the TEM cross sections. For an

accurate analysis of the particle packing, the recorded transmission SAXS of the drop casted layers was evaluated using an effective structure factor.

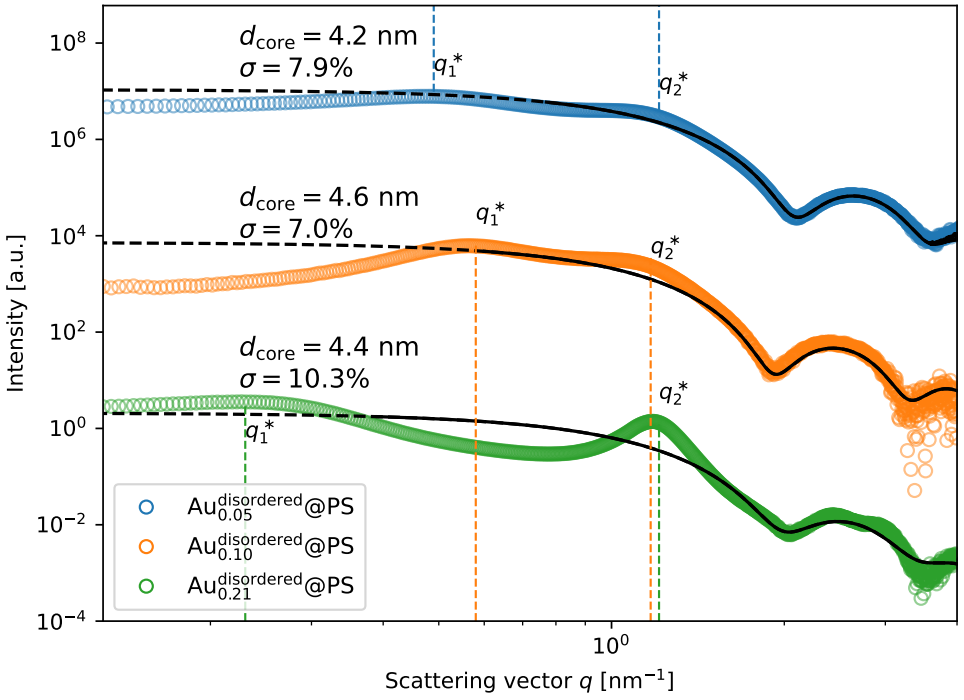

FIGURE 5.4: Transmission SAXS of drop casted Au@PS hybrid particles films on Kapton foils. The measurements were shifted in y-direction by a multiplication factor. The solid black line shows the form factor obtained from dispersion, the coloured lines mark the position of the q-peaks in the dried layers. The broad peaks in the AuNP@PS$_{11000}$ spectra indicate a random packing of the AuNPs. Reprinted (adapted) with permission of Wiley-VCH GmbH from the Supporting Information of [1].

We found two peaks in the effective structure factors of all drop casted $Au_{0.xx}^{disordered}$@PS samples (see Figure 5.7a). "The two maxima at q_1^* and q_2^* do not belong to the same geometrical feature of the film but indicate that two different length scales exist in particle packing."[1] Each characteristic length scale in the packing causes a corresponding maximum in the effective structure factor, whose positions are listed in Table 5.5. Equation (3.10) and Equation (3.14) were used to calculate the corresponding spacings d_{ss} as listed in Table 5.4.

This detailed analysis using the effective structure factors (see Figure 5.7 and Table 5.5) indicates that the spacings reported in Table 5.4 occurred in the films. "Their structure was thus characterized by a larger spacing d_{ss}^1 and by a smaller spacing d_{ss}^2. The overall packing density of the particles (and thus, the Au volume fraction) increased with decreasing grafting density. The smaller spacing d_{ss}^2 remained close to 1 nm for all shells, while the larger spacing d_{ss}^1 more than doubled for the smallest grafting density. The two values thus do not represent average particle distances in a fully random packing,

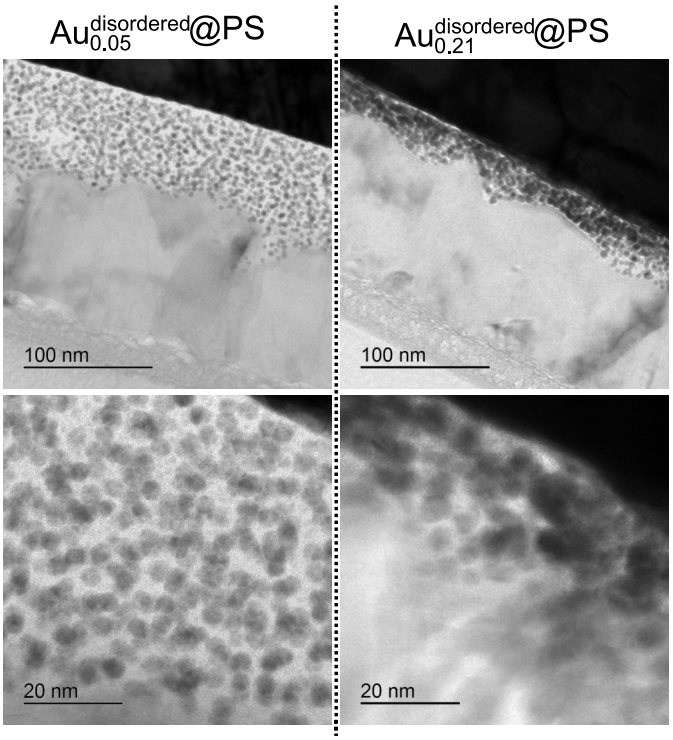

FIGURE 5.5: Transmission electron micrographs of focused ion beam cross sections of thin film capacitors with AuNP@PS_{11000} layers of the highest (ligand exchange 1 week, 20 °C, left side) and lowest (ligand exchange 4 weeks, 60 °C, right side) ligand density used. Reprinted with permission of Wiley-VCH GmbH from the Supporting Information of [1].

TABLE 5.5: Positions of peaks from the disordered packing of the layers $Au_{0.xx}^{disordered}$@PS. Values are taken from the effective structure factor originating from the SAXS in transmission in Figure 5.4. Reprinted with permission of Wiley-VCH GmbH from the Supporting Information of [1].

Sample name	q_1^* [nm^{-1}]	q_2^* [nm^{-1}]
$Au_{0.05}^{disordered}$@PS	0.49	1.21
$Au_{0.10}^{disordered}$@PS	0.58	1.17
$Au_{0.21}^{disordered}$@PS	0.23	1.21

but structural aspects of the films that are probably connected with chain-like particle arrangements visible in TEM."[1] These chain-like particle arrangements can be seen in Figure 5.8a and in Figure 5.9. "Such chains have been reported previously for the packing of 'patchy particles' with heterogeneous surfaces [165]. It is likely that the polymer ligand chains fold on the metal core and lead to a 'patchy' surface, in particular at low grafting density, where more space is available."[1]

As a reference for the dielectric results of the Au@PS hybrid films, capacitors with thin films of pure thiol-functionalized PS as dielectric layers were prepared via spin coating of thiol-functionalized PS solutions with a film thickness of $t = 248$ nm for PS_{5000}-SH

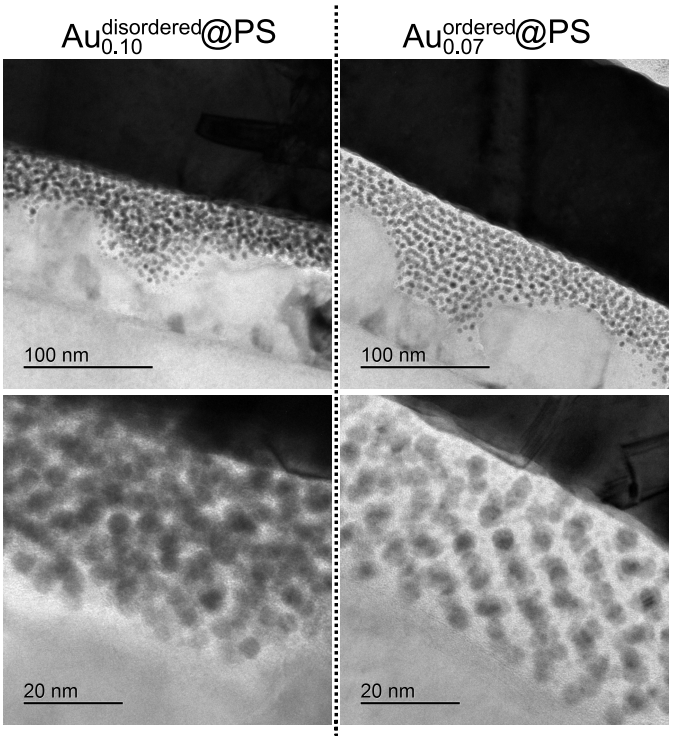

FIGURE 5.6: Transmission electron micrographs of focused ion beam cross sections of thin film capacitors with the AuNP@PS_{11000} layers on the left and the AuNP@PS_{5000} layers on the right (ligand exchange 1 week, 60 °C). Reprinted with permission of Wiley-VCH GmbH from the Supporting Information of [1].

and $t = 266\,\text{nm}$ for PS_{11000}-SH. Figure 5.10 shows the measured dielectric properties of the reference devices. The dielectric constants were in the range between 2.6 and 2.9, where larger values were seen at lower frequencies, slightly above the values reported for amorphous polystyrene at low frequencies ($\varepsilon_{r,PS} = 2.52$ [168]). Literature reports that functional groups such as S–H can be polarised at low frequencies [202], explaining the larger dielectric constant of the thiol-functionalized polystyrene. The polarization of the functional group also explains the higher dielectric constant of PS_{5000}-SH in comparison to PS_{11000}-SH, because PS_{5000}-SH has a larger fraction of S–H groups. The measured dielectric loss of the PS-SH layers was at 1 % for the most part of the measured frequency range, as it was also reported for dielectric layers of pure polystyrene in the literature [202].

"Figure 5.11 shows the dielectric constants and loss tangents of the hybrid films in the frequency range 1 Hz to 1×10^6 Hz (a,b) and a direct comparison of the change of dielectric constant with increasing metal fraction (c). The largest dielectric constant of 50 was observed for $Au_{0.21}^{disordered}$@PS at 1 Hz. The dielectric constants for films with low Au volume fractions below 10 vol% increased almost linearly with Au content, especially at high frequencies. The relationship became clearly non-linear at higher Au volume fractions in a way that would be hard to explain with the classical mixing rules used for

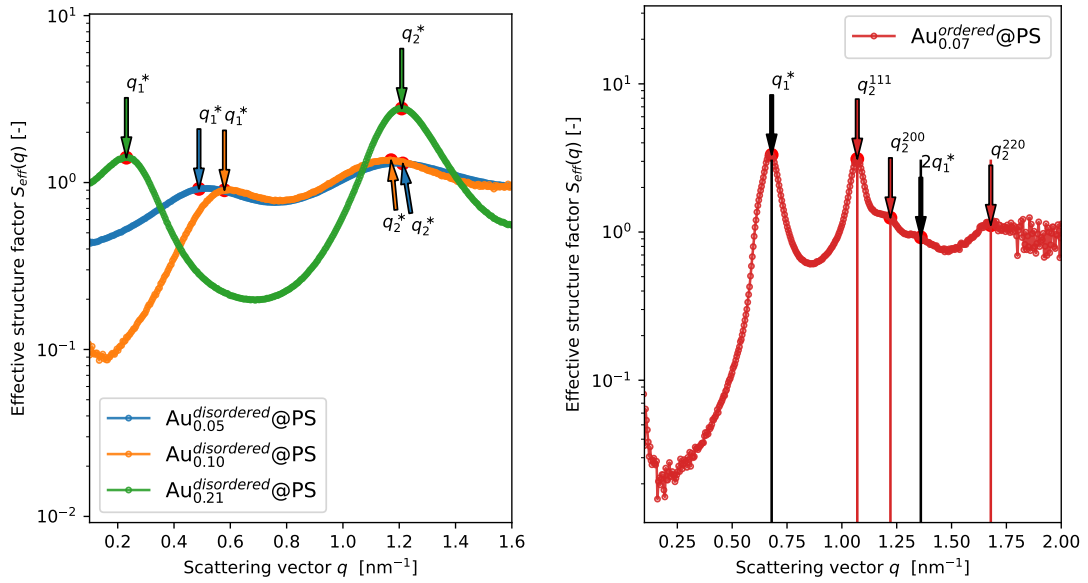

(A) (B)

FIGURE 5.7: Effective structure factors derived from SAXS measurements of drop casted samples on Kapton foil. a) Random packed structures are found for Au$^{\text{disordered}}_{0.xx}$@PS, while b) both fcc and random packing is found for Au$^{\text{ordered}}_{0.07}$@PS. Reprinted with permission of Wiley-VCH GmbH from the Supporting Information of [1].

Type I composites. In the following, we use a random resistor-capacitor network model in order to analyze the dielectric properties of our composites."[1]

The relative dielectric constants ε_r of Type II composites with different filling ratios f_v are often described by a power law resulting from percolation theory as shown in Equation (2.16) with a percolation threshold f_c, the percolation exponent q, and a pre-factor $\varepsilon_{r,0}$. "The underlying model by Efros and Shklovskii assumes a random distribution of homogeneous particles in a neutral, insulating matrix [38]. The particles in our Type III hybrids carry covalently attached shells that coalesce and form a 'matrix', which introduces a level of order that was not foreseen by Efros and Shklovskii, but does not invalidate the model. Figure 5.11c shows a fit of the dielectric constants of our films to Equation (2.16) at 10 kHz, where the dielectric losses were minimal."[1] For the fit, the data of Au@PS layers with three different Au volume fractions and of the PS_{11000}-SH reference sample without gold was used. This fit using the data of the Au@PS samples with PS_{11000} ligand and three different crafting densities and the data of the reference sample with PS_{11000}-SH layer returned a percolation threshold of $f_c = 0.24$ and a percolation exponent of $q = 1.3$. "This threshold is considerably above the value of $f_c = 0.14$ reported by Gaiser *et al.* for AgNPs in PDMS [203] and the threshold of $f_c = 0.16$ predicted for perfect spheres [29] and measured by Fredin *et al.* for AlNPs in polypropylene [41]. The values that we find are consistent with the existence of permanently

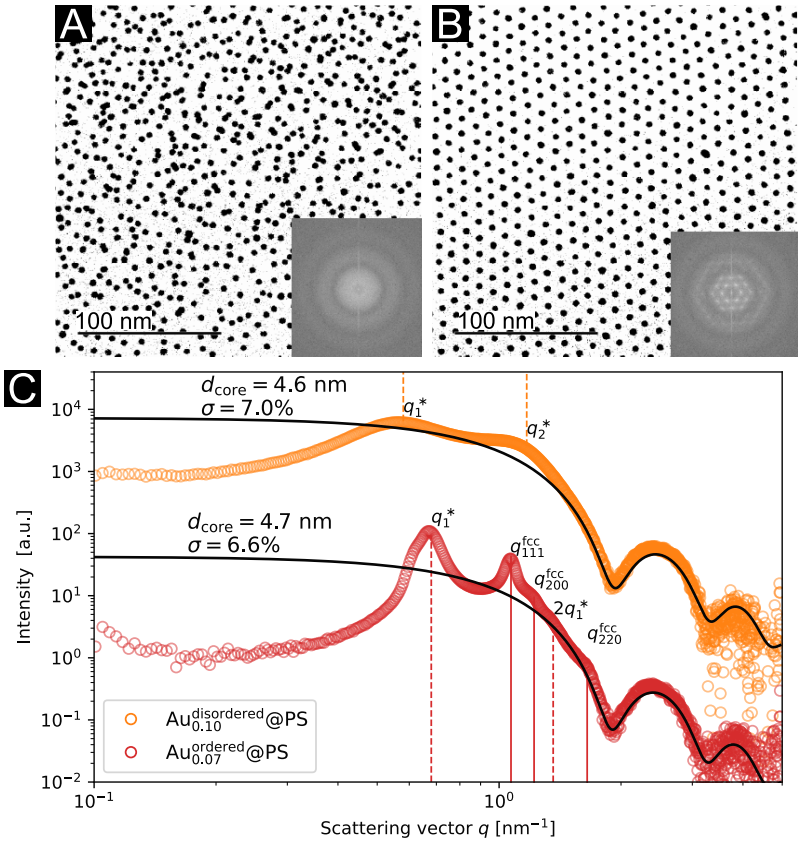

FIGURE 5.8: Particle packings in films of hybrid particles with different shells. a) Transmission electron micrographs of Au@PS_{11000} (medium ligand density) and b) Au@PS_{5000} from drop casting. The crystalline superlattice of particles with thinner shells is apparent visually and in the Fourier transform (insets). c) Transmission SAXS of dielectric films (data for $Au_{0.10}^{disordered}$@PS multiplied by 100) indicates that the form factor of the spherical gold cores (black lines) is superimposed by structure factor peaks. The broad peaks that occurred for particles with PS_{11000} shells (medium ligand density) are consistent with random packing, whereas some of the sharp peaks for PS_{5000} shells can be indexed with fcc packing reflexes (solid vertical lines). Reprinted (adapted) with permission of Wiley-VCH GmbH from [1].

attached shells: random percolation in Type III hybrids is prevented by the individual insulation and the filling ratio of the conductive component can surpass the value that would usually lead to DC conductivity (i.e. a short circuit). The exponent q only depends on the lattice type, not the particle shape; the value of $q = 1.3$ that we found here is slightly above the value of $q = 1$ expected for a 3D lattice [38, 117] and consistent with a certain degree of order due to the permanently attached shell that fixes the particle spacing in a narrow range.

Fits at low frequencies (e.g. 1 Hz) yielded physically unreasonable results with very high percolation thresholds and percolation exponents, indicating a failure of the model (see Table 5.6). The Efros-Shklovskii percolation model does not consider frequency-dependent polarization or relaxation processes and the strongly deviating dielectric constant and loss that we found below 1 kHz are consistent with the types of ionic and

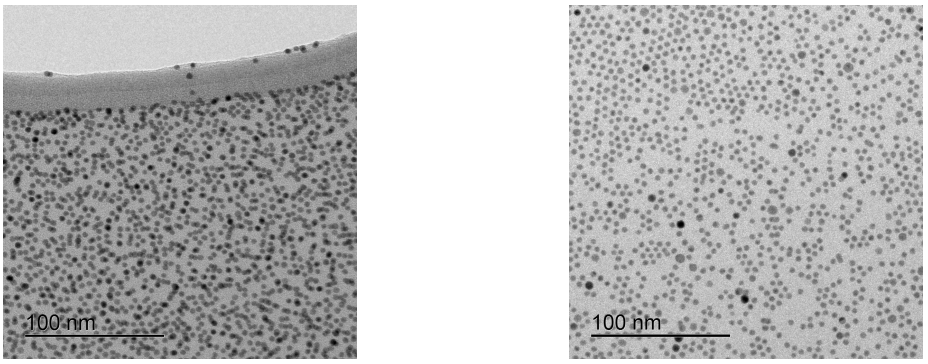

(A) $Au_{0.05}^{disordered}$@PS (B) $Au_{0.21}^{disordered}$@PS

FIGURE 5.9: Transmission electron micrographs of particles dropped on a transmission electron microscopy grid. a) $Au_{0.05}^{disordered}$@PS particles obtained after ligand exchange for 1 week at 20 °C and b) $Au_{0.21}^{disordered}$@PS particles obtained after ligand exchange for 4 weeks at 60 °C). Reprinted with permission of Wiley-VCH GmbH from the Supporting Information of [1].

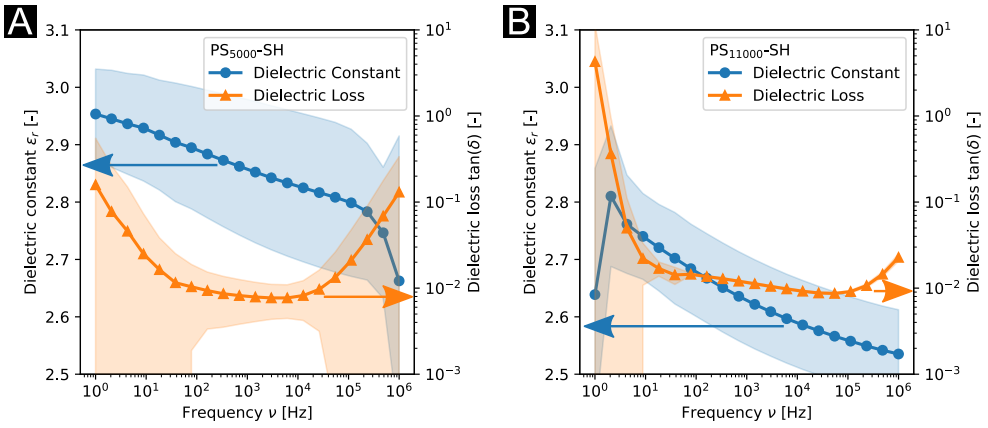

FIGURE 5.10: Dielectric properties of (a) PS_{5000}-SH and (b) PS_{11000}-SH reference capacitors with pure thiol-functionalized PS and without gold. The real part of the relative permittivity ε_r is plotted on the left axis (blue circles), the loss tangent $\tan\delta$ is plotted on the right axis (orange triangles). The lines are meant to guide the eye. Reprinted with permission of Wiley-VCH GmbH from the Supporting Information of [1].

orientational polarization previously reported for polymers by Zhu [204]. The dielectric constants close to 1 MHz decreased for the largest Au volume fraction; the dielectric losses at high frequencies increased for all samples. Matavž *et al.* suggested that a decrease of the dielectric constant connected with an increase of the dielectric loss at high frequencies can occur due to the resistivity of the electrodes [6]. Such resistivity may originate from oxidation of the sputtered aluminium electrode that we used, for example.

Above results indicate that the permittivity of our Type III hybrids at frequencies around 10 kHz can be explained by a network of RC elements [37], where the capacitors are created by neighbouring Au cores and the PS shells act as the dielectric. Resistors represent

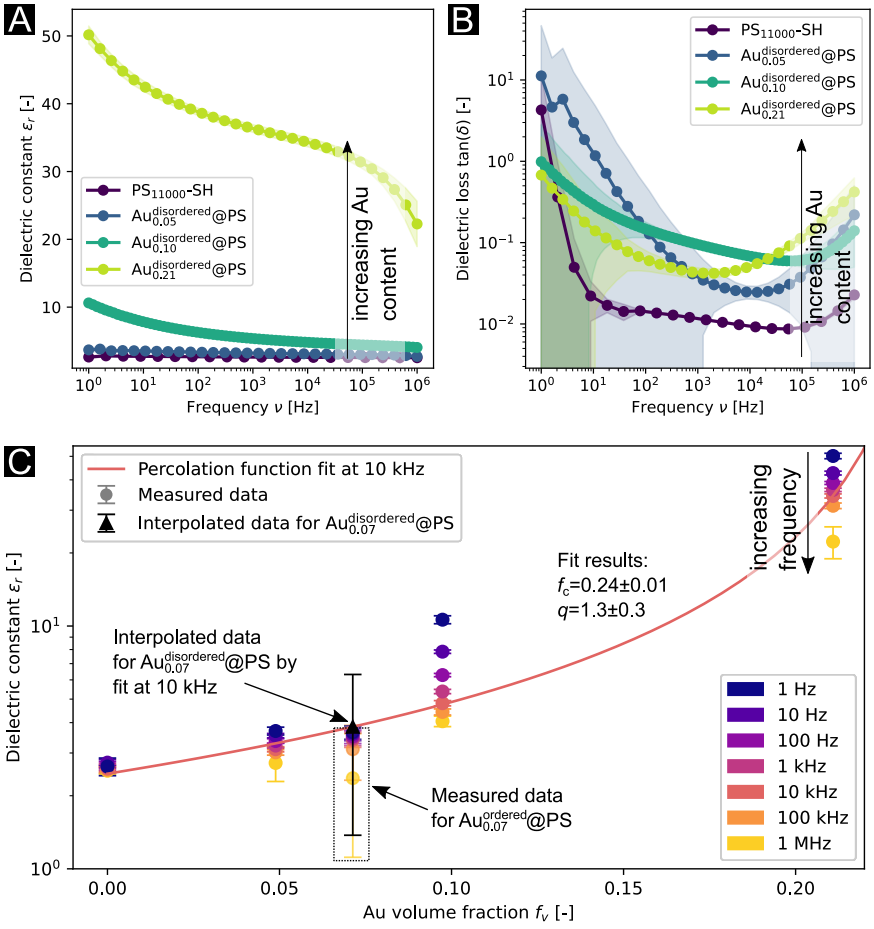

FIGURE 5.11: a) Frequency-dependent dielectric constants and b) loss tangents of $Au^{disordered}_{0.xx}$@PS films with with different ligand densities and of a polymer reference sample PS_{11000}-SH. c) Dielectric constants at selected frequencies as a function of gold volume fraction from TGA. Reference data for $f_{v,Au} = 0$ was measured on pure PS_{11000}-SH. The lines are fits with the power law from percolation theory in Equation (2.16). Reprinted (adapted) with permission of Wiley-VCH GmbH from [1].

the finite tunnel barriers formed by the nanoscale polymer shells. This interpretation is consistent with the dielectric losses shown in Figure 5.11b, where the minimum of the loss tangent increases for larger Au volume fractions. The losses are probably caused by the polarization of the gold-PS interfaces that are larger at higher Au volume fractions. The resulting trade-off between a high dielectric constant and a low dielectric loss has been reported for many Type II dielectric films [39, 40, 84, 202, 205–207].

The Efros-Shklovskii model above assumes a network of uniform capacitors and resistors. Network connectivity increases in a random fashion (that depends on the chosen lattice) when increasing the filling ratio. In reality, Type II composites are characterized by wide distributions of both capacitors and resistors and fractal network structures, because the spacing between particles varies strongly. The spacing of particles in Type III hybrids is characterized by the length scales discussed above, which narrows the width of the

TABLE 5.6: Fit parameters $\varepsilon_{r,0}$, f_c, and q for the experimental dielectric data of the PS_{11000}-SH reference and $Au_{0.xx}^{disordered}$@PS at different frequencies. The value of ε_r for $Au_{0.07}^{disordered}$@PS was interpolated using these parameters. Reprinted with permission of Wiley-VCH GmbH from the Supporting Information of [1].

Frequency [Hz]	$\varepsilon_{r,0}$	f_c	q	ε_r ($Au_{0.07}^{disordered}$@PS)
	fitting parameters			
1.0	$1.0 \times 10^{158} \pm \infty$	10.8 ± 284.3	$1.5 \times 10^2 \pm 4.1 \times 10^3$	$6.8 \pm \infty$
1.0×10^1	0.1 ± 0.2	0.62 ± 0.67	7.0 ± 9.9	5.4 ± 58.4
1.0×10^2	0.1 ± 0.1	0.32 ± 0.08	2.6 ± 1.2	4.6 ± 9.8
1.0×10^3	0.3 ± 0.2	0.26 ± 0.03	1.7 ± 0.5	4.2 ± 4.2
1.0×10^4	0.4 ± 0.2	0.24 ± 0.01	1.3 ± 0.3	3.8 ± 2.5
1.0×10^5	0.5 ± 0.2	0.23 ± 0.01	1.1 ± 0.2	3.6 ± 1.8
1.0×10^6	0.6 ± 0.3	0.23 ± 0.02	1.0 ± 0.4	3.4 ± 2.9

distributions of R and C."[1]

5.3 Dielectric Au@PS layers with ordered particle packing

"The connectivity of the RC network in the composites studied so far was dominated by random packing and the formation of linear particle chains. It is difficult to model the effect of such chains. In the following, we study the properties of Type III hybrids with regular particle packing in order to better distinguish the effects of R/C distributions and network structure."[1]

We prepared hybrid dielectric films with regular "superlattice" particle packings using the same gold cores as above with shells of PS_{5000} formed by stirring at 60 °C for 1 week. "The thinner shells provided a balance of mobility and attractive potential that enabled self-assembly. We thus obtained ordered films with a Au volume fraction of 7 vol% and fabricated capacitors with them."[1] TEM cross sections showed ordered particle packing in the dielectric layer in Figure 5.6 on the right. Table 5.7 shows the results of the TGA and SAXS measurements of $Au_{0.07}^{ordered}$@PS drop casted samples.

TABLE 5.7: Experimental results from TGA and SAXS for Au content and surface-to-surface distance between Au cores for $Au_{0.07}^{ordered}$@PS. Reprinted with permission of Wiley-VCH GmbH from the Supporting Information of [1].

Sample name	$x_{w,Au}$ [wt%]	$f_{v,Au}$ [vol%]	q_1^* [nm^{-1}]	q_2^{111} [nm^{-1}]	a^{fcc} [nm]	d_{ss}^1 [nm]	d_{ss}^2 [nm]
$Au_{0.07}^{ordered}$@PS	58.6	7.1	0.68	1.07	10.2	4.5	2.5

The degree of order in the $Au@PS_{5000}$ layers was analyzed using SAXS and TEM on drop casted samples. "Figure 5.8 shows the difference between the irregular particle

packings and the superlattices in SAXS (Figure 5.8c) and TEM (Figure 5.8b)."[1] The Fourier transform of Au@PS_{11000} NPs with medium ligand density dropped on a TEM grid (inset Figure 5.8a) only shows radial features caused by random packing, while that of Au@PS_{5000} NPs (inset Figure 5.8b) shows clear features of an ordered pattern.

The ordered packing was analyzed with SAXS of drop casted films on Kapton foil. Its SAXS scattering is shown in Figure 5.8c, the effective structure factor derived from these SAXS data in Figure 5.7b. "SAXS indicated that the regular films contained disordered regions: the first peak at q_1^* indicates a nearest neighbour distance of $d_{\mathrm{ss}}^1 = 4.5\,\mathrm{nm}$ that does not fit into the reflexes caused by the face-centred cubic (fcc) superlattice with the expected position ratio of $\sqrt{3} : \sqrt{4} : \sqrt{8}$."[1] The ordered and disordered regions cause different maxima in Figure 5.7b. The areas with random packing cause the maxima marked with black arrows. The first order scattering on the random packed particles results in the peak found at q_1^*, the second order scattering results in the peak found at $2q_1^*$. The mean corresponding surface-to-surface spacing d_{ss}^1 was calculated with Equation (3.10) and Equation (3.14).

The regions with a fcc superlattice cause the three maxima marked with red arrows in Figure 5.7b. The first peak was indexed as (111) and used to calculate the lattice constant a^{fcc} using Equation (3.11) with the miller indexes $h = k = l = 1$. The surface-to-surface distance d_{ss}^2 between the particles in ordered packing was calculated using Equation (3.13) and Equation (3.14). Table 5.7 lists all corresponding values derived from SAXS.

"The difference in particle packing may be connected to the polymer chain conformation on the particle surfaces. We analyzed the ligand polymer conformation using the method of Rahme *et al.* and compared the polymers' Flory radii F to the average distances between anchoring points $\langle D \rangle$ [153]."[1] It is

$$F = \alpha n_{\mathrm{mono}}^{\frac{3}{5}} \tag{5.1}$$

for a polymer in a good solvent with the length of a monomer α ($\alpha_{\mathrm{PS}} = 0.25\,\mathrm{nm}$) and the number of monomers n_{mono} per molecule [153]. We derived the number of monomers $n_{\mathrm{mono}} = 48$ for PS_{5000} and $n_{\mathrm{mono}} = 106$ for PS_{11000} from the atomic weight of a single repeat unit in a PS molecule (molecular formula C_8H_8, molecular mass 104 Da), resulting in the Flory radii $F = 2.55\,\mathrm{nm}$ for PS_{5000} and $F = 4.10\,\mathrm{nm}$ for PS_{11000}. These values were then compared to the theoretical distance of anchor points $\langle D \rangle$, for which we assumed a homogeneous distribution:

$$\langle D \rangle = \sqrt{\frac{A_{\mathrm{sphere,AuNP}}}{N_{\mathrm{Ligands}}}} = \sqrt{\frac{1}{\rho_{\mathrm{A,ligand}}}} \tag{5.2}$$

where $A_{\text{sphere,AuNP}}$ is the surface area of the AuNP, N_{Ligands} is the number of ligands on a single AuNP, and $\rho_{\text{A,ligand}}$ is the ligand density; the results are listed in Table 5.8.

TABLE 5.8: Estimated Flory radii F and average ligand anchor point distances $\langle D \rangle$ for the different inks. Reprinted with permission of Wiley-VCH GmbH from the Supporting Information of [1].

Ink label	Ligand	n_{mono} [−]	F [nm]	$\langle D \rangle$ [nm]
$Au_{0.05}^{\text{disordered}}$@PS	PS_{11000}	107	4.1	1.2
$Au_{0.10}^{\text{disordered}}$@PS	PS_{11000}	107	4.1	1.6
$Au_{0.21}^{\text{disordered}}$@PS	PS_{11000}	107	4.1	2.2
$Au_{0.07}^{\text{ordered}}$@PS	PS_{5000}	49	2.6	0.9

The average ligand anchor point distances were always smaller than the corresponding Flory radii, "indicating brush conformations of the polystyrene ligands on all hybrid particles used here. Dukes *et al.* proposed that polymer brushes form for short polymer ligands at high grafting densities, with a transition to semidiluted polymer brushes when the chains are long enough [157]. We conclude that all PS chains used here were short enough to form brushes, and that the transition from irregular to regular particle packing is mainly due to the change of interaction and shell mobility that depended on ligand shell thickness.

The polystyrene ligands efficiently prevented the agglomeration of the dispersed hybrid particles. SAXS in dispersion did only show little interaction of the hybrid particles"[1] (Figure 5.12). Some interaction of the dispersed particles caused a slight increase in intensity in the q-range around $0.25\,\text{nm}^{-1}$. All measurements reached a Guinier plateau at low q values, implying the absence of large agglomerates; strong agglomeration would cause a considerable increase in intensity at low q values as it was observed by Sindram *et al.* for aggregated Au@PS particles [155]. Dynamic light scattering (DLS) measurements of the diluted inks (see Chapter 3 for measurement parameters) indicated hydrodynamic diameters of 5.7 nm for $Au_{0.05}^{\text{disordered}}$@PS, 10.6 nm for $Au_{0.10}^{\text{disordered}}$@PS, 9.5 nm for $Au_{0.21}^{\text{disordered}}$@PS, and 16.3 nm for $Au_{0.07}^{\text{ordered}}$@PS. The DLS measurements did not indicate substantial agglomerates.

"The particles agglomerated during the drying of the liquid ink on the substrate. Studies on the agglomeration of similar gold cores with shorter alkanethiol ligands indicated that the onset concentration of agglomeration depends on the ligand length [12] and the solvent [142]. It is probably possible to further tune the dielectric layer structure through the variation of ligand shell thickness and solvent.

Figure 5.13a compares the dielectric constants of a partially ordered hybrid particle layer $Au_{0.07}^{\text{ordered}}$@PS with the interpolated constant of a disordered layer with the same

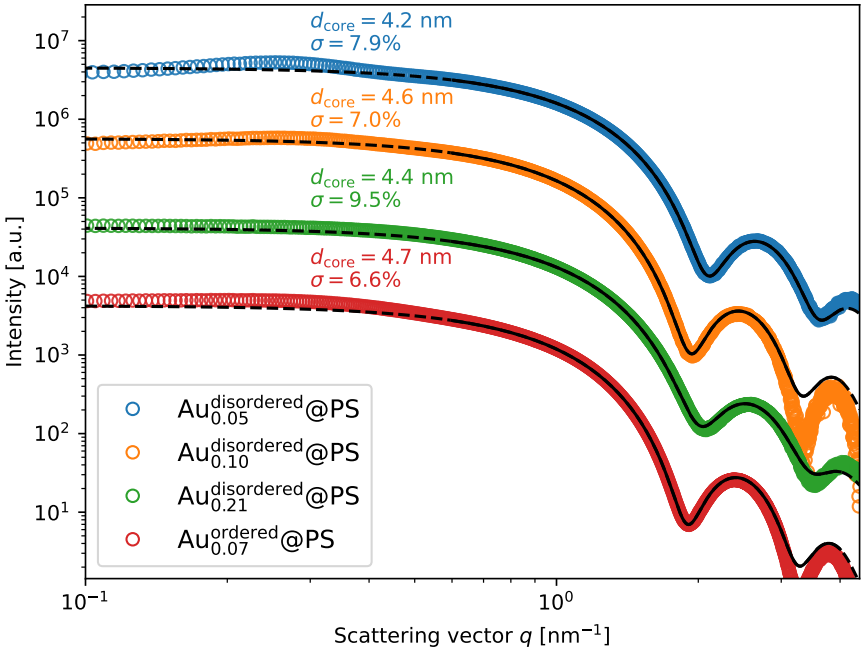

FIGURE 5.12: SAXS from dispersions of PS-coated gold cores dispersed in toluene. The measurements were shifted in y-direction. The form factor scattering did not change after the ligand exchange, indicating that the ligand exchange did not affect the particle size and shape. The black lines indicate the form factor fit used to quantify the core diameters d_{core} and the widths of the core size distributions σ. Reprinted (adapted) with permission of Wiley-VCH GmbH from the Supporting Information of [1].

volumetric gold content that was calculated using Equation (2.16) and the fit in Figure 5.11c."[1] The power law from percolation theory in Equation (2.16) was used for the interpolation, which allowed the comparison of Au@PS layers with ordered and disordered particles at the same Au volume fraction to check the influence of the particle packing on the dielectric properties. Percolation theory does not consider polarization or relaxation phenomena. Therefore, we limited the interpolation to the frequency of 10 kHz. At this frequency, the losses were minimal and the dielectric constants showed little frequency dependence (see discussion below).

The uncertainties in the interpolated value of a hypothetical sample $Au_{0.07}^{ordered}$@PS was estimated using standard error propagation with the uncertainty of the fit parameters and the corresponding partial derivatives:

$$\Delta\varepsilon_r = \sqrt{\left(\frac{\partial\varepsilon_r}{\partial\varepsilon_{r,0}}\right)^2 \Delta\varepsilon_{r,0}^2 + \left(\frac{\partial\varepsilon_r}{\partial f_c}\right)^2 \Delta f_c^2 + \left(\frac{\partial\varepsilon_r}{\partial q}\right)^2 \Delta q^2} \tag{5.3}$$

Finally, the interpolated value for a hypothetical sample $Au_{0.07}^{disordered}$@PS using Equation (2.16) and its uncertainty using Equation (5.3) are listed in Table 5.6 in the last column.

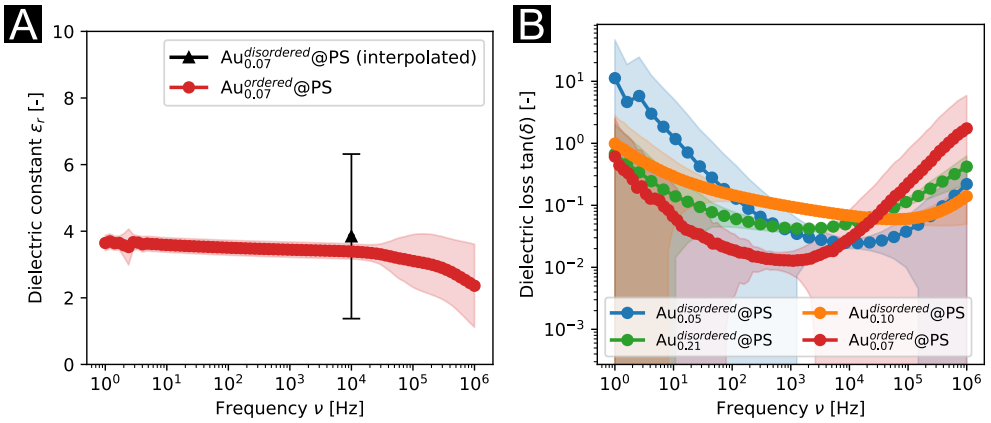

FIGURE 5.13: a) Dielectric constants of ordered superlattice films $Au_{0.07}^{ordered}$@PS and interpolated value for a disordered film of the same Au volume fraction. Interpolation was done using a fit to Equation (2.16) from percolation theory. The error bar shows the uncertainty of this interpolation. b) Loss tangents of the ordered film $Au_{0.07}^{ordered}$@PS and all disordered films. Reprinted with permission of Wiley-VCH GmbH from [1].

"The relative permittivities that we measured for the ordered films are in the same range as the one interpolated from the disordered films. The loss tangent (Figure 5.13b) of the ordered sample had a minimum at ≈800 Hz, while all disordered samples had minima in the range of ≈80 kHz.

We conclude from the similar dielectric constants of ordered and disordered films that the increased number of neighbours (12 in the fcc lattice) and thus, network density in the ordered films affected the permittivity less than the increased gold volume fraction. This suggests that a denser RC network does not increase the overall permittivity of the layer if the individual capacitances remain unchanged, which is consistent with the picture of Efros and Shklovskii. The change in dielectric loss is unexpected, however, and not explained by current models.

The distances between the AuNPs in an ordered packing are more homogeneous, which may prevent losses related to very densely spaced particles. Very densely spaced particles, as they were observed for the disordered samples with the chain-like particle arrangement, have overlapping electron wave function that can lead to collective excitation and dissipation. Moreover, it is conceivable that Coulomb blockades that depend on connectivity affect electron hopping and thus, loss currents [119, 120].

The dielectric breakdown of the hybrid dielectric layers was analyzed by steadily increasing the bias on the thin film capacitors."[1] We performed two measurements per sample type. Figure 5.14 shows the resulting data. The values of the breakdown strength E_{bd} were calculated using Equation (3.26) from the breakdown voltage V_{bd} that was found in the measurements and the corresponding layer thicknesses t in Table 5.1. "The breakdown strengths consistently were in the range of 39 MV m^{-1} to 154 MV m^{-1}. We found

no indications of reduced breakdown strengths at higher Au volume fraction. Detailed breakdown studies will require an analysis of the mechanism, for example, by imaging the defects through electron microscopy.

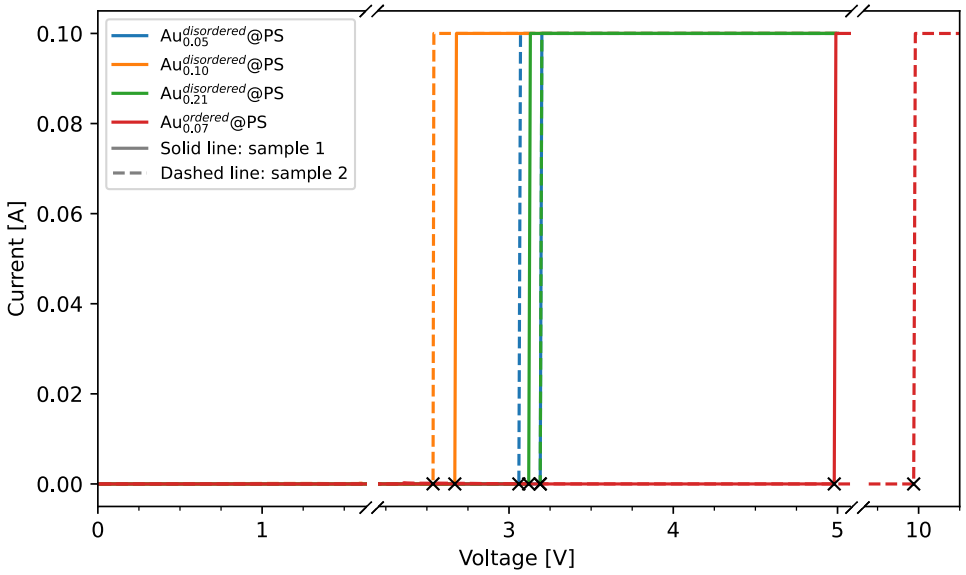

FIGURE 5.14: Breakdown characteristics of two representative capacitors of each sample type. The breakdown voltage V_{bd} is marked with an "X". Reprinted with permission of Wiley-VCH GmbH from the Supporting Information of [1].

TABLE 5.9: Estimated breakdown strengths E_{bd} of the dielectric films. The mean value of two measurements is reported. Reprinted with permission of Wiley-VCH GmbH from the Supporting Information of [1].

Name of sample	E_{bd} [MV m^{-1}]
$Au_{0.05}^{disordered}$@PS	39.1
$Au_{0.10}^{disordered}$@PS	59.9
$Au_{0.21}^{disordered}$@PS	115.3
$Au_{0.07}^{ordered}$@PS	154.3

The analysis of dielectric breakdown indicated reliably insulating properties of the hybrid dielectric layers below the breakdown voltage. The dielectric losses observed at low frequencies close to 1 Hz in Figure 5.13b are therefore unlikely to stem from leakage currents. We observed a similar increase of the dielectric loss with decreasing frequency in thin film capacitors with purely polymer-based dielectric layers (see Figure 5.10). It appears likely that the interfaces between metal electrodes and the dielectric layer cause losses that may be reduced by suitable passivation."[1]

5.4 Inkjet printed dielectric layers on rigid silicon substrates

"Type III hybrids are particularly promising for inkjet printing. The polymer shell on each individual nanoparticle increases the colloidal stability, thus preventing agglomeration and ensuring printability from small nozzles. We printed dielectric layers onto an aluminium-coated silicon wafer using the $Au_{0.10}^{disordered}$@PS ink. Gold top contacts with diameters of 1 mm were evaporated in order to form capacitors. Figure 5.15 illustrates the good printability of the ink that yielded a uniform printed layer (Figure 5.16a) after drying at room temperature. The surface profile of the inkjet printed sample (Figure 5.2c) shows that overlapping inkjet droplets formed a continuous, insulating dielectric layer.

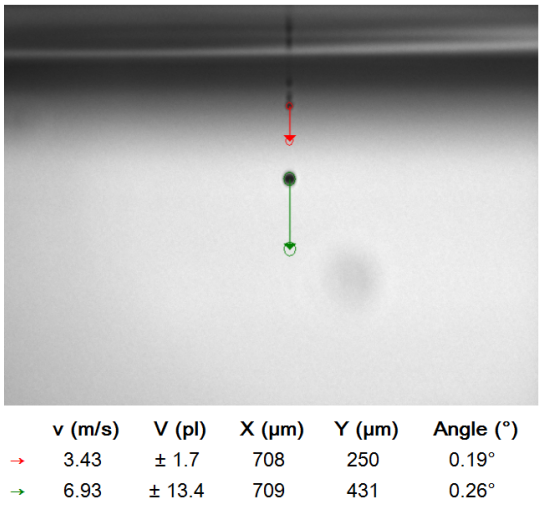

FIGURE 5.15: Drop formation of ink $Au_{0.10}^{disordered}$@PS. Reprinted with permission of Wiley-VCH GmbH from the Supporting Information of [1].

The capacitance of the inkjet printed devices was (2.2 ± 0.1) nF with a dielectric loss of (17.1 ± 6.8) % at 1 kHz. Both capacitance and dielectric loss increased at lower frequencies just as in the spin coated samples (cf. Figure 5.11).

The dielectric permittivity of the inkjet printed film was calculated based on a thickness of (16.7 ± 9.8) nm estimated from the TEM cross sections in Figure 5.16b and in Figure 5.17 using Equation (3.22). The uncertainty of the value is due to the variation in film thickness from the inkjet printing process. The surface roughness of $R_a = 19.58$ nm (see Table 5.2) exceeds the layer thickness, and we considered the thickness variation as uncertainty when calculating the dielectric constant (see Equation (3.23)). The uncertainty of the calculated dielectric constant was estimated with standard error propagation using Equation (3.23).

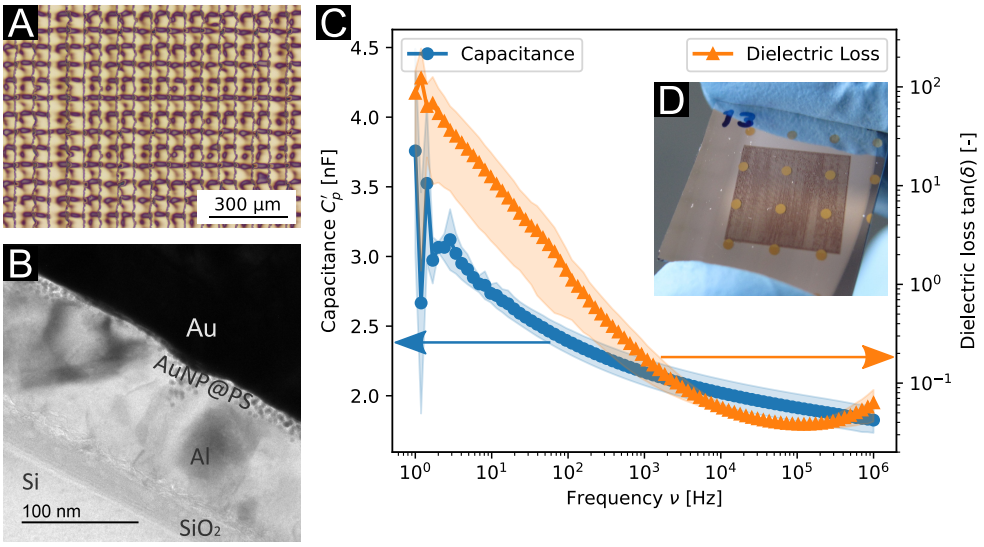

FIGURE 5.16: Inkjet printed capacitor with hybrid dielectric film $Au_{0.10}^{disordered}$@PS. (a) Optical micrograph of the film microstructure that was formed by two passes of inkjet printing. (b) Transmission electron micrograph of a cross-section with the 17 nm thick dielectric hybrid film. (c) Dielectric properties of the capacitor. (d) The inset shows a photograph of an inkjet printed thin film capacitor device. Reprinted with permission of Wiley-VCH GmbH from [1].

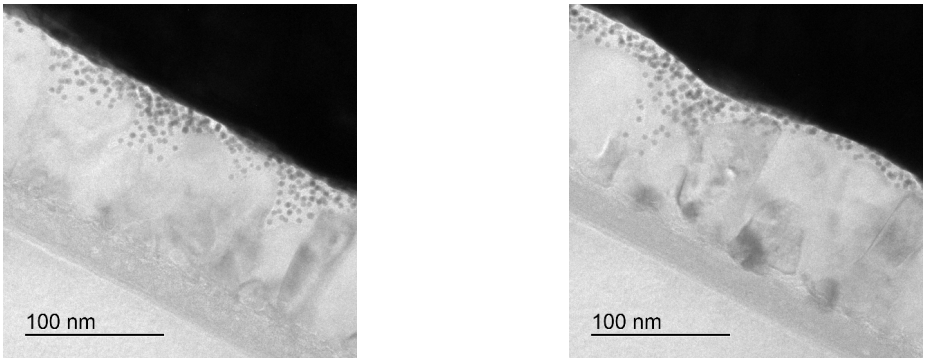

(A) (B)

FIGURE 5.17: Transmission electron micrographs of focused ion beam cross-sections of the inkjet printed dielectric hybrid film. Reprinted with permission of Wiley-VCH GmbH from the Supporting Information of [1].

The good film formation properties of our hybrid ink with the covalently attached polystyrene ligands allows the preparation of very thin inkjet printed dielectric layers."[1]

5.5 Conclusions

"We prepared capacitors with hybrid dielectric layers of gold-polystyrene core-shell particles. The dielectrics were deposited from liquid dispersions using spin coating and inkjet printing. Very thin layers down to 17 nm with good dielectric properties were obtained.

The covalently attached polymer aided the formation of homogeneous layers with embedded gold cores. We analyzed this novel type of dielectric nanocomposite by varying the polymer grafting densities on the AuNPs, thus changing the Au volume fractions between 5 vol% to 21 vol%. A non-linear dependence of the dielectric constant on metal content was explained using random resistor-capacitor network models previously applied for percolating systems. The strongly attached polymer shells prevented percolation, giving access to high metal filling ratios without the risk of short circuits due to percolation.

The effect of network structure was analyzed by comparing disordered particle films with self-assembled superlattices. Order did not change the permittivity much, but shifted the minimum of the loss tangent to much lower frequencies. The resistor-capacitor network models currently used for the analysis of dielectric composites with metal particles do not consider frequency-dependent polarization and relaxation effects. Improved models that combine nanoscale electron dynamics with electrical network theory are desirable in order to better connect the molecular structure of the composites with its dielectric properties. The composites introduced here provide considerable freedom in the chemical design of the composite; for example, diblock copolymer shells with defined structures could be covalently attached in order to tune structure and polarizability. Such tuned structures of AuNPs have been reported recently by the usage of PS block and random copolymers [208].

Inkjet printed thin film capacitors with a ≈ 17 nm thick dielectric layer and a capacitance of (2.2 ± 0.1) nF@1 kHz over 0.79 mm^2 were prepared in air at room temperature without any post-treatment of the dielectric. The polymer shells of the particles were sufficiently mobile to reliably form insulating layers.

Inkjet printable dielectrics of the type introduced here should find applications in flexible and printed electronics. We expect that hybrid dielectric films can be inkjet printed on thin polymer foils in order to form inherently deformable capacitors."[1]

Chapter 6

Core Diameter Variation and Printing on Flexible Substrates

This chapter reports on dielectric layers of hybrid Au@PS particles with varying core sizes and ligand lengths. Additionally to the effect of the Au volume fraction, which was discussed in the previous chapter, changes in the dielectric constant with the core sizes are expected and are discussed in the following. Thiol-functionalized PS_{5000} and PS_{11000} were grafted onto gold cores of small, medium, and large core sizes (d_{core} = 2.9 nm, 4.7 nm, and 8.2 nm). The resulting layers are denoted $Au_{0.xx}^{size}@PS_{x000}$, where *size* refers to the Au core, $0.xx$ represents the volume fraction of gold and $x000$ represents the molecular weight of the ligand. The results for the medium-sized particles with core diameter 4.7 nm are the same as from Chapter 5: $Au_{0.07}^{ordered}@PS$, now called $Au_{0.07}^{medium}@PS_{5000}$, and $Au_{0.10}^{disordered}@PS$, now called $Au_{0.10}^{medium}@PS_{11000}$. Figure 6.1 shows six different types of thin film capacitors with interference colours due to varying layer thickness and different plasmon resonances of the Au nanoparticle cores.

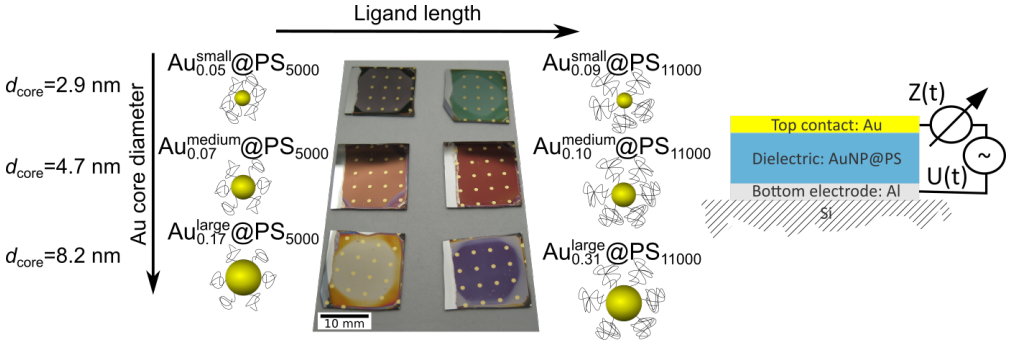

Figure 6.1: Thin film capacitors based on dielectric layers of Au@PS nanoparticles with three different core sizes and two different ligand lengths. The metal fraction of the films varied with the core size and the ligand length. The photograph shows the spin coated dielectric layers on aluminium/silicon substrates with evaporated gold contacts.

The thin film capacitors were fabricated by spin coating the Au@PS particles on rigid aluminium coated silicon substrates or on flexible aluminium coated PET foil substrates. An overview of the measured properties of thin film capacitors is given in Table 6.1.

TABLE 6.1: Dielectric properties of thin film capacitors with hybrid dielectric films of thickness t at 10 kHz with varying core sizes and polystyrene ligand lengths. C_p is the real part of the capacitance in parallel. Dielectric constants ε_r and losses $\tan\delta$ were obtained by dielectric spectroscopy on at least 11 measured thin film capacitors for the spin coated hybrid dielectric samples and 12 measured capacitors for the inkjet printed hybrid dielectric sample.

Sample label	preparation method	t [nm]	C_p [pF]	ε_r [−]	$\tan\delta$ [−]
$Au_{0.05}^{small}@PS_{5000}$	spin coated	135.4 ± 7.1	165 ± 3	3.2 ± 0.2	0.010 ± 0.003
$Au_{0.09}^{small}@PS_{11000}$	spin coated	68.2 ± 2.3	688 ± 29	6.7 ± 0.4	0.307 ± 0.013
$Au_{0.07}^{medium}@PS_{5000}$	spin coated	48.1 ± 3.0	490 ± 33	3.4 ± 0.2	0.029 ± 0.055
$Au_{0.10}^{medium}@PS_{11000}$	spin coated	51.1 ± 1.4	654 ± 16	4.8 ± 0.1	0.068 ± 0.004
$Au_{0.17}^{large}@PS_{5000}$	spin coated	30.6 ± 0.9	1107 ± 55	4.9 ± 0.3	0.023 ± 0.003
$Au_{0.31}^{large}@PS_{11000}$	spin coated	15.7 ± 1.0	6039 ± 677	13.6 ± 1.6	0.093 ± 0.033
$Au_{0.10}^{medium}@PS_{11000}$	inkjet printed	≈ 25	1316 ± 55	n.a.	0.071 ± 0.006

The dielectric constants of hybrid layers were calculated using Equation (3.22) that assumes a parallel plate capacitor. To check the validity of this model, the roughnesses of the substrates and the layers are compared. The spin coated samples had smooth surfaces with R_a values in the range of 0.8 nm to 1.0 nm as measured over a surface area of 700 µm x 530 µm. The surface profiles were numerically analyzed using the MetroPro software after subtraction of a plane (for the rigid spin coated samples) or a cylinder (for the flexible inkjet printed sample) to obtain the roughness values listed in Table 6.2. Figure 6.2a and Figure 6.2b show representative surface profiles of the dielectric spin coated samples. The surface roughness of the aluminium/silicon substrate ($R_a = 3.0$ nm, see Table 4.1 in Chapter 4) and of the aluminium/PET substrate ($R_a = 4.0$ nm, shown in Figure 6.2c) were both measured over an area of 100 µm x 100 µm with AFM.

The layer thickness of the spin coated samples exceeded the roughness of the substrates and of the dielectric layers by one order of magnitude, clearly fulfilling the parallel plate capacitor assumption and were used to determine the dielectric constants. The surface roughness of the inkjet printed sample was much larger; its effective thickness could only be estimated by the measured capacitance.

The chapter is structured as follows: First, the synthesis of the different inks and their stability depending on the core size and the ligand type are investigated and discussed in Section 6.1. Second, the structures of dried layers containing small and large particles are investigated by SAXS and TEM in Section 6.2. Third, the dielectric properties of the different layers with varying core size are presented in Section 6.3. These properties

TABLE 6.2: Average surface roughness R_a of the hybrid dielectric layers (from WLI) and of the aluminium electrode (from AFM).

Sample label	coating method	R_a [nm]
$Au^{small}_{0.05}$@PS_{5000}	spin coated	0.8
$Au^{small}_{0.09}$@PS_{11000}	spin coated	0.8
$Au^{medium}_{0.07}$@PS_{5000}	spin coated	1.0
$Au^{medium}_{0.10}$@PS_{11000}	spin coated	1.0
$Au^{large}_{0.17}$@PS_{5000}	spin coated	1.1
$Au^{large}_{0.31}$@PS_{11000}	spin coated	1.0
$Au^{medium}_{0.10}$@PS_{11000}	inkjet printed	110.9
Al coated PET foil	sputtered	4.0

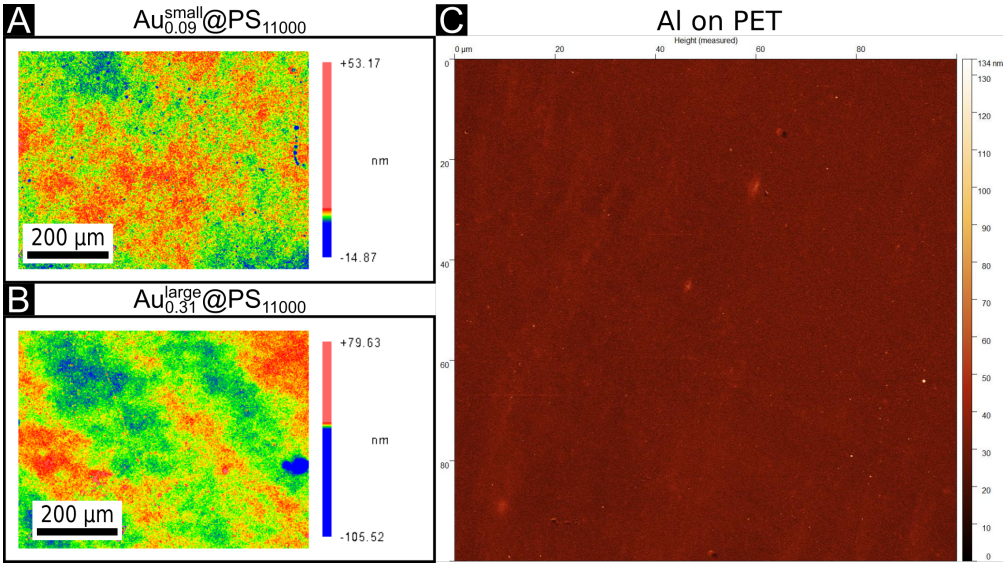

FIGURE 6.2: Surface profile measurements. Surface profiles measured with WLI of a) $Au^{small}_{0.09}$@PS_{11000} and b) $Au^{large}_{0.31}$@PS_{11000}. c) Surface profile measured with AFM of Al coated PET foil.

were investigated on rigid samples with spin-coated films on Al-coated silicon. Finally, the successful preparation of flexible thin film capacitors on an aluminium coated PET substrate with the hybrid dielectric ink of medium-sized particles is shown in Section 6.4.

6.1 Inks with variable core sizes

Differently to the previous chapters, Au@PS dielectric inks were prepared with different core sizes but with constant ligand exchange conditions in this chapter. The inks were prepared in a two step process: first, oleylamine (OAm) capped AuNPs were synthesized in different solvents, then a ligand exchange to thiol-terminated polystyrene was

performed (1 week stirring at 60 °C) to obtain the final inks with toluene solvent. The different core sizes are expected to influence the polymer shells and possibly the ink stabilities during ligand exchange and ageing.

6.1.1 Au cores of different sizes

Au cores with diameters of 2.9 nm, 4.7 nm, and 7.0 nm were synthesized by the usage of the solvents *n*-pentane, *n*-hexane, and benzene in the synthesis. Wu *et al.* proposed that linear solvent molecules such as alkanes allow dense OAm layers resulting in small particle sizes whereas more bulky aromatic solvent molecules lead to a less dense OAm protection layer and larger particle sizes [134].

TEM images of the small and large particles are shown in Figure 6.3. For $Au_{0.05}^{small}@PS_{5000}$ and $Au_{0.09}^{small}@PS_{11000}$, two batches of small Au@OAm NPs were synthesized (Figure 6.3a and Figure 6.3b); for $Au_{0.17}^{large}@PS_{5000}$ and $Au_{0.31}^{large}@PS_{11000}$, one batch of Au@OAm NPs synthesized in benzene (Figure 6.3c) was overgrown to reach a final core diameter of 8.2 nm (Figure 6.3d). The TEM images indicate a monodisperse size distribution of all the synthesized Au@OAm NPs.

The Au cores should ideally be unaffected by the ligand exchange. The mean and standard deviation of the core diameters of the Au@PS NPs that are reported in Table 6.3 were obtained by fitting measured SAXS data of dispersed particles with the form factor of spheres. The measurements of the medium-sized particles were shown in Figure 5.12 in Chapter 5, those of small and large hybrid particles are shown in Figure 6.4.

Scattering from the large particles fits very well to the form factor of spherical particles; there is no sign of agglomerates in the ink. The standard deviation σ was below 10 % and the monodispersity of the Au@PS particles is also seen on TEM images (Figure 6.6c,d). Therefore, there is no sign that the ligand exchange affected the large Au cores.

For the small particles, the scattering intensity at low q-values is above that expected for spherical particles. While strongly rising scattering intensities for Au@PS particles at low q-values was seen as a sign of particle agglomeration [155], the observed deviation for $Au_{0.05}^{small}@PS_{5000}$ and $Au_{0.09}^{small}@PS_{11000}$ particles is small and therefore large agglomerates in the inks are not expected. While for $Au_{0.05}^{small}@PS_{5000}$ the particle size distribution is below 10 % and in good agreement with the monodispersity observed in the TEM images (Figure 6.6a), $Au_{0.09}^{small}@PS_{11000}$ shows a size distribution of 12 % indicating a larger polydispersity. A TEM image of $Au_{0.09}^{small}@PS_{11000}$ reveals that noticeably larger particles have evolved during the ligand exchange process (Figure 6.6b). This alteration of the Au cores during ligand exchange is examined in more detail below.

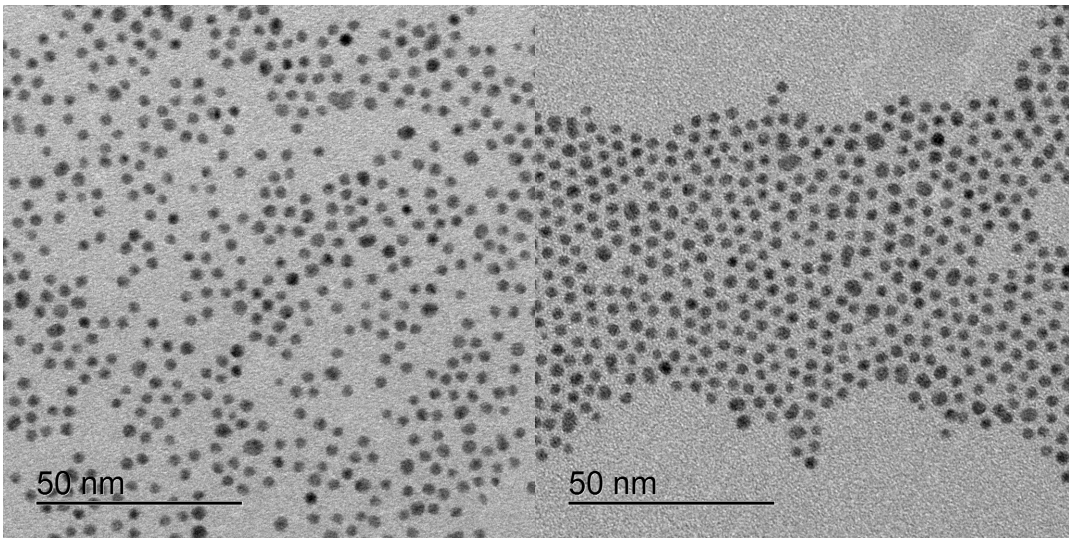

(A) Small Au@OAm NPs first batch. (B) Small Au@OAm NPs second batch.

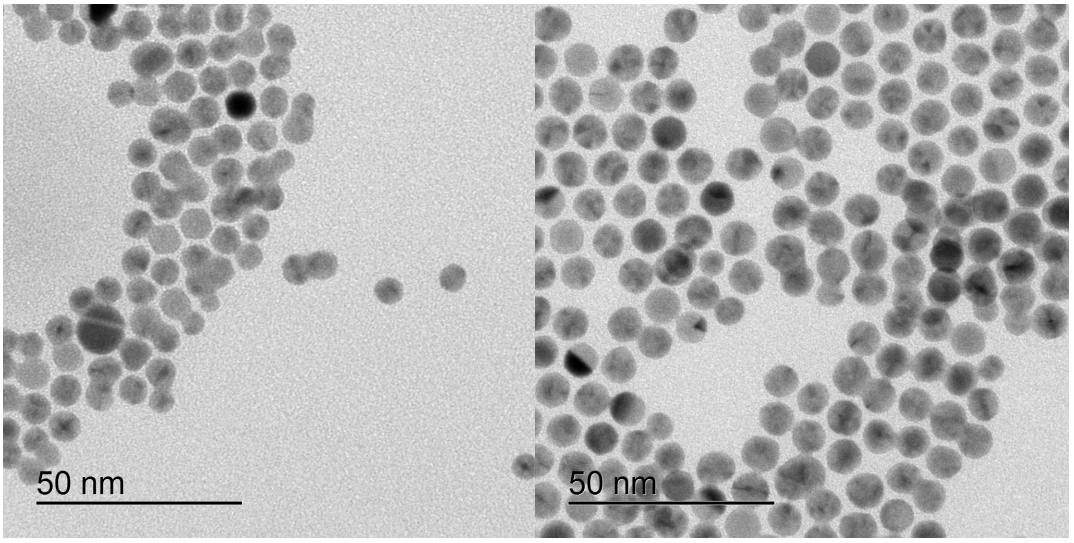

(C) Large Au@OAm NPs before overgrowth. (D) Large Au@OAm NPs after overgrowth.

FIGURE 6.3: TEM micrographs of synthesized Au@OAm NPs. a) The first batch of small Au@OAm NPs was used for $Au_{0.05}^{small}@PS_{5000}$. b) The second batch of small Au@OAm NPs was used for $Au_{0.09}^{small}@PS_{11000}$. c) The large Au@OAm NPs before overgrowth. d) The large Au@OAm NPs after overgrowth were used for $Au_{0.17}^{large}@PS_{5000}$ and $Au_{0.31}^{large}@PS_{11000}$.

6.1.2 Polymer shells with different core sizes

As it was shown before for medium-sized Au@PS particles, the resulting polymer shell structure is influenced by the ligand densities and the ligand length (see Chapter 4, Subsection 4.1.2). This polymer shell defines the Au volume fraction in Au@PS hybrids. TGA measurements of solid samples made of the different inks were performed to determine the gold volume fractions $f_{v,Au}$ from the Au weight content $x_{w,Au}$ using Equation (3.1) and the ligand grafting densities $\rho_{A,ligand}$ using Equation (3.4). Figure 6.5 shows that the main weight loss occurred at about 400 °C, where the thermal decomposition

TABLE 6.3: Core size data with the mean and standard deviation of the core diameters d_{core} and σ from SAXS, the hydrodynamic diameter d_{h} from DLS, and the positions of the peaks $d_{\text{TEM},1}$ and $d_{\text{TEM},2}$ in the size histogram of TEM image analysis.

Sample name	d_{core} [nm]	σ [%]	d_{h} [nm]	$d_{\text{TEM},1}$ [nm]	$d_{\text{TEM},2}$ [nm]
small Au@OAm 1st batch	2.9	8.5	6.5 ± 0.32	2.8 ± 0.4	3.8
$Au_{0.05}^{small}@PS_{5000}$	2.9	9.0	12.0 ± 0.23	3.0 ± 0.4	-
small Au@OAm 2nd batch	2.9	10.0	6.0 ± 0.53	2.8 ± 0.5	-
$Au_{0.09}^{small}@PS_{11000}$	2.9	12.9	11.2 ± 0.15	2.8 ± 0.9	4.8
$Au_{0.09}^{small}@PS_{11000}$ 161 days aged	2.8	14.4	N/A	2.6 ± 1.3	4.9
medium Au@OAm	4.7	6.7	7.7 ± 0.05	N/A	N/A
$Au_{0.07}^{medium}@PS_{5000}$	4.7	6.6	16.3 ± 0.09	N/A	N/A
$Au_{0.10}^{medium}@PS_{11000}$	4.6	7.0	16.2 ± 0.10	N/A	N/A
Large Au@OAm	7.0	10.0	N/A	6.7 ± 0.7	-
Large Au@OAm 1x overgrow	8.2	8.5	11.2 ± 0.62	7.8 ± 0.6	-
$Au_{0.17}^{large}@PS_{5000}$	8.2	9.3	20.3 ± 0.06	7.6 ± 0.6	-
$Au_{0.31}^{large}@PS_{11000}$	8.2	9.0	19.4 ± 0.02	7.7 ± 0.6	-

of PS is expected [190–192]. The gold concentrations of the inks after ligand exchange c_{Au} were measured by UV-Vis and were in the range of $12.8\,\text{mg}\,\text{mL}^{-1}$ to $34.0\,\text{mg}\,\text{mL}^{-1}$. The properties of the inks used in this chapter are summarized in Table 6.4, Table 6.5 lists the Au contents in solid layers of these inks as measured by TGA.

TABLE 6.4: Measured properties of the prepared Au@PS hybrid nanoparticle inks in this chapter with varying Au core sizes (dispersion medium toluene) with the diameter of the Au cores d_{core}, the ligand density $\rho_{\text{A,ligand}}$, and the Au concentration in the inks c_{Au}.

Ink label	d_{core} [nm]	Ligand	$\rho_{\text{A,ligand}}$ [nm^{-2}]	c_{Au} [$\text{mg}\,\text{mL}^{-1}$]
$Au_{0.05}^{small}@PS_{5000}$	2.9	PS_{5000}	1.2	19.8
$Au_{0.09}^{small}@PS_{11000}$	2.9	PS_{11000}	0.3	24.7
$Au_{0.07}^{medium}@PS_{5000}$	4.7	PS_{5000}	1.3	12.8
$Au_{0.10}^{medium}@PS_{11000}$	4.6	PS_{11000}	0.4	34.0
$Au_{0.17}^{large}@PS_{5000}$	8.2	PS_{5000}	0.8	23.0
$Au_{0.31}^{large}@PS_{11000}$	8.2	PS_{11000}	0.2	26.4

The differences of the hydrodynamic diameters measured by DLS, which are listed in Table 6.3, indicate the effect of the ligand exchange from oleylamine to polystyrene. For the OAm capped particles, the hydrodynamic diameter is always about 3 nm larger than the core diameter. This is in the same range as the distance between OAm capped Au nanowires in different solvents that was determined by SAXS measurements and molecular dynamics simulations from Gao *et al.* [209]. The hydrodynamic diameters were significantly increasing after ligand exchange: for the small particles by 5 nm to

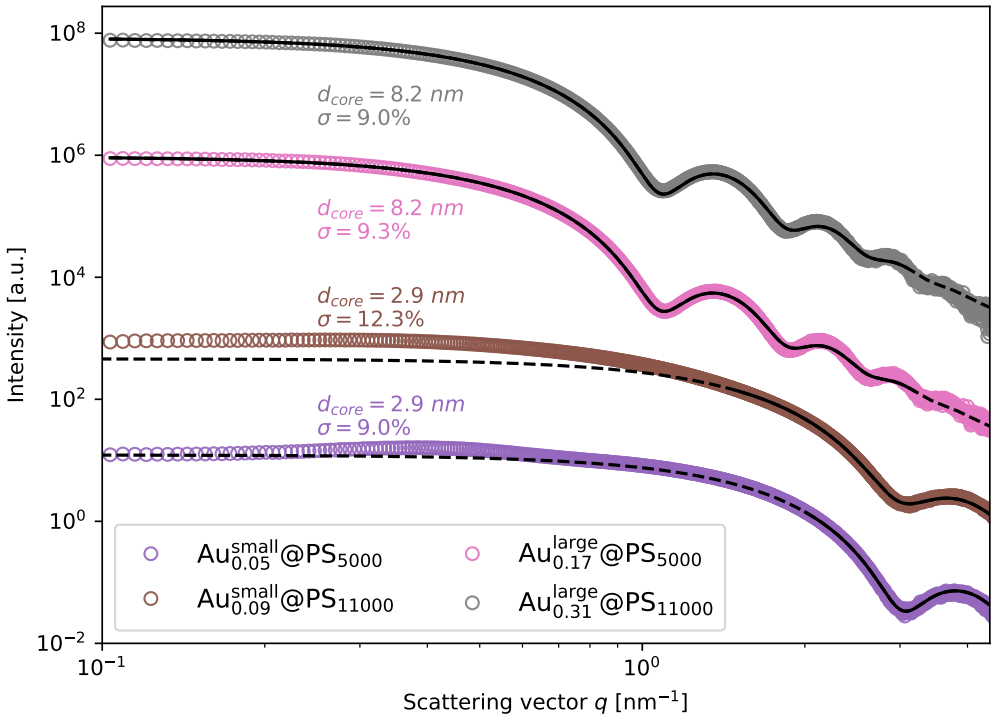

FIGURE 6.4: SAXS measurements of small Au@PS and large Au@PS particles dispersed in toluene after ligand exchange. The measurements were shifted in y-direction by a multiplication factor. The black lines indicate the form factor fit used to quantify the core diameters d_{core} and the widths of the core size distributions σ.

TABLE 6.5: Experimental results for layers of Au@PS hybrid particles from TGA and SAXS. d_{core} is the Au core diameter, $x_{\mathrm{w,Au}}$ and $f_{\mathrm{v,Au}}$ are the weight and volume content of gold in dried layers. d_{ss}^1, d_{ss}^2, and d_{ss}^3 are characteristic surface-to-surface distances of the AuNPs in the dielectric layers. Distances without mark are calculated for random packing. Distances marked with$^{(\mathrm{fcc})}$ are calculated for fcc packing.

Sample name	d_{core} [nm]	$x_{\mathrm{w,Au}}$ [wt%]	$f_{\mathrm{v,Au}}$ [vol%]	d_{ss}^1 [nm]	d_{ss}^2 [nm]	d_{ss}^3 [nm]
$Au_{0.05}^{small}@PS_{5000}$	2.9	48.3	4.8	3.5	0.3	-
$Au_{0.09}^{small}@PS_{11000}$	2.9	65.1	9.2	17.6	2.7	1.3
$Au_{0.07}^{medium}@PS_{5000}$	4.7	58.6	7.1	4.5	$2.5^{(\mathrm{fcc})}$	-
$Au_{0.10}^{medium}@PS_{11000}$	4.6	66.5	9.7	6.2	0.7	-
$Au_{0.17}^{large}@PS_{5000}$	8.2	79.2	17.2	4.2	$0.8^{(\mathrm{fcc})}$	-
$Au_{0.31}^{large}@PS_{11000}$	8.2	89.3	31.2	8.0	0.1	-

6 nm, for the medium-sized and large particles by 8 nm to 9 nm. This increase was slightly larger for PS_{5000} than for PS_{11000}, indicating a denser polymer shell for PS_{5000}. The stronger coiling of PS_{11000} ligand causes a mushroom conformation of the polymer ligands resulting in less dense shells [157], which are accompanied by measured ligand densities that are by a factor 3 to 4 lower for PS_{11000} than for PS_{5000} for all core sizes (see Table 6.4). The ligand densities dropped to about 50 % when the particle size was

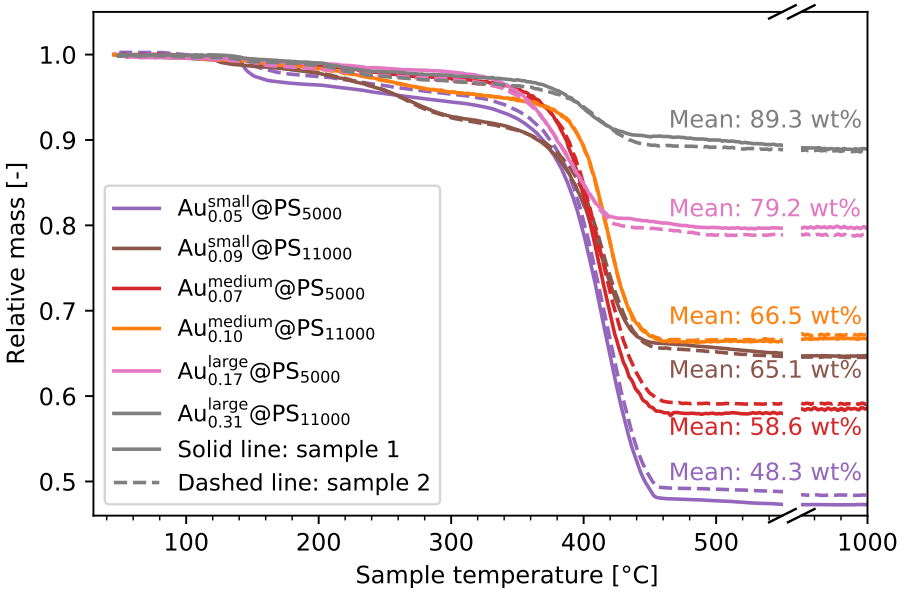

FIGURE 6.5: TGA results for all dielectric layers prepared with variation of Au core size. The mean value of two measured samples is reported.

increased from medium to large particles, a known effect of reduced curvature of larger particles [153]. Small particles exhibited 0.1 nm^{-2} lower grafting densities compared to medium-sized particles with the same ligand length; i.e. the trend of increased ligand density with increased particle curvature was not fulfilled for the small cores. The ligand densities stayed relatively low considering the high curvature of the 2.9 nm AuNPs, which was already indicated by the smaller increase of the hydrodynamic diameter after ligand exchange of only 5 nm to 6 nm. These results imply that the polymer shells are less dense for small cores than for medium-sized and large cores, especially in the case of PS_{11000} shells.

6.1.3 Core size effect on ink stability during ligand exchange and ageing

Ink stability is a requirement for practical handling of the Au@PS inks. Two different kinds of stability can be distinguished. The first kind, "ageing stability", describes the continuity of the ink properties with shelf life. Triggering influences like heat can accelerate the degradation of Au cores, e.g. by particle growth via Ostwald ripening. Theoretical studies have shown that Ostwald ripening occurs more pronounced at small particle diameters of 3 nm and below or at elevated temperatures [210]. The polymer shells can degrade, too, e.g. by detachment of the polymers or degradation of the polymer ligand chains. As a consequence, the ink would differ its properties and in the

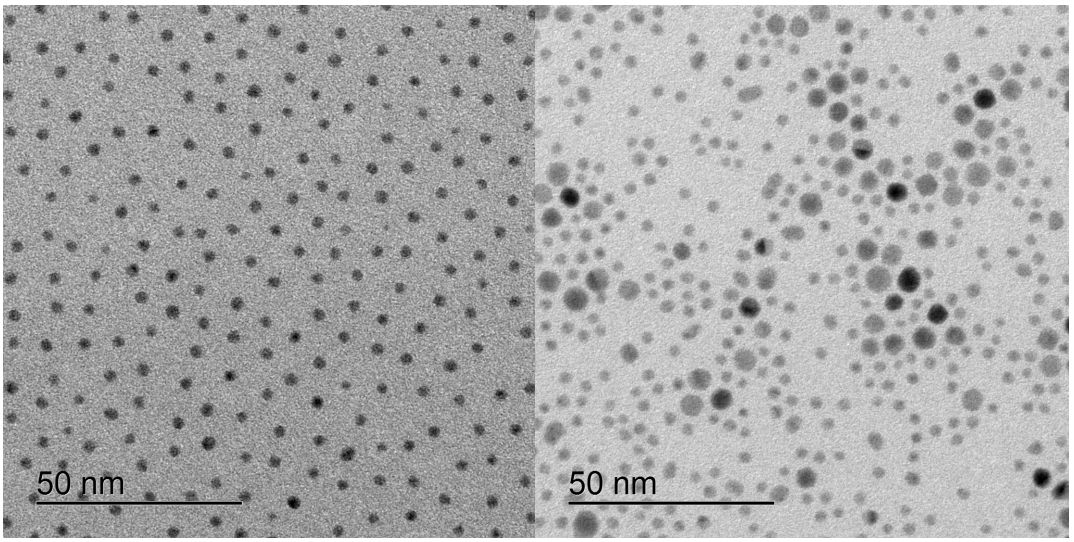

(A) $Au_{0.05}^{small}@PS_{5000}$ (B) $Au_{0.09}^{small}@PS_{11000}$

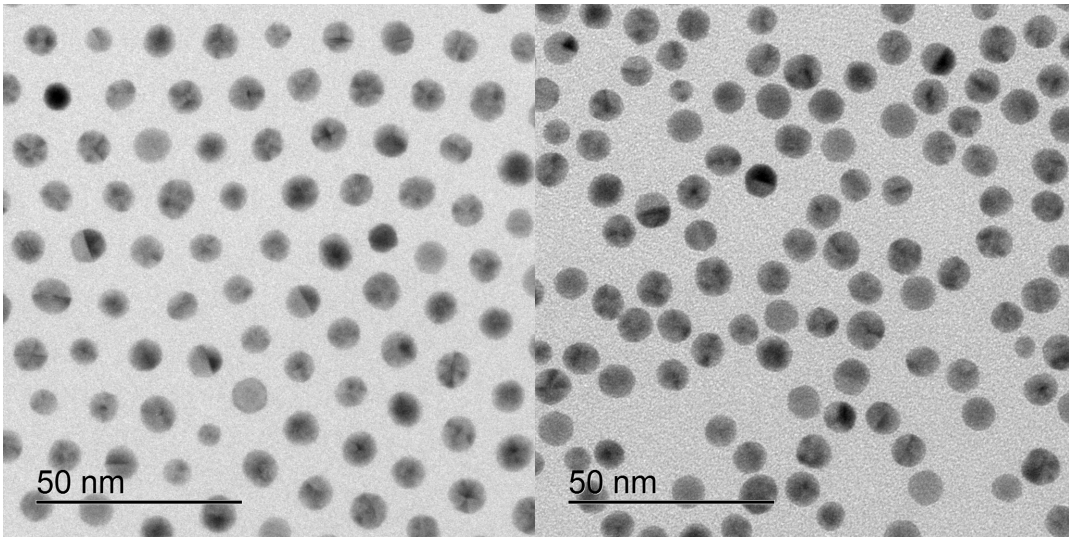

(C) $Au_{0.17}^{large}@PS_{5000}$ (D) $Au_{0.31}^{large}@PS_{11000}$

FIGURE 6.6: TEM micrographs of small and large Au@PS hybrid nanoparticles after ligand exchange.

worst case, e.g. after considerable degradation of the insulating polymer shell, it would become impossible to create dielectric layers with such an aged ink. The second kind, "colloidal stability", describes the instability of the ink by the formation of particle agglomerates. This agglomerate formation can be reversible – in this case, particles can be redispersed, e.g. by ultrasonication – or it can be permanent. Agglomerates can complicate the processing of the inks, e.g. the formation of nm thin homogeneous layers is difficult with large agglomerates. Both ageing effects can be hindered by a dense polymer shell that assures the steric stabilization of the ink. This section investigates the stability of the hybrid inks during ligand exchange and ageing in dependence of the Au core sizes, which also influenced the polymer shell grafting densities, as it was stated above.

Elevated temperatures of 60 °C were applied during the ligand exchange and can potentially accelerate degradation effects, such as the growth of Au cores. To gain further insight into the extent of this effect, several TEM images of particles with small and large core sizes before and after ligand exchange were analyzed. The size distributions were created from various TEM images with the Fiji image analysis software (see Chapter 3 for details) and are shown in Figure 6.7. Both small and large Au@OAm particles had monodisperse size distributions after the synthesis or overgrow step: the blue curves in the particle size distribution have peaks at diameters of 2.8 nm for the small particles (Figure 6.7a,b), the size distribution of the large particles has a peak at the diameter 6.7 nm after synthesis and before overgrowth (brown curve) and at the diameter 7.8 nm (blue curve) after overgrowth (Figure 6.7c). The ligand exchange did not affect the Au cores of the large particles: in Figure 6.7c, the peaks of the yellow and green curves of the Au@PS particles are located at the same position of about 7.7 nm as the peak of the blue curve of the Au@OAm particles in the size distribution histogram. $Au_{0.05}^{small}@PS_{5000}$ also maintained its monodisperse size distribution after ligand exchange at around 3.0 nm (Figure 6.7a). However, a smaller peak at 4.8 nm evolved next to the main peak at 2.6 nm in the size distribution of $Au_{0.09}^{small}@PS_{11000}$ after ligand exchange. This increase in the share of larger particles was even enhanced with ageing of the $Au_{0.09}^{small}@PS_{11000}$ ink, which is discussed in the following.

In order to investigate the long-time stability, the inks were stored for at least 4 months (exact values listed in Table 6.6) in the laboratory to investigate changes either by Au core growth or agglomeration of particles. Aged inks with medium Au cores of 4.7 nm diameter and large Au cores of 8.2 nm diameter maintained their monodisperse particle size distribution within at least 145 days according to SAXS (see Figure A.2 in the appendix). For these inks, the PS shells stabilized the inks against agglomeration and degradation. SAXS of the ink $Au_{0.05}^{small}@PS_{5000}$ indicated that this ink maintained its monodisperse size distribution after 121 days, too (Figure 6.8 on the bottom). The polymer shell with PS_{5000} was possibly dense enough to maintain a stable particle size distribution. SAXS of the ink $Au_{0.09}^{small}@PS_{11000}$ revealed a significant deviation of scattering intensity at low q-values from the form factor of spheres after 161 days, indicating a change in the particle size distribution (Figure 6.8 on the top). The particle size distributions for this aged ink was determined with TEM images (Figure 6.7b, red curve). While the Au cores were monodisperse after synthesis with mean diameters of 2.8 nm, larger particles with mean diameter of 4.8 nm appeared after ligand exchange and after ageing for 161 days the large particles grew further till diameters of up to 14.5 nm (Figure 6.9). It is assumed that Ostwald ripening first caused the appearance of larger particles during ligand exchange. During ageing, ongoing Ostwald ripening and additionally the coalescence of small particles, what has been observed for surfactant coated

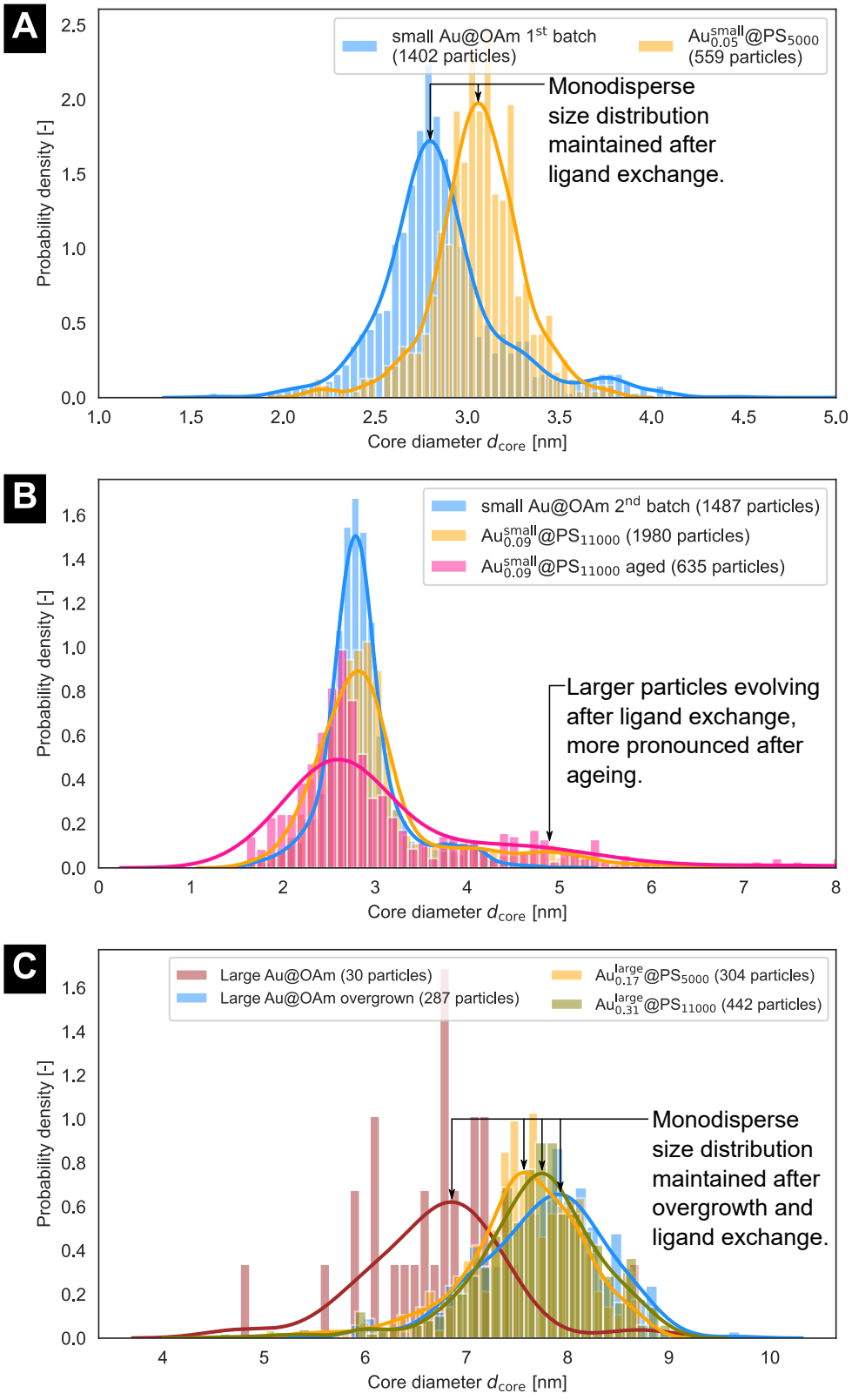

FIGURE 6.7: Size distribution from TEM image analysis of particles with small and large core size. a) Size distribution of first batch of small Au@OAm particles and $Au_{0.05}^{small}@PS_{5000}$ particles. b) Size distribution of a second batch of small Au@OAm particles and $Au_{0.09}^{small}@PS_{11000}$ particles after 161 days. c) Size distribution of large Au@OAm particles before and after overgrow step and $Au_{0.17}^{large}@PS_{5000}$ and $Au_{0.31}^{large}@PS_{11000}$ particles.

particles [211], likely led to the formation of large spheric and elongated particles (Figure 6.9c). These two growth states with Ostwald ripening and a transition to coalescence of particles at longer ageing times have been reported for alkanethiol capped AuNP in PMMA layers, which were annealed at 150 °C [212]. Moreover, the agglomeration of dodecanethiol-capped AuNPs that suffered ligand loss during ageing of at least 21 days in non-polar solvents has been reported in the literature [213, 214]. Consequently, it is proposed that the low ligand density of the $Au_{0.09}^{small}@PS_{11000}$ particles could not protect the cores from degradation via Ostwald ripening and coalescence, while the polymer shells were dense enough to prevent Au core degradation for all other inks within the observed time frame.

Molecular dynamics simulations showed that adsorption of alkanethiols on gold nanocrystals is different for the different crystalline facets: for smaller Au nanocrystals, less ligands are adsorbed. Additionally, these absorbed ligands have on trend less Au atoms to be in contact with [215]. The low ligand densities and crystalline facets of the Au cores in $Au_{0.09}^{small}@PS_{11000}$ might have favoured the observed particle instability.

TABLE 6.6: Shelf life after synthesis before measurements of aged inks was performed.

Ink label	Shelf life [days]
$Au_{0.05}^{small}@PS_{5000}$	121
$Au_{0.09}^{small}@PS_{11000}$	161
$Au_{0.07}^{medium}@PS_{5000}$	588
$Au_{0.10}^{medium}@PS_{11000}$	545
$Au_{0.17}^{large}@PS_{5000}$	145
$Au_{0.31}^{large}@PS_{11000}$	145

6.1.4 Conclusion

All three particle sizes had monomodal size distributions after synthesis of Au@OAm particles. The grafting densities for medium-sized particles with core diameters of 4.7 nm were larger than for large particles with core diameters of 8.2 nm due to increased curvature. Small particles with core diameters of 2.9 nm had grafting densities slightly below the medium-sized particles, despite their larger curvature. Grafting densities were lower for the PS_{11000} ligand in comparison to the PS_{5000} ligand for all Au core sizes. Particles with core diameters of 2.9 nm and PS_{11000} shells were unstable due to growth of the Au cores. The growth Au cores in the ink $Au_{0.09}^{small}@PS_{11000}$ started during the ligand exchange where the particles were stirred at 60 °C and further growth of large particles was later observed during ageing. Ostwald ripening and coalescence are suggested as possible mechanisms for this growth. Higher ligand densities

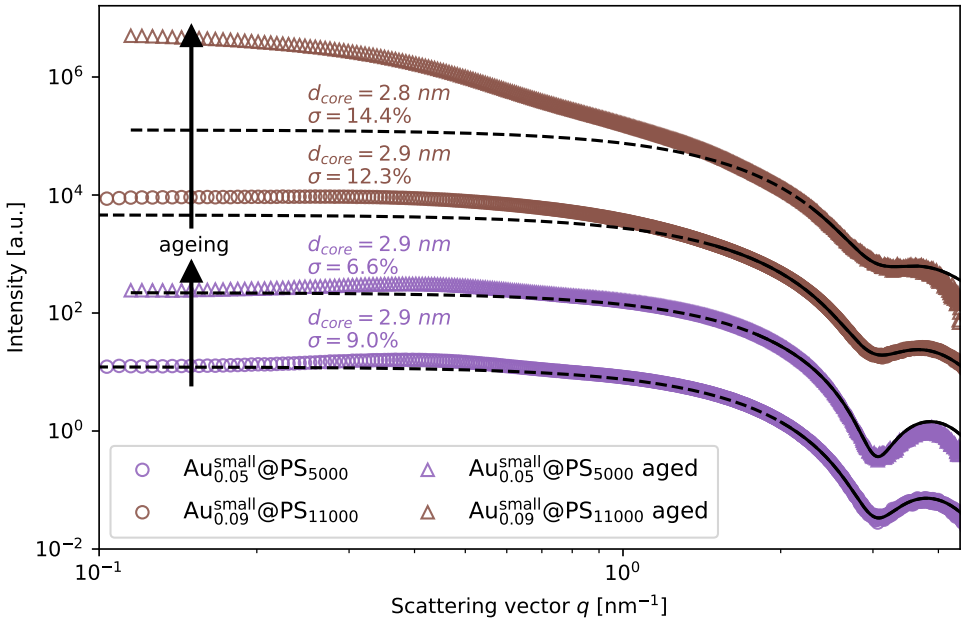

FIGURE 6.8: SAXS measurements of Au@PS hybrid inks with small core size fresh after synthesis (circles) and aged after respective shelf life (triangles) as indicated with the arrows.

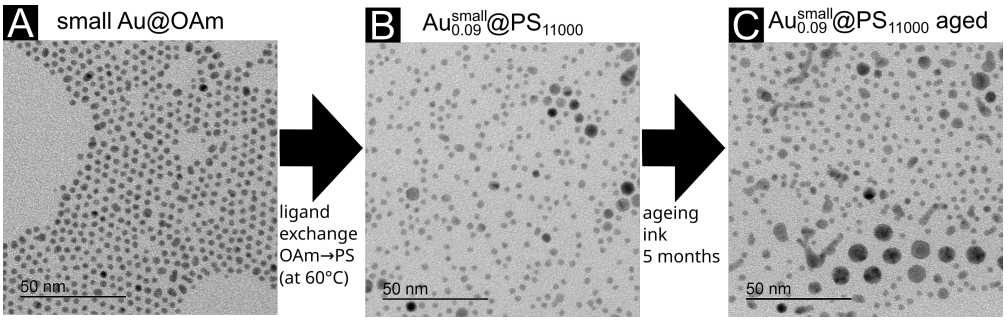

FIGURE 6.9: TEM images of a) small AuNP@OAm, b) $Au^{small}_{0.09}@PS_{11000}$ after ligand exchange and c) $Au^{small}_{0.09}@PS_{11000}$ after ageing of 5 months show the formation of large AuNPs in the ink with time.

as for the ink $Au^{small}_{0.05}@PS_{5000}$ or larger particles sizes as in the inks $Au^{medium}_{0.07}@PS_{5000}$, $Au^{medium}_{0.10}@PS_{11000}$, $Au^{large}_{0.17}@PS_{5000}$, or $Au^{large}_{0.31}@PS_{11000}$ might have been beneficial for the ink stability of the Au@PS hybrid particles as particle growth was not observed for these inks during ageing.

6.2 Core size effect on particle packing

The packing of Au@PS hybrid nanoparticles in dielectric films is affected by core size and ligand shell. In this section, the packing of Au@PS particles with different core size

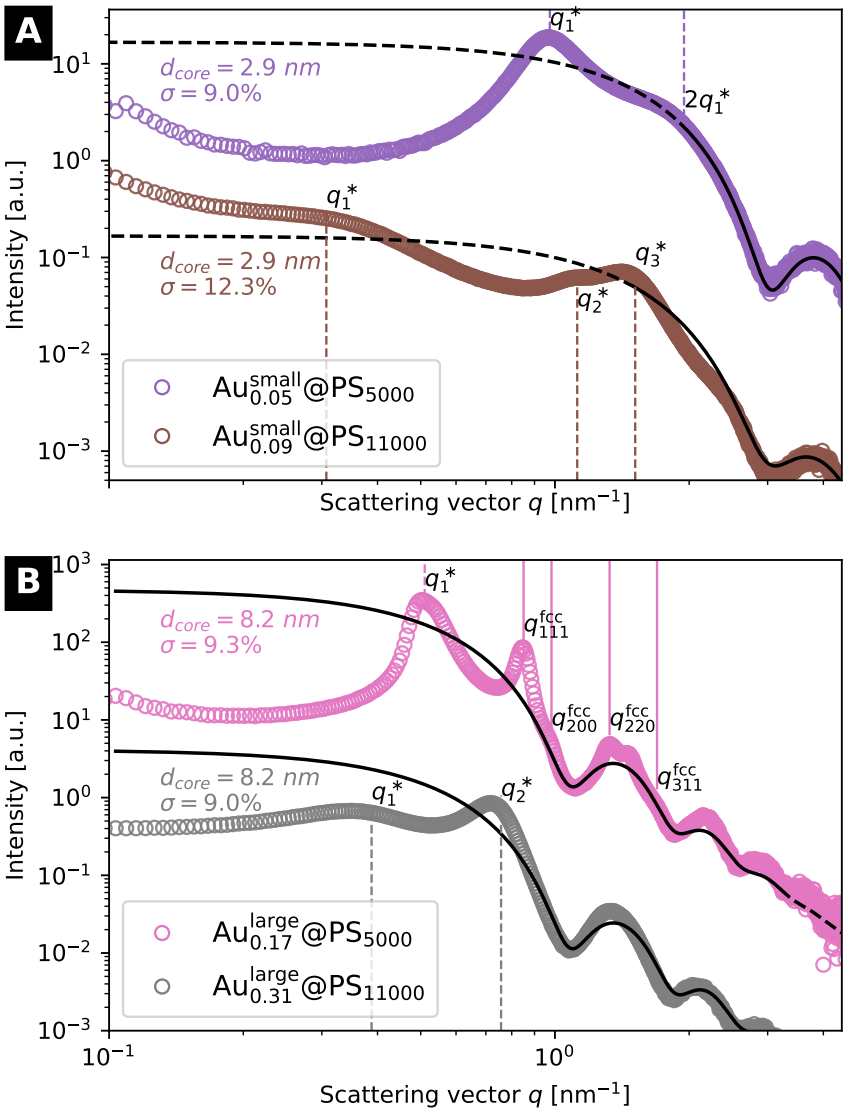

FIGURE 6.10: Transmission SAXS measurements of drop casted dielectric films on Kapton foil of Au@PS hybrid particles with a) small and b) large core sizes. The measurements were shifted in y-direction by a multiplication factor.

and with PS_{5000} and PS_{11000} shells is studied. As in Chapter 5 the packing of medium-sized cores with 4.7 nm diameter was already discussed, here the packing of small cores with 2.9 nm diameter and large cores with 8.2 nm diameter is investigated.

Drop casted layers were prepared on Kapton foil and analyzed by SAXS in transmission (Figure 6.10) and TEM. All samples except $Au_{0.17}^{large}@PS_{5000}$ had broad peaks indicating random particle packing; only $Au_{0.17}^{large}@PS_{5000}$ had sharper peaks indicating order. The structure factors in Figure 6.11 were used to determine the q-positions of the peaks in Table 6.7.

Using Equation (3.10) and Equation (3.14) for the data of $Au_{0.05}^{small}@PS_{5000}$ and $Au_{0.09}^{small}@PS_{11000}$,

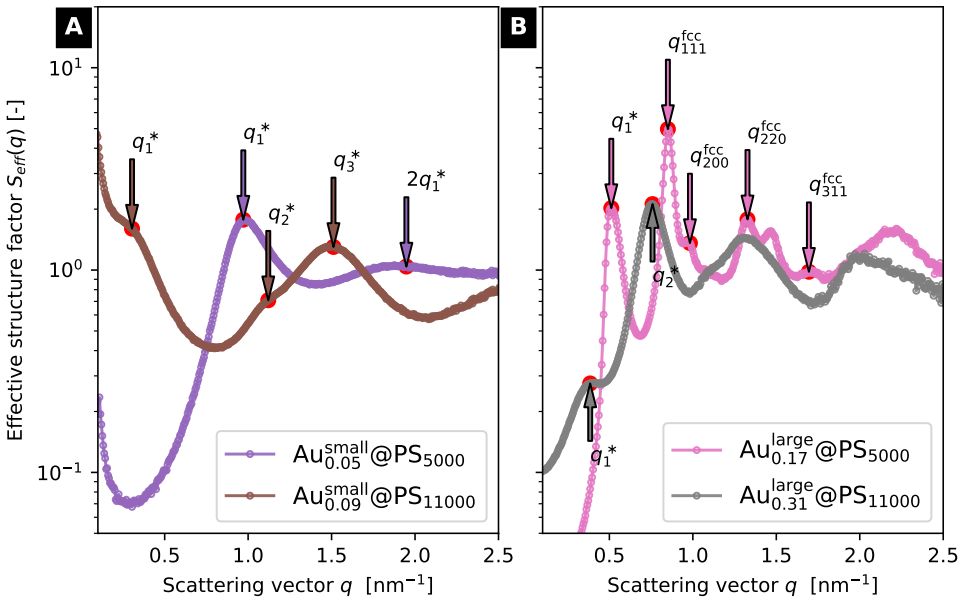

FIGURE 6.11: Effective structure factors $S_{\text{eff}}(q)$ that were determined for the small and large Au@PS drop casted films measured in SAXS as described in the Chapter 3. While for $Au_{0.17}^{large}@PS_{5000}$ both a fcc and random packing was found, for the other samples only a random packing was found.

TABLE 6.7: Positions of peaks in the effective structure factors from SAXS of hybrid dielectric films on Kapton foil with the q-values of the i-th peak corresponding to random packing q_i^* and the first peak and the lattice constant of fcc packings q_{111}^{fcc} and a^{fcc}.

Sample name	q_1^* [nm^{-1}]	q_2^* [nm^{-1}]	q_3^* [nm^{-1}]	q_{111}^{fcc} [nm^{-1}]	a^{fcc} [nm]
$Au_{0.05}^{small}@PS_{5000}$	0.97	1.95	—	—	—
$Au_{0.09}^{small}@PS_{11000}$	0.31	1.12	1.51	—	—
$Au_{0.17}^{large}@PS_{5000}$	0.51	—	—	0.85	12.8
$Au_{0.31}^{large}@PS_{11000}$	0.39	0.76	—	—	—

the q positions of the peaks in the structure factors translate into surface-to-surface distances between the particles as listed in Table 6.5. TEM micrographs of the Au@PS NPs dried on a TEM grid show the random packing of small Au@PS hybrid particles (Figure 6.12a,b); the Fourier transform of the images confirmed random packings.

Both samples are characterized by closer and larger packing distances. Two small surface-to-surface distances 1.3 nm and 2.7 nm and the larger surface-to-surface distance 17.6 nm were found for $Au_{0.09}^{small}@PS_{11000}$. Therefore, the closer packing distance in this sample is apparently subdivided in two different surface-to-surface distances. This nature of short and long characteristic distances in particle packing possibly corresponds to chain-like structures of the particles what can be recognized in the TEM picture of $Au_{0.09}^{small}@PS_{11000}$ (Figure 6.12b). Two surface-to-surface distances 0.3 nm and 3.5 nm

were found for $Au_{0.05}^{small}@PS_{5000}$ but in TEM images of $Au_{0.05}^{small}@PS_{5000}$, such chains are not as clearly seen (Figure 6.12a) as for the medium-sized particles in Chapter 5 (Figure 5.8a). The packing seems to be amorphous.

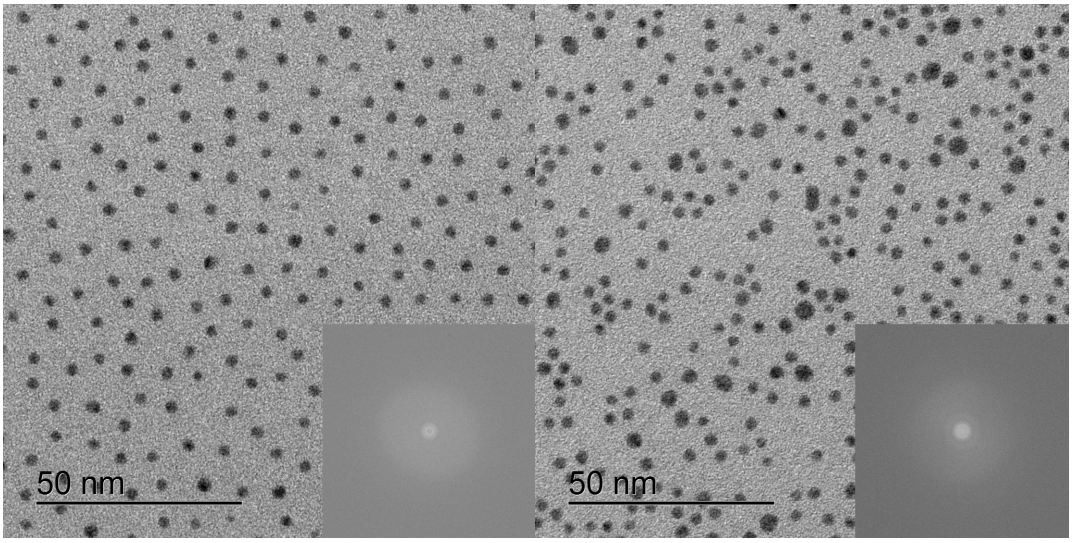

(A) $Au_{0.05}^{small}@PS_{5000}$ (B) $Au_{0.09}^{small}@PS_{11000}$

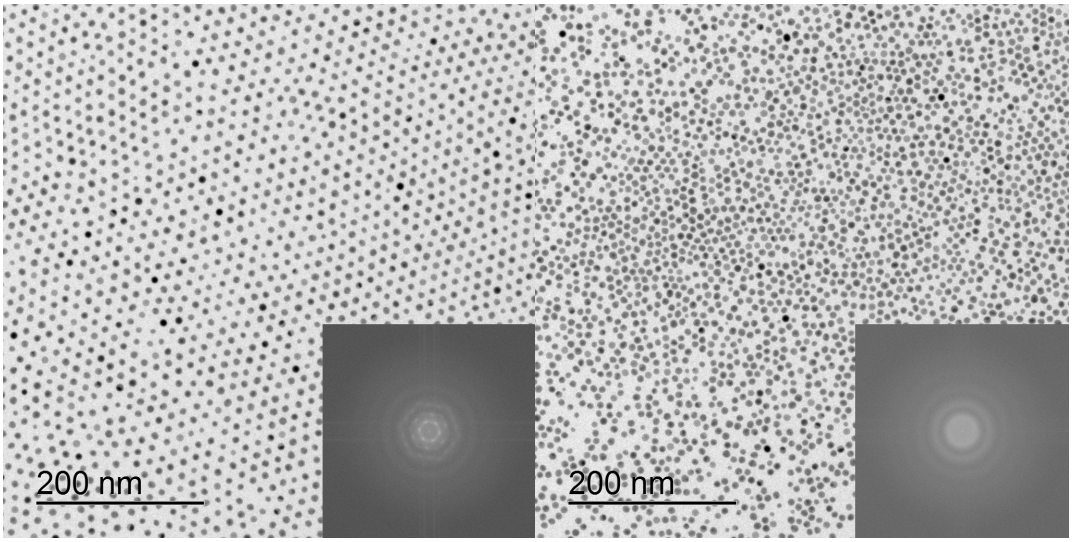

(C) $Au_{0.17}^{large}@PS_{5000}$ (D) $Au_{0.31}^{large}@PS_{11000}$

FIGURE 6.12: TEM micrographs of small and large Au@PS hybrid nanoparticles dropped on TEM grid and the Fourier transform (insets). The crystalline superlattice of $Au_{0.17}^{large}@PS_{5000}$ is seen in c).

The nanoparticles with large Au cores and PS_{11000} ligand also showed two broad peaks in transmission SAXS characteristic for a random particle packing; the Fourier transform of the TEM image in Figure 6.12d showed no reflexes of an ordered structure. Consequently, the q positions of the two peaks translate in characteristic surface-to-surface distances of the particle packing 0.1 nm and 8.0 nm. These distances are possibly connected to the chain-like structure of the particles as it is seen in Figure 6.12d. The SAXS data of $Au_{0.17}^{large}@PS_{5000}$ showed 4 peaks that were indexed as an fcc packing of ratios

$\sqrt{3} : \sqrt{4} : \sqrt{8} : \sqrt{11}$. The characteristic surface-to-surface distance in the fcc packing for (111) was 0.8 nm (lattice parameter $a = 12.8\,\text{nm}$) from Equations (3.12) to (3.14). A broad peak at $q = 0.51\,\text{nm}^{-1}$ could not be indexed and was attributed to random packing (surface-to-surface distance 4.2 nm). The Fourier transform of the TEM image in Figure 6.12c clearly shows the fcc particle packing. A similar mixture of fcc and random packing was observed in Chapter 5 for medium-sized particles with PS_{5000} ligands.

TEM images of FIB cross sections of thin film capacitors were evaluated to analyze the film structure in spin-coated devices. The TEM images for small Au cores of diameter 2.9 nm and large Au cores of diameter 8.2 nm are shown in Figure 6.13, for medium Au cores of diameter 4.7 nm see Figure 5.6 in Chapter 5. The TEM confirmed above results: only $Au_{0.07}^{medium}@PS_{5000}$ and $Au_{0.17}^{large}@PS_{5000}$ formed ordered particle packings.

It is assumed that the larger ligand density of PS_{5000} leads to more homogeneous ligand shells and therefore an ordered structure can be achieved for medium and large core sizes. However, $Au_{0.05}^{small}@PS_{5000}$ particles did not show an ordered particle packing although when the short ligands were used. Therefore, it is likely that the core diameter indirectly influences the particle packing, too: for small core sizes the polymer shell was less dense than for medium-sized particles. Its grafting density was apparently not dense enough to result in an ordered particle packing and a random packing was observed for $Au_{0.05}^{small}@PS_{5000}$. The lower ligand densities for the PS_{11000} ligands allow folding of the ligand on the particle surface and possibly lead to irregular polymer shells with "patchy surfaces" (compare TEM image in Figure 4.7 of Chapter 4) that stimulate chain-like particle arrangements. Particles in chain-like formation have been reported for "patchy particles" with heterogeneous surfaces [165].

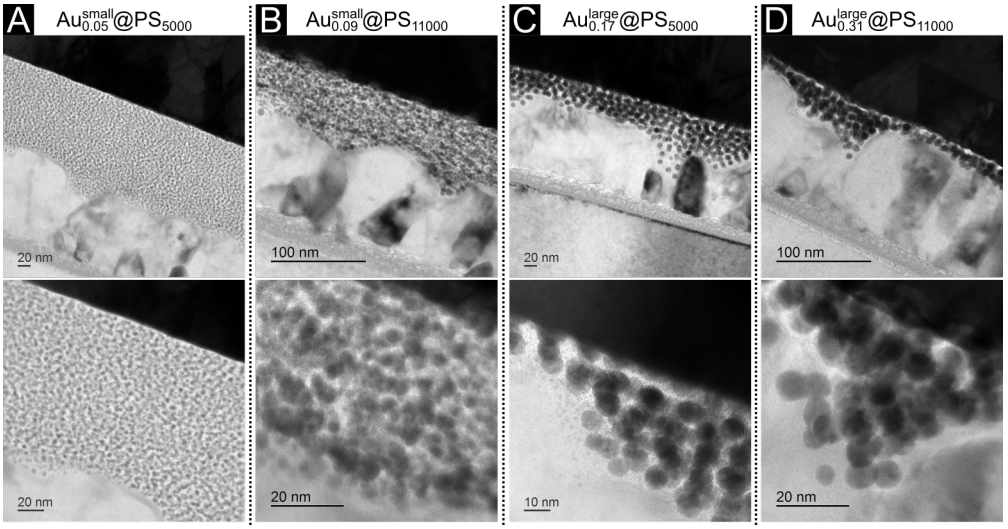

FIGURE 6.13: Transmission electron micrographs of focus ion beam cross sections of thin film capacitors with the a) $Au_{0.05}^{small}@PS_{5000}$, b) $Au_{0.09}^{small}@PS_{11000}$, c) $Au_{0.17}^{large}@PS_{5000}$, and d) $Au_{0.31}^{large}@PS_{11000}$ layers.

In summary, random packings with two characteristic distances were found for Au@PS hybrid particles with small core sizes of diameter 2.9 nm and for $Au@PS_{11000}$ particles with large core size of 8.2 nm diameter (same as for $Au_{0.10}^{medium}@PS_{11000}$). $Au_{0.17}^{large}@PS_{5000}$ and $Au_{0.07}^{medium}@PS_{5000}$ had mixed ordered fcc and random packing.

6.3 Dielectric properties of Au@PS hybrids with varying core size

This section reports on the core size effects on the dielectric properties of Au@PS hybrids. Chapter 5 explained Au@PS hybrids as a resistor-capacitor network as suggested by Efros and Shklovskii [38] and Dubrov *et al.* [37]. The individually attached polymer shells of Au@PS hybrids prevent percolation and enable high metal filling ratios. Here, the dielectric properties of Au@PS hybrids in dependence on the Au core diameter is discussed.

In the first section, the frequency-dependent dielectric constants and losses of Au@PS hybrids with small, medium, and large Au cores (diameters 2.9 nm, 4.7 nm, and 8.2 nm) are presented. The results are used to extend the model for Au@PS hybrids by considering the dependence of internal interfacial areas on the core diameters and the Maxwell-Wagner-Sillars (MWS) polarization that takes place at these interfaces. Finally, the effect of ageing of Au@PS samples on dielectric properties was investigated and analyzed using the extended model. The second section presents the dielectric strengths of the Au@PS hybrids with varying core sizes.

6.3.1 Core size effect on dielectric constant and loss

Dielectric constants and dielectric losses over the frequency range 1 Hz to 1×10^6 Hz were measured on thin film capacitors with spin coated Au@PS layers on aluminium coated silicon (Figure 6.14). The dielectric constants were larger for hybrid layers with PS_{11000} than PS_{5000} ligand at any given core diameter and at 10 kHz, where the dielectric losses were close to the minimum value (Figure 6.15). The Au volume fraction was always larger for $Au@PS_{11000}$ than for $Au@PS_{5000}$, whereas the latter had higher ligand densities, and the dielectric constant rises with the Au volume fraction, in accordance with simple mixing rules, e.g. a linear mixing model. At low frequencies, the largest dielectric constant of 98.3 was observed for $Au_{0.09}^{small}@PS_{11000}$ at 1 Hz; at 10 kHz, the largest dielectric constant of ≈ 15 was found for $Au_{0.31}^{large}@PS_{11000}$.

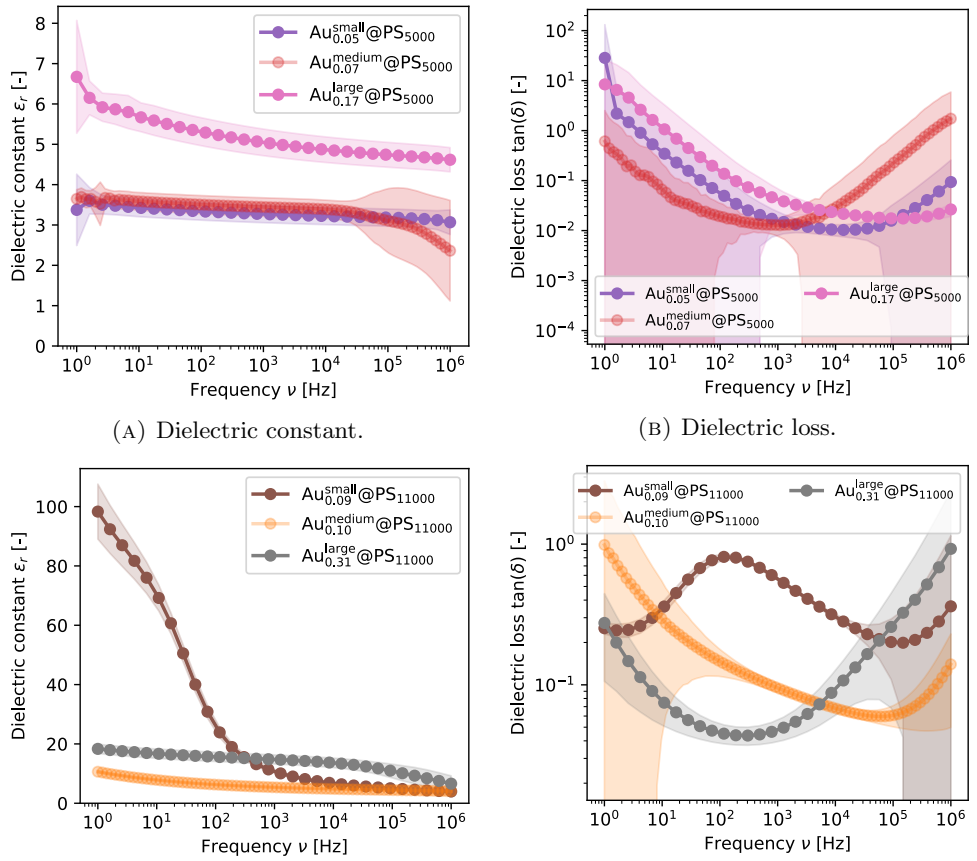

(A) Dielectric constant.

(B) Dielectric loss.

(C) Dielectric constant.

(D) Dielectric Loss.

FIGURE 6.14: Dielectric constants and losses of Au@PS hybrids with small, medium, and large AuNP core size and PS_{5000} or PS_{11000} ligand.

Figure 6.15 shows the dielectric constants at 10 kHz including reference thin film capacitors with PS-SH dielectric layers and thin film capacitors with hybrids containing medium-sized Au@PS_{11000} particles with low and high ligand density (see Table 5.1 in Chapter 5). The dielectric constant increased non-linearly with increasing Au volume fraction for all core sizes, showing that the linear mixing rule is not sufficient to predict dielectric constants. The dashed lines in Figure 6.15 represent a fit to the percolation function in Equation (2.16) with reference thin film capacitors with PS_{11000}-SH dielectric layers. Equation (2.16) uses a model following Efros and Shklovskii [38] where the dielectric is represented by a resistor-capacitor network [37]. The capacitors are formed between individual Au particles with the polymer shell around the particles acting as the dielectric. The tunnelling barrier between the Au cores is represented by parallel resistors that define the leakage currents, which contribute to the dielectric losses in the Au@PS hybrids.

The gold content in the hybrids strongly influences the resistor-capacitor network and the resulting dielectric properties. Samples with PS_{11000} had larger Au volume fractions than with PS_{5000} and showed higher dielectric constants than the samples with PS_{5000}

(Figure 6.14a,c), but the minima of the dielectric losses were also larger (Figure 6.14b,d). The denser PS_{5000} shells of Au@PS_{5000} hybrids decrease tunnelling and losses by leakage currents. This trade-off between high dielectric constants and low dielectric losses has been frequently described for Type II composites [39, 40, 84, 202, 205–207].

Chapter 5 showed that the effect of network structure is negligible in comparison to the Au volume fraction. Fits using Equation (2.16) were used to describe the dependence of the dielectric constant on the Au volume fraction. The resulting fit parameters for the hybrids of medium-sized particles ($f_c = 0.24$, $q = 1.3$, and $\varepsilon_{r,0} = 0.4$, see Table 5.6) were already shown in Chapter 5; the values for the hybrids with small particles are $f_c = 0.10$, $q = 0.3$, and $\varepsilon_{r,0} = 1.2$ and for hybrids with large particles $f_c = 0.41$, $q = 1.2$, and $\varepsilon_{r,0} = 0.9$. However, the accuracy of the latter fits is lower because only two different Au volume fractions were available. The percolation exponent found for large particles of core diameters 8.2 nm was $q = 1.2$, close to the exponent $q = 1$ of a 3D-lattice [38] and similar as the exponent found for the medium-sized particles ($q = 1.3$). The values of the percolation threshold f_c for the medium-sized and large particles are clearly above $= 0.16$ predicted for perfect spheres [29] and measured by Fredin *et al.* for aluminium nanoparticles (AlNPs) in polypropylene (PP) [41]. The polymer shells of the Au@PS hybrids isolate the particles, preventing the formation of conductive pathways.

The fit values for small particles of diameter 2.9 nm were with $q = 0.3$ and $f_c = 0.10$ smaller than the expected values for 3-D lattices and spheres. Polarization and relaxation seem to play an important role; these effects are not considered in the model of Efros and Shklovskii. They can be treated by models based on the Maxwell-Wagner-Sillars polarization (see below).

The discussions so far compared hybrids with constant Au core diameters and varying Au volume fractions but not hybrids with different core sizes. When a certain Au concentration is considered, the dielectric constant of the hybrids with smaller Au cores lay above the hybrids with larger particles: while $Au_{0.09}^{small}$@PS_{11000} with 2.9 nm cores has a dielectric constant of 6.7 at 10 kHz, it was only 4.8 for $Au_{0.10}^{medium}$@PS_{11000} with 4.6 nm cores at similar Au volume contents of 9 vol% and 10 vol%. Similarly, the dielectric constant for Au@PS_{11000} hybrids with 4.4 nm cores and 21 vol% Au content ($\varepsilon_r = 34.3$@10 kHz, from Table 5.1 in Chapter 5) is more than double than for $Au_{0.31}^{large}$@PS_{11000} with 8.2 nm cores and 31 vol% Au.

Decreasing Au core diameters increase the number density of particles at comparable Au volume fractions. This increases the number of microcapacitors formed between the Au particles and results in larger dielectric constants, consistently with the Efros-Shklovskii model. The Efros-Shklovskii model can be expanded to consider the polarization of interfaces between AuNPs. Maxwell-Wagner-Sillars (MWS) polarization occurs at the

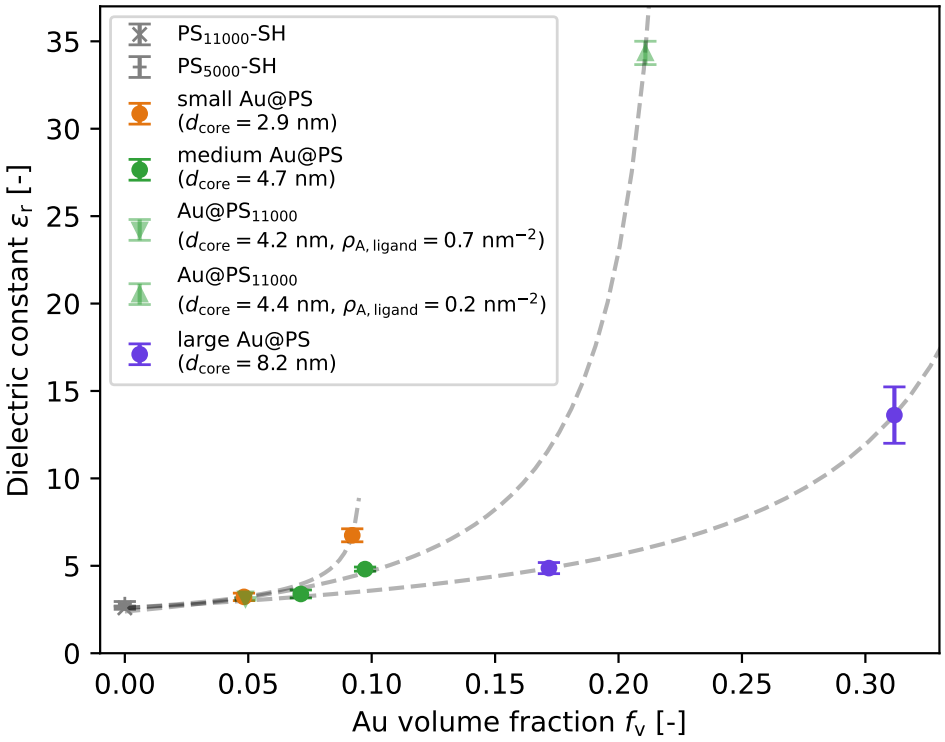

FIGURE 6.15: Dielectric constants at 10 kHz as a function of gold volume fractions from TGA. Reference data for $f_{v,Au} = 0$ was measured on pure PS_{11000}-SH layers (see Table 5.1 in Chapter 5), the dielectric constants for medium-sized particles with high and low ligand density were taken from the values of the samples $Au_{0.05}^{disordered}$@PS and $Au_{0.21}^{disordered}$@PS from Chapter 5. The dashed lines are fits to the percolation function as stated in Equation (2.16).

interface of the conductive Au phase and the insulating PS phase [27, 59, 60]. Larger specific interfaces in the dielectric thus increase the amount of shifted charges, polarization, and the dielectric constants.

Consider the specific interfacial area $a_{s,interface}$ of

$$a_{s,interface} = \frac{A_{interface}}{V_C} \tag{6.1}$$

by dividing the interfacial area $A_{interface}$ in the hybrid dielectric of the thin film capacitor by the thin film capacitor's volume V_C. The interfacial area in the hybrid dielectric of the thin film capacitor is

$$A_{interface} = N_{AuNP} A_{AuNP} = \frac{V_{Au}}{V_{AuNP}} A_{AuNP} = \frac{V_C f_{v,Au}}{V_{AuNP}} A_{AuNP} \tag{6.2}$$

with the number of the AuNP N_{AuNP}, the AuNP surface area $A_{AuNP} = 4\pi(\frac{d_{core}}{2})^2$, the volume of the Au fraction V_{Au}, the AuNP volume $V_{AuNP} = \frac{4}{3}\pi(\frac{d_{core}}{2})^3$, the volume of the thin film capacitor V_C, and the Au volume fraction f_v. The volume of the thin film

capacitors is

$$V_C = At \tag{6.3}$$

where $A = 0.79\,\mathrm{mm}^2$ is the area of the top contact and t the thickness of the respective dielectric layer. Figure 6.16 shows the measured dielectric constants at 10 kHz as a function of the hybrids' specific interfacial areas; Table 6.8 summarizes the dielectric constants at 10 kHz, the Au volume fractions, and the specific interfacial areas of Au@PS hybrids with varying core diameters.

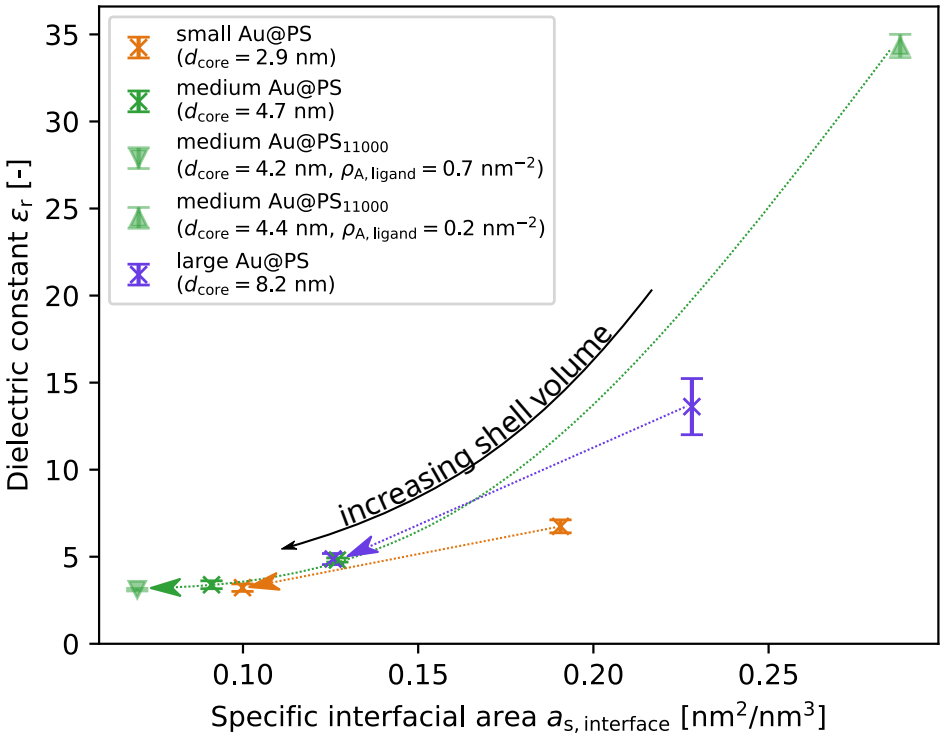

FIGURE 6.16: Dielectric constants at 10 kHz as a function of the calculated specific interfacial area in thin film capacitors with small, medium, and large AuNPs. The arrows indicate increasing shell volume and decreasing Au volume fraction at constant core diameters.

The Au volume fractions and the specific interfacial areas decrease with increasing shell volume, resulting in decreasing dielectric constants for all core sizes. The Au core size explicitly influences the interfacial areas: for instance, the interfacial surface area of $Au_{0.09}^{small}@PS_{11000}$ is $0.19\,\mathrm{nm}^2\,\mathrm{nm}^{-3}$ while it is only $0.13\,\mathrm{nm}^2\,\mathrm{nm}^{-3}$ for $Au_{0.10}^{medium}@PS_{11000}$ at similar Au volume fractions of about 10 vol%.

Figure 6.16 shows that the specific interfacial areas are strongly correlating with the dielectric constants. It is assumed that the specific interfacial area is the dominating parameter for the resulting dielectric constant in comparison to the Au volume fraction because MWS polarization takes place at the interfaces. For instance, due to smaller

TABLE 6.8: Overview of the dielectric constants ε_r at 10 kHz, the Au volume fractions f_v, and the specific interfacial areas $a_{s,interface}$ for Au@PS hybrids with different core sizes. Samples marked with * were shown as $Au_{0.05}^{disordered}$@PS and $Au_{0.21}^{disordered}$@PS in Chapter 5 (see Table 5.1).

Name	ε_r [−]	f_v [−]	$a_{s,interface}$ [$nm^2\,nm^{-3}$]
$Au_{0.05}^{small}$@PS_{5000}	3.2 ± 0.2	0.05	0.10
$Au_{0.09}^{small}$@PS_{11000}	6.7 ± 0.4	0.09	0.19
$Au_{0.07}^{medium}$@PS_{5000}	3.4 ± 0.2	0.07	0.09
$Au_{0.10}^{medium}$@PS_{11000}	4.8 ± 0.1	0.10	0.13
Au@PS_{11000} ($d_{core} = 4.2\,nm$, $\rho_{A,ligand} = 0.7\,nm^{-2}$)*	3.1 ± 0.1	0.05	0.07
Au@PS_{11000} ($d_{core} = 4.4\,nm$, $\rho_{A,ligand} = 0.2\,nm^{-2}$)*	34.3 ± 0.7	0.21	0.29
$Au_{0.17}^{large}$@PS_{5000}	4.9 ± 0.3	0.17	0.13
$Au_{0.31}^{large}$@PS_{11000}	13.6 ± 1.6	0.31	0.23

core sizes, $Au_{0.09}^{small}$@PS_{11000} has a by 50 % larger interfacial area than $Au_{0.10}^{medium}$@PS_{11000} without increasing the Au volume fraction and the dielectric constant increased by 40 % to $\varepsilon_r = 6.7$@10 kHz. $Au_{0.10}^{medium}$@PS_{11000} and $Au_{0.17}^{large}$@PS_{5000} have both the same specific interfacial area of $0.13\,nm^2\,nm^{-3}$ and about the same dielectric constant of $\varepsilon_r \approx 4.9$@10 kHz, even that the sample with large particles had a considerably larger Au volume fraction of 17 vol% in comparison to 10 vol%.

The Au volume fraction itself provides a minor contribution to the dielectric constant by an increased amount of mobile charges that can be accumulated at the interfaces. For instance, the Au volume fraction of $Au_{0.07}^{medium}$@PS_{5000} is 2 % larger than $Au_{0.05}^{small}$@PS_{5000} and compensated the 9 % reduced interfacial area of $Au_{0.07}^{medium}$@PS_{5000} than $Au_{0.05}^{small}$@PS_{5000} resulting in a similar dielectric constant of $\varepsilon_r \approx 3.3$@10 kHz for both samples. The MWS polarization at the interfacial areas is dominant and discussed in more detail in the following.

Fredin *et al.* successfully applied MWS polarization to describe the relaxation processes in AlNP/PP nanocomposites with Al volume contents up to 12.4 vol% in the frequency range from 1 MHz up to 7 GHz [41, 57]. Their model employed the Wagner model of dielectric composites considering conductive spheres in an insulating medium [62], which was later extended by Sillars [63]. These theories predict a peak of the dielectric loss at the relaxation frequency together with a drop in the dielectric constant, mostly in the MHz range. Fredin *et al.* argued in their MWS model that conductive particles come close at increased metal volume fractions and behave like single "joint particles" [57]. These joint particles can either form in chain-like structures leading to "prolate aggregates" or they can form planar "oblate aggregates" [57]. In both cases, the MWS polarization is enhanced: elongated joint particles consist of particles aligned along an axis and have longer single dipole moments; prolate aggregates consist of particles in

planar arrangement and have increased interfacial areas where charges accumulate during polarization, especially when the axis perpendicular to the plane is aligned along the electric field [57]. The model was used by Fredin *et al.* to explain the shift of the relaxation frequency for AlNP/PP composites with 12.4 vol% Al towards lower frequencies [57]. In the following, we use the MWS model of Fredin *et al.* in combination with the model of Efros and Shklovskii [38] based on networks of RC elements [37] to rationalize the dielectric properties of Au@PS hybrids.

Figure 6.14b,d shows the dielectric losses of Au@PS hybrids that can be used to determine dielectric relaxations. For all samples except $Au_{0.09}^{small}@PS_{11000}$, the minimum of the dielectric losses was between 0.01 and 0.06 and was measured at frequencies between 1 kHz ($Au_{0.07}^{medium}@PS_{5000}$) and 61 kHz ($Au_{0.10}^{medium}@PS_{11000}$). The increase of dielectric losses towards 1 MHz accompanied by a decrease of the dielectric constant may be caused by the onset of a MWS relaxation. Such a relaxation around 1 MHz was reported for AlNP/PP composites by Fredin *et al.* [57]. Matavž *et al.* argued that limited conduction of the electrodes can cause an additional decrease of the dielectric constant connected with an increase of the dielectric loss at high frequencies [6]. The sputtered Al bottom electrodes show a considerable contact resistivity due to an intrinsic oxidation layer (see Chapter 4, Section 4.2.2) that may contribute to the dielectric loss at high frequencies. Another increase of the dielectric loss to values in the range from 0.3 to 30 observed towards 1 Hz for all core sizes was not connected with a decrease of the dielectric constant and could be due to losses at the interface of the electrodes and the hybrids.

The minimum of the dielectric loss did not always increase with increasing dielectric constants: for instance, $Au_{0.31}^{large}@PS_{11000}$ hybrids had a larger dielectric constant than $Au_{0.10}^{medium}@PS_{11000}$, while the minimum of the dielectric loss was only at 0.04 for $Au_{0.31}^{large}@PS_{11000}$ and was 0.06 for $Au_{0.10}^{medium}@PS_{11000}$. This can be explained by the core size effect: while the specific interfacial area of $Au_{0.31}^{large}@PS_{11000}$ hybrids was only 20 % larger than $Au_{0.10}^{medium}@PS_{11000}$, the Au volume fraction tripled. The increased charge accumulated during MWS polarization causes an increase of the dielectric constant that is more strongly pronounced than the increase of the interfacial area between AuNPs and the PS shells, where MWS relaxations contribute to the dielectric loss.

A special case in the measured dielectric loss is the sample $Au_{0.09}^{small}@PS_{11000}$, where a maximum of the dielectric loss at about 100 Hz coincided with a strong decrease of the dielectric constant from $\varepsilon_r = 98.3$ at 1 Hz to $\varepsilon_r = 10.8$ at 1 kHz. This combination indicates a MWS relaxation process that was not observed in this frequency range for the other samples. Following Fredin *et al.*, it is suggested that lowering the relaxation frequency is connected with an increase of the effective size of "joint particles", which

increases both the number of reorganized charges during polarization in the oscillating field and the necessary reorganization time [57]. For the ink $Au_{0.09}^{small}@PS_{11000}$, large particles that grew after ligand exchange were found and it is presumed that these grown particles behave like large "joint particles" in the MWS model of Fredin *et al.*. Hence, the peak of the dielectric loss and the strong drop of the dielectric constant around the frequency 100 Hz is probably connected to the presence of large particles from ligand exchange (see Figure 6.9b) that cause a dielectric relaxation at this low frequency. This growth of particles during ligand exchange was not observed for the other samples and no maximum of the dielectric loss at about 100 Hz was observed for these samples.

Figure 6.17 and Figure 6.18 show two different kind of aged hybrids with small (d_{core} = 2.9 nm) and large (d_{core} = 8.2 nm) Au@PS particles. Samples were prepared after ink ageing of about 5 months (triangles) and measurements were performed on aged films about 6 months after preparation (squares) (storage in vessels at 20 °C in the laboratory).

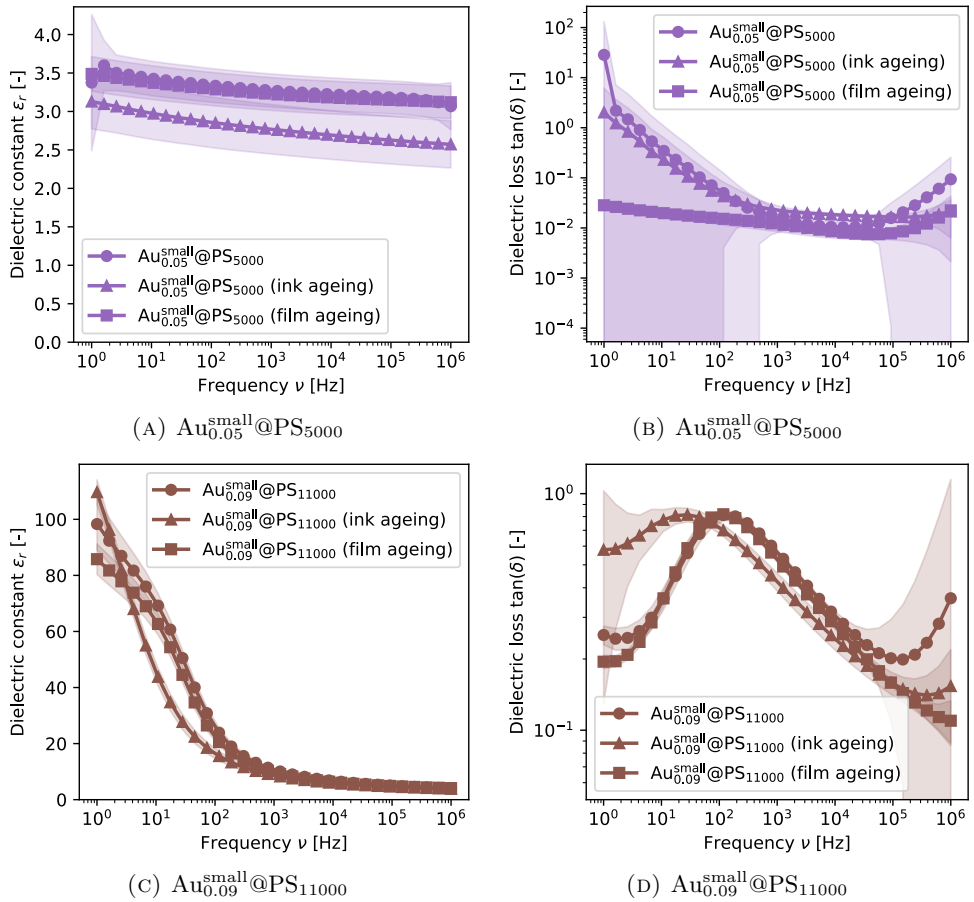

(A) $Au_{0.05}^{small}@PS_{5000}$ (B) $Au_{0.05}^{small}@PS_{5000}$

(C) $Au_{0.09}^{small}@PS_{11000}$ (D) $Au_{0.09}^{small}@PS_{11000}$

FIGURE 6.17: Dielectric constant and dielectric loss of Au@PS hybrids with small Au core size for freshly prepared samples with freshly synthesized ink (circles) in comparison to aged samples. Ink ageing (triangles) was investigated on samples that were prepared with inks with shelf life of about 5 months, film ageing (squares) was investigated on samples that had been stored for about 6 months.

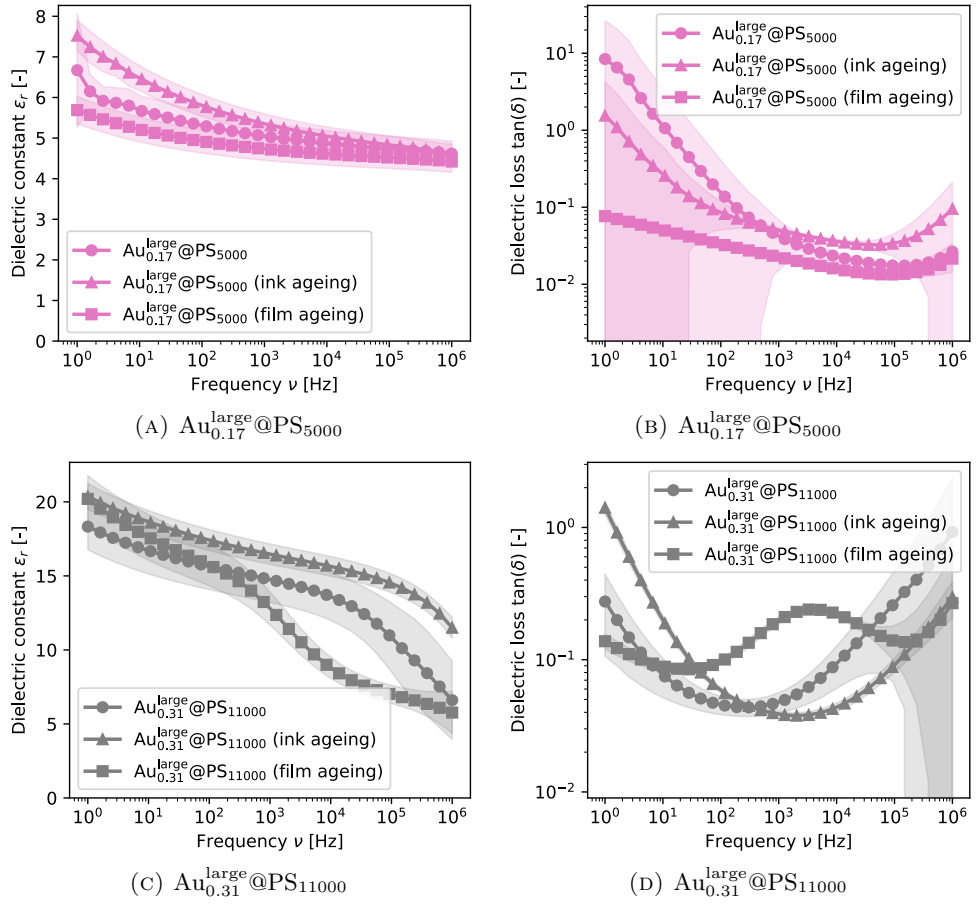

(A) $Au_{0.17}^{large}$@PS_{5000} (B) $Au_{0.17}^{large}$@PS_{5000}

(C) $Au_{0.31}^{large}$@PS_{11000} (D) $Au_{0.31}^{large}$@PS_{11000}

FIGURE 6.18: Dielectric constant and dielectric loss of Au@PS hybrids with large Au core size for freshly prepared samples with freshly synthesized ink (circles) in comparison to aged samples. Ink ageing (triangles) was investigated on samples that were prepared with inks with shelf life of about 5 months, film ageing (squares) was investigated on samples that had been stored for about 6 months.

The inks with large 8.2 nm Au cores and medium-sized 4.7 nm Au cores and the ink with small 2.9 nm Au cores and PS_{5000} were stable and the samples $Au_{0.05}^{small}$@PS_{5000}, $Au_{0.17}^{large}$@PS_{5000}, and $Au_{0.31}^{large}$@PS_{11000} prepared with aged inks did not deviate from samples prepared with freshly synthesized inks in the dielectric properties. Au cores in the ink $Au_{0.09}^{small}$@PS_{11000} grew during ageing, which increased the specific interfacial surface area and amount of reorganized charge and should reduce the relaxation frequency for this sample. A reduction of the relaxation frequency, a drop of the dielectric constant, and a peak in the dielectric loss is indeed seen for the hybrids prepared with the aged $Au_{0.09}^{small}$@PS_{11000} ink at 20 Hz (Figure 6.17c,d), while the relaxation was seen at about 100 Hz for $Au_{0.09}^{small}$@PS_{11000} hybrids prepared with freshly synthesized $Au_{0.09}^{small}$@PS_{11000} ink (see above).

Film ageing experiments can give insights into possible particle densification via the dielectric results. Film densification is characterized by an approaching of the gold cores, which is accompanied by a phase separation process. The approaching of the

cores is driven by Van-der-Waals forces and hindered by the steric repulsion of the polymer ligands in the insulating shells. Therefore, the strongest densification effect is expected for $Au_{0.31}^{large}@PS_{11000}$, where large Au cores are combined with the less dense PS_{11000} shells and the largest Au volume fraction of 31 vol% was measured. Indeed, while the dielectric properties of aged films of all other samples did not deviate from the freshly prepared films, the aged $Au_{0.31}^{large}@PS_{11000}$ film evolved a new peak in the dielectric loss connected with a drop of the dielectric constant near the frequency 4 kHz (Figure 6.18c,d). Particle densification and the connected decrease in tunnelling barriers between close particles due to phase separation possibly caused the newly evolved relaxation in the aged $Au_{0.31}^{large}@PS_{11000}$ film. Similar densification in the particle packing of layers made up of conductive Au@PEDOT:PSS particles [3] was observed by scanning electron microscopy (SEM) cross sections of particle films after pressing that led to increased conductivity of the AuNP films [216]. Furthermore, an increase in conductivity was also seen for Au@PEDOT:PSS particle layers that experienced ageing for 1 year and it is assumed that this improved conductivity was also caused by decreased AuNP spacing due to enhanced particle packing density [216].

6.3.2 Dielectric strength

The dielectric strength of Au@PS hybrids with small 2.9 nm and large 8.2 nm particles was measured by slowly increasing DC bias until a non-linear increase of the current at the breakdown voltage V_{bd} was observed (see Figure 6.19). The resulting breakdown strengths E_{bd} (average of two measurements) were calculated with Equation (3.26) and found to be in the range of 71.1 MV m^{-1} to 158.7 MV m^{-1} and are similar to these of Au@PS hybrids with medium core size particles taken from Table 5.9 in Chapter 5. The dielectric breakdown strengths with varying core sizes are listed in Table 6.9. There was no sign of decreased breakdown strength at larger Au volume fractions. The covalently attached PS shells ensure electric insulation of the hybrid nanoparticles and prevent the creation of a conductive pathway, with breakthrough voltages around 71.1 MV m^{-1} to 158.7 MV m^{-1} even for large 8.2 nm particles with Au volume fractions of up to 31 vol%.

The density of the shells influenced the breakdown strengths that remained below 71.1 MV m^{-1} for PS_{11000}, but exceeded 100.9 MV m^{-1} for PS_{5000} shells. Therefore, the PS_{5000} shells with the higher ligand densities seem to enable higher dielectric strengths, especially with values above 150 MV m^{-1} for $Au_{0.07}^{medium}@PS_{5000}$ and $Au_{0.17}^{large}@PS_{5000}$ hybrids, where an ordered particle packing was found. Regular particle spacings may reduce locally enhanced fields, which occur when interparticle distance is low and thus provoke dielectric breakdown. The effect of the polymer shell appears dominant in dielectric breakdown.

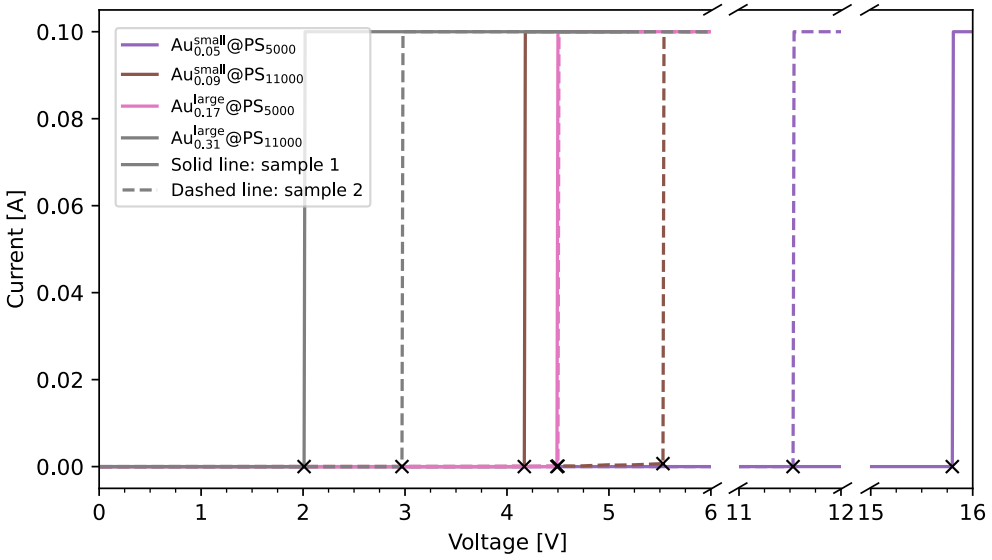

FIGURE 6.19: Dielectric breakthrough for dielectric layers with small and large gold cores.

TABLE 6.9: Estimated breakdown strengths E_{bd} of the dielectric films with Au cores of various sizes. The mean value of two measurements is reported.

Name of sample	E_{bd} [MV m^{-1}]
$Au^{small}_{0.05}$@PS$_{5000}$	100.9
$Au^{small}_{0.09}$@PS$_{11000}$	71.1
$Au^{medium}_{0.07}$@PS$_{5000}$	154.3
$Au^{medium}_{0.10}$@PS$_{11000}$	59.9
$Au^{large}_{0.17}$@PS$_{5000}$	158.7
$Au^{large}_{0.31}$@PS$_{11000}$	71.1

6.3.3 Conclusion

Au core sizes were found to affect dielectric properties of Au@PS hybrids mainly via the specific interfacial areas between AuNPs and the PS shells. At larger interfacial areas, the MWS polarization is enhanced leading to increased dielectric constants. For instance, the interfacial area increased by a factor of 1.5 from $Au^{medium}_{0.10}$@PS$_{11000}$ to $Au^{small}_{0.09}$@PS$_{11000}$ at comparable Au volume fractions and the dielectric constant increased by 40 % to $\varepsilon_r = 6.7$@10 kHz.

Ligand exchange and further ageing caused a growth of the Au cores for $Au^{small}_{0.09}$@PS$_{11000}$ and a possible densification of the particle packing in films of $Au^{large}_{0.31}$@PS$_{11000}$. It is proposed that increased particle sizes or very close "joint particles" decrease the frequency for dielectric relaxation because larger amount of charge has to reorganize in the oscillating electric field during polarization [57]. This caused the appearance of additional

dielectric relaxation for the $Au_{0.09}^{small}@PS_{11000}$ hybrids at around 100 Hz and for the aged film of $Au_{0.31}^{large}@PS_{11000}$ at around 4 kHz, being identified by peaks in the dielectric losses connected with a decrease of the dielectric constants.

The polymer shells dominate the breakdown strength of Au@PS hybrids. Higher dielectric breakthrough voltages were measured for hybrids with PS_{5000} with denser polymer shells; ordered particle packing was observed for layers of $Au_{0.07}^{medium}@PS_{5000}$ and $Au_{0.17}^{large}@PS_{5000}$ that probably decreases locally enhanced electric fields between neighbouring particles with low interparticle distance.

6.4 Inkjet printed dielectric layers on flexible PET substrates

Au@PS hybrids are promising materials for inkjet printed samples on flexible substrates. The ink $Au_{0.10}^{medium}@PS_{11000}$ was used to inkjet print dielectric layers on aluminium coated PET substrates and to test the flexibility of the samples in bending tests. Gold top contacts with diameters of 1 mm were evaporated to form thin film capacitors. An optical micrograph and WLI surface profile of the inkjet printed sample on PET in Figure 6.20a,b show the overlapping structure of the dried ink droplets on the substrate that form an insulating layer. The second layer printed perpendicular to the first layer is clearly seen. The surface roughness determined from the WLI surface profile over an area of 700 µm x 530 µm was $R_a = 110.9$ nm.

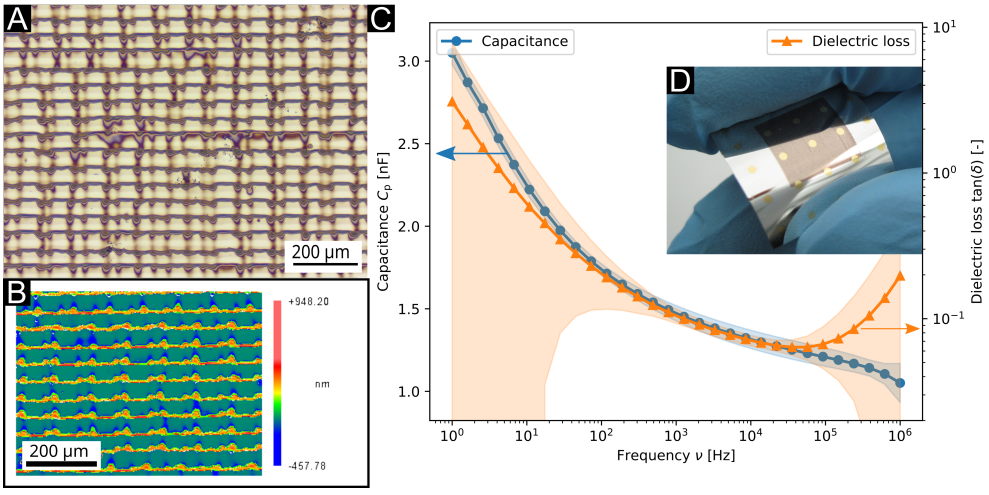

FIGURE 6.20: Flexible thin film capacitors on aluminium coated PET substrate and inkjet printed film $Au_{0.10}^{medium}@PS_{11000}$. a) Optical micrograph and b) WLI surface profile of the film structure that was printed in two passes with 500 DPI resolution. c) Dielectric properties of the flexible thin film capacitors. d) The inset shows a photograph of the flexible thin film capacitor device.

The capacitance of the flexible thin film capacitors was (1.30 ± 0.06) nF over an area of $0.79\,\mathrm{mm}^2$ with a dielectric loss of (0.071 ± 0.006) at 10 kHz. The development of the capacitance and dielectric loss was similar to the spin coated samples; both values increased towards decreasing frequencies.

The absolute capacitance of the inkjet printed thin film capacitors are reported as it proofed difficult to obtain FIB cuts on the insulating PET substrate to create TEM samples and measure the layer thickness. Equation (3.22) and the measured dielectric constant of the spin coated $\mathrm{Au}_{0.10}^{\mathrm{medium}}@\mathrm{PS}_{11000}$ samples ($\varepsilon_\mathrm{r} = 4.8 \pm 0.1$ at 10 kHz) allowed to estimate an effective thickness of ≈ 25 nm, slightly above that of the inkjet printed layers on Al coated silicon (thickness was (16.7 ± 9.8) nm, see Table 5.1).

An inkjet printed sample was taped on a PET foil and bent from the relaxed state to a maximum bending radius of ≈ 8 mm in a bending machine (see Figure 6.21b) over 3500 bending cycles. After a set of 500 bending cycles, the sample was removed and the dielectric properties were measured. Figure 6.21a shows the dielectric constant and the dielectric loss at 10 kHz and the yield of the functional thin film capacitors in dependence on the bending cycles. The capacitance at 10 kHz dropped from 1.3 nF to 1.2 nF after the first 500 bending cycles and stayed constant until 3500 bending cycles. A plausible explanation is nanoparticle rearrangement and phase separation in these first bending cycles, similarly as the ageing with possible film densification and phase separation of the solid $\mathrm{Au}_{0.31}^{\mathrm{large}}@\mathrm{PS}_{11000}$ sample. Such densification of the particle packing was assumed for Au@PEDOT:PSS films, where an increase of conductivity was observed after bending of the films [216]. 20 % of the thin film capacitors failed after 2000 bending cycles but the yield then stayed constant. The capacitors did not fail in the dielectric layer according SEM images (see Figure 6.22b,c). The sequential contacting and measuring of the samples caused damage on the Au top contacts (see Figure 6.22a) and could cause short circuits and failure. Since the SEM images show only small sections of the bent sample, a detailed study of the failure mechanism would require more extensive statistical data.

The results show that the good film formation of the Au@PS hybrid ink with covalently attached polystyrene ligands allows the fabrication of flexible samples on PET foil. The flexible thin film capacitors were functional over up to 3500 bending cycles.

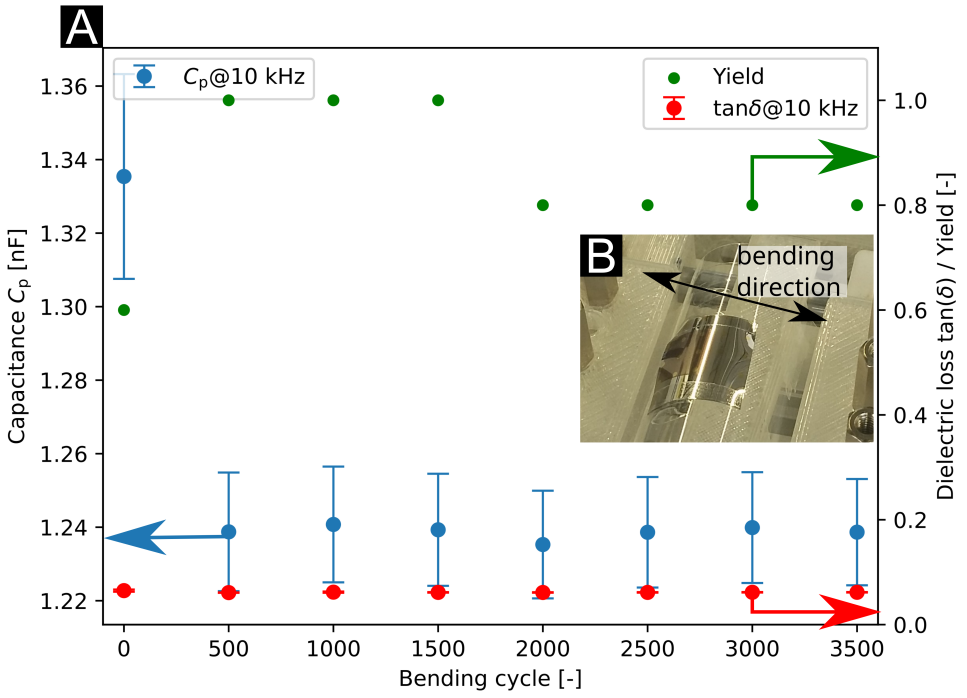

FIGURE 6.21: Bending study of flexible thin film capacitors on aluminium coated PET foil with inkjet printed $Au_{0.10}^{medium}$@PS_{11000} dielectric layer. a) Dielectric constant, dielectric loss, and yield of functional thin film capacitors on the sample measured after sets of 500 bending cycles until up to 3500 bending cycles. b) The inset shows a photograph of the sample in the bending machine.

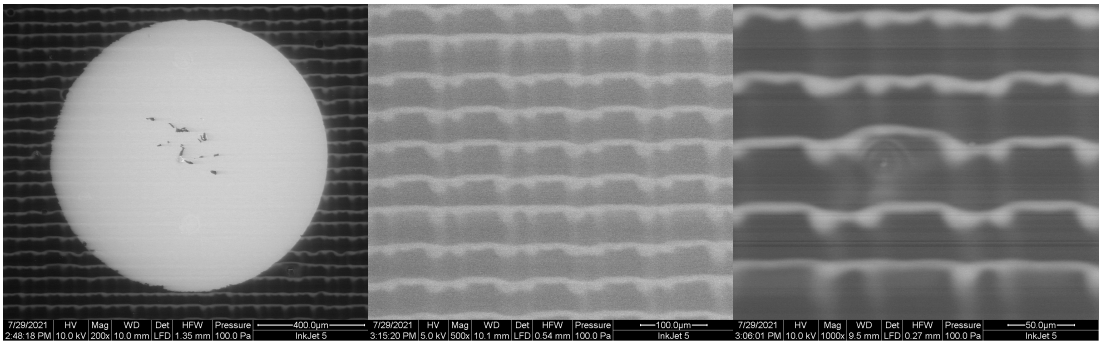

(A) (B) (C)

FIGURE 6.22: SEM micrographs of the inkjet printed $Au_{0.10}^{medium}$@PS_{11000} film after bending. a) The contacts showed damage from sequential contacting with the contact pins. b) Low magnification and c) high magnification micrographs of the film structure revealed no damage after bending.

6.5 Conclusions

The effect of the core size on the properties of Au@PS hybrids was investigated. To this end, inks with Au core diameters of 2.9 nm, 4.7 nm, and 8.2 nm were synthesized and the inks were processed to dielectric films via spin coating and inkjet printing. The shell density of the prepared Au@PS core-shell particles depended on the Au core size and increased for large 8.2 nm Au@PS NPs in comparison to medium-sized 4.7 nm Au@PS NPs due to reduced curvature; for small 2.9 nm Au@PS NPs the ligand densities were by 0.1 nm^{-2} decreased in comparison to medium-sized 4.7 nm particles. The grafting density for PS_{5000} was higher than for PS_{11000} for all core sizes. Thin layers with thicknesses of only up to 16 nm could be fabricated and the insulating polymer shells allowed Au volume fractions in the range of 5 vol% to 31 vol% while preventing conductive pathways.

A core size effect on the dielectric constant was observed. The dielectric constant rose with reduced core sizes at comparable Au volume fractions, e.g. $Au_{0.09}^{small}@PS_{11000}$ had 40 % larger dielectric constant than $Au_{0.10}^{medium}@PS_{11000}$ with comparable Au volume fractions. The dielectric behaviour of Au@PS hybrids was rationalized using the combination of a resistor-capacitor network with the Maxwell-Wagner-Sillars (MWS) model. A decrease of core sizes at constant Au volume fractions led qualitatively to an increase of the number of microcapacitors in the hybrid. This effect was quantified via the specific interfacial area where the MWS polarization occurs. It was found that increasing specific interfacial areas correlated with increasing dielectric constants. The contribution of the increasing specific interfacial areas to increase of the dielectric constants of Au@PS hybrids is presumed to dominate compared to the contribution of the increased Au volume fractions.

Ageing of Au@PS hybrids can take place either in the liquid ink by core degradation or particle agglomeration or in the layer by phase separation. The growth of larger Au cores was observed for the ink $Au_{0.09}^{small}@PS_{11000}$ after ligand exchange and during ageing; ageing of solid $Au_{0.31}^{large}@PS_{11000}$ films occurred probably due to film densification. For these samples, MWS relaxations were observed between 20 Hz and 4 kHz, which were accompanied by a peak in dielectric loss and a decrease in dielectric constant.

The dielectric breakdown strengths of the Au@PS hybrids were in the range 71.1 MV m^{-1} to 158.7 MV m^{-1} and were dominated by the polymer shells. The highest breakdown strengths were measured for $Au_{0.07}^{medium}@PS_{5000}$ and $Au_{0.17}^{large}@PS_{5000}$, where ordered particle packing reduced the local enhancement of the electric field between nearby particles.

The wide tuneability of the dielectric properties of Au@PS hybrids via Au volume fraction and Au particle size makes them interesting for applications in printed electronics. Flexible thin film capacitors on aluminium coated PET foil could be fabricated by inkjet

printing of $Au_{0.10}^{medium}@PS_{11000}$ particles without post treatment of the dielectric. The capacitors showed a capacitance of $(1.30 \pm 0.06)\,nF$ over an area of $0.79\,mm^2$, which indicates an effective layer thickness of about 25 nm. The sample could be bent 3500 times over a radius of $\approx 8\,mm$ while maintaining its functionality. The Au@PS hybrid dielectric layers therefore showed capable of potential application in flexible electronics.

Chapter 7

Conclusion

This thesis reports a new concept for a hybrid dielectric ink based on molecularly insulated Au@PS nanoparticles and its deposition as dielectric layers. The concept enabled high Au volume fractions while preventing conductive pathways, differently to classical nanocomposites with conductive particles simply mixed into an insulating polymer matrix. Gold nanoparticles capped with oleylamine (OAm) were synthesized via reduction of gold acid in organic solvent. The OAm ligand was exchanged by thiol-functionalized polystyrene in a grafting-to approach. The synthesis protocol allowed the variation of the diameter of the Au core, which was varied in the range of 2.9 nm to 8.2 nm, the lengths of the polymer ligand (PS_{5000}-SH with 5000 Da molecular weight and PS_{11000}-SH with 11 000 Da molecular weight in this thesis), and the grafting density.

The synthesized Au@PS hybrid particle inks were thoroughly analyzed. TGA provided the Au weight content which was used to determine the Au volume fractions in the dried Au@PS layers and the grafting densities of the polymer ligand. SAXS and TEM determined the size distributions of the Au cores in the synthesized inks. The grafting density depended on the conditions during ligand exchange, and DLS showed that the thiol-functionalized PS coiled at temperatures above 45 °C in the used solvent toluene. Therefore, ligand exchange at 60 °C led to lower ligand densities of the Au@PS particles and increased Au volume fractions in the layers in comparison to particles where the ligand exchange was performed at 20 °C.

Thin film capacitors were prepared on rigid and flexible substrates, where the dielectric layer was prepared via spin coating or inkjet printing. The bottom electrode of the thin film capacitors was aluminium coated silicon (for rigid samples) or aluminium coated PET foil (for flexible samples); the top electrodes were evaporated Au. The dielectric layers were investigated by impedance spectroscopy, TEM cross sections, and dielectric breakdown estimation. The results indicated that the covalently attached polymer shells effectively prevented the formation of agglomerates in the ink and in the dielectric. The

metal cores increased the dielectric constant up to about ten times in the frequency range 1 Hz to 1×10^6 Hz in comparison to pure polystyrene layers. The breakdown strength of the Au@PS layers was found to be above 39.1 MV m^{-1}, indicating the reliable insulation of the Au cores by the covalently attached polymer. Surface profiles of the layers were created with WLI and AFM. Spin coated layers were much smoother than inkjet printed layers due to the different processing methods. Flexible thin film capacitors with an inkjet printed Au@PS dielectric layer on an aluminium coated PET foil substrate maintained the functionality over 3500 bending cycles.

The dielectric constants of the Au@PS layers mainly depended on Au core size and Au volume fraction but not on the particle arrangement. The non-linear increase of the dielectric constant with increasing Au volume fraction within a certain particle size could be described by the percolation equation, based on a model of a resistor-capacitor network [37, 38] with percolation thresholds above the value expected for perfect spheres. The covalently attached polymers form an effective insulating shell that exceeds random percolation. At low frequencies, fitting the experimental data to the percolation equation did not lead to reasonable results, because interfacial polarization and relaxations have to be considered, which are not considered in the resistor-capacitor network model. The highest dielectric constant measured at the frequency 10 kHz was 34.3 and seen for the sample $Au_{0.21}^{disordered}$@PS with Au cores of the diameter $d_{core} = 4.4$ nm, PS_{11000}-SH in the organic shell, and 21 vol% Au.

When core sizes were compared, larger dielectric constants were found for hybrids with smaller core sizes at comparable Au volume fractions. In the resistor-capacitor model, this is explained by an increase of the number of microcapacitors forming between the nanoparticles and resulting in larger dielectric constants. The Maxwell-Wagner-Sillars (MWS) model was used to describe the MWS polarization taking place at the interfacial areas between Au and polystyrene, which is defined both by the Au core size and the Au volume fraction. Increasing specific interfacial areas are seen as the dominant contribution for the increase of the dielectric constant in Au@PS hybrids, while the increase of Au volume fraction without increase of specific interfacial areas only provides a minor contribution. For all dielectric layers, the dielectric losses were seen to increase towards the highest measured frequencies around 1 MHz and it was assumed that the Au@PS layers experience the onset of a MWS relaxation towards the frequency 1 MHz.

Most inks studied in this thesis exhibited good stability during ligand exchange and over time, only inks with particle diameters of $d_{core} = 2.9$ nm and a PS_{11000} ligand shell with low grafting density grew during the ligand exchange process at 60 °C and during ageing of the ink at room temperature within the observed time range of at least 4 months. Samples with these 2.9 nm particles and PS_{11000} shells exhibited additional relaxations

with peaks in the dielectric losses and decrease of the dielectric constant in frequencies around 100 Hz that were connected with the presence of grown particles. A similar relaxation appeared around 4 kHz for aged films containing large particles with diameters of $d_{\mathrm{core}} = 8.2\,\mathrm{nm}$ and the PS_{11000} ligand shell with low grafting density, which was connected to the probable densification of the film and the formation of "joint particles" [57]. Low ligand densities are seen as a reason for the particle growth or densification of dry films. Future studies could investigate how the stability of Au@PS hybrid inks and hybrid layers can be improved and which parameters are most important for good stability. More insights into the influences of the material composition on the dielectric properties could be achieved by the development of more elaborated models considering nanoscale electron dynamics, electrical network theory, and frequency dependent polarization mechanisms.

The Au@PS hybrid inks presented in this thesis are suitable for application as dielectric layers in flexible and printed electronics. In future studies, completely inkjet printed devices such as capacitors with printed electrodes and printed dielectric layers could be developed. The hybrid concept with insulated conductive particles allowed an increase of the dielectric constant. Besides, the usage of the Au@PS nanoparticles with core diameters below 10 nm enabled the fabrication of very thin but still insulating layers with several tenths of nm thickness and allowed the fabrication of thin film capacitors with a high absolute capacitance, which were compatible with flexible PET substrates. This thesis can form the starting point for the development of hybrid dielectric inks with conductive cores of less costly metals than Au that still allow high dielectric constants and the sinter-free application in printed electronics. Hybrid dielectric films could be used as sensitive chemical sensors when solvent vapours selectively swell polymer shells, changing the interparticle distances and dielectric constants. Hybrid dielectric inks could also find possible application in soft robotics, where dielectric layers with high dielectric constants and mechanical flexibility could improve the performance of functional elements such as capacitors, actuators, or thin film transistors in comparison to classical polymer dielectrics or conventional oxide particle dielectric nanocomposites, which are not easily printable as very thin films with high filler levels. Furthermore, future work could investigate whether the plasmon coupling between the Au cores can be altered by the applied voltage to the layers and whether layers of the here presented Au@PS hybrids could possibly serve as electro-optical modulators.

Bibliography

[1] Roman Buchheit, Björn Kuttich, Lola González-García, and Tobias Kraus. Hybrid Dielectric Films of Inkjet-Printable Core-Shell Nanoparticles. *Advanced Materials*, 33(41):2103087, 2021.

[2] Jenny Wiklund, Alp Karakoç, Toni Palko, Hüseyin Yiğitler, Kalle Ruttik, Riku Jäntti, and Jouni Paltakari. A Review on Printed Electronics: Fabrication Methods, Inks, Substrates, Applications and Environmental Impacts. *Journal of Manufacturing and Materials Processing*, 5(3):89, 2021.

[3] Dong Jin Kang, Yvonne Jüttke, Lola González-García, Alberto Escudero, Marcel Haft, and Tobias Kraus. Reversible Conductive Inkjet Printing of Healable and Recyclable Electrodes on Cardboard and Paper. *Small*, 16(25):2000928, 2020.

[4] Habeom Lee, Sukjoon Hong, Jinhwan Lee, Young Duk Suh, Jinhyeong Kwon, Hyunjin Moon, Hyeonseok Kim, Junyeob Yeo, and Seung Hwan Ko. Highly Stretchable and Transparent Supercapacitor by Ag-Au Core-Shell Nanowire Network with High Electrochemical Stability. *ACS Applied Materials & Interfaces*, 8 (24):15449–15458, 2016.

[5] Fan Zhang, Christopher Tuck, Richard Hague, Yinfeng He, Ehab Saleh, You Li, Craig Sturgess, and Ricky Wildman. Inkjet printing of polyimide insulators for the 3D printing of dielectric materials for microelectronic applications. *Journal of Applied Polymer Science*, 133(18):43361, 2016.

[6] A. Matavž, B. Malič, and V. Bobnar. Inkjet printing of metal-oxide-based transparent thin-film capacitors. *Journal of Applied Physics*, 122(21):214102, 2017.

[7] Cheng-Lin Cho, Hsuan-ling Kao, Yung-Hsien Wu, Li-Chun Chang, and Chun-Hu Cheng. Direct Fabrication of Inkjet-Printed Dielectric Film for Metal–Insulator–Metal Capacitors. *Journal of Electronic Materials*, 47(1):677–683, 2018.

[8] Morten Mikolajek, Timo Reinheimer, Nicole Bohn, Christian Kohler, Michael J. Hoffmann, and Joachim R. Binder. Fabrication and Characterization of Fully Inkjet Printed Capacitors Based on Ceramic/Polymer Composite Dielectrics on Flexible Substrates. *Scientific Reports*, 9(1):13324, 2019.

[9] Robyn Worsley, Lorenzo Pimpolari, Daryl McManus, Ning Ge, Robert Ionescu, Jarrid A. Wittkopf, Adriana Alieva, Giovanni Basso, Massimo Macucci, Giuseppe

Iannaccone, Kostya S. Novoselov, Helen Holder, Gianluca Fiori, and Cinzia Casiraghi. All-2D Material Inkjet-Printed Capacitors: Toward Fully Printed Integrated Circuits. *ACS Nano*, 13(1):54–60, 2019.

[10] Timo Reinheimer, Raheleh Azmi, and Joachim R. Binder. Polymerizable Ceramic Ink System for Thin Inkjet-Printed Dielectric Layers. *ACS Applied Materials & Interfaces*, 12(2):2974–2982, 2020.

[11] Johannes H. M. Maurer, Lola González-García, Indra K. Backes, Beate Reiser, Sarah M. Schlossberg, and Tobias Kraus. Direct Nanoimprinting of a Colloidal Self-Organizing Nanowire Ink for Flexible, Transparent Electrodes. *Advanced Materials Technologies*, 2(6):1700034, 2017.

[12] Thomas Kister, Johannes H. M. Maurer, Lola González-García, and Tobias Kraus. Ligand-Dependent Nanoparticle Assembly and Its Impact on the Printing of Transparent Electrodes. *ACS Applied Materials & Interfaces*, pages 6079–6083, 2018.

[13] Garret McKerricher, Robert Maller, Vaseem Mohammad, Martyn A. McLachlan, and Atif Shamim. Inkjet-printed thin film radio-frequency capacitors based on sol-gel derived alumina dielectric ink. *Ceramics International*, 43(13):9846–9853, 2017.

[14] David Pech, Magali Brunet, Pierre-Louis Taberna, Patrice Simon, Norbert Fabre, Fabien Mesnilgrente, Véronique Conédéra, and Hugo Durou. Elaboration of a microstructured inkjet-printed carbon electrochemical capacitor. *Journal of Power Sources*, 195(4):1266–1269, 2010.

[15] H. Nesser, J. Grisolia, T. Alnasser, B. Viallet, and L. Ressier. Towards wireless highly sensitive capacitive strain sensors based on gold colloidal nanoparticles. *Nanoscale*, 10(22):10479–10487, 2018.

[16] Jooho Moon and Keunkyu Song. Inkjet Printing of Metal Oxide Thin-Film Transistors. In Jan G. Korvink, Patrick J. Smith, and Dong-Youn Shin, editors, *Inkjet-based Micromanufacturing*, Advanced micro & nanosystems, pages 237–255. Wiley-VCH, Weinheim, 2012. ISBN 1283596954.

[17] Sheida Faraji, Teruo Hashimoto, Michael L. Turner, and Leszek A. Majewski. Solution-processed nanocomposite dielectrics for low voltage operated OFETs. *Organic Electronics*, 17:178–183, 2015.

[18] Seungbeom Choi, Kyung-Tae Kim, Sung Kyu Park, and Yong-Hoon Kim. High-Mobility Inkjet-Printed Indium-Gallium-Zinc-Oxide Thin-Film Transistors Using Sr-Doped Al_2O_3 Gate Dielectric. *Materials*, 12(6), 2019.

[19] Yuzhi Li, Linfeng Lan, Shiben Hu, Peixiong Gao, Xingqiang Dai, Penghui He, Xifeng Li, and Junbiao Peng. Fully Printed Top-Gate Metal–Oxide Thin-Film Transistors Based on Scandium-Zirconium-Oxide Dielectric. *IEEE Transactions on Electron Devices*, 66(1):445–450, 2019.

[20] Siting Chen, Yuzhi Li, Yilong Lin, Penghui He, Teng Long, Caihao Deng, Zhuo Chen, Geshuang Chen, Hong Tao, Linfeng Lan, and Junbiao Peng. Inkjet-Printed Top-Gate Thin-Film Transistors Based on InGaSnO Semiconductor Layer with Improved Etching Resistance. *Coatings*, 10(4):425, 2020.

[21] Hanna Haverinen and Ghassan E. Jabbour. Application of Inkjet Printing in High-Density Pixelated RGB Quantum Dot-Hybrid LEDs. In Jan G. Korvink, Patrick J. Smith, and Dong-Youn Shin, editors, *Inkjet-based Micromanufacturing*, Advanced micro & nanosystems, pages 217–236. Wiley-VCH, Weinheim, 2012. ISBN 1283596954.

[22] Heather A. S. Platt and Maikel F. A. M. van Hest. Photovoltaics. In Jan G. Korvink, Patrick J. Smith, and Dong-Youn Shin, editors, *Inkjet-based Micromanufacturing*, Advanced micro & nanosystems, pages 279–294. Wiley-VCH, Weinheim, 2012. ISBN 1283596954.

[23] Arshad Khan, Joan Sol Roo, Tobias Kraus, and Jürgen Steimle. Soft Inkjet Circuits. In François Guimbretière, editor, *Proceedings of the 32nd Annual ACM Symposium on User Interface Software and Technology*, ACM Digital Library, pages 341–354, New York,NY,United States, 2019. Association for Computing Machinery. ISBN 9781450368162.

[24] Joseph R. Corea, Anita M. Flynn, Balthazar Lechêne, Greig Scott, Galen D. Reed, Peter J. Shin, Michael Lustig, and Ana C. Arias. Screen-printed flexible MRI receive coils. *Nature Communications*, 7:10839, 2016.

[25] Woei Chang Ee and Kuan Yew Cheong. Effects of annealing temperature on ultra-low dielectric constant SiO_2 thin films derived from sol–gel spin-on-coating. *Physica B: Condensed Matter*, 403(4):611–615, 2008.

[26] Fritz Liebscher and Wolfgang Held. *Kondensatoren: Dielektrikum Bemessung Anwendung*. Springer, Berlin/Heidelberg, 1968.

[27] Ellen Ivers-Tiffée and Waldemar von Münch. *Werkstoffe der Elektrotechnik: Mit 40 Tabellen*. Lehrbuch Elektrotechnik. Teubner, Wiesbaden, 10., überarb. und erw. Aufl., 2007. ISBN 3835100521.

[28] Young-Geun Ha, Ken Everaerts, Mark C. Hersam, and Tobin J. Marks. Hybrid gate dielectric materials for unconventional electronic circuitry. *Accounts of Chemical Research*, 47(4):1019–1028, 2014.

[29] Zhi-Min Dang, Jin-Kai Yuan, Sheng-Hong Yao, and Rui-Jin Liao. Flexible nanodielectric materials with high permittivity for power energy storage. *Advanced Materials*, 25(44):6334–6365, 2013.

[30] Sungjun Park, Chang-Hyun Kim, Won-June Lee, Sujin Sung, and Myung-Han Yoon. Sol-gel metal oxide dielectrics for all-solution-processed electronics. *Materials Science and Engineering: R: Reports*, 114:1–22, 2017.

[31] David Wallace. Overview of Inkjet-Based Micromanufacturing. In Jan G. Korvink, Patrick J. Smith, and Dong-Youn Shin, editors, *Inkjet-based Micromanufacturing*, Advanced micro & nanosystems, pages 1–17. Wiley-VCH, Weinheim, 2012. ISBN 1283596954.

[32] Alan Hudd. Inkjet Printing Technologies. In Shlomo Magdassi, editor, *The chemistry of inkjet inks*, pages 3–18. World Scientific, Singapore, 2010. ISBN 978-981-281-821-8.

[33] Ankita Mohapatra, Sayema K. Tuli, Kwei-Yu Liu, Tomoko Fujiwara, Robert W. Hewitt Jr., Frank Andrasik, and Bashir I. Morshed. Inkjet Printed Parallel Plate Capacitors Using PVP Polymer Dielectric Ink on Flexible Polyimide Substrates. In James Patton, editor, *2018 40th Annual International Conference of the IEEE Engineering in Medicine and Biology Society (EMBC)*, pages 4277–4280, Piscataway, NJ, 2018. IEEE. ISBN 978-1-5386-3646-6.

[34] Jinkai Yuan, Shenghong Yao, and Philippe Poulin. Dielectric Constant of Polymer Composites and the Routes to High-k or Low-k Nanocomposite Materials. In Xingyi Huang and Chunyi Zhi, editors, *Polymer Nanocomposites*, pages 3–28. Springer International Publishing, Cham, 2016. ISBN 978-3-319-28236-7.

[35] J. Y. Li, L. Zhang, and Stephen Ducharme. Electric energy density of dielectric nanocomposites. *Applied Physics Letters*, 90(13):132901, 2007.

[36] C.-W. Nan, Y. Shen, and Jing Ma. Physical Properties of Composites Near Percolation. *Annual Review of Materials Research*, 40(1):131–151, 2010.

[37] V. E. Dubrov, M. E. Levinshtein, and M. S. Shur. Permittivity anomaly in metal-dielectric transitions. Theory and simulation. *Soviet Physics JETP*, 43:1050–1056, 1976.

[38] A. L. Efros and B. I. Shklovskii. Critical behaviour of conductivity and dielectric constant near the metal-non-metal transition threshold. *physica status solidi (b)*, 76(2):475–485, 1976.

[39] Anju Toor, Hongyun So, and Albert P. Pisano. Dielectric properties of ligand-modified gold nanoparticle/SU-8 photopolymer based nanocomposites. *Applied Surface Science*, 414:373–379, 2017.

[40] Anju Toor, Hongyun So, and Albert P. Pisano. Improved Dielectric Properties of Polyvinylidene Fluoride Nanocomposite Embedded with Poly(vinylpyrrolidone)-Coated Gold Nanoparticles. *ACS Applied Materials & Interfaces*, 9(7):6369–6375, 2017.

[41] Lisa A. Fredin, Zhong Li, Michael T. Lanagan, Mark A. Ratner, and Tobin J. Marks. Substantial Recoverable Energy Storage in Percolative Metallic Aluminum-Polypropylene Nanocomposites. *Advanced Functional Materials*, 23(28):3560–3569, 2013.

[42] B. Reiser, L. González-García, I. Kanelidis, J. H. M. Maurer, and T. Kraus. Gold nanorods with conjugated polymer ligands: Sintering-free conductive inks for printed electronics. *Chemical Science*, 7(7):4190–4196, 2016.

[43] Indra K. Backes, Lola González-García, Anne Holtsch, Frank Müller, Karin Jacobs, and Tobias Kraus. Molecular Origin of Electrical Conductivity in Gold-Polythiophene Hybrid Particle Films. *The Journal of Physical Chemistry Letters*, 11(24):10538–10547, 2020.

[44] Jianjun Wang, Ling Sun, Konstantino Mpoukouvalas, Karen Lienkamp, Ingo Lieberwirth, Birgit Fassbender, Elmar Bonaccurso, Gunther Brunklaus, Andreas Muehlebach, Tilman Beierlein, Robert Tilch, Hans-Jurgen Butt, and Gerhard Wegner. Construction of Redispersible Polypyrrole Core-Shell Nanoparticles for Application in Polymer Electronics. *Advanced Materials*, 21(10-11):1137–1141, 2009.

[45] Suzhu Yu, Terence K.S. Wong, Xiao Hu, and Kantisara Pita. Sol-gel derived mesoporous silica films used as low dielectric constant materials. *Thin Solid Films*, 462-463:311–315, 2004.

[46] M. L. Green, E. P. Gusev, R. Degraeve, and E. L. Garfunkel. Ultrathin (<4 nm) SiO_2 and Si–O–N gate dielectric layers for silicon microelectronics: Understanding the processing, structure, and physical and electrical limits. *Journal of Applied Physics*, 90(5):2057–2121, 2001.

[47] Young-Geun Ha, Sunho Jeong, Jinsong Wu, Myung-Gil Kim, Vinayak P. Dravid, Antonio Facchetti, and Tobin J. Marks. Flexible low-voltage organic thin-film transistors enabled by low-temperature, ambient solution-processable inorganic/organic hybrid gate dielectrics. *Journal of the American Chemical Society*, 132(49): 17426–17434, 2010.

[48] Christophe Avis and Jin Jang. High-performance solution processed oxide TFT with aluminum oxide gate dielectric fabricated by a sol–gel method. *Journal of Materials Chemistry*, 21(29):10649–10652, 2011.

[49] Jens Adam, Tobias Lehnert, Gabi Klein, and Robert M. McMeeking. Ferroelectric properties of composites containing $BaTiO_3$ nanoparticles of various sizes. *Nanotechnology*, 25(6):065704, 2014.

[50] Damien Thuau, Konstantinos Kallitsis, Fabrice Domingues Dos Santos, and Georges Hadziioannou. All inkjet-printed piezoelectric electronic devices: energy generators, sensors and actuators. *Journal of Materials Chemistry C*, 5(38):9963–9966, 2017.

[51] Helmut Lindner, Harry Brauer, and Constans Lehmann. *Taschenbuch der Elektrotechnik und Elektronik*. Thun, Frankfurt / Main, 1986. ISBN 3871447528.

[52] Peter Atkins and Julio de Paula. *Physical Chemistry*. Oxford University Press, New York, 9th edition, 2010. ISBN 978-0-19-954337-3.

[53] A. J. Moulson and J. M. Herbert. *Electroceramics*. John Wiley & Sons, West Sussex, England, 2nd Edition, 2003. ISBN 0 471 49748 7.

[54] Elmar Schrüfer, Leonhard M. Reindl, and Bernhard Zagar. *Elektrische Messtechnik: Messung elektrischer und nichtelektrischer Größen*. Fachbuchverlag Leipzig im Carl Hanser Verlag, München, 12., aktualisierte Auflage, 2018. ISBN 9783446456983.

[55] A. Schönhals and F. Kremer. Theory of Dielectric Relaxation. In Friedrich Kremer and Andreas Schönhals, editors, *Broadband Dielectric Spectroscopy*, pages 1–33. Springer, Berlin, Heidelberg, 2003. ISBN 978-3-642-56120-7.

[56] Ekbert Hering, Rolf Martin, Martin Stohrer, and Hanno Käß. *Physik für Ingenieure*. Springer-Lehrbuch. Springer, Berlin, 11., bearb. Aufl., 2012. ISBN 978-3-642-22568-0.

[57] Lisa A. Fredin, Zhong Li, Michael T. Lanagan, Mark A. Ratner, and Tobin J. Marks. Sustainable high capacitance at high frequencies: metallic aluminum-polypropylene nanocomposites. *ACS Nano*, 7(1):396–407, 2013.

[58] R. Pelster and U. Simon. Nanodispersions of conducting particles: preparation, microstructure and dielectric properties. *Colloid and Polymer Science*, 227:2–14, 1999.

[59] P. A. M. Steeman and J. van Turnhout. Dielectric Properties of Inhomogeneous Media. In Friedrich Kremer and Andreas Schönhals, editors, *Broadband Dielectric Spectroscopy*, pages 495–522. Springer, Berlin, Heidelberg, 2003. ISBN 978-3-642-56120-7.

[60] Chetan Chanmal and Jyoti Jog. Dielectric Relaxation Spectroscopy for Polymer Nanocomposites. In Vikas Mittal, editor, *Characterization Techniques for Polymer Nanocomposites*, Polymer Nano-, Micro- and Macrocomposites, pages 167–184. Wiley-VCH, s.l., 2012. ISBN 978-3-527-33148-2.

[61] Anju Toor. *Polymer Nanocomposite Materials with High Dielectric Permittivity and Low Dielectric Loss Properties*. Dissertation, University of California, Berkeley, 2017.

[62] Karl Willy Wagner. Erklärung der dielektrischen Nachwirkungsvorgänge auf Grund Maxwellscher Vorstellungen. *Archiv für Elektrotechnik*, 2(9):371–387, 1914.

[63] R. W. Sillars. The properties of a dielectric containing semiconducting particles of various shapes. *Institution of Electrical Engineers - Proceedings of the Wireless Section of the Institution*, 12(35):139–155(16), 1937.

[64] Michael Berger. *Nanotechnology: The Future is Tiny*. The Royal Society of Chemistry, 2016. ISBN 978-1-78262-526-1.

[65] Shlomo Magdassi. Ink Requirements and Formulations Guidelines. In Shlomo Magdassi, editor, *The chemistry of inkjet inks*, pages 19–41. World Scientific, Singapore, 2010. ISBN 978-981-281-821-8.

[66] Abraham Marmur. Equilibrium Wetting Fundamentals. In Shlomo Magdassi, editor, *The chemistry of inkjet inks*, pages 43–54. World Scientific, Singapore, 2010. ISBN 978-981-281-821-8.

[67] Rory Wolf and Amelia Carolina Sparavigna. Role of Plasma Surface Treatments on Wetting and Adhesion. *Engineering*, 02(06):397–402, 2010.

[68] Anke Teichler, Jolke Perelaer, and Ulrich S. Schubert. Combinatorial Screening of Materials Using Inkjet Printing as a Patterning Technique. In Jan G. Korvink, Patrick J. Smith, and Dong-Youn Shin, editors, *Inkjet-based Micromanufacturing*, Advanced micro & nanosystems, pages 19–39. Wiley-VCH, Weinheim, 2012. ISBN 1283596954.

[69] Takashi Ogi, Luis Balam Modesto-Lopez, Ferry Iskandar, and Kikuo Okuyama. Fabrication of a large area monolayer of silica particles on a sapphire substrate by a spin coating method. *Colloids and Surfaces A: Physicochemical and Engineering Aspects*, 297(1-3):71–78, 2007.

[70] L. E. Scrieven. Physics and Applications of Dip Coating and Spin Coating. *Materials Research Society Symposium Proceedings*, 121:717–729, 1988.

[71] David B. Hall, Patrick Underhill, and John M. Torkelson. Spin coating of thin and ultrathin polymer films. *Polymer Engineering & Science*, 38(12):2039–2045, 1998.

[72] Eduardo Napadensky. Inkjet 3D Printing. In Shlomo Magdassi, editor, *The chemistry of inkjet inks*, pages 255–267. World Scientific, Singapore, 2010. ISBN 978-981-281-821-8.

[73] R. Noguera, C. Dossou-Yovo, M. Lejeune, and T. Chartier. 3D fine scale PZT skeletons of 1-3 ceramic polymer composites formed by ink-jet prototyping process. *Journal de Physique IV (Proceedings)*, 126:133–137, 2005.

[74] Patrick J. Smith. The Behaviour of a Droplet on the Substrate. In Shlomo Magdassi, editor, *The chemistry of inkjet inks*, pages 55–72. World Scientific, Singapore, 2010. ISBN 978-981-281-821-8.

[75] Neil Graddage, Ta-Ya Chu, Heping Ding, Christophe Py, Afshin Dadvand, and Ye Tao. Inkjet printed thin and uniform dielectrics for capacitors and organic thin film transistors enabled by the coffee ring effect. *Organic Electronics*, 29:114–119, 2016.

[76] Afshin Dadvand, Jianping Lu, Christophe Py, Ta-Ya Chu, Raluca Movileanu, and Ye Tao. Inkjet printable and low annealing temperature gate-dielectric based on polymethylsilsesquioxane for flexible n-channel OFETs. *Organic Electronics*, 30: 213–218, 2016.

[77] T. Kaydanova, A. Miedaner, J. D. Perkins, C. Curtis, J. L. Alleman, and D. S. Ginley. Direct-write inkjet printing for fabrication of barium strontium titanate-based tunable circuits. *Thin Solid Films*, 515(7-8):3820–3824, 2007.

[78] Jongwoo Lim, Jihoon Kim, Young Joon Yoon, Hyotae Kim, Ho Gyu Yoon, Sung-Nam Lee, and Jonghee Kim. All-inkjet-printed Metal-Insulator-Metal (MIM) capacitor. *Current Applied Physics*, 12:e14–e17, 2012.

[79] Byung Ju Kang, Chang Kyu Lee, and Je Hoon Oh. All-inkjet-printed electrical components and circuit fabrication on a plastic substrate. *Microelectronic Engineering*, 97:251–254, 2012.

[80] Morten Mikolajek, Andreas Friederich, Christian Kohler, Melanie Rosen, Andreas Rathjen, Klaus Krüger, and Joachim R. Binder. Direct Inkjet Printing of Dielectric Ceramic/Polymer Composite Thick Films. *Advanced Engineering Materials*, 17(9): 1294–1301, 2015.

[81] Daryl McManus, Sandra Vranic, Freddie Withers, Veronica Sanchez-Romaguera, Massimo Macucci, Huafeng Yang, Roberto Sorrentino, Khaled Parvez, Seok-Kyun Son, Giuseppe Iannaccone, Kostas Kostarelos, Gianluca Fiori, and Cinzia Casiraghi. Water-based and biocompatible 2D crystal inks for all-inkjet-printed heterostructures. *Nature Nanotechnology*, 12(4):343–350, 2017.

[82] Shiheng Lu, Jorge A. Cardenas, Robyn Worsley, Nicholas X. Williams, Joseph B. Andrews, Cinzia Casiraghi, and Aaron D. Franklin. Flexible, Print-in-Place 1D-2D Thin-Film Transistors Using Aerosol Jet Printing. *ACS Nano*, 13(10):11263–11272, 2019.

[83] L. Qi, B. I. Lee, S. Chen, W. D. Samuels, and G. J. Exarhos. High-Dielectric-Constant Silver-Epoxy Composites as Embedded Dielectrics. *Advanced Materials*, 17(14):1777–1781, 2005.

[84] Y. Shen, Y. Lin, M. Li, and C.-W. Nan. High Dielectric Performance of Polymer Composite Films Induced by a Percolating Interparticle Barrier Layer. *Advanced Materials*, 19(10):1418–1422, 2007.

[85] Benjamin S. Cook, James R. Cooper, and Manos M. Tentzeris. Multi-Layer RF Capacitors on Flexible Substrates Utilizing Inkjet Printed Dielectric Polymers. *IEEE Microwave and Wireless Components Letters*, 23(7):353–355, 2013.

[86] Yi Li, Russel Torah, Steve Beeby, and John Tudor. An all-inkjet printed flexible capacitor on a textile using a new poly(4-vinylphenol) dielectric ink for wearable applications. In *2012 IEEE Sensors*, pages 1–4. IEEE, 28.10.2012 - 31.10.2012. ISBN 978-1-4577-1767-3.

[87] E. M. Hamad, S. E. R. Bilatto, N. Y. Adly, D. S. Correa, B. Wolfrum, M. J. Schöning, A. Offenhäusser, and A. Yakushenko. Inkjet printing of UV-curable adhesive and dielectric inks for microfluidic devices. *Lab on a chip*, 16(1):70–74, 2016.

[88] Jené Kruger, Petroné H. Bezuidenhout, Ulrich Hilleringmann, and Trudi-Heleen Joubert. Characterization of inkjet-printed dielectric on different substrates. In Monuko Du Plessis, editor, *Fifth Conference on Sensors, MEMS, and Electro-Optic Systems*, page 69. SPIE, 08.10.2018 - 10.10.2018. ISBN 9781510627529.

[89] Young-Jae Kim, Joohee Kim, Youn Sang Kim, and Jin-Kyu Lee. TiO_2-poly(4-vinylphenol) nanocomposite dielectrics for organic thin film transistors. *Organic Electronics*, 14(12):3406–3414, 2013.

[90] Tomasz Marszalek, Maciej Gazicki-Lipman, and Jacek Ulanski. Parylene C as a versatile dielectric material for organic field-effect transistors. *Beilstein Journal of Nanotechnology*, 8:1532–1545, 2017.

[91] Shan Wang and Qi Li. Design, synthesis and processing of PVDF–based dielectric polymers. *IET Nanodielectrics*, 1(2):80–91, 2018.

[92] Rubaiyet Iftekharul Haque, Rémy Vié, Michel Germainy, Laurie Valbin, Patrick Benaben, and Xavier Boddaert. Inkjet printing of high molecular weight PVDF-TrFE for flexible electronics. *Flexible and Printed Electronics*, 1(1):015001, 2016.

[93] Weimin Xia and Zhicheng Zhang. PVDF–based dielectric polymers and their applications in electronic materials. *IET Nanodielectrics*, 1(1):17–31, 2018.

[94] B. Huber, P. B. Popp, M. Kaiser, A. Ruediger, and C. Schindler. Fully inkjet printed flexible resistive memory. *Applied Physics Letters*, 110(14):143503, 2017.

[95] J. Jehn, M. Kaiser, U. Moosheimer, A. Ruediger, and C. Schindler. Printed resistive switching memory operated by screen-printed microbattery via shared electrode. *Microelectronic Engineering*, 239-240:1–5, 2021.

[96] Wei Cai, Honglong Ning, Zhennan Zhu, Jinglin Wei, Shangxiong Zhou, Rihui Yao, Zhiqiang Fang, Xiuqi Huang, Xubing Lu, and Junbiao Peng. Investigation of direct inkjet-printed versus spin-coated ZrO_2 for sputter IGZO thin film transistor. *Nanoscale research letters*, 14(1):80, 2019.

[97] Yuzhi Li, Linfeng Lan, Sheng Sun, Zhenguo Lin, Peixiong Gao, Wei Song, Erlong Song, Peng Zhang, and Junbiao Peng. All Inkjet-Printed Metal-Oxide Thin-Film Transistor Array with Good Stability and Uniformity Using Surface-Energy Patterns. *ACS Applied Materials & Interfaces*, 9(9):8194–8200, 2017.

[98] Sonia Sharma, Sumukh S. Pande, and P. Swaminathan. Top-down synthesis of zinc oxide based inks for inkjet printing. *RSC Advances*, 7(63):39411–39419, 2017.

[99] Giuseppe Arrabito, Yana Aleeva, Riccardo Pezzilli, Vittorio Ferrara, Pier Gianni Medaglia, Bruno Pignataro, and Giuseppe Prestopino. Printing ZnO Inks: From Principles to Devices. *Crystals*, 10(6):449, 2020.

[100] A. Matavž, R. C. Frunză, A. Drnovšek, V. Bobnar, and B. Malič. Inkjet printing of uniform dielectric oxide structures from sol–gel inks by adjusting the solvent composition. *Journal of Materials Chemistry C*, 4(24):5634–5641, 2016.

[101] Rixuan Wang, Hyeok-jin Kwon, Xiaowu Tang, Heqing Ye, Chan Eon Park, Juyoung Kim, Hoyoul Kong, and Se Hyun Kim. Slot-die coating of sol–gel-based organic–inorganic nanohybrid dielectric layers for flexible and large-area organic thin film transistors. *Applied Surface Science*, 529:147198, 2020.

[102] R. E. Newnham, D. P. Skinner, and L. E. Cross. Connectivity and piezoelectric-pyroelectric composites. *Materials Research Bulletin*, 13(5):525–536, 1978.

[103] Peter Barber, Shiva Balasubramanian, Yogesh Anguchamy, Shushan Gong, Arief Wibowo, Hongsheng Gao, Harry Ploehn, and Hans-Conrad Zur Loye. Polymer Composite and Nanocomposite Dielectric Materials for Pulse Power Energy Storage. *Materials*, 2(4):1697–1733, 2009.

[104] D.A.G. Bruggeman. Berechnung verschiedener physikalischer Konstanten von heterogenen Substanzen. I. Dielektrizitätskonstanten und Leitfähigkeiten der Mischkörper aus isotropen Substanzen. *Annalen der Physik*, 416(7):636–664, 1935.

[105] Dang-Hyok Yoon, Jianping Zhang, and Burtrand I. Lee. Dielectric constant and mixing model of $BaTiO_3$ composite thick films. *Materials Research Bulletin*, 38 (5):765–772, 2003.

[106] Sung-Dong Cho, Joo-Yeon Lee, Jin-Gul Hyun, and Kyung-Wook Paik. Study on epoxy/$BaTiO_3$ composite embedded capacitor films (ECFs) for organic substrate applications. *Materials Science and Engineering B: Solid-State Materials for Advanced Technology*, 110(3):233–239, 2004.

[107] P. Kim, S. C. Jones, P. J. Hotchkiss, J. N. Haddock, B. Kippelen, S. R. Marder, and J. W. Perry. Phosphonic Acid-Modified Barium Titanate Polymer Nanocomposites with High Permittivity and Dielectric Strength. *Advanced Materials*, 19(7):1001–1005, 2007.

[108] Tobias Lehnert, Petra Herbeck-Engel, Jens Adam, Gabi Klein, Terho Kololuoma, and Michael Veith. Dielectric Properties of a Printed Sol-Gel Matrix Composite. *Advanced Engineering Materials*, 12(5):379–384, 2010.

[109] Sung Gap Lee, Sang Man Park, Youngjae Shim, and Youngchul Rhee. Structural and Dielectric Properties of Screen Printed PZT(70/30) Multilayered Thick Films. *Solid State Phenomena*, 124-126:663–666, 2007.

[110] Matthias Dietze and Mohammed Es-Souni. Structural and functional properties of screen-printed PZT–PVDF-TrFE composites. *Sensors and Actuators A: Physical*, 143(2):329–334, 2008.

[111] Xiaoya Hou, Yijie Xia, Siu Choon Ng, Jie Zhang, and Joseph Sylvester Chang. Formulation of novel screen-printable dielectric ink for fully-printed TIPs-pentacene OFETs. *RSC Advances*, 4(71):37687–37690, 2014.

[112] Aswani K. Mogalicherla, Seungcheol Lee, Peter Pfeifer, and Roland Dittmeyer. Drop-on-demand inkjet printing of alumina nanoparticles in rectangular microchannels. *Microfluidics and Nanofluidics*, 16(4):655–666, 2014.

[113] Morten Mikolajek. *Tintenstrahldruck organisch/anorganischer Komposite*. Dissertation, Karlsruhe Institut für Technologie, Karlsruhe, 2018.

[114] Giovanni Vescio, Gemma Martín, Albert Crespo-Yepes, Sergi Claramunt, Daniel Alonso, Julian López-Vidrier, Sonia Estradé, Marc Porti, Rosana Rodríguez, Francesca Peiró, Albert Cornet, Albert Cirera, and Montserrat Nafría. Low-Power, High-Performance, Non-volatile Inkjet-Printed HfO_2-Based Resistive Random Access Memory: From Device to Nanoscale Characterization. *ACS Applied Materials & Interfaces*, 11(26):23659–23666, 2019.

[115] Zhi-Min Dang, Jin-Kai Yuan, Jun-Wei Zha, Tao Zhou, Sheng-Tao Li, and Guo-Hua Hu. Fundamentals, processes and applications of high-permittivity polymer–matrix composites. *Progress in Materials Science*, 57(4):660–723, 2012.

[116] Angel Mary Joseph, Baku Nagendra, E. Bhoje Gowd, and Kuzhichalil Peethambharan Surendran. Screen-Printable Electronic Ink of Ultrathin Boron Nitride Nanosheets. *ACS Omega*, 1(6):1220–1228, 2016.

[117] Scott Kirkpatrick. Percolation and conduction. *Reviews of Modern Physics*, 45 (4):574, 1973.

[118] Gérard Perrier and Anne Bergeret. Polystyrene-glass bead composites: Maxwell-Wagner-sillars relaxations and percolation. *Journal of Polymer Science Part B: Polymer Physics*, 35(9):1349–1359, 1997.

[119] Jiongxin Lu, Kyoung-Sik Moon, Jianwen Xu, and C. P. Wong. Synthesis and dielectric properties of novel high-K polymer composites containing in-situ formed silver nanoparticles for embedded capacitor applications. *Journal of Materials Chemistry*, 16(16):1543, 2006.

[120] Jiongxin Lu and C. Wong. Recent advances in high-k nanocomposite materials for embedded capacitor applications. *IEEE Transactions on Dielectrics and Electrical Insulation*, 15(5):1322–1328, 2008.

[121] C. Pecharromán and J. S. Moya. Experimental Evidence of a Giant Capacitance in Insulator-Conductor Composites at the Percolation Threshold. *Advanced Materials*, 12(4):294–297, 2000.

[122] Carlos Pecharromán, Fátima Esteban-Betegón, José F. Bartolomé, Sonia López-Esteban, and José S. Moya. New Percolative $BaTiO_3$-Ni Composites with a High and Frequency-Independent Dielectric Constant (k = 80000). *Advanced Materials*, 13:1541–1544, 2001.

[123] Zhi-Min Dang, Ce-Wen Nan, Dan Xie, Yi-He Zhang, and S. C. Tjong. Dielectric behavior and dependence of percolation threshold on the conductivity of fillers in polymer-semiconductor composites. *Applied Physics Letters*, 85(1):97–99, 2004.

[124] Yang Shen, Ce-Wen Nan, and Ming Li. Anisotropic electrical properties of semiconductive Bi_2S_3 nanorod filled ferroelectric polyvinylidene fluoride. *Chemical Physics Letters*, 396(4-6):420–423, 2004.

[125] Y. Shen, Y. H. Lin, and C.-W. Nan. Interfacial Effect on Dielectric Properties of Polymer Nanocomposites Filled with Core/Shell-Structured Particles. *Advanced Functional Materials*, 17(14):2405–2410, 2007.

[126] Jianwen Xu and C. P. Wong. Low-loss percolative dielectric composite. *Applied Physics Letters*, 87(8):082907, 2005.

[127] J. Xu, K.-S. Moon, C. Tison, and C. P. Wong. A Novel Aluminum-Filled Composite Dielectric for Embedded Passive Applications. *IEEE Transactions on Advanced Packaging*, 29(2):295–306, 2006.

[128] Cheng Yang, Yuanhua Lin, and C. W. Nan. Modified carbon nanotube composites with high dielectric constant, low dielectric loss and large energy density. *Carbon*, 47(4):1096–1101, 2009.

[129] Jiongxin Lu, Kyoung-Sik Moon, and C. P. Wong. Silver/polymer nanocomposite as a high-k polymer matrix for dielectric composites with improved dielectric performance. *Journal of Materials Chemistry*, 18(40):4821, 2008.

[130] Anju Toor, Jim C. Cheng, and Albert P. Pisano. Synthesis and Characterization of Gold Nanoparticle/SU-8 Polymer based Nanocomposite. In *The 9th IEEE International Conference on Nano/Micro Engineered and Molecular Systems (NEMS)*, pages 664–668, Piscataway, NJ, 2014. IEEE. ISBN 9781479947256.

[131] Anju Toor and Albert P. Pisano. Gold Nanoparticle/PVDF Polymer Composite with Improved Particle Dispersion. In *2015 IEEE 15th International Conference on Nanotechnology (IEEE-NANO)*, pages 706–709, Piscataway, NJ, 2015. IEEE. ISBN 978-1-4673-8156-7.

[132] G. Frens. Controlled Nucleation for the Regulation of the Particle Size in Monodisperse Gold Suspensions. *Nature Physical Science*, 241(105):20–22, 1973.

[133] D. Fennell Evans and Håkan Wennerström. *The colloidal domain: Where physics, chemistry, biology, and technology meet.* Advances in interfacial engineering series. Wiley-VCH, New York, NY, 2. ed., 1999. ISBN 0-471-24247-0.

[134] Bing-Hui Wu, Hua-Yan Yang, Hua-Qi Huang, Guang-Xu Chen, and Nan-Feng Zheng. Solvent effect on the synthesis of monodisperse amine-capped Au nanoparticles. *Chinese Chemical Letters*, 24(6):457–462, 2013.

[135] Thomas Kister. *The stability and assembly of sterically stabilized non-polar nanoparticles.* Dissertation, Universität des Saarlandes, Saarbrücken, 2021.

[136] Siddique J. Khan, F. Pierce, C. M. Sorensen, and A. Chakrabarti. Self-assembly of ligated gold nanoparticles: phenomenological modeling and computer simulations. *Langmuir*, 25(24):13861–13868, 2009.

[137] Tihamér Geyer, Philip Born, and Tobias Kraus. Switching between crystallization and amorphous agglomeration of alkyl thiol-coated gold nanoparticles. *Physical review letters*, 109(12):1–5, 2012.

[138] Dominik Gerstner and Tobias Kraus. Rapid nanoparticle self-assembly at elevated temperatures. *Nanoscale*, 10(17):8009–8013, 2018.

[139] Thomas Kister, Debora Monego, Paul Mulvaney, Asaph Widmer-Cooper, and Tobias Kraus. Colloidal Stability of Apolar Nanoparticles: The Role of Particle Size and Ligand Shell Structure. *ACS Nano*, 12(6):5969–5977, 2018.

[140] Debora Monego, Thomas Kister, Nicholas Kirkwood, Paul Mulvaney, Asaph Widmer-Cooper, and Tobias Kraus. Colloidal Stability of Apolar Nanoparticles: Role of Ligand Length. *Langmuir*, 34(43):12982–12989, 2018.

[141] Debora Monego, Thomas Kister, Nicholas Kirkwood, David Doblas, Paul Mulvaney, Tobias Kraus, and Asaph Widmer-Cooper. When Like Destabilizes Like: Inverted Solvent Effects in Apolar Nanoparticle Dispersions. *ACS Nano*, 14(5): 5278–5287, 2020.

[142] David Doblas, Thomas Kister, Marina Cano-Bonilla, Lola González-García, and Tobias Kraus. Colloidal Solubility and Agglomeration of Apolar Nanoparticles in Different Solvents. *Nano Letters*, 19(8):5246–5252, 2019.

[143] Gustav Mie. Beiträge zur Optik trüber Medien, speziell kolloidaler Metallösungen. *Annalen der Physik*, 330(3):377–445, 1908.

[144] Stephan Link and Mostafa A. El-Sayed. Size and Temperature Dependence of the Plasmon Absorption of Colloidal Gold Nanoparticles. *The Journal of Physical Chemistry B*, 103(21):4212–4217, 1999.

[145] Marie-Christine Daniel and Didier Astruc. Gold Nanoparticles: Assembly, Supramolecular Chemistry, Quantum-Size-Related Properties, and Applications Toward Biology, Catalysis, and Nanotechnology. *Chemical Reviews*, 104(1):293–346, 2004.

[146] David Doblas, Jonas Hubertus, Thomas Kister, and Tobias Kraus. A Translucent Nanocomposite with Liquid Inclusions of a Responsive Nanoparticle Dispersion. *Advanced Materials*, page 1803159, 2018.

[147] Thomas Hendel, Maria Wuithschick, Frieder Kettemann, Alexander Birnbaum, Klaus Rademann, and Jörg Polte. In situ determination of colloidal gold concentrations with UV-vis spectroscopy: limitations and perspectives. *Analytical Chemistry*, 86(22):11115–11124, 2014.

[148] Anna C. Balazs, Todd Emrick, and Thomas P. Russell. Nanoparticle Polymer Composites: Where Two Small Worlds Meet. *Science*, 314(5802):1107–1110, 2006.

[149] Xingyi Huang and Pingkai Jiang. Core-Shell Structured High-k Polymer Nanocomposites for Energy Storage and Dielectric Applications. *Advanced Materials*, 27 (3):546–554, 2015.

[150] Rainer C. Hoft, Michael J. Ford, Andrew M. McDonagh, and Michael B. Cortie. Adsorption of Amine Compounds on the Au(111) Surface: A Density Functional Study. *The Journal of Physical Chemistry C*, 111(37):13886–13891, 2007.

[151] Abraham Ulman. Formation and Structure of Self-Assembled Monolayers. *Chemical Reviews*, 96(4):1533–1554, 1996.

[152] Thomas Bürgi. Properties of the gold-sulphur interface: from self-assembled monolayers to clusters. *Nanoscale*, 7(38):15553–15567, 2015.

[153] Kamil Rahme, Lan Chen, Richard G. Hobbs, Michael A. Morris, Caitriona O'Driscoll, and Justin D. Holmes. PEGylated gold nanoparticles: polymer quantification as a function of PEG lengths and nanoparticle dimensions. *RSC Advances*, 3(17):6085–6094, 2013.

[154] Muriel K. Corbierre, Neil S. Cameron, and R. Bruce Lennox. Polymer-Stabilized Gold Nanoparticles with High Grafting Densities. *Langmuir*, 20(7):2867–2873, 2004.

[155] Julian Sindram, Marcel Krüsmann, Marius Otten, Thomas Pauly, Luitgard Nagel-Steger, and Matthias Karg. Versatile Route toward Hydrophobically Polymer-Grafted Gold Nanoparticles from Aqueous Dispersions. *The Journal of Physical Chemistry B*, 125(29):8225–8237, 2021.

[156] C. M. Wijmans and E. B. Zhulina. Polymer Brushes at Curved Surfaces. *Macromolecules*, 26(26):7214–7224, 1993.

[157] Douglas Dukes, Yu Li, Sarah Lewis, Brian Benicewicz, Linda Schadler, and Sanat K. Kumar. Conformational Transitions of Spherical Polymer Brushes: Synthesis, Characterization, and Theory. *Macromolecules*, 43(3):1564–1570, 2010.

[158] Peter W. Atkins and Arno Höpfner, editors. *Physikalische Chemie*. Wiley-VCH, Weinheim, 3., korrigierte Aufl., 1. Nachdr, 2004. ISBN 3527302360.

[159] Michael Rubinstein and Ralph H. Colby. *Polymer Physics*. Oxford University Press, New York, Reprinted 2013, 2003. ISBN 9780198520597.

[160] Alessandro Vetere. An Empirical Method To Predict the Liquid−Liquid Equilibria of Binary Polymer Systems. *Industrial & Engineering Chemistry Research*, 37(11): 4463–4469, 1998.

[161] P. G. de Gennes. Collapse of a polymer chain in poor solvents. *Journal de Physique Lettres*, 36(3):55–57, 1975.

[162] Aaron M. Forster, Jimmy W. Mays, and S. Michael Kilbey. Effect of temperature on the frictional forces between polystyrene brushes. *Journal of Polymer Science Part B: Polymer Physics*, 44(4):649–655, 2006.

[163] Jiqun Yu, Zhulun Wang, and Benjamin Chu. Kinetic study of Coil-to-Globule transition. *Macromolecules*, 25:1618–1620, 1992.

[164] Pinar Akcora, Hongjun Liu, Sanat K. Kumar, Joseph Moll, Yu Li, Brian C. Benicewicz, Linda S. Schadler, Devrim Acehan, Athanassios Z. Panagiotopoulos, Victor Pryamitsyn, Venkat Ganesan, Jan Ilavsky, Pappanan Thiyagarajan, Ralph H. Colby, and Jack F. Douglas. Anisotropic self-assembly of spherical polymer-grafted nanoparticles. *Nature Materials*, 8(4):354–359, 2009.

[165] Zhenli Zhang and Sharon C. Glotzer. Self-Assembly of Patchy Particles. *Nano Letters*, 4(8):1407–1413, 2004.

[166] Zhenli Zhang, Zhiyong Tang, Nicholas A. Kotov, and Sharon C. Glotzer. Simulations and analysis of self-assembly of CdTe nanoparticles into wires and sheets. *Nano Letters*, 7(6):1670–1675, 2007.

[167] Dennis Huebner, Christian Rossner, and Philipp Vana. Light-induced self-assembly of gold nanoparticles with a photoresponsive polymer shell. *Polymer*, 107:503–508, 2016.

[168] Johannes Brandrup, editor. *Polymer handbook*. A Wiley-Interscience publication. Wiley, New York, NY, 4. ed., 1999. ISBN 0-471-16628-6.

[169] Bruce J. Berne and Robert Pecora. *Dynamic Light Scattering: With Applications to Chemistry, Biology, and Physics*. Dover Books on Physics. Dover Publications, Newburyport, 2013. ISBN 0-486-41155-9.

[170] Puthusserickal A. Hassan, Suman Rana, and Gunjan Verma. Making Sense of Brownian Motion: Colloid Characterization by Dynamic Light Scattering. *Langmuir*, 31(1):3–12, 2015.

[171] M. D. Lechner. *Refractive Indices of Inorganic, Organometallic, and Organononmetallic Liquids, and Binary Liquid Mixtures*, volume 38A. Springer, Berlin, Heidelberg, 1996. ISBN 3-540-60539-8.

[172] Ch. Wohlfarth. Viscosity of toluene. In W. Martienssen and M. D. Lechner, editors, *Supplement to IV/18*, volume 25 of *Landolt-Börnstein - Group IV Physical Chemistry*, pages 447–458. Springer, Berlin, Heidelberg, 2009. ISBN 978-3-540-56050-0.

[173] Rayleigh. On the Theory of Long Waves and Bores. *Proceedings of the Royal Society of London. Series A, Containing Papers of a Mathematical and Physical Character*, 90(619):324–328, 1914.

[174] Ingo Breßler, Joachim Kohlbrecher, and Andreas F. Thünemann. SASfit: a tool for small-angle scattering data analysis using a library of analytical expressions. *Journal of Applied Crystallography*, 48(Pt 5):1587–1598, 2015.

[175] Tao Li, Andrew J. Senesi, and Byeongdu Lee. Small Angle X-ray Scattering for Nanoparticle Research. *Chemical Reviews*, 116(18):11128–11180, 2016.

[176] S. Förster, A. Timmann, M. Konrad, C. Schellbach, A. Meyer, S. S. Funari, P. Mulvaney, and R. Knott. Scattering curves of ordered mesoscopic materials. *The journal of physical chemistry. B*, 109(4):1347–1360, 2005.

[177] Martin Treß. *Breitbandige dielektrische Spektroskopie zur Untersuchung der molekularen Dynamik von Nanometer-dünnen Polymerschichten*. Dissertation, Universität Leipzig, Leipzig, 15.12.2014.

[178] Evgenij Barsoukov and J.Ross Macdonald. *Impedance Spectroscopy: Theory, Experiment, and Applications: Second Edition*. John Wiley & Sons, Hoboken, New Jersey, 2005. ISBN 0-471-64749-7.

[179] A. Schönhals and F. Kremer. Broadband Dielectric Measurement Techniques (10^{-6} Hz to 10^{12} Hz). In Friedrich Kremer and Andreas Schönhals, editors, *Broadband Dielectric Spectroscopy*, pages 35–57. Springer, Berlin, Heidelberg, 2003. ISBN 978-3-642-56120-7.

[180] Martin Kluenker, Mihail Mondeshki, Muhammad Nawaz Tahir, and Wolfgang Tremel. Monitoring Thiol-Ligand Exchange on Au Nanoparticle Surfaces. *Langmuir : the ACS journal of surfaces and colloids*, 34(4):1700–1710, 2018.

[181] Nguyen Hoang Ly and Sang-Woo Joo. Raman Spectroscopy of Di-(2-picolyl)amine on Gold Nanoparticles for Hg(II) Detection. *Bulletin of the Korean Chemical Society*, 36(1):226–229, 2015.

[182] Cory A. Szafranski, Weslene Tanner, Paul E. Laibinis, and Robin L. Garrell. Surface-Enhanced Raman Spectroscopy of Aromatic Thiols and Disulfides on Gold Electrodes. *Langmuir*, 14(13):3570–3579, 1998.

[183] B. Jasse, R. S. Chao, and J. L. Koenig. Laser Raman Scattering in Uniaxially Oriented Atactic Polystyrene. *Journal of Polymer Science: Polymer Physics Edition*, 16:2157–2169, 1978.

[184] W. M. Sears, J. L. Hunt, and J. R. Stevens. Raman scattering from polymerizing styrene. I. Vibrational mode analysis. *The Journal of Chemical Physics*, 75(4): 1589–1598, 1981.

[185] Michael Mazilu, Anna Chiara de Luca, Andrew Riches, C. Simon Herrington, and Kishan Dholakia. Optimal algorithm for fluorescence suppresion of modulated Raman spectroscopy. *Optics Express*, 18(11):11382–11395, 2010.

[186] P. P. Hong, F. J. Boerio, S. J. Clarson, and S. D. Smith. An Investigation of the Interdiffusion of Polystyrene and Deuterated Polystyrene Using Surface-Enhanced Raman Scattering. *Macromolecules*, 24(17):4770–4776, 1991.

[187] Ewen J. C. Kellar, Costas Galiotis, and Edgar H. Andrews. Raman Vibrational Studies of Syndiotactic Polystyrene. 1. Assignments in a Conformational/Crystallinity Sensitive Spectral Region. *Macromolecules*, 29(10):3515–3520, 1996.

[188] J. R. Anema, A. G. Brolo, A. Felten, and C. Bittencourt. Surface-enhanced Raman scattering from polystyrene on gold clusters. *Journal of Raman Spectroscopy*, 41 (7):745–751, 2010.

[189] A. Girlando, M. R. Philpott, D. Heitmann, J. D. Swalen, and R. Santo. Raman spectra of thin organic films enhanced by plasmon surface polaritons on holographic metal gratings. *The Journal of Chemical Physics*, 72(9):5187–5191, 1980.

[190] H. Nishizaki, K. Yoshida, and J. H. Wang. Comparative study of various methods for thermogravimetric analysis of polystyrene degradation. *Journal of Applied Polymer Science*, 25(12):2869–2877, 1980.

[191] Jin Zhu and Charles A. Wilkie. Thermal and fire studies on polystyrene-clay nanocomposites. *Polymer International*, 49(10):1158–1163, 2000.

[192] Bok Nam Jang and Charles A. Wilkie. The thermal degradation of polystyrene nanocomposite. *Polymer*, 46(9):2933–2942, 2005.

[193] Shu-Yi Lin, Yi-Ting Tsai, Chien-Chih Chen, Chia-Mei Lin, and Chun-hsien Chen. Two-Step Functionalization of Neutral and Positively Charged Thiols onto Citrate-Stabilized Au Nanoparticles. *The Journal of Physical Chemistry B*, 108(7):2134–2139, 2004.

[194] Guohua Yang, Nabil A. Amro, Zane B. Starkewolfe, and Gang-yu Liu. Molecular-level approach to inhibit degradations of alkanethiol self-assembled monolayers in aqueous media. *Langmuir*, 20(10):3995–4003, 2004.

[195] J. Christopher Love, Lara A. Estroff, Jennah K. Kriebel, Ralph G. Nuzzo, and George M. Whitesides. Self-assembled monolayers of thiolates on metals as a form of nanotechnology. *Chemical Reviews*, 105(4):1103–1169, 2005.

[196] Dileep Mampallil and Huseyin Burak Eral. A review on suppression and utilization of the coffee-ring effect. *Advances in Colloid and Interface Science*, 252:38–54, 2018.

[197] R. A. Ismail, A. K. Ali, and K. I. Hasson. Characteristics of a silicon Schottky photodetector produced from colloidal gold nanoparticles. *Micro & Nano Letters*, 7(6):536, 2012.

[198] Didier Juhue and Jacques Lang. Film Formation from Dispersion of Core-Shell Latex Particles. *Macromolecules*, 28(4):1306–1308, 1995.

[199] P. A. Steward, J. Hearn, and M. C. Wilkinson. An overview of polymer latex film formation and properties. *Advances in Colloid and Interface Science*, 86(3): 195–267, 2000.

[200] Hendrik Schlicke, Jan H. Schröder, Martin Trebbin, Alexey Petrov, Michael Ijeh, Horst Weller, and Tobias Vossmeyer. Freestanding films of crosslinked gold nanoparticles prepared via layer-by-layer spin-coating. *Nanotechnology*, 22(30): 305303, 2011.

[201] Yiyi Liu, Bo Fan, Qianqian Shi, Dashen Dong, Shu Gong, Bowen Zhu, Runfang Fu, San H. Thang, and Wenlong Cheng. Covalent-Cross-Linked Plasmene Nanosheets. *ACS Nano*, 13(6):6760–6769, 2019.

[202] Parth N. Vakil, Faheem Muhammed, David Hardy, Tarik J. Dickens, Subramanian Ramakrishnan, and Geoffrey F. Strouse. Dielectric Properties for Nanocomposites Comparing Commercial and Synthetic Ni- and Fe_3O_4-Loaded Polystyrene. *ACS Omega*, 3(10):12813–12823, 2018.

[203] Patrick Gaiser, Jonas Binz, Bruno Gompf, Audrey Berrier, and Martin Dressel. Tuning the dielectric properties of metallic-nanoparticle/elastomer composites by strain. *Nanoscale*, 7(10):4566–4571, 2015.

[204] Lei Zhu. Exploring Strategies for High Dielectric Constant and Low Loss Polymer Dielectrics. *The Journal of Physical Chemistry Letters*, 5(21):3677–3687, 2014.

[205] Z.-M. Dang, Y. Shen, and C.-W. Nan. Dielectric behavior of three-phase percolative Ni–$BaTiO_3$/polyvinylidene fluoride composites. *Applied Physics Letters*, 81 (25):4814–4816, 2002.

[206] Zhi-Min Dang, Yi-He Zhang, and S.-C. Tjong. Dependence of dielectric behavior on the physical property of fillers in the polymer-matrix composites. *Synthetic Metals*, 146(1):79–84, 2004.

[207] Lucía Fernández-García, Marta Suárez, José Luis Menéndez, Carlos Pecharromán, Rosa Menéndez, and Ricardo Santamaría. Dielectric behavior of ceramic-graphene composites around the percolation threshold. *Nanoscale research letters*, 10:216, 2015.

[208] Jingyu Huang, Aaron Hall, Ivan Jayapurna, Samana Algharbi, Valeriy Ginzburg, and Ting Xu. Nanocomposites Based on Coil-Comb Diblock Copolymers. *Macromolecules*, 54(2):1006–1016, 2021.

[209] Hongyu Gao, Simon Bettscheider, Tobias Kraus, and Martin H. Müser. Entropy Can Bundle Nanowires in Good Solvents. *Nano Letters*, 19(10):6993–6999, 2019.

[210] Sulei Hu and Wei-Xue Li. Influence of Particle Size Distribution on Lifetime and Thermal Stability of Ostwald Ripening of Supported Particles. *ChemCatChem*, 10 (13):2900–2907, 2018.

[211] Bridget Ingham, Teck H. Lim, Christian J. Dotzler, Anna Henning, Michael F. Toney, and Richard D. Tilley. How Nanoparticles Coalesce: An in Situ Study of Au Nanoparticle Aggregation and Grain Growth. *Chemistry of Materials*, 23(14): 3312–3317, 2011.

[212] Luciana Meli and Peter F. Green. Aggregation and coarsening of ligand-stabilized gold nanoparticles in poly(methyl methacrylate) thin films. *ACS Nano*, 2(6):1305–1312, 2008.

[213] Johann Lacava, Anika Weber, and Tobias Kraus. Ageing of Alkylthiol-Stabilized Gold Nanoparticles. *Particle & Particle Systems Characterization*, 32(4):458–466, 2015.

[214] Johann Lacava. *Assembly of gold nanoparticles into regular clusters inside emulsion droplets.* Dissertation, Universität des Saarlandes, Saarbrücken, 24.11.2014.

[215] Takieddine Djebaili, Johannes Richardi, Stéphane Abel, and Massimo Marchi. Atomistic Simulations of the Surface Coverage of Large Gold Nanocrystals. *The Journal of Physical Chemistry C*, 117(34):17791–17800, 2013.

[216] Arshia Atashpendar. *Geometric percolation and electrical conductivity in suspensions of conductive nanoparticles.* Dissertation, Albert-Ludwigs-Universität Freiburg, Freiburg, 11.02.2021.

Appendix A

Additional Data

Comparison of WLI and TEM thickness measurements

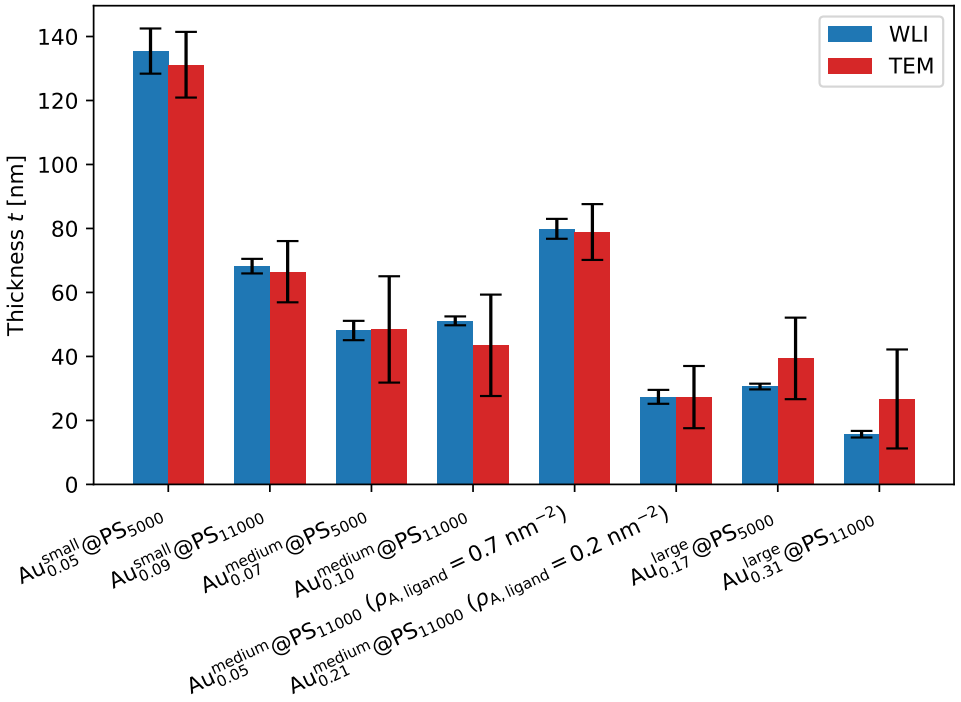

Figure A.1: Comparison of the layer thicknesses measured with white light interferometry (WLI) and with transmission electron microscopy images (TEM) for samples shown in Chapters 5 and 6. If not labelled differently, the samples had a medium ligand density $\rho_{A,ligand}$ with ligand exchange at 60 °C and stirring time 1 week; samples with low and high ligand density $\rho_{A,ligand}$ were prepared for the study in Chapter 5.

Yield of measured thin film capacitors

TABLE A.1: Overview of the yield of the prepared thin film capacitors derived from the number of working capacitors N_{working} and the total number of measured capacitors N_{measured} in this thesis.

Name	Method	N_{working}	N_{measured}	Yield
$Au_{0.05}^{\text{small}}@PS_{5000}$	spin coated	16	23	0.70
$Au_{0.05}^{\text{small}}@PS_{5000}$ ink aged	spin coated	10	12	0.83
$Au_{0.05}^{\text{small}}@PS_{5000}$ solid aged	spin coated	16	20	0.80
$Au_{0.09}^{\text{small}}@PS_{11000}$	spin coated	16	21	0.76
$Au_{0.09}^{\text{small}}@PS_{11000}$ ink aged	spin coated	9	16	0.56
$Au_{0.09}^{\text{small}}@PS_{11000}$ solid aged	spin coated	16	19	0.84
$Au_{0.07}^{\text{medium}}@PS_{5000}$	spin coated	19	39	0.49
$Au_{0.10}^{\text{medium}}@PS_{11000}$	spin coated	24	28	0.86
$Au_{0.05}^{\text{medium}}@PS_{11000}$ ($\rho_{\text{A,ligand}} = 0.7\,\text{nm}^{-2}$)	spin coated	17	27	0.63
$Au_{0.21}^{\text{medium}}@PS_{11000}$ ($\rho_{\text{A,ligand}} = 0.2\,\text{nm}^{-2}$)	spin coated	14	30	0.47
$Au_{0.17}^{\text{large}}@PS_{5000}$	spin coated	11	26	0.42
$Au_{0.17}^{\text{large}}@PS_{5000}$ ink aged	spin coated	12	25	0.48
$Au_{0.17}^{\text{large}}@PS_{5000}$ solid aged	spin coated	14	23	0.61
$Au_{0.31}^{\text{large}}@PS_{11000}$	spin coated	11	19	0.58
$Au_{0.31}^{\text{large}}@PS_{11000}$ ink aged	spin coated	6	15	0.40
$Au_{0.31}^{\text{large}}@PS_{11000}$ solid aged	spin coated	13	17	0.76
PS_{5000}-SH	spin coated	12	24	0.50
PS_{11000}-SH	spin coated	3	9	0.33
$Au_{0.10}^{\text{medium}}@PS_{11000}$ on Si/Al	inkjet printed	2	4	0.50
$Au_{0.10}^{\text{medium}}@PS_{11000}$ on PET/Al	inkjet printed	12	15	0.80

SAXS of aged inks with medium-sized and large Au@PS particles

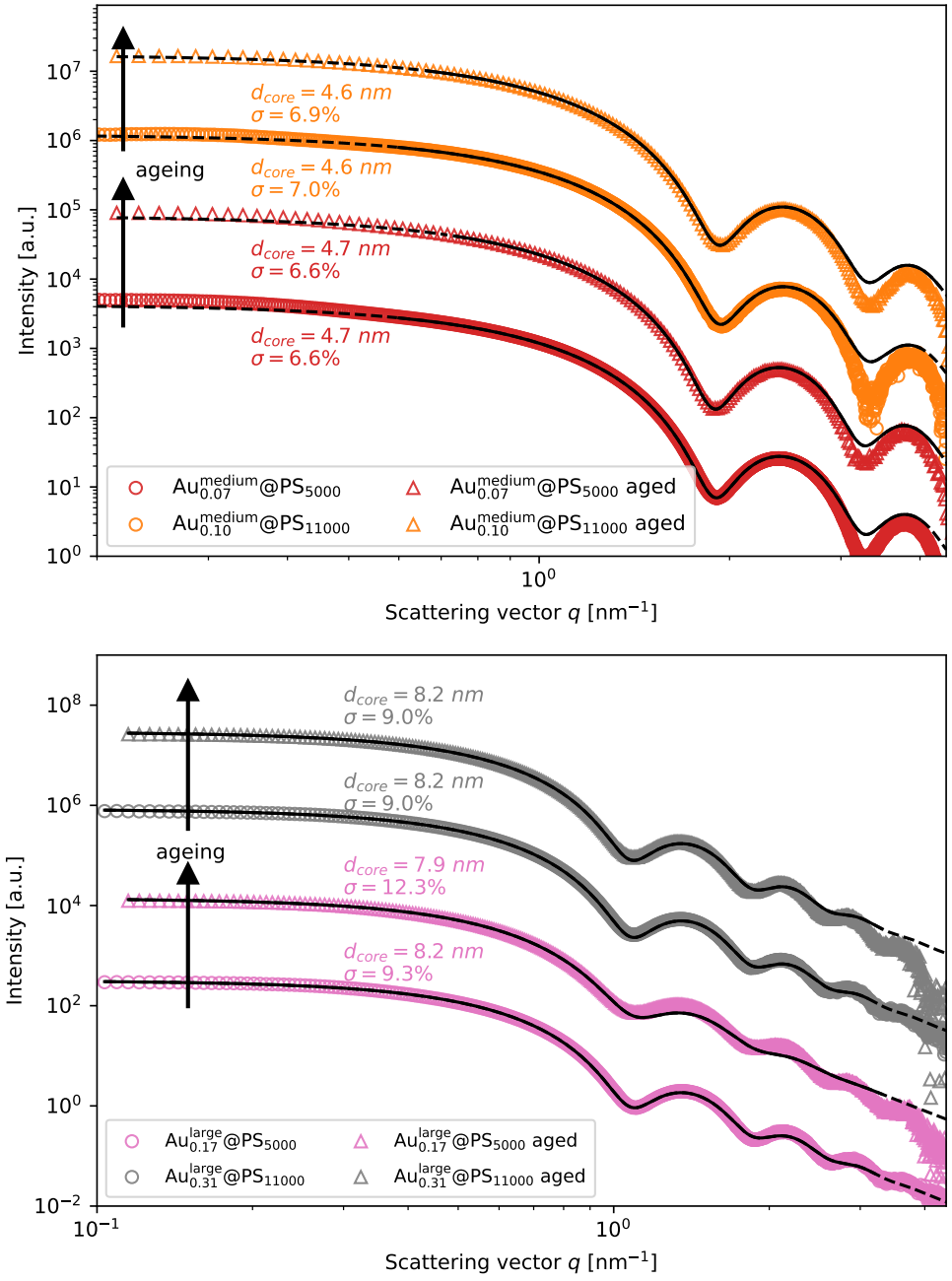

FIGURE A.2: SAXS measurements of Au@PS hybrid inks with medium (top) and large (bottom) core size fresh after synthesis (circles) and aged after respective shelf life (triangles) as indicated with the arrows.

Appendix B

Own Publications

In the following, the author's publications in the context of this thesis are listed.

Written publications

- Roman Buchheit, Björn Kuttich, Lola González-García, Tobias Kraus, Hybrid Dielectric Films of Inkjet-Printable Core–Shell Nanoparticles. *Advanced Materials* 2021, 33, 2103087. https://doi.org/10.1002/adma.202103087

Oral lectures

- Roman Buchheit, Björn Kuttich, Lola González-García, Tobias Kraus. *Dielectric properties of thin gold@polystyrene hybrid nanoparticle films* [Conference presentation]. 16th Zsigmondy Colloquium "Soft Colloids" (9–11 March 2020). Düsseldorf, Germany.

- Roman Buchheit, Lola González-García, Tobias Kraus. *Dielectric properties of nanostructured polymer-metal films* [Conference presentation]. MSE2020 - Virtual Material Science and Exhibition Congress (22–25 September 2020). Web-based congress.

- Roman Buchheit, Björn Kuttich, Lola González-García, Tobias Kraus. *Late News: Printable Dielectric Thin Films of Metal- Polymer Core-Shell Nanoparticles* [Conference presentation]. 2021 MRS Spring Meeting, Symposium: NM05: Functional Nanoparticle Materials - Synthesis, Property and Applications IX (17–23 April 2021). Web-based congress.

Posters

- Roman Buchheit, Anna Zimmermann, Lola González-García, Tobias Kraus. *Dielectric Properties of Au Nanoparticle Layers with Insulating Ligands* [Poster presentation]. Doktorandentag der Fakultät NT der Universität des Saarlandes 2018 (14 November 2018). Saarbrücken, Germany.

- Roman Buchheit, Anna Zimmermann, Björn Kuttich, Lola González-García, Tobias Kraus. *Dielectric Properties of Thin Gold@Polystyrene Hybrid Nanoparticle Films* [Poster presentation]. Particle Based Materials Symposium 2019 (26-27 September 2019). Ulm, Germany.

Danksagung

Zum Schluss möchte ich allen danken, die zum Gelingen meiner Dissertation beigetragen haben. Besonderer Dank gilt meinem Doktorvater Prof. Dr. Tobias Kraus für die Gelegenheit, ein interessantes Forschungsthema bearbeiten zu können, die vielen Diskussionen über die Ergebnisse und die wertvollen Hinweise zum Präzisieren meiner Texte. Priv.-Doz. Dr.-Ing. habil. Guido Falk danke ich für die Übernahme des Zweitgutachtens meiner Dissertation.

Großer Dank gilt all meinen Kollegen im Fachbereich Strukturbildung, ohne die diese Arbeit nicht möglich gewesen wäre. Dr. Lola González-García danke ich für die Betreuung während der Promotionsphase und die Anregungen in vielen Diskussionen. Besonderer Dank gilt für die gegenseitige Unterstützung im Labor, vor allem an Lukas Engel für die vielen praktischen Tipps und Diskussionen, Anna Zimmermann, Indra Backes und Andrea Pyttlik für die Einweisung in die Chemie der Nanopartikelsynthese, Anja Colbus für die tolle Organisation unseres Labors, Robert Strahl für die Unterstützung beim Tintenstrahldruck, Louis Weber für die Tipps bei der Nanopartikelzentrifugation, Timon Dörzapf für die Unterstützung bei einigen Laborarbeiten und Dr. Thomas Kister und Simon Bettscheider für viele anregende Diskussionen. Dr. Björn Kuttich und Dr. Bart-Jan Niebuur danke ich für die SAXS Messungen und die vielen hilfreichen Diskussionen zur Interpretation der SAXS Daten. Dr. David Doblas Jiménez danke ich für die Diskussionen über meine SAXS Daten und für die umfassende Einführung in die Datenauswertung mit Python.

Allen Kollegen am INM danke ich für die gute Zusammenarbeit, die zum Gelingen meiner Dissertation beigetragen hat. Besonders danke ich Dr. Marcus Koch und Birgith Nothdurft für das Erstellen der TEM- und SEM-Bilder sowie FIB-Schnitte, Robert Drumm für die TGA Messungen, der Werkstatt für die Hilfe beim Errichten des dielektrischen Messaufbaus, Wiebke Buhrow von der Arbeitsgruppe von Prof. Dr. Roland Bennewitz für die AFM Messungen und Bruno Schäfer für die Hilfestellung zur optischen Charakterisierung von Schichten. Meinen Bürokollegen Dr. Kira Fries und Dr. Peter Rogin danke ich für eine gute Arbeitsatmosphäre und vielen hilfreiche Diskussionen während der vergangenen Jahre. Ich danke Prof. Dr.-Ing. Frank Mücklich, dass ich am Lehrstuhl für Funktionswerkstoffe WLI Messungen durchführen konnte.

Zuletzt möchte ich noch meinen Mitbewohnern Daria Fedorova und David van Impelen für die ungebrochen gute Stimmung in Zeiten der Mobilarbeit zu Hause während der Coronalockdowns und meinen Freunden sowie meiner Familie für die Unterstützung in der nicht immer einfachen Zeit während der Promotionsphase danken. Vielen Dank!